BEHAVIOUR OF CAISSON BREAKWATER SUBJECT TO BREAKING WAVES

ZHANG XI YING

NATIONAL UNIVERSITY OF SINGAPORE

2006

BEHAVIOUR OF CAISSON BREAKWATER SUBJECT TO BREAKING WAVES

ZHANG XI YING

(M.E., HUST)

A THESIS SUBMITTED

FOR THE DEGREE OF DOCTOR OF PHILOSOPHY

DEPARTMENT OF CIVIL ENGINEERING

NATIONAL UNIVERSITY OF SINGAPORE

2006

致

亲爱的父亲母亲

感谢你们不倦的教诲和无私的关爱!

Acknowledgements

I wish to express sincere gratitude to my supervisors, Professor Leung Chun Fai and Associate Professor Lee Fook Hou for their patient guidance and encouragement during my study in NUS. In particular, the valuable comments and advice of Associate Professor Lee Fook Hou in shaping the final draft of this dissertation is greatly appreciated.

Acknowledgements are also due to:

- Port of Singapore Authority, for the sponsorship of the collaborative research between PSA and NUS.

- Prof. Vrijling, J.K. and Prof. de Groot, M.B. for their valuable suggestions during my study leave in Division of Hydraulic and Geotechnical Engineering, Delft University of Technology, Netherlands in 2001.

- Mr Shen Rui Fu for his help in research problem discussion.

- Mr Wong Chew Yuen and Mr Tan Lye Heng, Mdm Jamilah and Mr John Choy for their help in experimental setup and apparatus quotation.

- Dr Zheng Xiang Yuan for his help in writing the Matlab program.

- Fellow research scholars, such as Mr Okky, Dr Chen Xi, Mr Cheng Yong Gang, Mr Yang Hai Bo, for their friendship and assistance in Latex and Matlab.

- My best friends, Mr Zhang Jian Xin and Mr Liu Tao, for their always care and encouragement.

The study is sponsored by the National University of Singapore Research Grant number R-264-000-119-112. Without this funding, the research program could not be materialized.

Contents

Summary

The cyclic behavior of caisson breakwater on sand and the failure mechanism giving rise to it have been studied in this thesis by both physical and analytical modeling approaches. In the former approach, by means of an in-flight wave actuator system, centrifuge model tests on caisson breakwater subjected to regular, reversal or non-reversal wave loadings were conducted on the National University of Singapore Geotechnical Centrifuge, simulating caisson infilling and wave loading stages. In the latter approach, lump-mass-spring model was used to simulate the oscillatory caisson displacements. An analytical model was also developed to simulate the permanent caisson tilt based on partial optimization of a circular slip surface. The validity of the two models is evaluated against centrifuge test results.

Results of centrifuge tests suggest that caisson response appears to be sensitive to irregularities in regular, non-reversal wave loading. In this study, two types of irregularities were observed. The first is a wave spike, which has a peak load that is much higher than the designed wave cycles. The second is a suction wave, that is, a wave cycle which has a small amount of reversal loading. The effects of these irregularities were observed to be much more significant than the effects of sand bed relative density (RD). Excess pore pressures are generally small and appear insignificant. The results of parametric studies conducted to examine the effects of RD of sand bed, caisson width,

caisson weight, presence of rock berm, slamming on top slab of caisson and cyclic preloading on the behavior of caisson breakwater are also presented in the thesis.

When a caisson breakwater is subjected to regular, reversal wave loads, positive pore pressure are generated which softens the sand bed and hence reduces the shear strength of the soil. RD of sand bed is the key factor that influences the movement of caisson breakwater and the pore pressure build-up. Although strong wave loading may be detrimental to foundations with partial liquefaction occurring in a loose sand, the likelihood of failure is greatly diminished with increasing RD of sand bed. The two different mechanisms associated with wave spikes and reversal wave loading have to be addressed differently in design. For the case of reversal wave loading, the results suggest that densification of sand bed is a possible solution. On the other hand, dynamic analysis may well be viable to tackle the wave spike events.

The results of dynamic analysis showed a reasonably good agreement between the magnitudes of computed and measured oscillatory and permanent tilting displacements of the caisson, but the phase angle does not match well. In wave spike events, exceedence of shear resistance is found to be the mechanism causing the observed permanent deformation. Moreover, by appropriately normalizing the parameters from a wide range of soil properties, foreshore geometry, wave and structure parameters, the tilt angle for one wave cycle are summarized in chart form and bounded into a certain range. The charts may be used for predictive purposes.

List of Tables

List of Figures

List of Notations

Chapter 1

Introduction

1.1 Caisson Breakwater: A Harbor Protection Structure

Breakwaters and related marine structures are primarily built to provide protection against wave effects on ship moorings, maneuvering areas, port facilities and adjoining areas of land. Other functions of breakwaters include reducing the amount of dredging required at the harbor entrance and shielding currents at the entrance channel or along a coast. Harbor breakwaters and related marine structures can be divided into two different categories:

- Rubble mound structures with permeable and rough side slopes

- Caisson type structures which are impermeable with vertical or very steep faces as shown in Fig. 1.1.

A caisson breakwater is a box-type structure that sinks through water to the prescribed depth to protect the coast line from wave attack. It is frequently employed for harbor protection around the world because of its relatively low construction cost and short installation time when compared with rubble mounds (Takahashi, 1996). The construction of a typical caisson breakwater involves the following activities:

(1) Dredging, formation and densification of sand key foundation,

(2) Floating, towing and aligning the caisson to form a row,

(3) Infilling the caisson breakwater with sand.

1.2   Potential Problems Caused by Wave Loading on Caisson

Oumeraci (1994a) reviewed 17 failure cases of vertical breakwaters in deep waters in Europe, Asia, Africa and South America. He established that large wave impacts could generate severe loads to induce the failure of the breakwater-foundation system. The major reasons for failure include the exceedance of design wave conditions, breaking waves, wave overtopping, weakness of concrete, seabed scour and erosion, erosion of rubble mound foundation and differential settlement (Fig. 1.2). As shown in Fig. 1.3, the foundation is checked for stability against sliding, overturning, settlement followed by slip failure and tilting. In the past several decades, the stability of caisson breakwater has been investigated (e.g. Takahashi, 1996; de Groot et al., 1999; Oumeraci et al., 2001) and issues related to bearing capacity and overturning have been examined by Terashi and Kitazume (1987), Kobayashi (1987a), Sekiguchi and Ohmaki (1992) and Sekiguchi and Kobayashi (1994) among others. In addition, local failure modes also need to be thoroughly examined such as erosion, punching failure and seabed scour at seaward and shoreward edges as illustrated in Fig. 1.3. The present study will focus primarily on the overall stability of the structure-foundation system in deep water, with the wave impact force in the consideration.

1.3   Necessity of Dynamic Analysis

The stability of caisson breakwater foundation is usually analyzed as a pseudo-static problem, which considers the dynamic effects as a static overload and neglects the cyclic loading effects. Such analysis is not applicable if the magnitude of breaking wave force is large. Existing studies and case histories revealed that most of the collapses of caisson breakwater were caused by the impulsive loads due to breaking waves (e.g. Hitachi, 1994 and Takahashi et al., 1994a). The wave-generated loads with a short rising time are generally called impact loads. The response of a structure to such load depends on the resonance-frequencies of the structure and the variation of load with time. The energy imposed on the structure caused by impact loads are much larger than that by regular waves. Hence the caisson movements, soil movement and excess pore water pressure build-up of the foundation soil are more severe. Therefore, the stability of caisson breakwaters exposed to wave impacts is a dynamic and multi-disciplinary problem requiring consideration of soil, structure and fluid dynamics.

With the rapid increase in sea cargo traffic and draught of large vessels, caisson breakwaters are likely located in deep open seas with unprotected boundaries and water depth as deep as -35 mCD. Catastrophic failures of vertical seafront structures in deep open seas had occurred in many parts of the world. The impulsive wave loads are transferred to the foundation soil through swaying and rocking of the structure (Oumeraci, 1994a). Nowadays, more attention is being paid to the configuration of caisson breakwater and its potential damage induced by impulsive wave loads.

1.4   Scope and Outline of Thesis

The present study aims to examine the performance of caisson breakwaters on sand beds subjected to impulsive breaking wave loads with sea bed at -20 mCD by means of physical and analytical modelings. The physical modelling was carried out on the National University of Singapore (NUS) Geotechnical Centrifuge using $1/100^{th}$ scaled model caisson. The behavior of caisson breakwater were studied under regular, non-reversal as well as reversal wave loading. An in-flight wave simulator with high excitation frequency using servo-controlled electric actuator has been developed. To ensure the consistency between dynamic and consolidation time scaling, centrifuge model tests on saturated sands were conducted using viscous silicone oil as model pore fluid. On the other hand, a simple analytical model was developed to back-analyze the field results published in the literature review and tilting behavior of caisson breakwater in the present centrifuge model study. Moreover, the tilt angle per wave cycle were summarized into parametric studies for predictive purposes.

   The following section briefly describes the contents of each chapter that follows:

- Chapter 2 presents a review of work done by other researchers on the stability of caisson breakwaters subject to breaking wave loads covering 1g model studies, centrifuge model studies, numerical and analytical studies.

- Chapter 3 introduces the details of centrifuge modeling, covering principles of scaling laws, wave actuator apparatus, data acquisition and servo-control systems, experimental set-up and test procedures.

- Chapter 4 covers the interpretation of experimental data of caisson performance

in regular, non-reversal wave loading tests.

- Chapter 5 presents and discusses a series of centrifuge test results of caisson breakwater subject to regular reversal wave loading.

- Chapter 6 covers the development of an analytical model for the oscillatory and permanent tilt displacements of caisson breakwater exposed to wave storms. Some parametric studies are also carried out.

- Chapter 7 summarizes the main findings of the present study and discusses design implications based on the findings. Besides, recommendations are made for future studies.

(a) Vertical Caisson
    Breakwater

(b) Composite Caisson
    Breakwater

(c) Armoured Caisson
    Breakwater
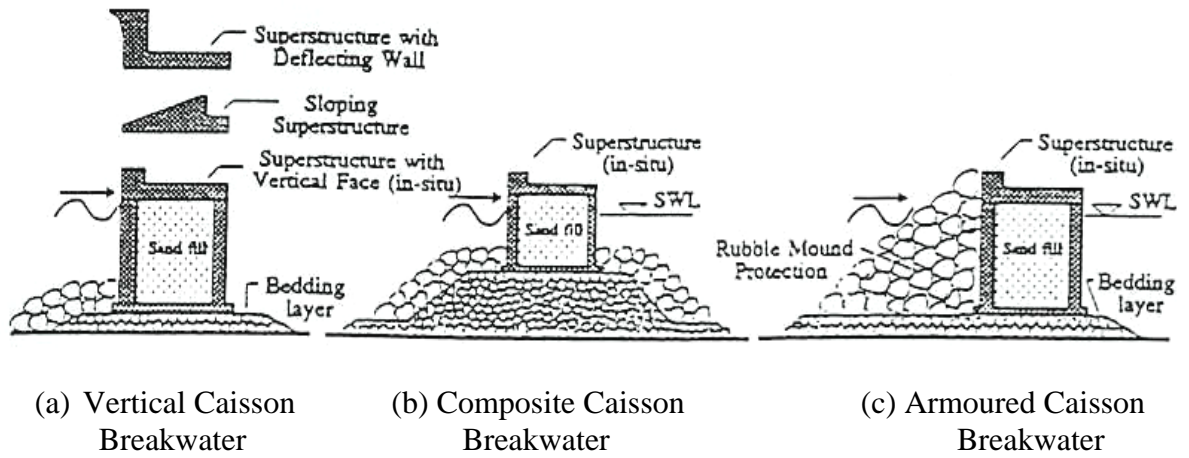
Fig.1.1 Three different types of vertical breakwaters (after Oumeraci et al., 1994b)
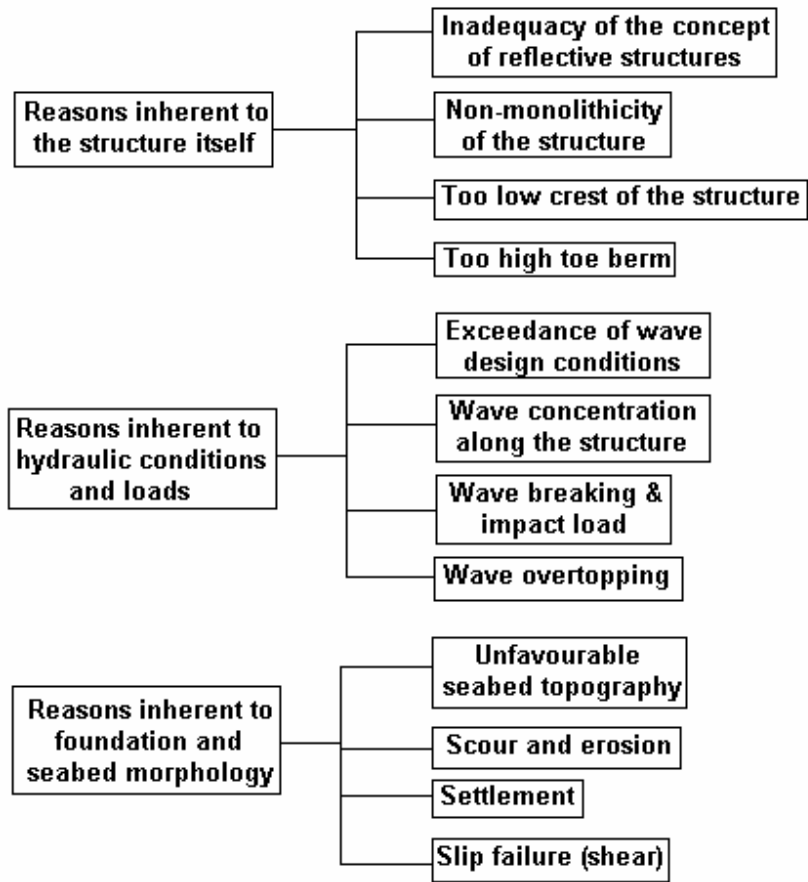
Fig. 1.2 Reasons for failure of vertical structures (after Oumeraci, 1994a)

Overall Failure Modes

a) Sliding

b) Overturning

c) settlement followed by slip failure & seaward tilt

d) settlement followed by slip failure & seaward tilt

Local Failure Modes

e) Erosion beneath seaward & shoreward edges

f) Punching failure at seaward & shoreward edges

g) Seabed scour & toe erosion
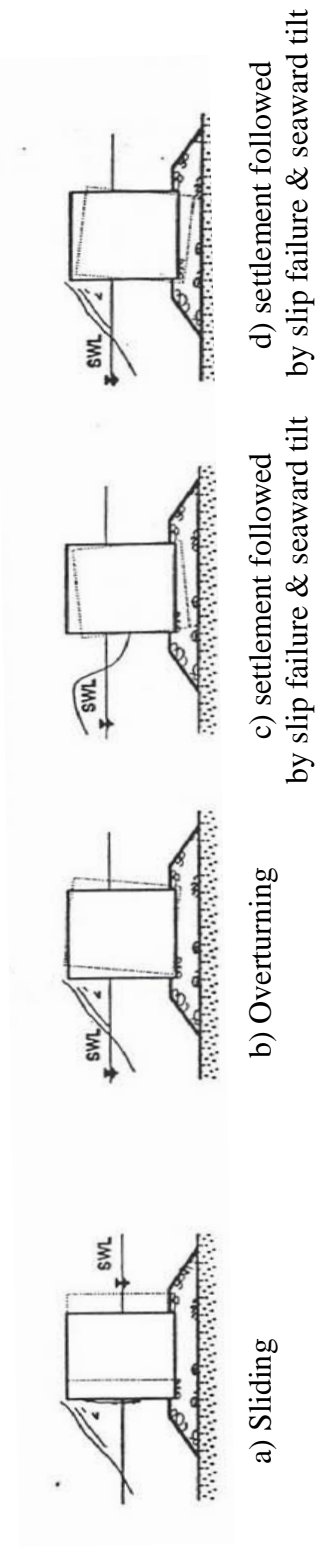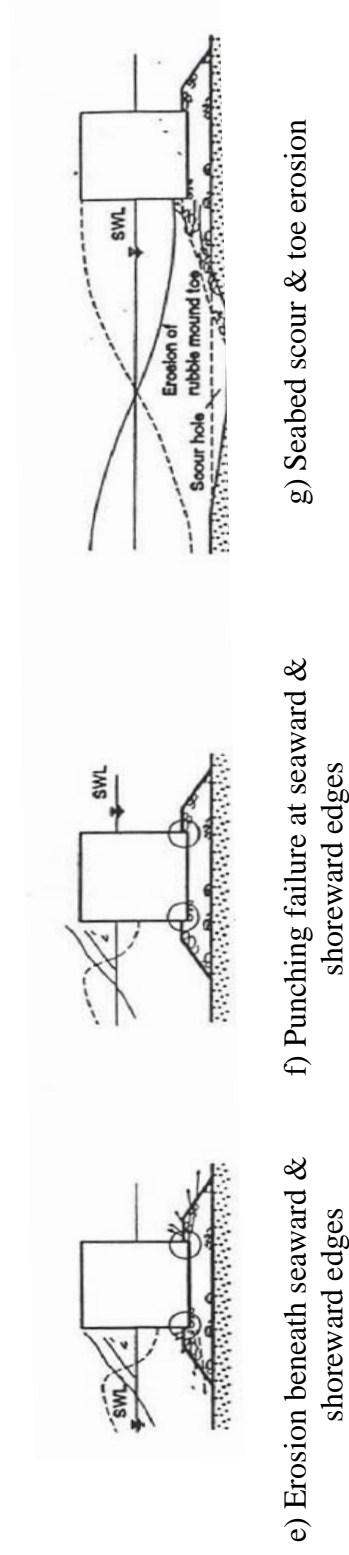
Fig. 1.3 Modes of failure of monolithic vertical breakwaters (after Oumeraci, 1994a)

Chapter 2

Literature Review

2.1   Introduction

A fairly large number of severe and catastrophic failures of caisson breakwater had taken place in the 1930s. In view of huge reconstruction costs, the vertical type of breakwater was almost abandoned in favor of the rubble mound type breakwater. After a series of catastrophic failures experienced by large rubble mound breakwaters at the end of 1970s and the beginning of 1980s, a number of actions were taken to revive the use of vertical breakwaters and the development of new breakwater concepts (Oumeraci, 1991). Furthermore, in order to suit the increasing draught of large vessels, breakwaters were increasingly founded in deeper water, thus making the cost of such structures more prohibitive. In this respect, a type of structure is needed which represents a better alternative not only in terms of technical performance and total cost, but also in terms of standardization, quality control, environmental aspects, construction time and maintenance.

Existing studies of caisson breakwater cover case histories, failure modes, foundation aspects, structure aspects and probabilistic design tools. Since early 1970s, there had been an increased interest in the soil-structure-foundation interaction and dynamic

behavior of caisson breakwater due to wave loads. The studies can be broadly divided

into three categories:

(1) 1g model studies,

(2) Centrifuge model studies, and

(3) Analytical and numerical studies.

2.2   1g Model Studies

2.2.1   Yamamoto et al. (1981)

The head of the west breakwater in the Himekawa Harbour was damaged by big wave

storms in 1978. Previously design waves in Himekawa Harbour were estimated by

numerical modification of regular waves. Yamamoto et al. (1981) considered that the

breakwater had been damaged because waves larger than the design waves struck the

breakwater. The design waves were subsequently estimated by random wave tests as

shown in Fig. 2.1. The model scale was fixed at 1/120 after consideration of the wave

generator performance, wave height, and the size of wave basin. The results showed that

the wave-height distribution along the west breakwater was different from that obtained

by the regular wave computation and that, as the wave converged, the wave height

became larger at the damaged location of the breakwater. Yamamoto et al. (1981)

also performed several stability tests to simulate the actual conditions, and the sliding

distance of the caissons. He concluded that the caisson sliding distance obtained by the

random wave tests was smaller than that obtained by regular wave tests.

2.2.2   Oumeraci et al. (1992)

Hydraulic model tests and pendulum tests were performed by Oumeraci et al. (1992) in a large wave flume in Hannover on caisson breakwater with rubble mound foundation lying on sand bed as shown in Fig. 2.2. Horizontal impact force, uplift forces and the related overturning moments were determined. Oumeraci et al. (1992) attributed the free damped nonlinear oscillations of the structure foundation to the plastic deformation of the foundation, as well as the hydrodynamic mass and geodynamic mass both of which increase with the amplitude of oscillation of the structure.

2.2.3   Klammer et al. (1994)

The relationship between impulsive loading induced by wave breaking on a caisson breakwater and the subsequent displacements was studied by Klammer et al. (1994) in a wave flume. The caisson model consisted of two distinct parts which can move independently of each other, as illustrated in Fig. 2.3. The first part was used for the measurement of impact pressure in front of caisson, the uplift pressure on caisson bottom, as well as the acceleration and displacements of caisson. The second part was used for the measurement of total horizontal force on the caisson structure.

Klammer et al. (1994) noted that for oscillatory motions with small peak amplitude, almost no permanent caisson displacement occurred. However, when the amplitude was larger than a certain value, permanent displacements started to occur, suggesting that there was some threshold value above which permanent displacement was initiated. Klammer also found that successive permanent displacement may accumulate and lead to collapse of the structure.

2.2.4   Kimura et al. (1996)

Small scale model tests were conducted by Kimura et al. (1996) to investigate the stability of a breakwater subject to tsunamis so as to determine better damage prevention measures. The model was a 1/40 scale of the North Breakwater in Okushiri Port, Japan (see Fig. 2.5). Kimura et al. (1996) found that an increase in buoyancy due to increase in water depth was more responsible for damage than an increase in wave pressure on the front of the breakwater. Moreover, the stability against sliding was significantly influenced by the mound conditions. The stability enhanced when the mound extended toward the rear and reinforced with stainless steel micro-piles beneath the caisson base. Kimura et al. (1996) concluded that an unnecessarily heavy breakwater or high mound was not advisable as it was easier to sustain fatal damage when exceeding the critical values.

2.2.5   De Groot et al. (1999)

Large scale model tests and field tests on existing breakwaters have been performed by De Groot et al. (1999) to evaluate a simple spring-mass model and to study non-stationary effects in the pore flow. These were done with the analytical equations and finite element computer code TITAN. De Groot et al. (1999) characterized the foundation response by the inertia of the caisson and the non-stationary pore water flow in the rubble mound. It was found that the spring-mass model with 2 degrees of freedom can be used to quantify the influence of inertia on the foundation loading. The spring coefficient and natural periods can be determined by equations with reasonable accuracy if the foundation was fairly homogeneous. If the foundation was inhomogeneous, the numerical model was used for an accurate estimate of the foundation response to

impacts.

In addition, De Groot et al. (1999) attributed the direct flow to the water pressure variation at the sea side and on the other hand attributed the indirect flow to the caisson movements, as indicated in Fig. 2.6. In case of non-breaking waves, the pore water flow in the rubble mound without caisson movement was generally considered as a quasi-stationary event and the pressure head was assumed to vary linearly along the bottom of caisson. The non-stationary flow due to caisson movement which was caused by wave impact from breaking wave was thought to have both favorable and unfavorable effects. It may enlarge the uplift force with up to 30% compared to the value found with stationary flow, which often occurred when the caisson fell back to the soil bed. However, more than 30% reduction of the uplift force can be found at the moment of maximum impact load.

2.3   Analytical and Numerical Modeling

2.3.1   Tsai et al. (1990)

A linear two-dimensional analytical model for soil responses due to waves and caisson motion was proposed by Tsai et al. (1990). The caisson was founded on a rubble bedding layer overlying a linearly poro-elastic soil of finite depth. Two approximations were employed to solve the boundary-value problem analytically: (1) a boundary layer approximation to decouple pore pressure and soil motion in the Biot equations; and (2) a contact solution approximation for a thin elastic layer to address the missed-type mud line condition. Tsai et al. (1990) found that the caisson motion induced much larger displacements, stresses, and pore water pressure in the soil than the wave alone, which indicated that the caisson-foundation interaction necessitated a dynamic analy-

sis. Under the caisson, the pore water pressure in the soil increased with depth because of confinement by the impermeable rigid boundary below, which were observed in both analytical and physical models. The predicted pore water pressure agreed reasonably well with the measured field data. However, the analytical and experimental comparison of horizontal, vertical and rotational caisson displacements showed highly variable degrees of concurrence. Tsai (1990) attributed it to a very poor noise-to-signal ratio in the displacement measurements.

2.3.2   Sekiguchi et al. (1992)

Caisson stability against overturning subject to wave loading was studied by Sekiguchi et al. (1992). They analyzed the stability of a leaning caisson as a single degree-of-freedom system and then derived an expression for the lower bound estimate of the driving moment needed to overturn a caisson as shown in Fig. 2.7. A review was then made on the damages induced to a composite breakwater, which consisted of two adjoining stretches B and C with slightly different size of caissons (see Fig. 2.8) which had been observed to respond very differently under large wave loading. Most caissons in stretch B were overturned, whereas no caisson in stretch C was overturned.

Sekiguchi et al. (1992) attributed the different damage of stretches B and C to two reasons. First, the caissons in stretch B were slightly slender than those in stretch C. Second, the destructive wave heights were slightly greater in stretch B, but they were large enough to overturn the caisson. However, only the limiting overload factor was obtained in the analysis. The analysis could not yield any results on the caisson tilt angle.

2.3.3   Goda (1994)

Goda (1994) derived a relationship for the elastic motion of an upright section of a composite breakwater activated by an impulsive force due to breaking waves. The foundation, including a rubble mound, was represented by a system of mass and dual springs for rotational and horizontal motions (see Fig. 2.9). The validity of the model was later confirmed using a small model test with a concrete block resting on a crushed stone mound being impacted by a pendulum of known momentum. The spring constant of the rubble mound and the sea bed was represented as the coefficient of elastic uniform shear of soil reaction by Goda (1994), and its magnitude for prototype breakwaters was estimated in the range of 100 to 200 tf/m^3. The equivalent pressure of the breaking waves needed to cause breakwater sliding was then estimated to be no more than 3 times the hydrostatic head of the wave height.

2.3.4   Oumeraci et al. (1994c)

Oumeraci et al. (1994c) analyzed the effects of some parameters on the dynamic response of a caisson breakwater subject to breaking wave loads using a numerical model validated by large-scale model tests. The caisson breakwater model, tested in a large wave flume was idealized by a two-degree-of-freedom system as shown in Fig. 2.10 for the computation. The computed angular acceleration in Fig. 2.11 was found to be slightly delayed after the 5th cycle with respect to the measured acceleration. Oumeraci et al. (1994c) attributed the linearity of the oscillating system to a number of effects such as soil parameters as well as added mass of soil and water that were forced to move with the structure. The parametric studies also showed that the amplitude and period of oscillations both decreased with increasing stiffness and a variation of 10% of

the stiffness may affect the dynamic response. However, the period of oscillation and the maximum amplitude of the response were only slightly affected by the variation of damping terms.

2.3.5 Ling et al. (1999)

Ling et al. (1999) proposed a design procedure for caisson breakwater based on permanent displacement and sliding stability. The horizontal wave force and uplift force acting on the caisson were determined from the Goda formula and expressed as a fraction of the effective weight of caisson using wave coefficients. A yield wave coefficient was defined as the horizontal wave force when the limiting condition against direct sliding was reached. For a storm that had a wave coefficient C_h larger than this yield value C_{hy}, rigid-body motion would be induced in the caisson as illustrated in Fig. 2.12. The equation of motion was double-integrated to obtain the magnitude of permanent displacement. The proposed procedure was later compared with 35 case histories among which sliding were observed for 24 cases. For certain cases, the calculated permanent displacement per wave cycle was much larger than the measured one. For other cases, the total number of wave cycles leading to the measured displacement ranged from 2 to 38. Ling et al. (1999) suggested that 20 wave cycles may be reasonable for the consideration of permanent-displacement design.

2.4 Centrifuge Model Studies

2.4.1 Rowe and Craig (1976)

In order to study the incidence of liquefaction and effectiveness of densification methods, an in-situ test was performed by the Laboratorium voor Grondmechanica Delft

(LGM) with a one-third scale model caissons on in-situ and treated ground subjected to static and cyclic loading. Concurrently, two series of centrifuge models were run at the University of Manchester (Rowe and Craig 1976). Rowe and Craig (1976) found that the first series, run before the in situ test, gave a realistic prediction for the caisson on sand densified to 70% relative density. However, the initial in-situ test of undisturbed ground showed a stage of large displacement which differed from model predictions using specified bed of 50% relative density. A second series of model tests, run after the in situ test but before the test data were worked out, showed that only 4-10% loose zones in the foundation would exert a profound influence on temporary liquefaction and associated displacements. Moreover, shakedown and lateral movements were found to accelerate immediately on raising the cyclic force and rapidly attained equilibrium, as shown in Fig. 2.13. Small pore pressure swings were detected but no net increase in pressure was observed (see Fig. 2.14).

2.4.2   Poel and De Groot (1998)

As a part of the European MASK III programme on the probabilistic design of vertical breakwaters, Delft Geotechnics performed centrifuge tests to study the cyclic behavior of caisson breakwater placed on clean and fine sand. The tests were executed by Poel and De Groot (1998) at 60g on a breakwater model, consisting of 3 caissons, placed in a relatively loose sand model with a relative density of 58%. The caissons were loaded by an irregular breaking wave load in the first test and a regular load in the second test, as shown in Fig. 2.15(a) & (b), respectively.

Poel and De Groot (1998) found that the failure mechanism was progressive with a combination of horizontal sliding and tilting. In the first test, there was sufficient time

between the peaks for dissipation of residual pore water pressures. In the second test, the time between peaks was 0.2 s, which was too short for all residual pore pressures to dissipate. Hence, it was considered by Poel and De Groot (1998) that the load signal and load sequence significantly affect the behavior and bearing capacity of caisson break-water due to dissipation of excess pore water pressures between peaks and pre-shearing effects. Large vertical displacements was found to occur in test 2 with regular wave load due to cyclic compaction of the sand as shown in Fig. 2.16. Furthermore, Poel and De Groot (1998) considered that the rotational and horizontal stiffness increased due to cyclic compaction. As the load increased, the stiffness decreased due to plastic effects. The reduction in horizontal stiffness was larger than in rotational stiffness.

2.5   Summary

Caisson breakwaters subject to impact waves are conventionally designed by treating the wave loading as a quasi-static load and then checked for stability against sliding, overturning and bearing capacity failure (PHRI, 1991). Oumeraci (1994a) noted that this design approach may involve an unintended increase in risk because the possibility of dynamic amplification of load on the caisson foundation is not considered in such analysis.

A good number of 1g model studies and full scale model tests on caisson break-waters subject to breaking wave loads have been conducted (e.g. Kimura et al., 1996; Klammer et al., 1994; Marinski and Oumeraci, 1992; Oumeraci, 1991; Yamamoto et al., 1981). However, most of these studies employed relatively short loading episodes, which are unlikely to be representative of wave storm loading on a caisson breakwater. Furthermore, as prototype soil behavior cannot be correctly reproduced in reduced-scale

models tested in 1g conditions, the dynamic response of caisson and its foundation is unlikely to be fully representative of the prototype. Finally, little attention has been paid to the generation and dissipation of excess pore pressure in the foundation soil.

Numerical and analytical models were developed by Shimosako et al. (1994), Ling et al. (1999) and Ling (2001) to estimate the sliding distance of composite breakwaters due to wave forces. The proposed procedure may be simple and practical, but only sliding distance is obtained during the whole wave loading. Sekiguchi (1994) developed an approximate theory of overturning of caisson and proposed an overload factor sufficient to overturn a given caisson, but the specific caisson movement was not obtained. The dynamic response of caisson breakwater has been idealized by a system of mass and spring for horizontal and rotational motions (Goda, 1994; Oumeraci et al., 1994c; Gao et al., 1988). Nonetheless, only elastic motions were calculated and the selection of spring constants is not apparent. A realistic analysis of caisson motion and seabed response may be modeled using Biot consolidation theory (Tsai et al., 1990; McDougal et al., 1986) where the soil stresses, the surface displacement and pore water pressures are modeled realistically. Such a procedure, because of its complex and arbitrary assumptions, is not considered a practical design method.

Rowe and Craig (1976) and Rowe (1981) studied the behavior of caissons subjected to several parcels of cyclic wave loadings using in-situ and centrifuge model tests. In contrast to the 1g tests summarized above, excess pore pressures and their effects on permanent settlement and deformation featured strongly in Rowe and Craig's (1976) and Rowe's (1981) studies. This striking difference suggests that the complexity of caisson-foundation interaction might not have been fully captured in some of the

early studies. Rowe and Craig's (1976) and Rowe's (1981) results indicated that where patches of loose sand underlie the caisson, significant excess pore pressure is likely to be generated and substantial caisson settlement may result. However, the various factors affecting the magnitude of excess pore pressure were not investigated. In addition, Rowe (1981) noted that their model predictions for the lateral displacement were likely to be over-estimated due to an incorrect allowance for elastic strain in the loading rig under the sustained horizontal force. Poel and De Groot (1998) also conducted centrifuge model tests on caisson breakwater subject to regular and irregular breaking wave loads. The results indicated that the response and stability of the caisson are strongly influenced by the wave pattern.

The above review highlights the complexity of caisson-foundation interaction and the multitude of factors which can affect caisson response to wave loading. For instance, many aspects of the cyclic behavior of caisson breakwater, such as the mechanism leading to the build-up of tilting, sliding and settlement, as well as progressive softening of soil bed remain unclear. The needs to study cyclic caisson behavior both experimentally and analytically constitute the main motivation for the present study. This thesis deals with the centrifuge model tests and analytical modeling of caisson behaviour, with emphasis on the following issues:

1) The development of various centrifuge equipments, experimental setups and reliable testing procedures for centrifuge tests on caisson breakwaters subject to breaking wave loads.

2) The investigation of different loading patterns, such as regular non-reversal and reversal wave loading on the movements of caisson breakwater and pore pressure

build-up of soil bed using centrifuge modeling technique.

3) Further studies into the caisson behavior upon regular, non-reversal wave loading with emphasis on

   a) Examination of degree of densification of sand bed to resist a given wave loading condition,

   b) Arriving at an optimum caisson dimension for the given water depth and wave loading conditions,

   c) Studying the effect of weight of caisson on the performance of caisson breakwater,

   d) Investigating the effect of presence of rock sill on limiting the horizontal sliding of caisson,

   e) Investigating the effect of slamming on caisson top slab when the caisson breakwater is exposed to impulsive wave loading,

   f) Studying the effect of cyclic preloading on caisson movements.

4) The study of different loading strength and RD of soil bed on the movements of caisson breakwater upon reversal wave loading.

5) The development of an analytical model to back-analyze the tilting movements of caisson breakwater.

The present research hopes to establish the key control parameters of caisson breakwater, which could help improve the understanding of stability and failure mechanism

of caisson breakwaters, and developing proper tools for port engineers for the dynamic

analysis of such structure.
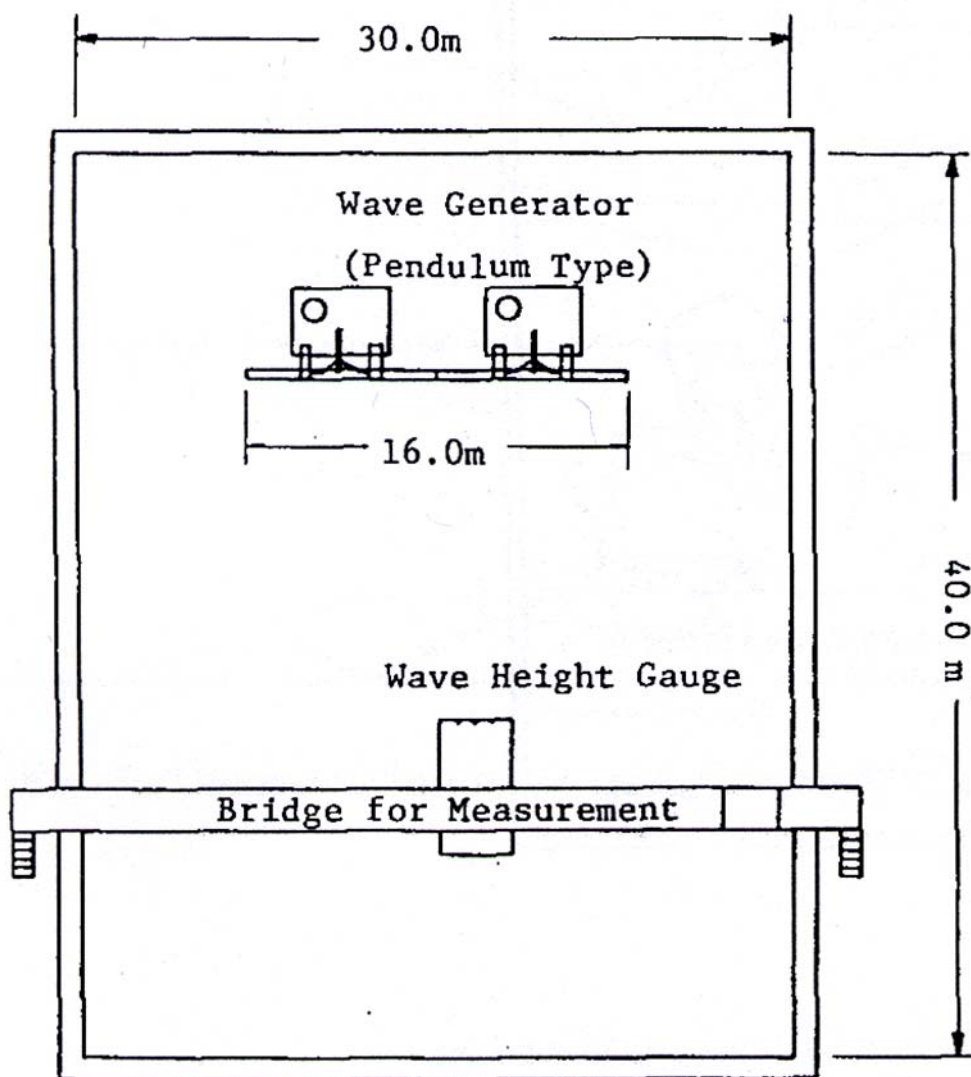
Fig. 2.1 Three dimensional wave basin (after Yamamoto, 1981)
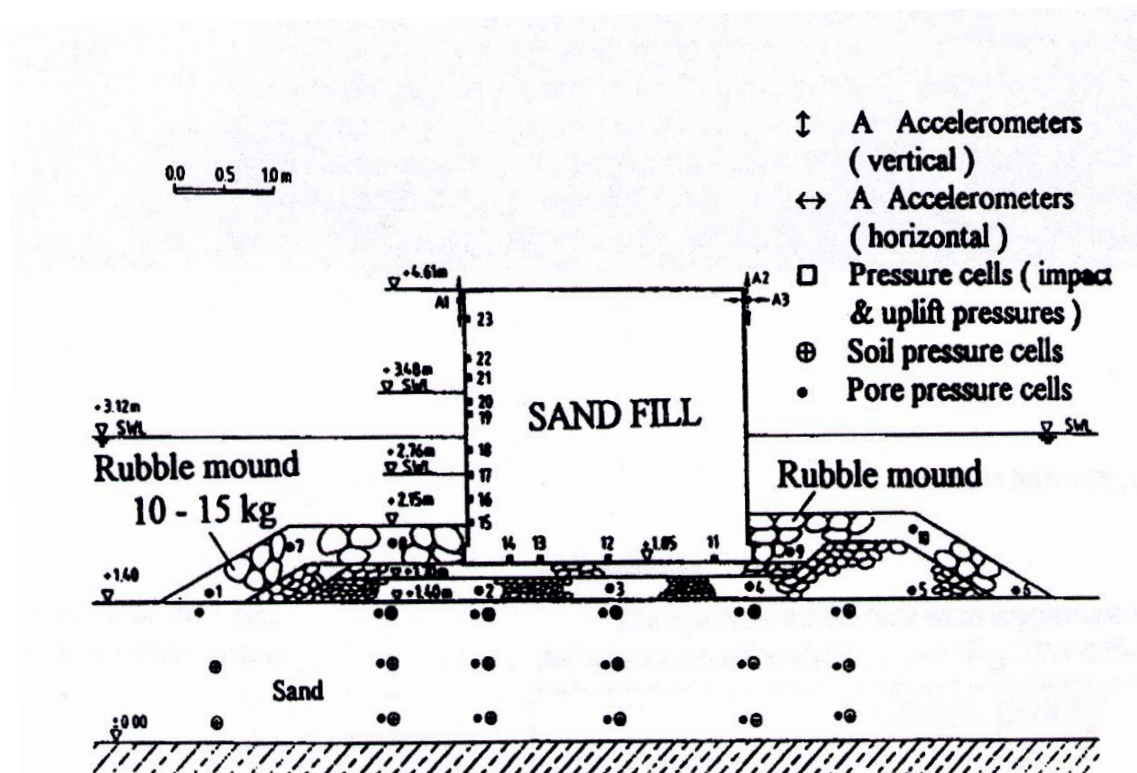
Fig. 2.2 Caisson breakwater test in large wave flume (GWK) (after Oumeraci, 1992)
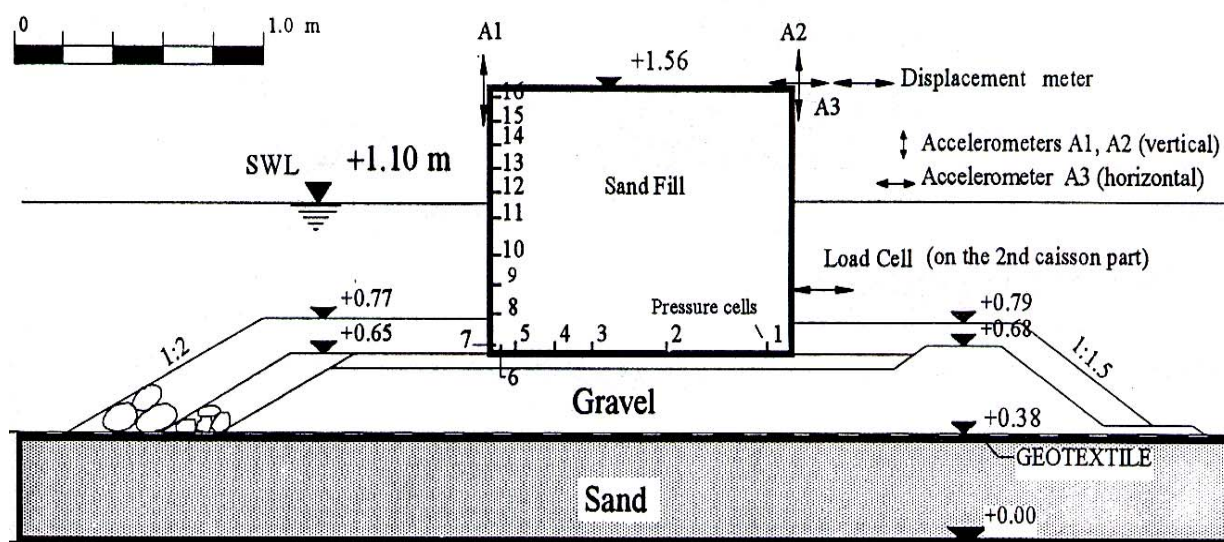
Fig. 2.3 Instrumented model caisson breakwater (after Klammer et al., 1994)
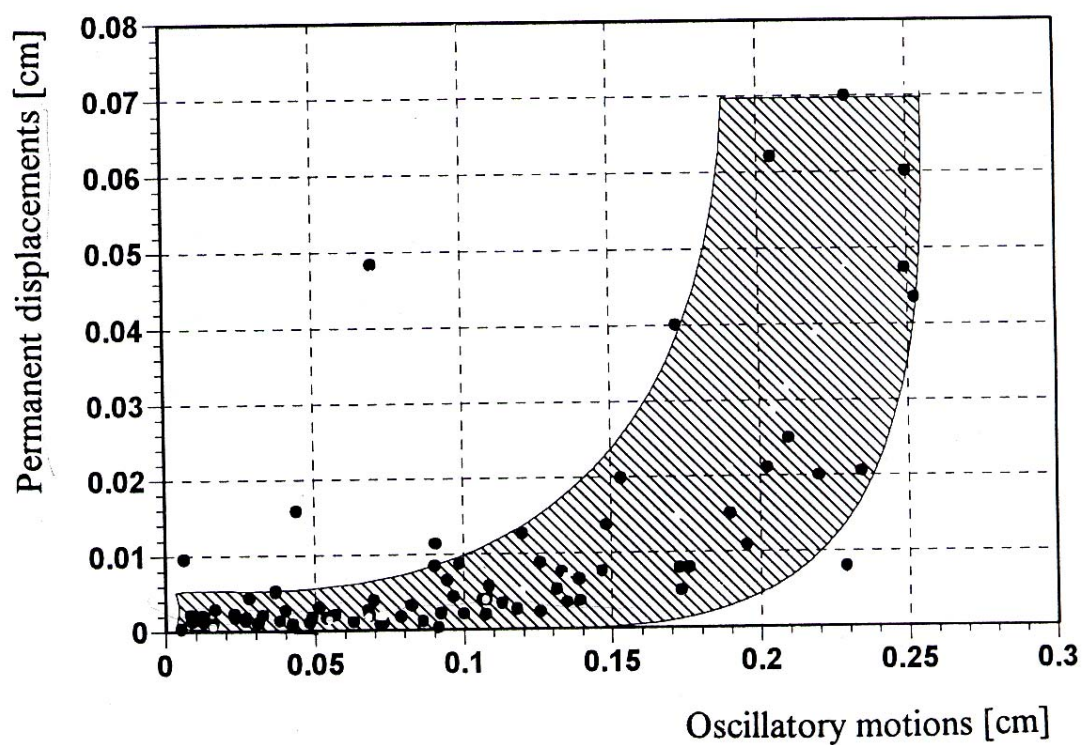
Fig. 2.4 Peak values of oscillatory motions vs. permanent displacements (after Klammer et al., 1994)
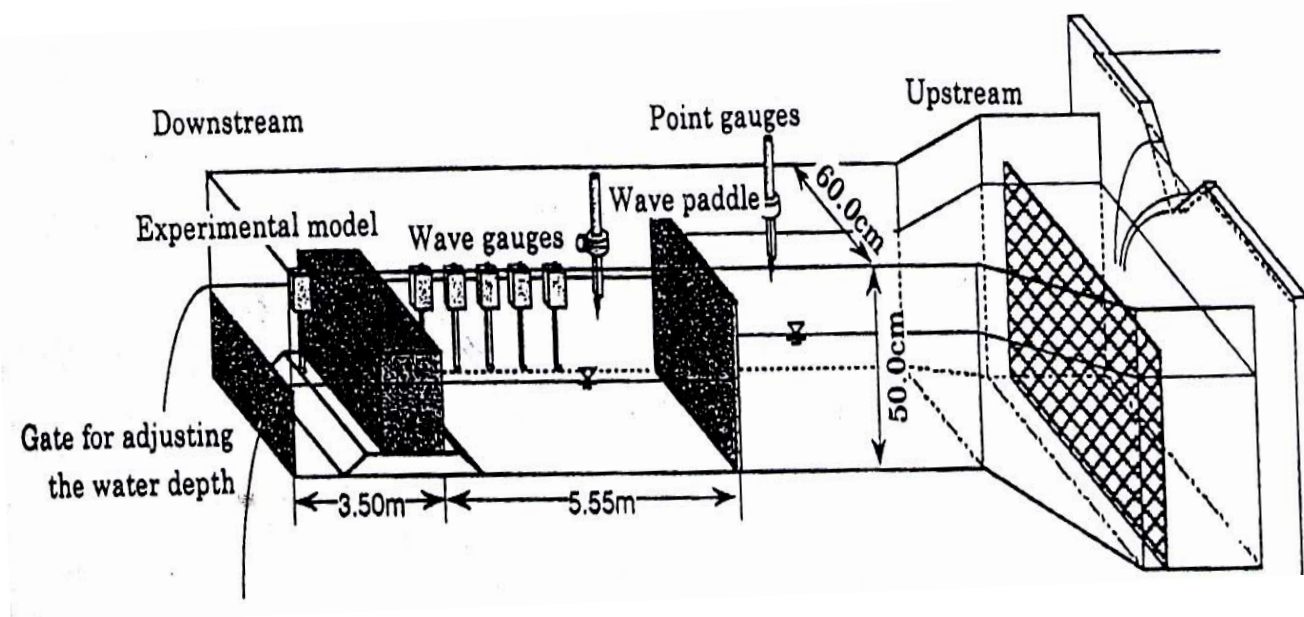
Fig. 2.5 Experimental channel and position of model (after Kimura et al., 1996)
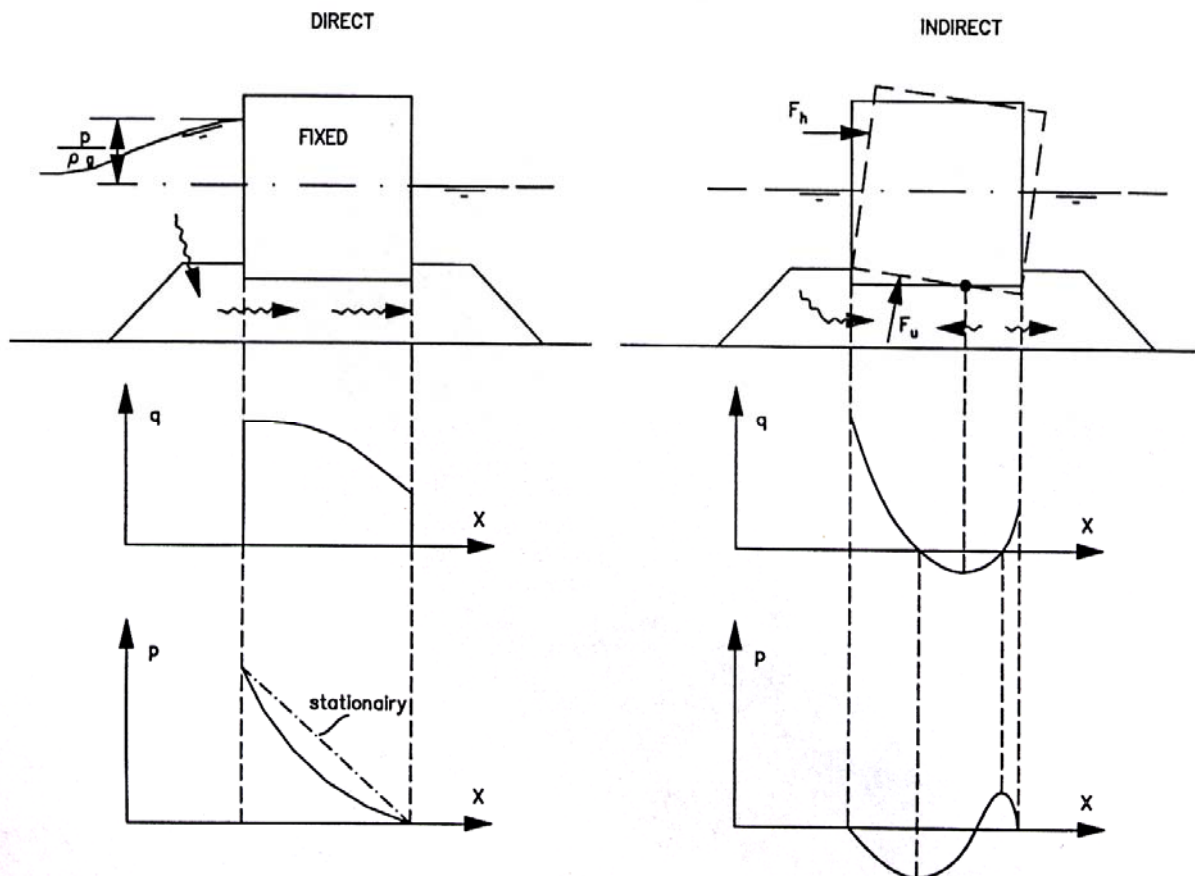
Fig. 2.6 Pore pressures in mound: distinction between direct and indirect components
(after de Groot et al., 1999)
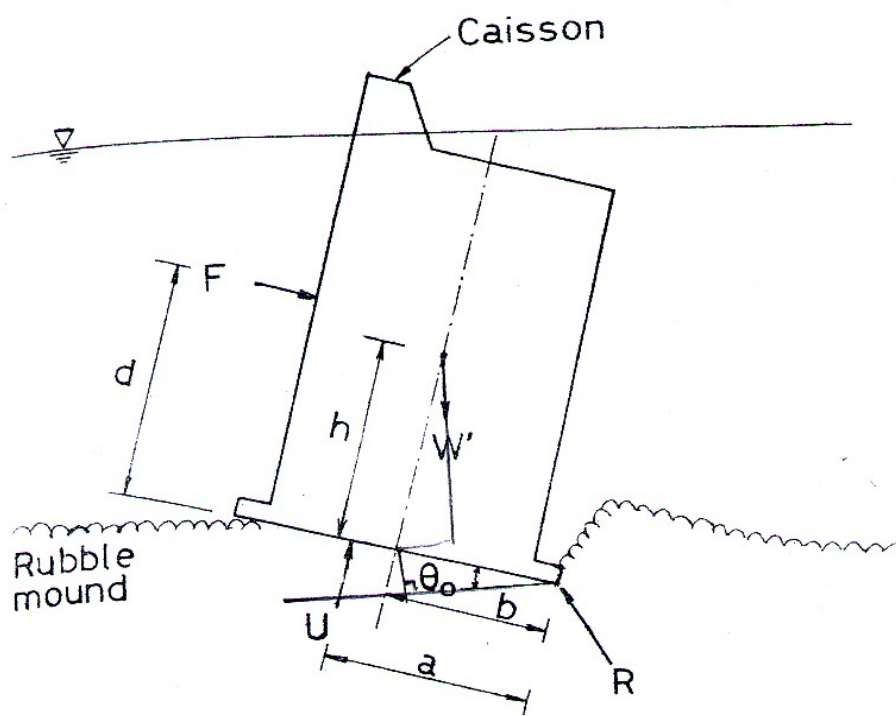
Fig. 2.7 Sketch illustrating forces acting on a leaning caisson

(after Sekiguchi et al., 1992)

$H_{1/3} = 4.7$ m

$T_{1/3} = 10.0$ s
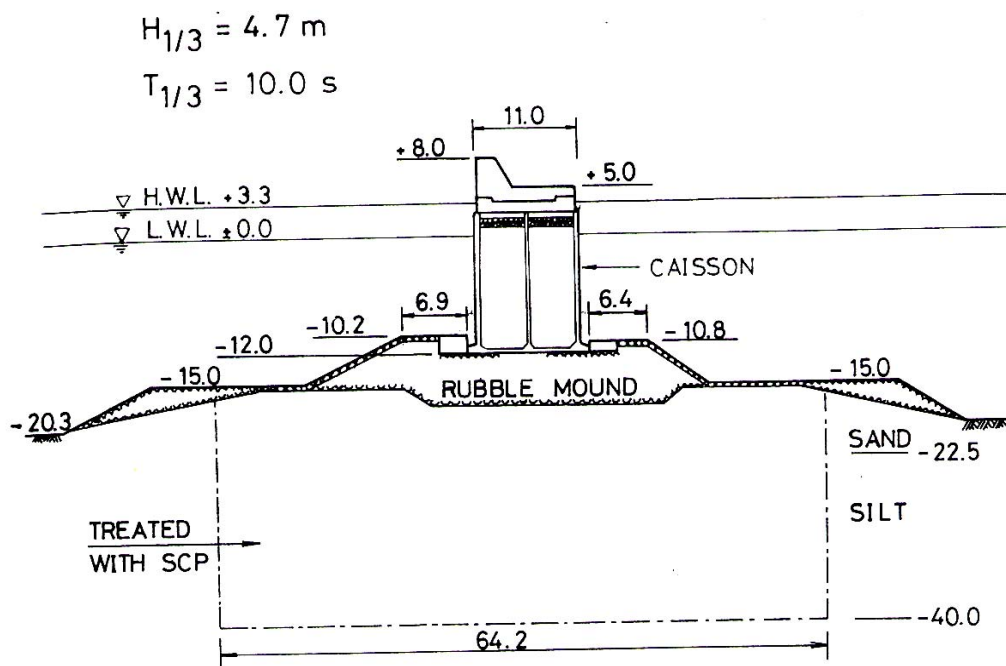
(a) Representative cross section through Stretch B (Length in meters)

$H_{1/3} = 5.5$ m

$T_{1/3} = 10.0$ s
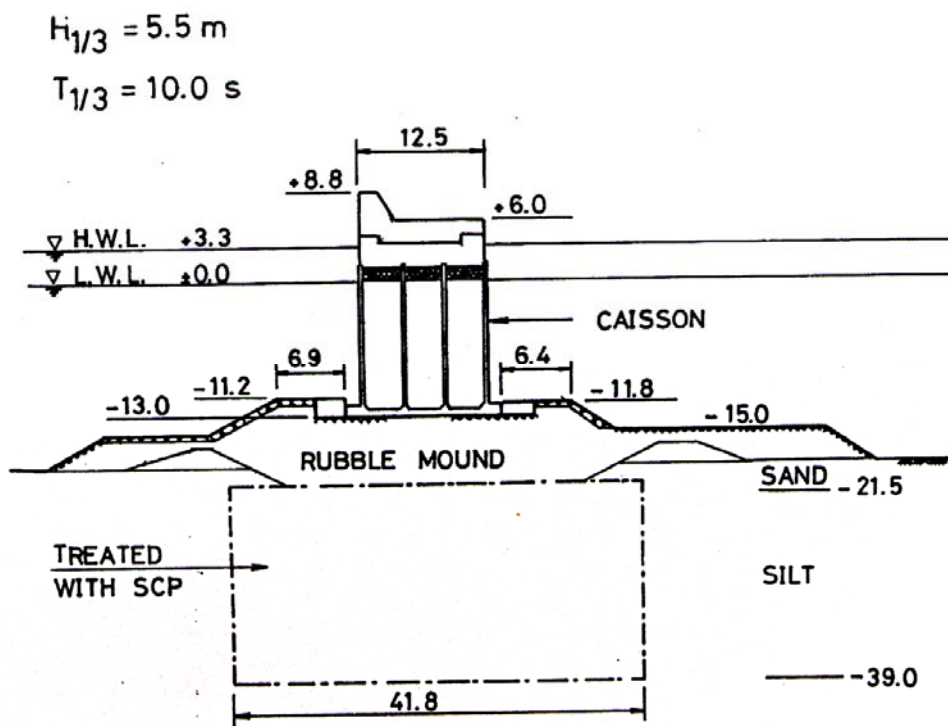
(b) Representative cross section through Stretch C (Length in meters)
Fig. 2.8 Cross-section of caisson breakwaters (after Sekiguchi et al., 1992)
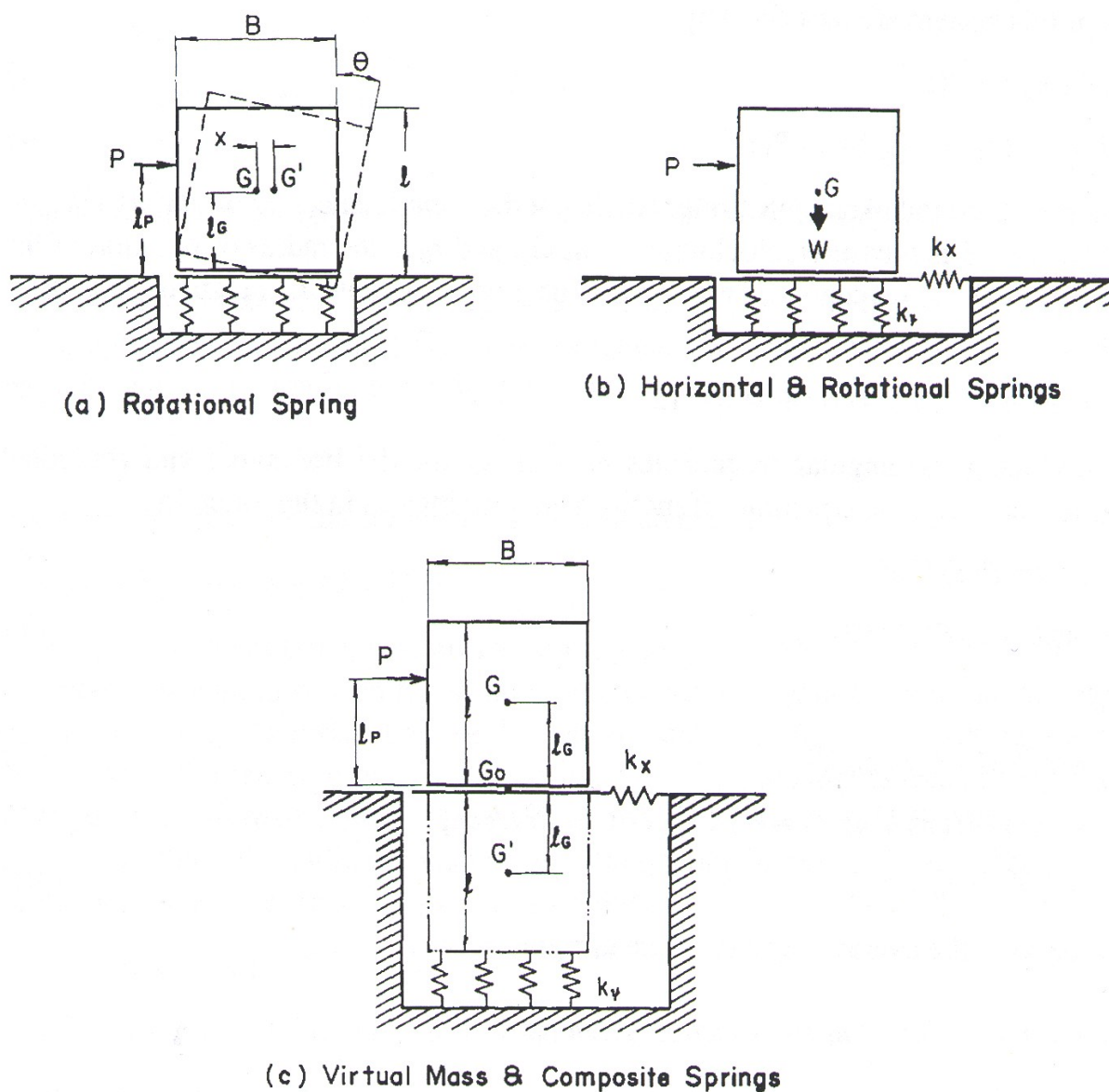
Fig. 2.9 Mass and spring models of upright breakwater and its foundation
(after Goda, 1994)
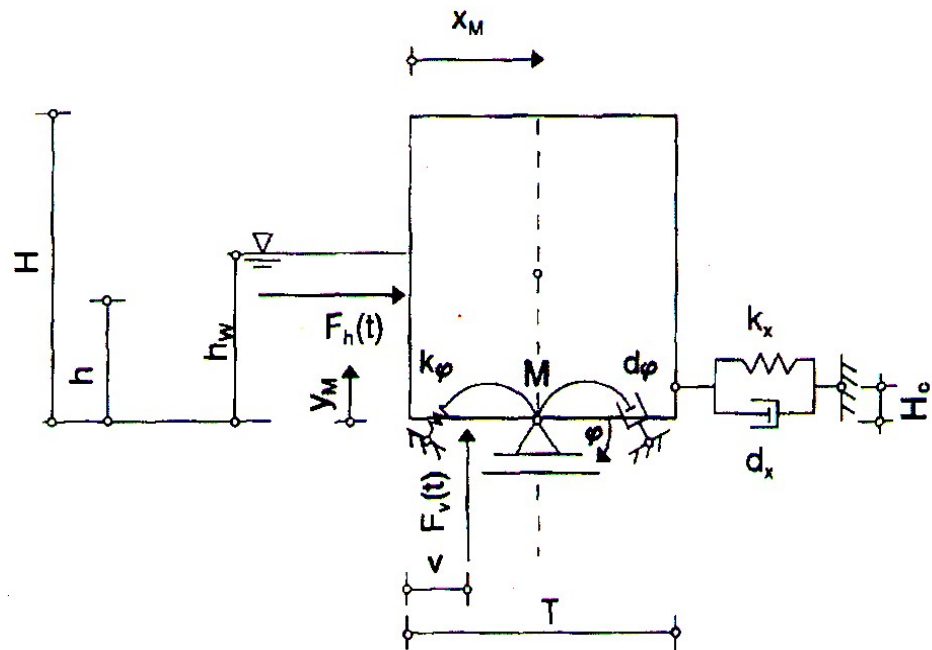
a) Lumped System
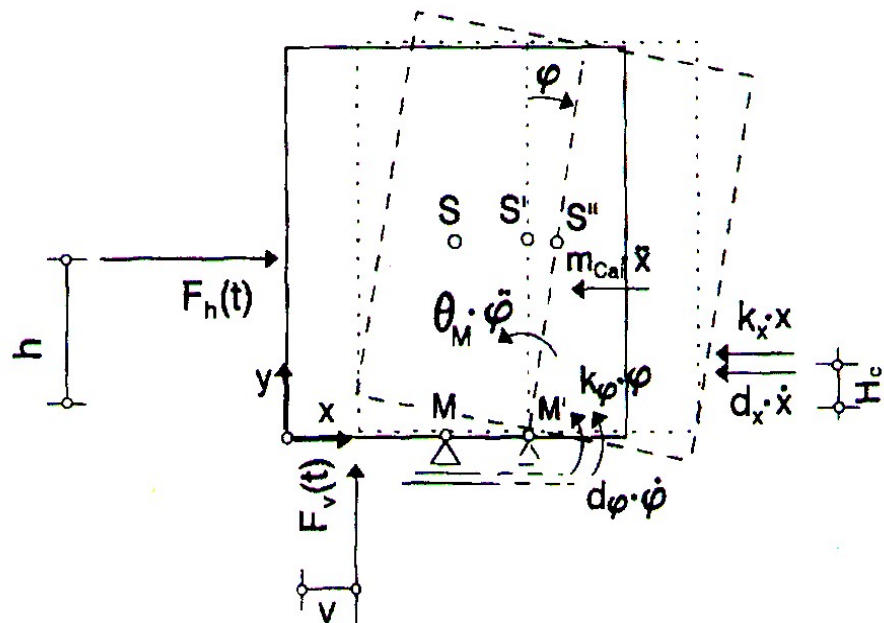
b) Modes considered

Fig. 2.10 Idealized lumped system (after Oumeraci et al., 1994c)
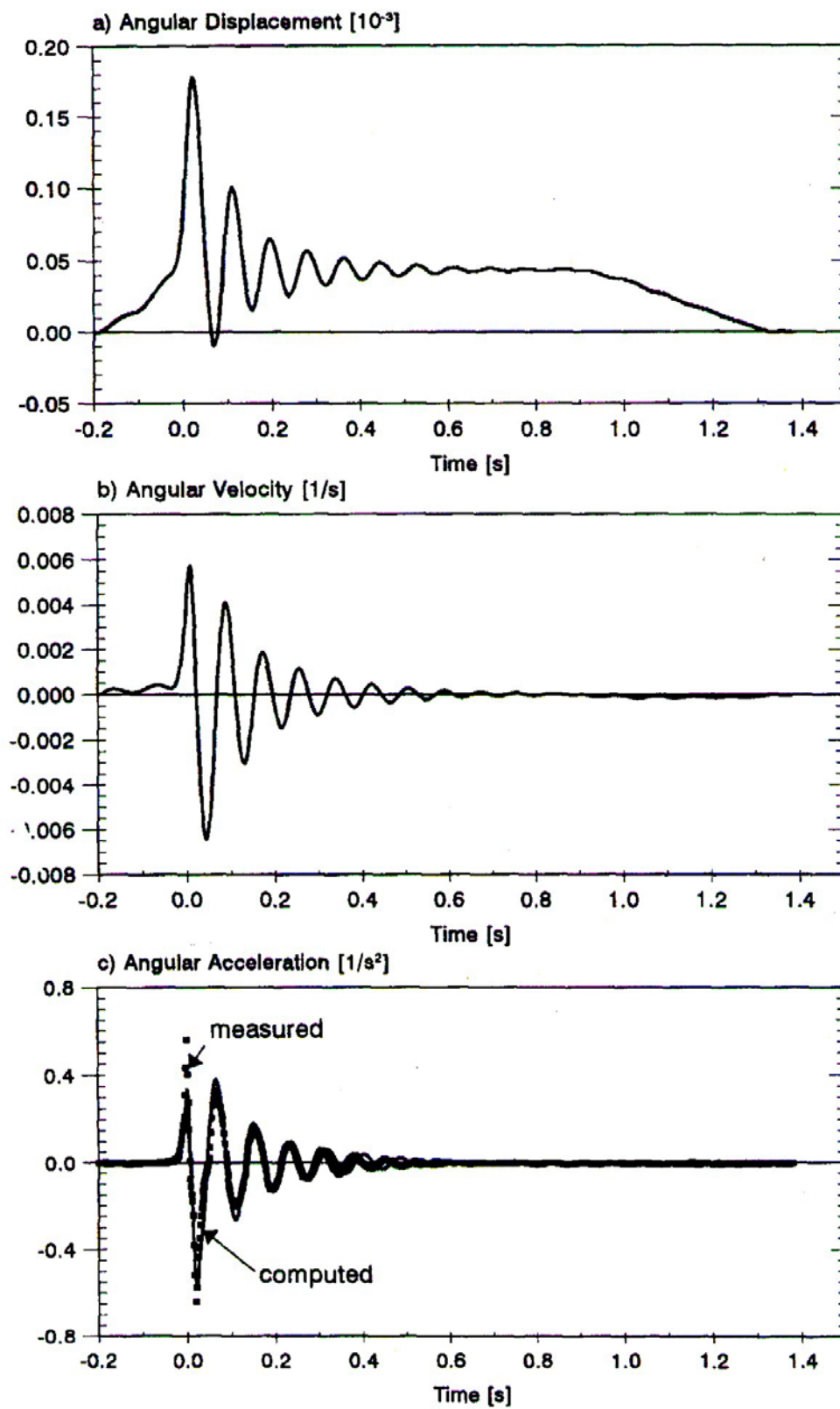
Fig. 2.11 Plots of angular displacement, velocity and acceleration versus time

(after Oumeraci et al., 1994c)
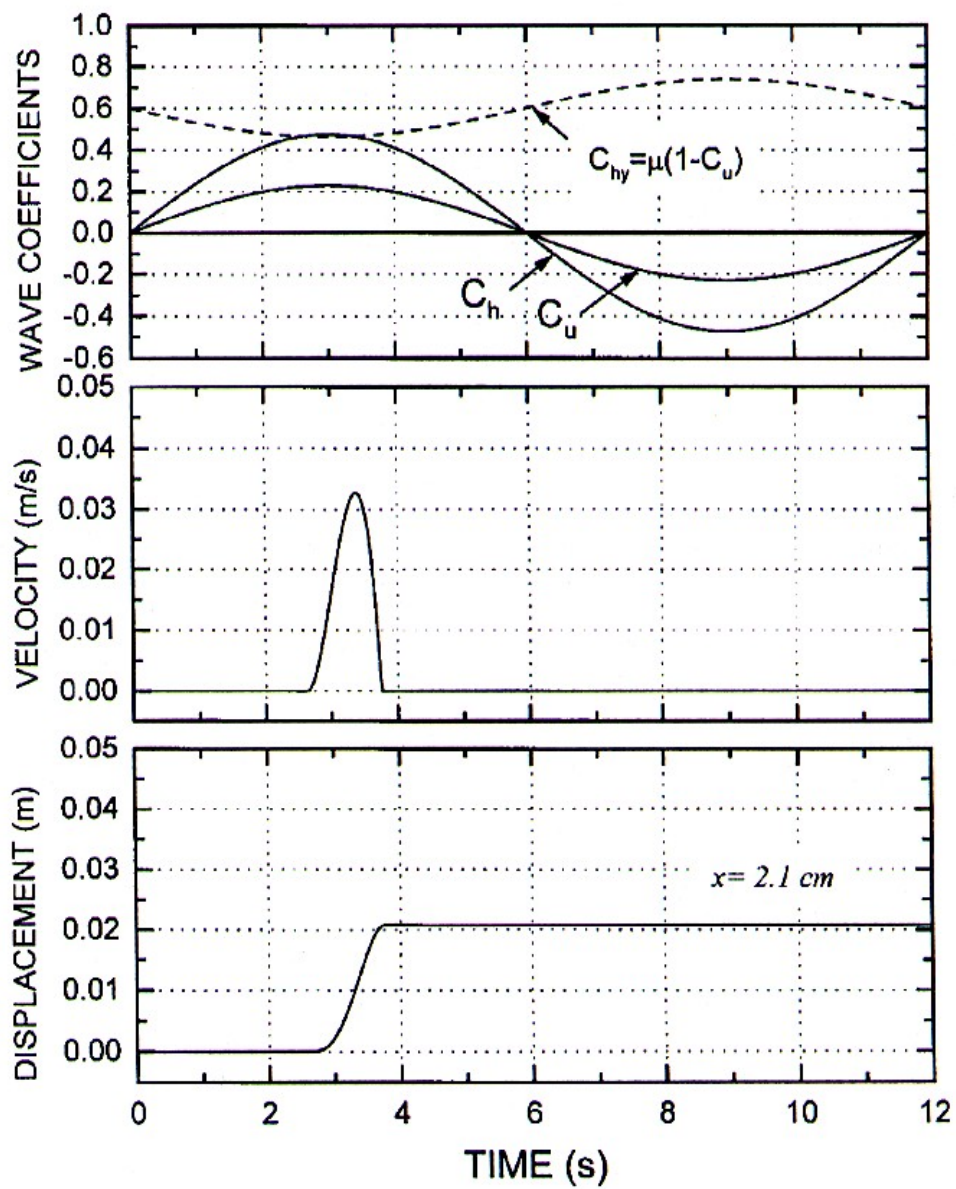
Fig. 2.12 Response of caisson subject to sinusoidal wave (after Ling et al., 1999)
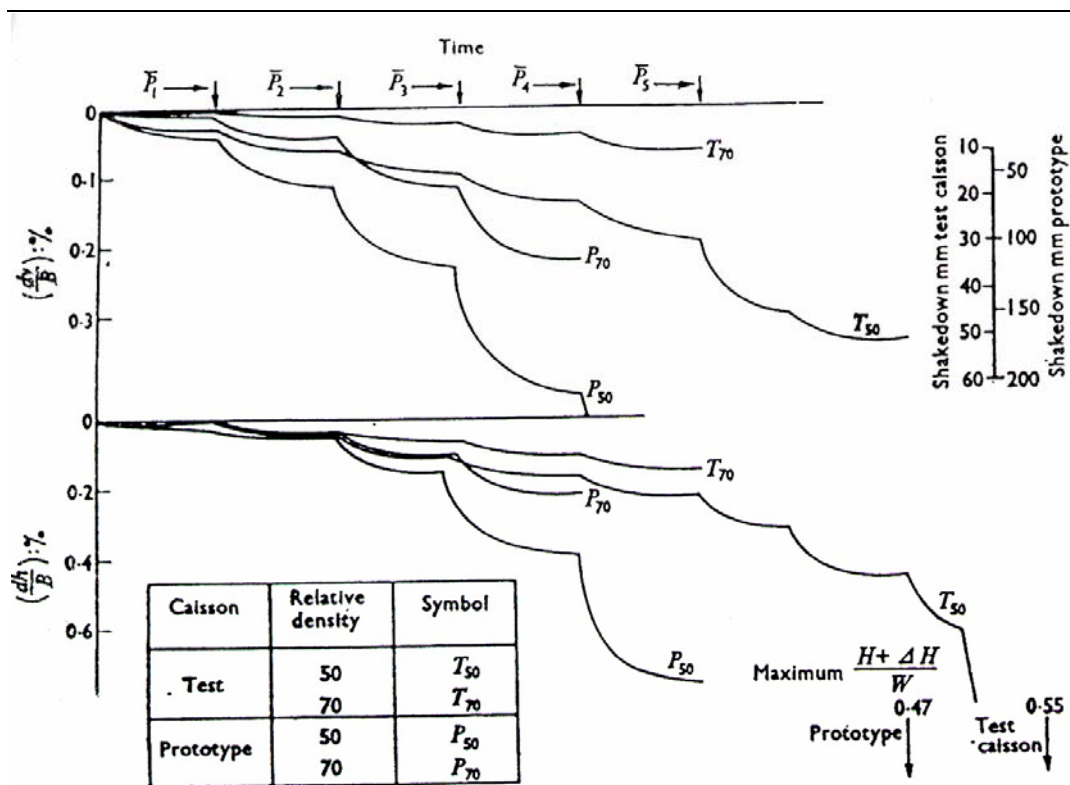
Fig. 2.13 Typical model time-displacement records for caisson on uniform sand beds
(after Rowe & Craig, 1976)
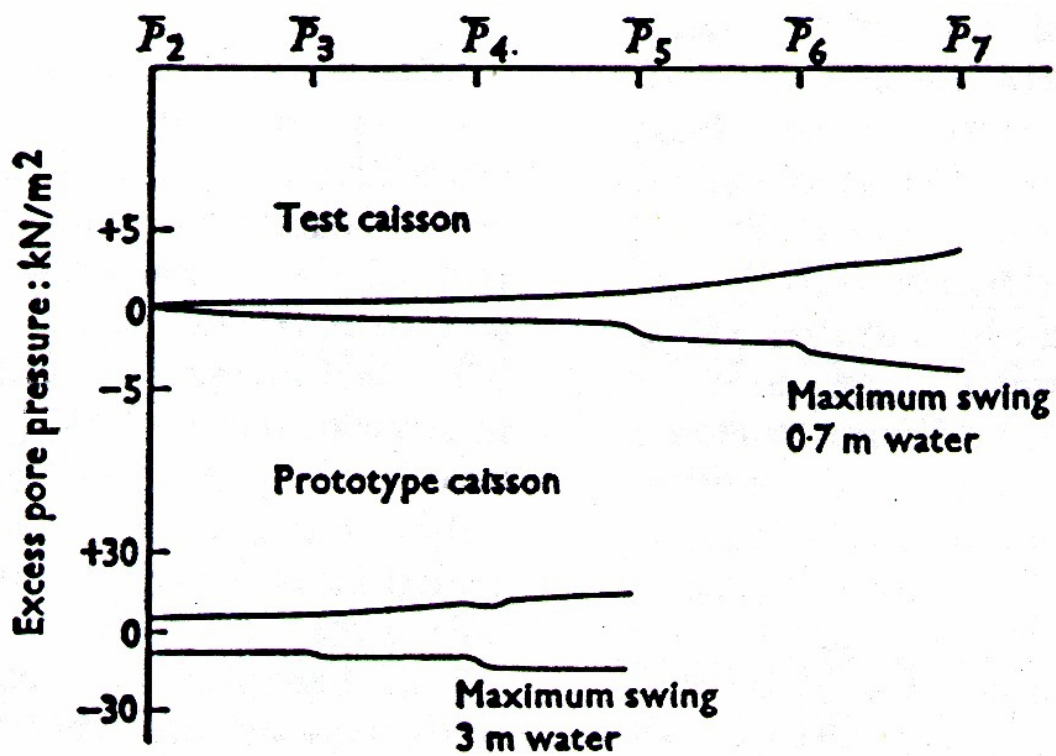
Fig. 2.14 Typical pore pressure records for caisson on uniform sand beds
(after Rowe & Craig, 1976)
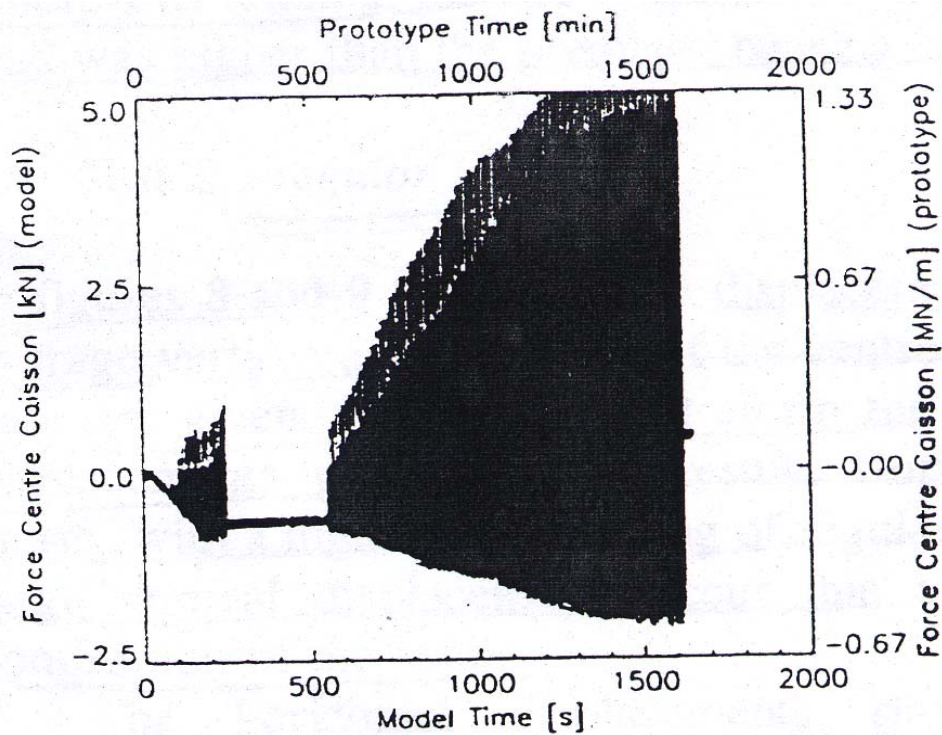
(a) Irregular breaking wave load
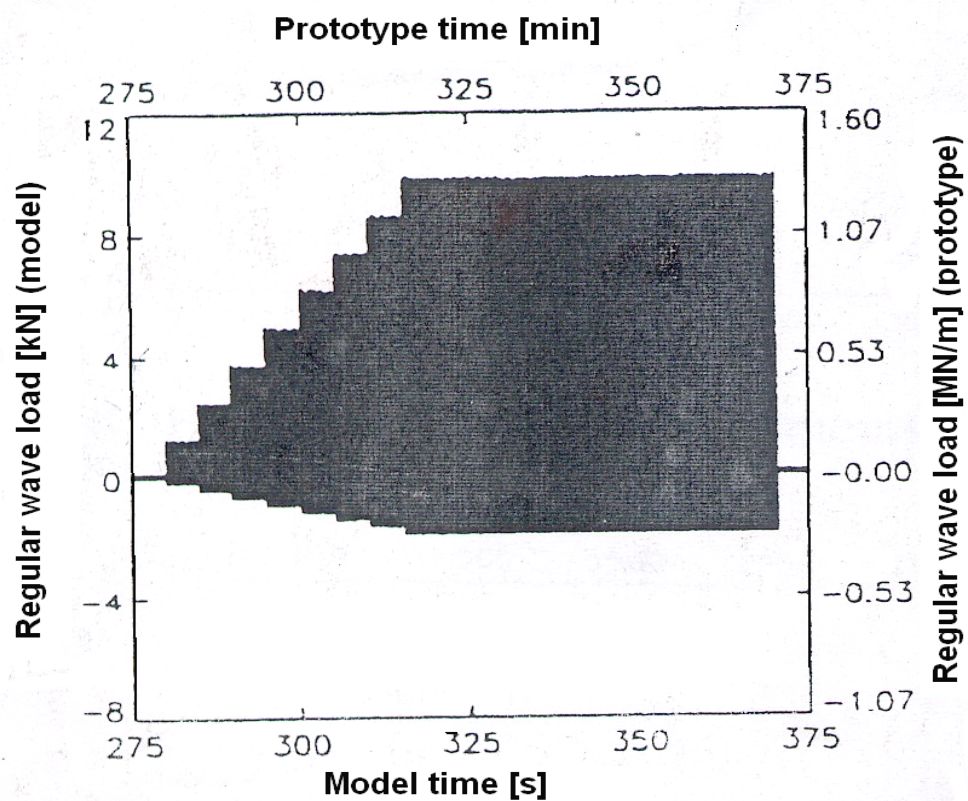
Fig. 2.15 Regular storm load signal in test 2 (after Poel et al., 1998)
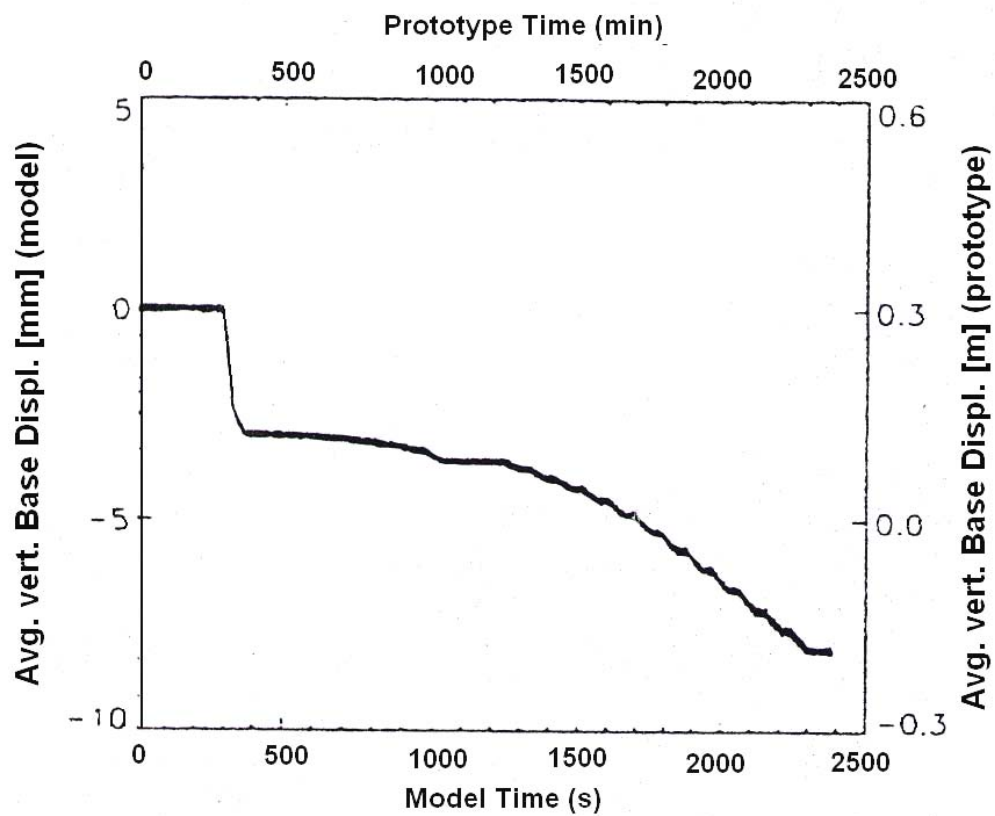
Fig. 2.16 Average vertical base displacement in test 2 (after Poel et al., 1998)

Chapter 3

Centrifuge Model Setup

3.1 Introduction

This chapter presents the centrifuge model setup, model caisson as well as zinc chloride (Z_nCl_2) chamber. The simulation of breaking wave loads and in-flight impulse actuator apparatus used to simulate wave loading are then discussed in detail. This is followed by the test procedures and the preparation of saturated soil bed. The performance of miniature pore pressure transducers (PPT) and load cell used in the experiments is evaluated. The data acquisition equipment is then described. Finally, the typical sequence of activities in the model tests is presented.

3.2 Centrifuge Modeling

3.2.1 Centrifuge scaling relations

The principles of centrifuge modeling involves subjecting the scale model to a gravitational field of Ng in which N is the linear scale factor. By so doing, prototype overburden stress levels are preserved in the model soil, thereby enabling prototype soil behaviour to be preserved. The scaling relations for various variables are then obtained by applying the requirements of dimensional analysis. For instance, in consolidation or dynamic events, Schofield (1988) noted that there are two basic underlying principles

to centrifuge modeling, namely:

1) increasing the self-weight of model by increasing the acceleration to which the model is subjected to in an acceleration field created by the centrifuge, hence leading to a reduction of model scale.

2) reducing the time or duration of the model tests as the scale is reduced when the model is subjected to acceleration.

When a centrifuge model test is conducted under Ng, where Ng is the acceleration field, the scaling relations between the prototype and centrifuge model are:

$$\frac{F_m}{F_p} = \frac{1}{N^2} \tag{3.1}$$

For modeling of dynamic events,

$$\frac{T_m}{T_p} = \frac{1}{N} \tag{3.2}$$

$$\frac{L_m}{L_p} = \frac{1}{N} \tag{3.3}$$

where F = Force,

T = Time (dynamic),

L = Linear dimensions, and

The subscripts m and p denote centrifuge model and prototype quantities, respectively. Scaling relations for other quantities are given in many publications e.g. Leung et al. (1991). A summary of the various scaling relationships is given in Table 3.1.

3.2.2   NUS geotechnical centrifuge

The centrifuge model tests were conducted on the NUS geotechnical centrifuge. The NUS centrifuge has a capacity of 40,000 g-kg and operates up to a maximum g-level of 200g. The allowable payloads at 200g and 100g are 200kg and 400kg, respectively. The structure of the centrifuge is based on the conventional dual-swing platform configuration. The model is normally loaded onto one of the platforms while the opposite platform either carries an appropriate counterweight or an identical model. In the present configuration, 45 differential channels are available for data transmission. The centrifuge system incorporates two separate close-circuit TVs. One is mounted on the centrifuge beam and another is mounted on a rigid supporting frame attached to the strong box to facilitate a close-up side view of the experimental process through the perspex window. The details of this centrifuge are given in Lee et al. (1991, 1992).

3.2.3   Viscosity scaling

As can be seen in Table 3.1, the time scale for dynamic events differs from that for consolidation events if the same soil and pore fluid as in the prototype are used in a model test. In order to satisfy the scaling relationship for centrifuge tests involving both dynamic and consolidation events, one should slow down the consolidation process so that it is consistent with the dynamic time scale. This can be done by either using a finer soil in the model, or using a more viscous pore fluid to replace water in saturated tests (Lee, 1985). However, to change the particle size of soils may lead to other changes in the mechanical properties of soil such as strength and stress-strain relationship and is hence seldom used. The most commonly used method to achieve consistent time-scaling for consolidation and dynamic events is to slow down the dissipation of excess

pore pressure by using pore fluid of higher viscosity in the model. According to the

Kozeny-Carman equation, the permeability of a soil, k, is given by

$$k = \frac{e^3 r}{k_0 s^2 \mu (1 + e)} \tag{3.4}$$

where

μ = viscosity of permeant,

e = void ratio,

r = unit weight of permeant,

s = specific surface area of soil particles, and

k_0 = factor depending on pore shape and ratio of the length of actual flow path to

soil bed thickness.

If the same soil is used as in the prototype, e, s and k_0 will remain the same.

Therefore, permeability is expected to be inversely proportional to the viscosity of the

permeant. If the permeant has a viscosity N times that of water and the same unit

weight, its permeability is expected to be 1/N that of water. The density of silicone

oil is 970 kg/m³which is very close to that of water. As a result, silicone oil has been

widely used in centrifuge tests by researchers such as Lee & Schofield (1988), Sassa

(1999) and Ko (1994).

When a viscous fluid such as silicone oil is used, it is important to know whether the

mechanical properties of a soil such as strength, stress-strain relationships and damp-

ing characteristics will be changed since these fluids have quite different physical and

chemical properties from that of water. Research results on the effects of silicone oil on

sand properties have been highly variable. Tan and Scott (1985) showed that the viscos-

ity scaling broke down when soil particles larger than 0.1 mm are moving in the fluid during complete liquefaction. However, as complete liquefaction is unlikely to happen in the present study, the use of silicone oil is acceptable. On the other hand, Eyton (1982) and Madabhushi (1994) conducted laboratory tests on different soils with silicone oil as the pore fluid and concluded that the effect of silicone oil on the stress-strain behavior is insignificant. Besides that, Bielby (1989) found that at a cell pressure of 200 kPa, the friction angle of oil-saturated sand was about $4°$ lower than that of water-saturated sand. However, the difference in friction angle at much higher cell pressure became negligible. Taking all these findings into consideration, it is likely that silicone oil may alter the friction angle of sand by no more than $4°$ in the worst case. This may be important if the centrifuge model study is a site-specific study in which a specific sand needs to be used to simulate in-situ conditions. In this case, however, the study is a mechanistic investigation and is aimed at examining broad trends of behaviour rather than providing numbers for design. The sand used is also not identical to any of the sand on any specific site. As such, the difference in the friction angle is unlikely to have a material effect on the conclusions.

3.3 Experimental Setup

Figs. 3.1 and 3.2 show the sketch and photograph of centrifuge model setup and instrumentation of present study, respectively. The model consists essentially of model concrete caisson [1] seated on a model sand bed [2] which may or may not incorporate a rock berm. The ballast in the model caisson was provided by filling the latter up with heavy zinc chloride solution. Wave loading on the model caisson was simulated by impulsive loading from an actuator driven by a closed-loop electric servo-motor. These

components will be discussed further below. All the tests were conducted at 100g.

3.3.1 Model concrete caisson [1]

As shown in Fig. 3.2, the model is placed in a rectangular stainless steel strong box with internal dimensions of 570x200 mm^2 (i.e. 57x20 m^2 in prototype scale) and a height of 470 mm (47 m). The model caisson, which was 250 mm high (25 m), 180 mm long (18 m) and 200 mm wide (20 m), spans across the whole width of the model container and simulates a plane strain model condition. The width was determined by bearing capacity considerations using Hansen and Christensen's (1969) method, and assuming the caisson base to be at -20 mCD. The 20-mm (2-m) wide base protrusions at both ends of caisson were designed to reduce the caisson bearing pressure on the sand bed. The base of the caisson incorporated a 3-mm thick (0.3 m) steel plate on the inside and a 7-mm thick (0.7 m) concrete layer on the outside; the latter being used to simulate approximately the typical roughness of the base of a prototype caisson, as illustrated in Fig. 3.3.

3.3.2 Sand bed [2]

The sand key was simulated by a layer of medium sand. The properties of this sand are as follows: effective mean diameter of 0.42 mm, uniformity coefficient of 1.32, minimum dry density of 1280 kg/m^3 and maximum dry density of 1540 kg/m^3. The properties of the sand are shown in Table 3.2. The particle size distribution curve of the sand obtained from sieving test is illustrated in Fig. 3.4. The tests were conducted to examine the behavior of gravity caisson resting on sand bed with relative density ranging from about 50% to 80%. The dry density and void ratio of the sand beds are

summarized in Appendix A. Ovesen (1975) showed that the critical ratios below which particle size effects become significant are ratios between 20 and 40 for foundations in quartz sand. The effect of soil particle size is reduced since the resultant ratio of caisson width to the mean particle size is 524. The thickness of sand key is determined by the thickness of soft clay that has been replaced. In the present study, a 15-m thick prototype sand key is used in all the tests.

3.3.3   Rock berm

In the present study, majority of breakwaters used are the basic one without rock berm. When doing parametric study on presence of rock berm, 4-m-thick rock berm is placed underneath the caisson base, as shown in Fig. 3.5. The layer of rock berm used between the caisson base and sand key seems to have several advantages: (1) to raise and level the foundation bed; (2) to enhance the lateral stability of the structure (e.g., Tan et al. 1991); (3) to provide drainage of excess pore pressures and to act as filter against the loss of sand particles (Oumeraci et al., 2001).

   Rock berm should be hard, dense and durable, and free from the possibility of breaking due to weathering and freezing. The shape of the rock should not be flat or oblong. The typical grain size of rock berm is at least 10 mm. The angle of friction of rubble stones with ordinary materials is 40°, while that with brittle materials is 35° (PHRI, 1991). Based on the results of large triaxial tests, the apparent cohesion C=2 tf/m^2 and the angle of shear resistance ϕ=35° are applied for normal rubble which is predominantly used in Japan for harbor construction (Takahashi, 1996). The properties of the rock berm used in centrifuge tests are also shown in Table 3.2, with the effective mean diameter of 3.25 mm (325 mm in prototype), minimum dry density of 1250 kg/m^3

and maximum dry density of 1435 kg/m^3.

3.3.4 $ZnCl_2$ **chamber [3]**

Each model test can be divided essentially into two stages. In stage 1, the caisson was ballasted onto the sand bed by infilling it with zinc chloride solution. In stage 2, the wave loading was simulated by repeated impulse on the seaward side of the caisson using the servo-driven impulse actuator. Before ballasting the caisson, the heavy zinc chloride ($ZnCl_2$) solution was held in a storage container placed on the centrifuge beam, as indicated in Fig. 3.6. The storage container is sub-divided into two chambers. For most tests, only one chamber was used to simulate the ballasting stage. The other chamber was used to simulate wave overtopping on caisson. The outlets of each of the two chambers are fitted with a solenoid valve operated by 24 V DC supply. In all but one test, heavy zinc chloride solution was only released from chamber 1 into the caisson to simulate the infilling stage, chamber 2 was not used. However, when doing parametric study in test WL1, where after the infilling stage, more $ZnCl_2$ was released through solenoid valve No. 2 into the caisson to simulate overtopping of the caisson during wave loading.

3.3.5   **Pore pressure transducer (PPT)**

Druck PDCR 81 miniature pore pressure transducers were used to record the instantaneous pore pressure of the soil bed during centrifuge flight. The ranges of these PPTs are 7 bar and 3 bar using 5 volts power supply. Before the experimental set-up, PPTs were de-aired using a vacuum machine so as to remove air bubbles from the inside of the PPTs. Each PPT was re-calibrated before every test.

3.3.6   Load cell [4]

Interface SML-500 load cell was used to record the horizontal impulsive loading applied by the actuator on the seaward face of the caisson. This load cell can measure both tension or compression and has a capacity of 500 lbf. It is only sensitive to the axial component of the actuator, any shear component between the actuator and caisson was not measured. One side of the load cell was bolted into the shaft head, while the other side was fitted with a jam nut, which bears against the caisson. The load cell output factor supplied by the factory was 2.0272 mV/V which was calibrated under 1 g as shown in Fig. 3.7. It is found that the linear regression between the standard weight and the calculated force obtained from the output factor yields R^2=0.9998 and hence the output factor is satisfactory.

3.4   Design of Breaking Wave Loads

From hydrodynamic aspects, there are a large number of wave pressure formulas, such as Sainflou formula (Oumeraci et al., 2001), Hiroi formula (Oumeraci et al., 2001), Minikin formula (Oumeraci et al., 2001), Nagai formula (Oumeraci et al., 2001), Goda's formula (Goda, 1972) and the extended formula developed by Takahashi et al. (1994b), Allsop and Vicinanza's method (Oumeraci et al., 2001), and Oumeraci and Kortenhaus' method (Oumeraci et al., 2001). Currently, the original and extended Goda formula is the most widely used. In 1973, Goda used his own theoretical and laboratory studies (Goda, 1972) to establish a comprehensive formula to calculate the design wave forces. This formula was successfully applied to the design of vertical breakwaters, and a modification was made later by Takahashi et al. (1994b) to account for the frequent

wave breaking close to and at a vertical breakwater.

3.4.1 Original Goda formula

In 1973, Goda used his own theoretical and laboratory studies (Goda, 1972) to establish a comprehensive formula to calculate the horizontal pressure and uplift pressure, as shown in Fig. 3.8. The notation shown in the figure as d , h , h' and h_c represent the depth of water measured from the surface to the top of armor block, the depth of water in front of caisson breakwater, the depth of design water table to the bottom of caisson, and the crest elevation of caisson above the design water table, respectively. Only the salient features of the Goda formulas are described here.

In the Goda formula, the maximum wave height at the site $H_{\max}$ is used to calculate the wave pressure calculation and is taken as the smaller value of $1.8H_{1/3}$ and H_b , where $H_{1/3}$ is the significant wave height and H_b is the wave height estimated at a distance of $5H_{1/3}$ from the breakwater. Given the deep water wavelength $L_0 = gT^2/2\pi$, where g is gravity acceleration and T is the wave period. The design wavelength L is calculated from the following relationship (Dean and Dalrymple, 1991):

$$L = \frac{gT^2}{2\pi} \tanh \frac{2\pi h}{L} \tag{3.5}$$

The elevation at which the wave pressure is exerted, η^* , and the representative wave pressure intensities, p_1, p_3, p_4 and p_u can be written in a general form as follows:

$$\eta^* = 0.75 * (1 + \cos \beta) * \lambda_1 * H_{\max} \tag{3.6}$$

$$p_1 = 0.5 * (1 + \cos \beta)(\lambda_1 \alpha_1 + \lambda_2 \alpha_2 \cos^2 \beta) * \rho_w * g * H_{\max} \tag{3.7}$$

$$p_2 = \frac{p_1}{\cosh(\frac{2\pi}{L} * h)} \tag{3.8}$$

$$p_3 = \alpha_3 * p_1 \tag{3.9}$$

$$p_4 = \alpha_4 * p_1 \tag{3.10}$$

$$p_u = 0.5(1 + \cos\beta)\lambda_3\alpha_1\alpha_3\rho_w gH_{\max} \tag{3.11}$$

and

$$\alpha_1 = 0.6 + 0.5 * \left[\frac{4\pi h/L}{\sinh(4\pi h/L)}\right]^2 \tag{3.12}$$

$$\alpha_2 = \min[\frac{h_b - d}{3h_b}(\frac{H_{\max}}{d})^2, \frac{2d}{H_{\max}}] \tag{3.13}$$

$$\alpha_3 = 1 - \frac{h'}{h}[1 - \frac{1}{\cosh(2\pi h/L)}] \tag{3.14}$$

$$\alpha_4 = 1 - \frac{h_c^*}{\eta^*} \tag{3.15}$$

$$h_c^* = \min(\eta^*, h_c), \tag{3.16}$$

β = angle between the wave crests and the normal of the front of the structure.

L = wave length corresponding to that of significant wave $T_s = 1.1 * T_m$, where T_m is the average period, and

h_b = water depth at the location at a distance of $5H_s$ seaward of the breakwater front wall.

For a vertical caisson, $\lambda_1 = \lambda_2 = \lambda_3 = 1$.

The original Goda formula has many advantageous features:

- It can be employed for all wave conditions, both for standing and breaking waves.

- The formula's design wave is the maximum wave height and can be evaluated by given diagrams and equations.

- It is partially based on the nonlinear wave theory and can represent wave pressure.

- The Goda formula clarifies the concept of uplift pressure on the caisson bottom, since the buoyancy of the uplift section in still water and its uplift pressure due to wave action are defined separately. The distribution of the uplift pressure has a triangular shape.

3.4.2   Extended Goda formula by Takahashi et al. (1994b)

The Goda formula was subsequently extended to include the following parameters:

(1) The incident wave direction (Tanimoto et al., 1976)

(2) Modification factors applicable to other types of vertical walls

(3) The impulsive pressure coefficient (Takahashi et al., 1994b)

Goda's formula did not consider frequent wave breaking close to and at a vertical breakwater. Takahashi et al. (1994b) subsequently derived the impulsive wave coefficient to account for this effect, based on caisson sliding experiments. The pressure p_1 at the water surface in the Goda formula can be expressed as:

$$p_1 = 0.5 * (1 + \cos \beta)(\lambda_1 \alpha_1 + \lambda_2 \alpha^* \cos^2 \beta) * \rho_w * g * H_{\max} \qquad (3.17)$$

where α^* represents the coefficient of impulsive pressure and α_1 is the pressure coefficient for the slowly varying pressure. The coefficient α^* is expressed by:

$$\alpha^* = max(\alpha_2, \alpha_I) \qquad (3.18)$$

$$\alpha_I = \alpha_{I0} * \alpha_{I1} \qquad (3.19)$$

where α_{I0} represents the effect of wave height on the mound, i.e.,

$$\alpha_{I0} = H_{\max}/1.8 * d \quad (if \quad H_{\max}/1.8 * d \leq 2) \qquad (3.20)$$

$$\alpha_{I0} = 2.0 \quad (if \quad H_{\max}/1.8 * d > 2) \qquad (3.21)$$

and α_{I1} represents the shape of the rubble mound:

$$\alpha_{I1} = \frac{\cos \delta_2}{\cosh \delta_1}, \quad (if \quad \delta_2 \leq 0) \qquad (3.22)$$

$$\alpha_{I1} = \frac{1}{\cosh \delta_1 * \sqrt{\cosh \delta_2}}, \quad (if \quad \delta_2 > 0) \qquad (3.23)$$

$$\delta_1 = 20 * \delta_{11}, \quad (if \quad \delta_{11} \leq 0) \qquad (3.24)$$

$$\delta_1 = 15 * \delta_{11}, \quad (if \quad \delta_{11} > 0) \qquad (3.25)$$

$$\delta_{11} = 0.93(\frac{B_b}{L} - 0.12) + 0.36(\frac{h_s - d}{h_s} - 0.6) \tag{3.26}$$

$$\delta_2 = 4.9 * \delta_{22}, \quad (if \quad \delta_{22} \leq 0) \tag{3.27}$$

$$\delta_2 = 3 * \delta_{22}, \quad (if \quad \delta_{22} > 0) \tag{3.28}$$

$$\delta_{22} = -0.36(\frac{B_b}{L} - 0.12) + 0.93(\frac{h_s - d}{h_s} - 0.6) \tag{3.29}$$

where L is defined as the wave length for the Goda formula and B_b is the width of the rubble berm at the toe of the wall of a vertical breakwater.

Fig. 3.9 shows the transition of wave pressure from non-breaking to impulsive pressure, where the pressure component is indicated by the coefficients α_1, α_2 and α_I. α_1 represents the slowly-varying pressure component and α_2 the breaking pressure component, while α_I represents the impulsive pressure component, which includes the dynamic effect on caisson sliding. The total external horizontal pressure acting on the caisson, due to the wave pressure, are determined as

$$p = 0.5[(p_1 + p_3)h' + (p_1 + p_4)h_c] \tag{3.30}$$

3.4.3 Comparison of Goda formulas with field tests

A model that accounts for the nonlinear behavior of the foundation of a vertical structure subjected to breaking wave impact loads has been suggested by Loginov (1969). The wave impact force obtained by the original and extended Goda formula, Loginov model

and VNIIG-77 model are summarized in Table 3.3. By comparing the measured force on a breakwater in the field, it is concluded that the wave force distribution developed by Goda (1985) produced a far better estimation of wave impact force than the earlier methods such as Longinov (1969). Therefore, the original and extended Goda formulas could give a reasonable estimation of wave impact force on a prototype caisson.

3.4.4   Wave loading profile

For wave breaking directly on the caisson wall, the impact force may be distinguished as a single-peak force followed by a rather smooth quasi-static component generally called "church roof load" (Oumeraci, 1995) (Fig. 3.10). The single-peak force is induced by a wave breaking on the structure with a negligible amount of air entrapped. In the case of non-resonant loading conditions, the "church roof load" may be substituted by a triangular load which is characterized by the peak value $F_{\max}$, the rise time t_r and the total peak duration t_d as shown in Fig. 3.11. Schmidt et al. (1992) studied the relationships between $F_{\max}$, t_r and t_d by means of hydraulic model tests and found that depending on the amount of entrapped air and the magnitude of peak force, the ratio between rise time t_r and total peak duration t_d ranges from about 0.3 to about 0.65.

In Singapore, the wave height can be up to 1.5 m and the wave period up to 6 s during the monsoon period. Storm wave heights are often larger overseas. In Japan, Kashima port, the wave height can be as high as 11.7 m with the wave period of 14 s (Ling, 1999). In the present study, a wave height and period of 3 m and 6 s, respectively, were typically used. Table 3.4 shows some typical wave heights and periods computed using Goda's formula. A summary of various scaling relationships about the wave impulsive forces and wave characteristics is given in Table 3.5.

3.5 Centrifuge Model Configurations

3.5.1 Wave actuator apparatus and servo-control system

The impulsive wave force was applied on the seaward face of the model caisson break-water using the wave actuator apparatus by load-control via a brushless DC/AC servo motor, see Fig. 3.12. The wave actuator apparatus includes three main parts: namely torque arm, gear box and electric motor. The apparatus fixed on the steel base support structure of sand hopper and mounted on the left side of caisson is able to operate up to 100g in the centrifuge. The gear box just beneath the servo motor can bring about the movement of torque arm and hence push the caisson forward. Feedback to the servo-motor was provided by the load cell mounted on the head of torque arm, as shown in Fig. 3.13. The servo motor in Fig. 3.14 is available with a variety of waveform and feedback combinations. The wave actuator apparatus was controlled by a servo-controller fixed on the top of the centrifuge beam.

3.5.2 Data acquisition systems

A schematic drawing of the wave actuator system is shown in Fig. 3.15. The wave form was generated digitally from a desktop personal computer which resides in the control room. The digital wave form signals were then converted to analogue via the software Hyper Terminal driving a digital-analog card and then sent to the servo-controller. By comparing the instantaneous target load with the applied load measured by the load cell, the servo-controller continuously corrects the load signal to the motor. This was found to work reasonably well at low frequency. However, at frequency above 20 Hz, the response deteriorated owing to the inability of the servo-control system to keep up with the rapidity of the loading fluctuations. Details can be found in Zhang et al. (2004).

The program needs to be pre-calibrated so that the prescribed peak wave load is actually delivered to the caisson. Fig. 3.16 shows the calibration results under 1g. As can be seen, the peak wave force increases linearly as the programmable code increases. It is found that at the same programmable code, 2 kN of model peak wave force can be achieved at 1 g, while the responding achievable peak wave force at 100g is only about 800 N. This is because part of the force is used to overcome the large friction force between the head of torque arm and the bearing.

As shown in Fig. 3.17, the single-peak force was reasonably well simulated under 100g. However, the peak value of the single-peak wave was not exactly constant due to rocking and swaying of the caisson, which the servo-motor cannot fully compensate. It should be noted that, even in the field, peak wave force fluctuate from cycle to cycle, depending upon the caisson motion and wave conditions. So, while this cannot be controlled, it is not completely unrealistic.

3.6   Preparation of Saturated Sand Bed

3.6.1   Preparation of sand bed with high RD

For the sand bed with high relative density, dry sand is pluviated from a hopper into the container. The hopper was calibrated and the height of pluviation and the flow rate of hopper were adjusted according to the desired relative density of the sand. During the sand pouring, the height from the bottom of the hopper to the surface of sand bed is maintained at the prescribed height. The pluviation process was interrupted at pre-determined depths and de-aired PPTs were placed at designated locations. Cables of the transducers were laid on the sand surface and secured to the container wall using masking tapes. The pluviation process was then resumed until the sand bed reached

the prescribed level for the next placement of transducers. This process continued until all the transducers were placed and the sand bed reached the final height. In one test involving rock berm, sand of 40 mm thickness placed within an area of about 370 mm (37 m) long and 200 mm (20 m) wide will then be carefully suck out by a vacuum cleaner to be replaced by the rock berm.

The sand bed was saturated using a vacuum saturation approach similar to that reported by Lee and Schofield (1988). Fig. 3.18 shows the vacuum saturation system used. The vacuum gauge on the top of perspex rectangular cover was used to control the vacuum so as to ensure that there is a pressure gradient between the de-aired silicone oil storage chamber and the container. The ball valve was used to control the open and close of the vacuum container. The incoming silicone oil was distributed over the base of the sand bed via a multiply-perforated copper pipe, as shown in Fig. 3.19. The rate of silicone oil ingress was maintained at a low enough level to prevent partial or localized liquefaction of the sand sample. The upward seepage of the de-aired silicone oil and the vacuum environment within the model container minimizes the likelihood of air bubbles being trapped. Whatever small air bubbles that remained in the sand bed would be dissolved in the silicone oil once atmospheric pressure is restored after saturation and when the pressure is increased under high-g condition in-flight.

3.6.2   Preparation of sand bed with low RD

Sand beds with very low relative density could not be readily prepared using the vacuum saturation method. This is because piping was found to take place readily when vacuum was applied. In addition, the wetting of the sand during the upward seepage was found to cause some densification of the very loose sand. This probably arises due to the

zone of transient negative pore pressure around the wetting front. For such models, another method was used to prepare the loose sand bed, as reported by Lee (1985). About 22 kg of dry sand was thoroughly mixed with about 45 kg of silicone oil and the mixture de-aired under vacuum for about 1 hour. Next, the sand and silicone oil mixture was transferred to the container in small portions of about 500g each using a stainless steel beaker. The beaker was then fully immersed in the oil already present in the container and tipped over, thus allowing the sand to pluviate through silicone oil without bubble formation. During this process, the beaker was moved slowly over the area of construction. This facilitates an approximately equal rise of surface at all points. The process was repeated until the sand bed was built up to the prescribed level.

3.7   Experimental Procedures

3.7.1   Installation of model caisson

As shown in Fig. 3.2, the model consists of a sand layer of 150 mm (15 m) thick, a 250-mm (25 m) high model caisson, silicone oil with a free surface at 200 mm (20 m) above the seabed. When the caisson was unballasted, that is empty, the upward buoyancy force is only slightly less than the caisson weight. This allows the empty caisson to rest on the seabed with a minimum loading pressure. As mentioned earlier, in-flight ballasting of the caisson was achieved by infilling it with $ZnCl_2$ from a storage chamber mounted on the centrifuge arm.

In order to minimize the side friction between the model caisson and container wall, Taniguchi et al. (1988) lubricated the side walls of the model container with a 100μm thick layer of silicone grease. In the present tests, a 100μm thick layer of silicone grease was brushed on the rear side of the container, then a 0.2 mm thick layer

of polyethylene sheet was placed to prevent sand from penetrating into the grease. After

that the silicone grease was applied again on the polyethylene sheet and finally placed

on the second layer of polyethylene sheet. The front perspex side of the container was

treated the same way as the back side except that transparent grease was used so that

the experimental process could be observed clearly during the tests. This arrangement

greatly reduces the friction interface between the container sides and the model, as

reported by Khoo (1994).

During the siphoning of the silicone oil into the container to raise the oil level, it

was found that scouring could easily occur on the sand bed due to the flow of viscous

silicone oil. To prevent this, a piece of styrofoam plate was put on the sand bed and

silicone oil was siphoned on the plate so as not to disturb the sand bed. After the oil level

reached the proscribed depth, the styrofoam plate was removed. The model caisson

was then slowly lowered onto the prescribed location of the sand bed. To monitor the

caisson movements during the tests, four vertical displacement transducers (V1, V2,

V3 and V4) and one horizontal displacement transducer (H5) were employed, see Fig.

3.20. One pore pressure transducer (P7) was placed inside the model caisson to monitor

the ballast liquid pressure and hence obtaining the total weight of the caisson.

3.7.2   Two stages simulated in centrifuge

There were two stages simulated in the experiments:

1) Once the centrifuge was spun up to 100g, heavy zinc chloride solution ($ZnCl_2$)
   was infilled into the caisson to simulate the ballasting process.

2) Then the wave actuator was activated to apply impulsive wave load on the cais-

son breakwater for about 17,000 wave cycles to investigate the progressive move-
ments of caisson and the change of excess pore pressure in the sand bed.

3.8   Infilling Stage

Fig. 3.21 shows the vertical displacement of the four potentiometers during infilling
stage in test WL4. As can be seen, the vertical displacement measured by the four
potentiometers are in reasonably good agreement, thereby indicating that the caisson
settled fairly uniformly during infilling. Assuming that the caisson displaced as a rigid
body, the settlement at the centreline of the caisson can be determined by taking the
average of the four measured settlements. Similarly, the angle of tilt θ of the caisson
can be computed using the relationship:

$$\theta = \frac{1}{B} \left(\frac{V1 + V2}{2} - \frac{V3 + V4}{2} \right) \tag{3.31}$$

in which B is the longitudinal offset between potentiometer pairs V1 & V3 and V2
& V4. V1 to V4 denote the settlement measured by the respective potentiometers as
indicated in Fig. 3.20. The horizontal movement refers to the displacement measured
by displacement transducer H1 which was placed at about 2 m above the water ta-
ble. Positive vertical movement denotes a downward settlement of the caisson while a
negative horizontal movement and positive tilt denotes movement in the landward di-
rection away from wave loading. All the test results are presented in prototype scale,
hereinafter, unless otherwise stated.

Before infilling, the effective caisson pressure on the foundation sand is about 100
kPa. During infilling, this pressure increases to about 320 kPa. Fig. 3.21 shows that

caisson settlement increases approximately linearly during infilling. The horizontal displacement and tilt in this stage is relatively insignificant. This relatively small tilt and horizontal displacement is to be expected and indicates that the prepared sand bed is reasonably uniform. The linear settlement suggests that the caisson foundation is still well away from the point of bearing capacity failure. Ng (1998) reported a similar observation that the load-displacement response of a spud-can footing is linear.

Table 4.1 and Table 5.1 which will be discussed later in Chapter 4 and Chapter 5, respectively, summarize the observed caisson tilt angle, settlement of center and horizontal displacement during infilling for the reversal and non-reversal wave loading tests. The loading stiffness which is defined as the gradient of the load-settlement response, is also given in the tables. Fig. 3.22 shows the loading stiffness plotted against the initial RD. As can be seen, there is a trend of increasing loading stiffness as sand RD increases. This is not surprising; a similar trend has been reported by Ng (1998) for spud-can footings. The scatter of the data points about the trend line can be attributed to several factors. Firstly, the initial sand RD quoted here is merely an approximate value that is estimated from the weight and volume of sand prepared (see Appendix A). Ng (1998) noted that the measurement of RD is highly susceptible to errors since a relatively small error in the sand density will give rise to a much larger error in RD. Secondly, the initial RD represents the RD at the point when the model is pluviated (i.e. in dry state). The subsequent vacuum saturation and movement of the model onto the centrifuge platform may cause changes to the model RD. This is likely to be especially so for the loose sand models which were observed to densify slightly upon saturation and movement. Thirdly, the very loose models (i.e. tests WL16 and WL17) which were

prepared by depositing sand under silicone oil may not be as uniform as those prepared by pluviation through air. Finally, the settlement of model WL6 might have been influenced by the rock berm on which it sits. Notwithstanding all these factors, the fact that there is a clear trend of increasing loading stiffness with RD indicates that there is a consistent change of behaviour as the RD changes.

Based on the assumption that the initial RD are affected by the errors, whereas the loading stiffness is likely to give a better indication of the sand RD of the model at the start of the test, Ng (1998) used the loading stiffness to obtain a "corrected" RD_c . A similar approach was used in this study to "correct" the RD. The trend shown in Fig. 3.22 suggests that the loading stiffness of sand increases linearly with RD with a R^2 value of 0.89. As shown in Table 4.1 and Table 5.1, the difference between initial and "corrected" RD is no more than 5 % in most cases. This and the relatively high R^2 value suggests that the RD is a reasonably good indicator of the model state at the start of a test.

Table 3.1 Summary of scaling relations between model and prototype

(after Leung et al., 1991)

Parameter	Prototype	Centrifuge Model at Ng
Linear Dimension	1	1/N
Area	1	$1/N^2$
Volume	1	$1/N^3$
Density	1	1
Mass	1	$1/N^3$
Acceleration	1	N
Velocity	1	1
Displacement.	1	1/N
Strain	1	1
Energy Density	1	1
Energy	1	$1/N^3$
Stress	1	1
Force	1	$1/N^2$
Time (Viscous Flow)	1	1
Time (Dynamics)	1	$1/N$
Time (Seepage)	1	$1/N^2$

Table 3.2 Properties of sand bed and rock berm

	Sand	Rock berm
Effective Size, D_{50} (mm)	0.42	3.25
Uniformity Coefficient, U	1.32	-
Specific Gravity, G_s	2.65	2.75
Minimum Dry Density, ρ_{min} (kg/m^3)	1280	1250
Maximum Dry Density, ρ_{max} (kg/m^3)	1540	1435
Minimum Void Ratio, e_{min}	0.72	0.91
Maximum Void Ratio, e_{max}	1.07	1.2
Coefficient of permeability k (m/s)	3.18×10^{-3}	-

Table 3.3 Comparison of Goda formula results with field and prototype tests
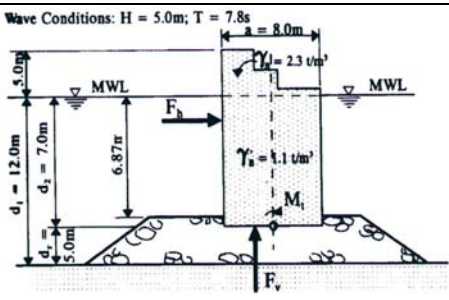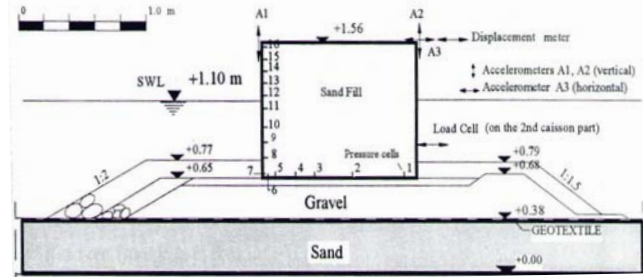
(a) Prototype Study by Marinski et al. (1992)				
Condition	Wave Impact Force (kN/m)			
	Prototype Measurements	Goda Formula	Nonlinear Calculations (Loginov,1969)	Linear Calculation (Vniig 77)
	715	722	497.3	497.3
(b) Field Test by Klammer et al. (1994)				
Condition		Wave Impact Force ($F_H/\rho g H^2$)		
		Field Measurements	Goda Formula	
		6.58	5.4	

Table 3.4 Wave impact forces with different wave height and period (prototype)

Wave height (m)	Wave frequency (Hz)	Wave period (s)	Wave force on caisson (kN)
1	0.167	6	2417
1.5	0.167	6	3606
2	0.167	6	4834
2	0.125	8	5249
2	0.1	10	5923
3	0.167	6	7251

Table 3.5 Summary of scaling relations between model and prototype

Parameter	Prototype	Model at 100g
Wave period (sec)	1	1/100
Wave frequency	1	100
Angular wave velocity	1	100
Wave impulsive force	1	$1/100^2$
Caisson pressure	1	1
Caisson mass	1	$1/100^3$
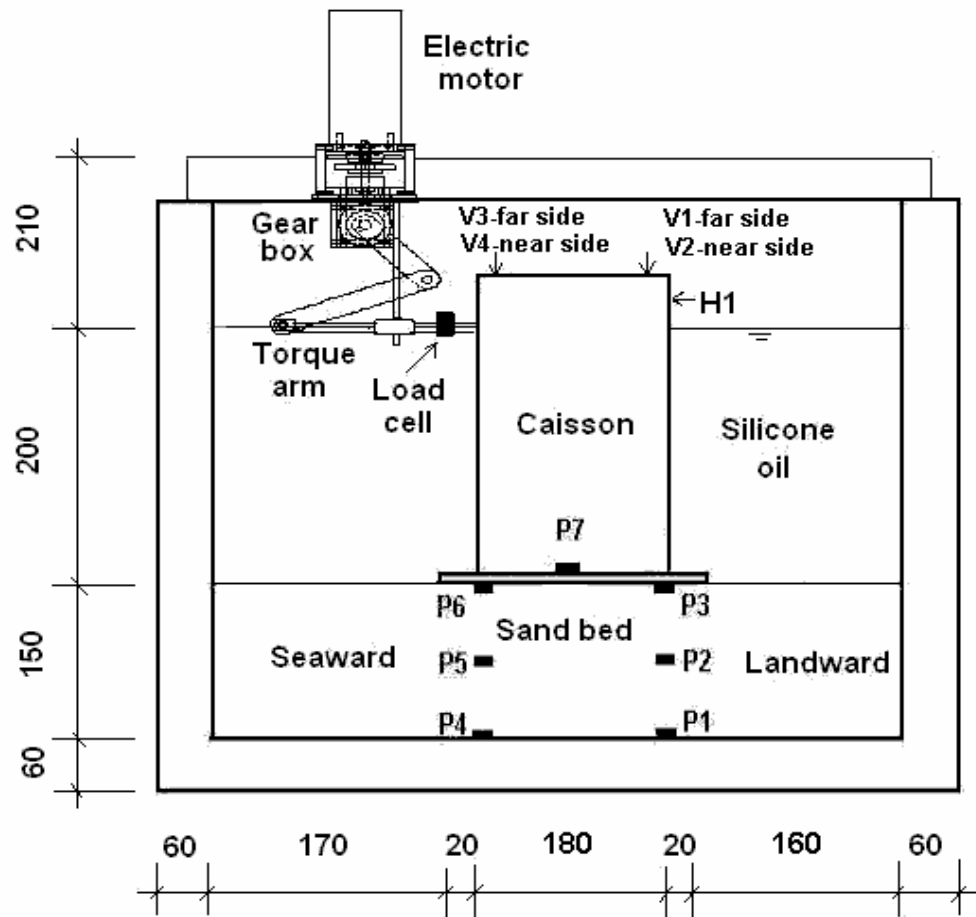
Fig. 3.1 Sketch of experimental setup and instrumentation

Fig. 3.2 Photograph of centrifuge package

A-A Section (mm)

B-B Section (mm)

Top View (mm)

Photograph of caisson

box
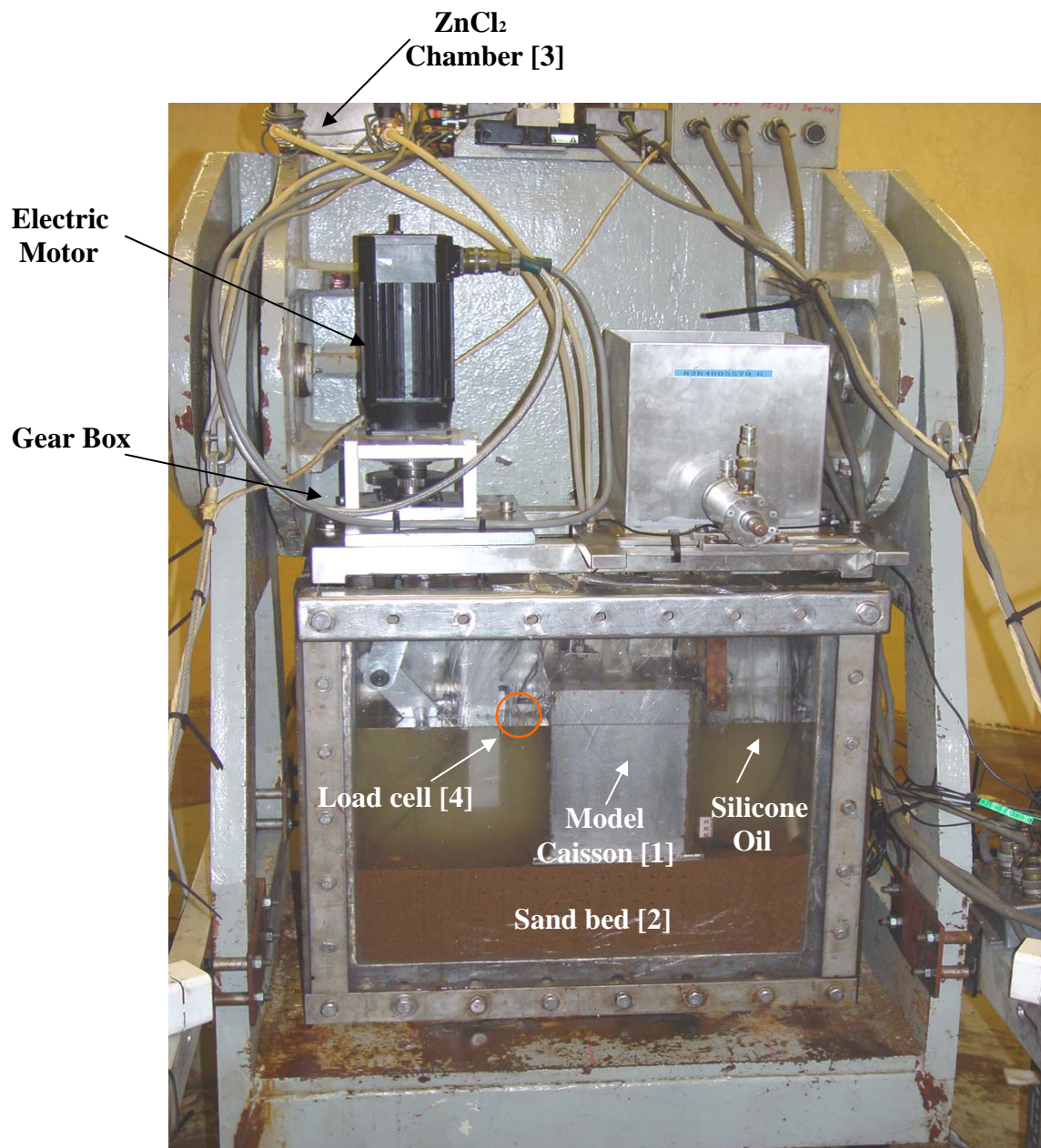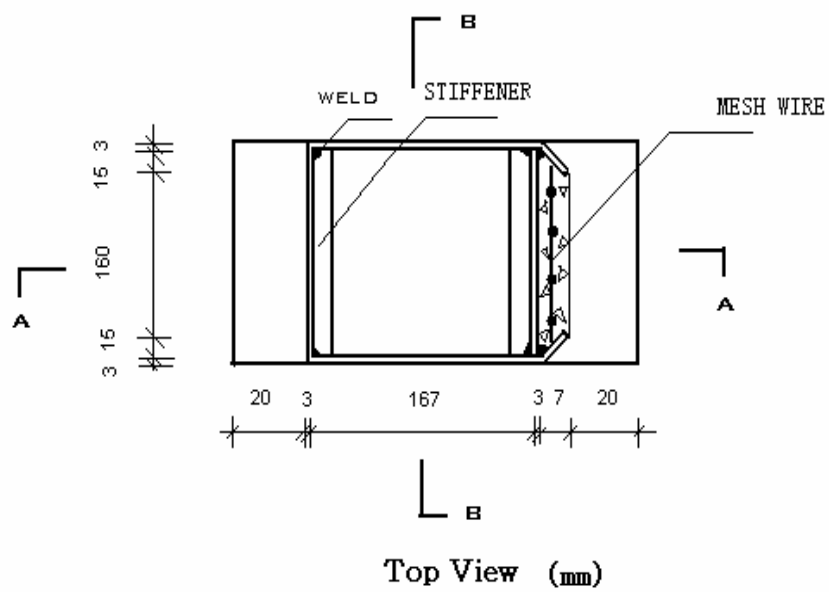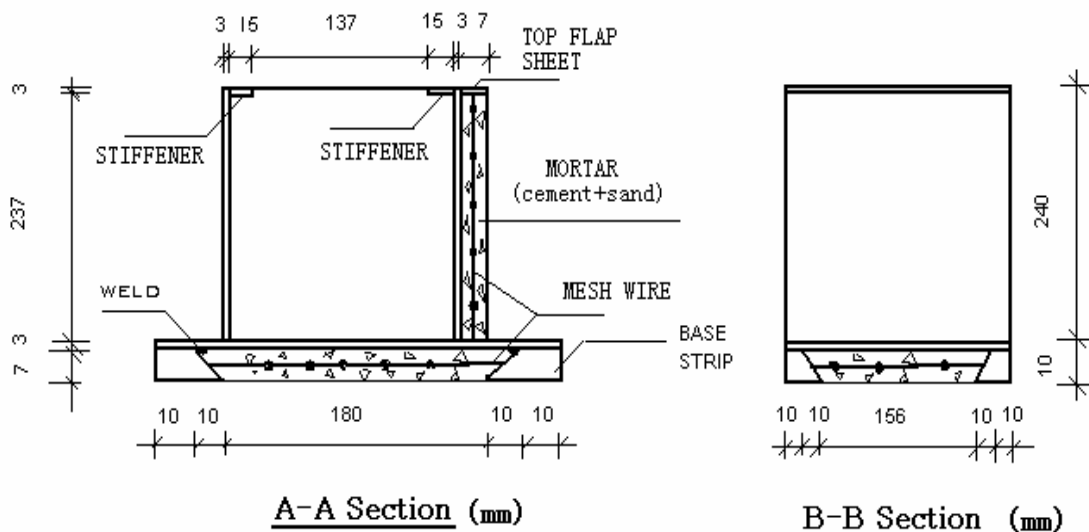
Fig 3.3 Model concrete caisson
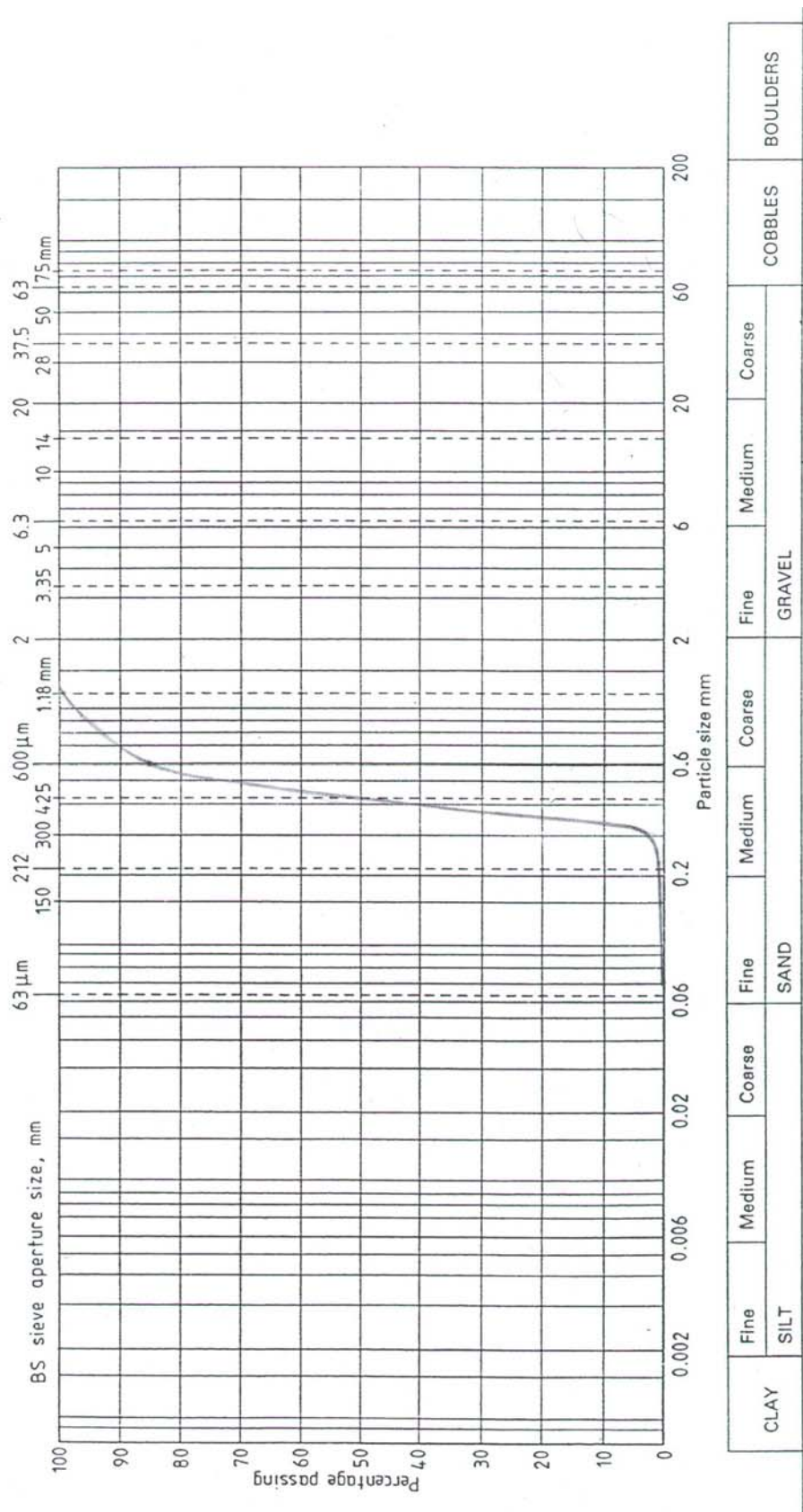
Fig. 3.4 Particle size distribution curve for sand

Fig. 3.5 Photograph of centrifuge package setup with rock berm underneath caisson base

(a) Plan view of $ZnCl_2$ chamber

(b) Isotropic view of $ZnCl_2$ chamber

(c) Side view of $ZnCl_2$ chamber
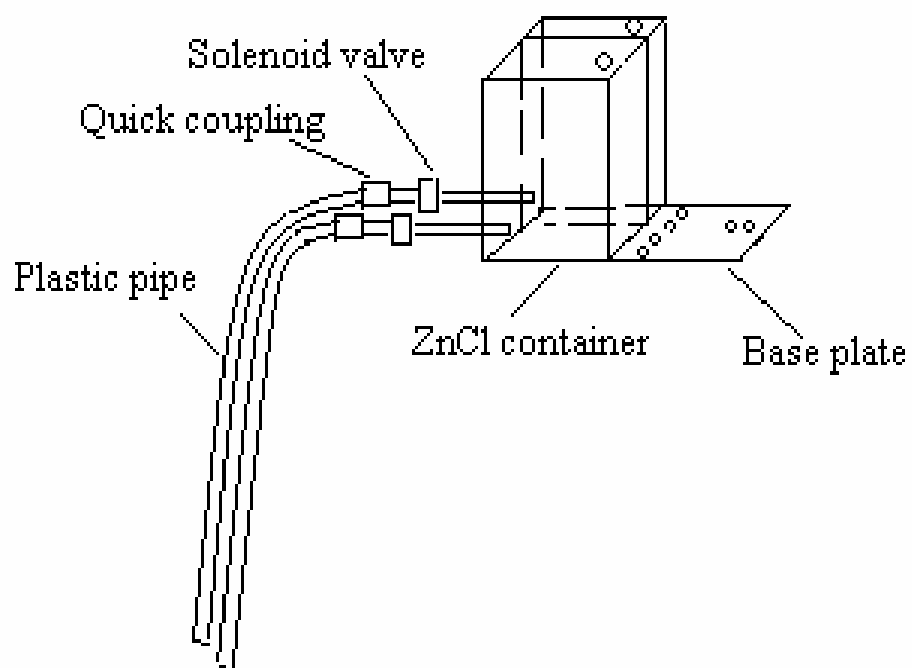
(d) Assembly drawing of $ZnCl_2$ chamber

(e) Photograph of $ZnCl_2$ chamber

Fig 3.6 Design of $ZnCl_2$ chambers (all dimensions in mm)
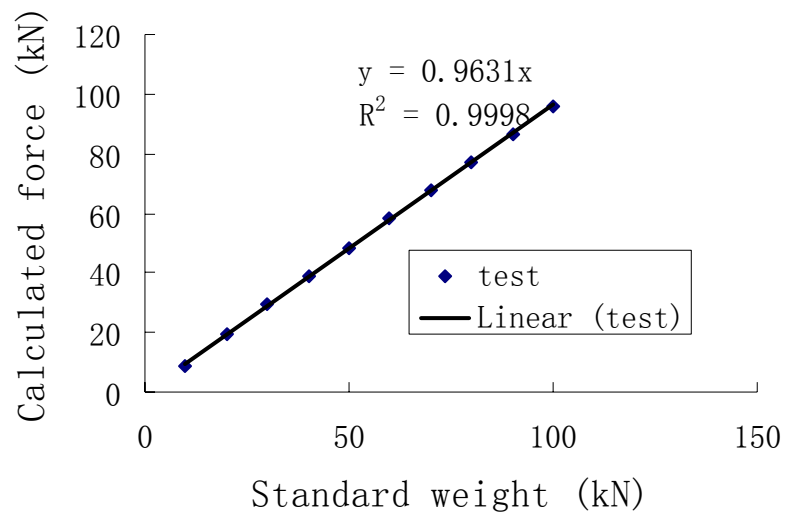
Fig. 3.7 Calibration of load cell output factor under 1g
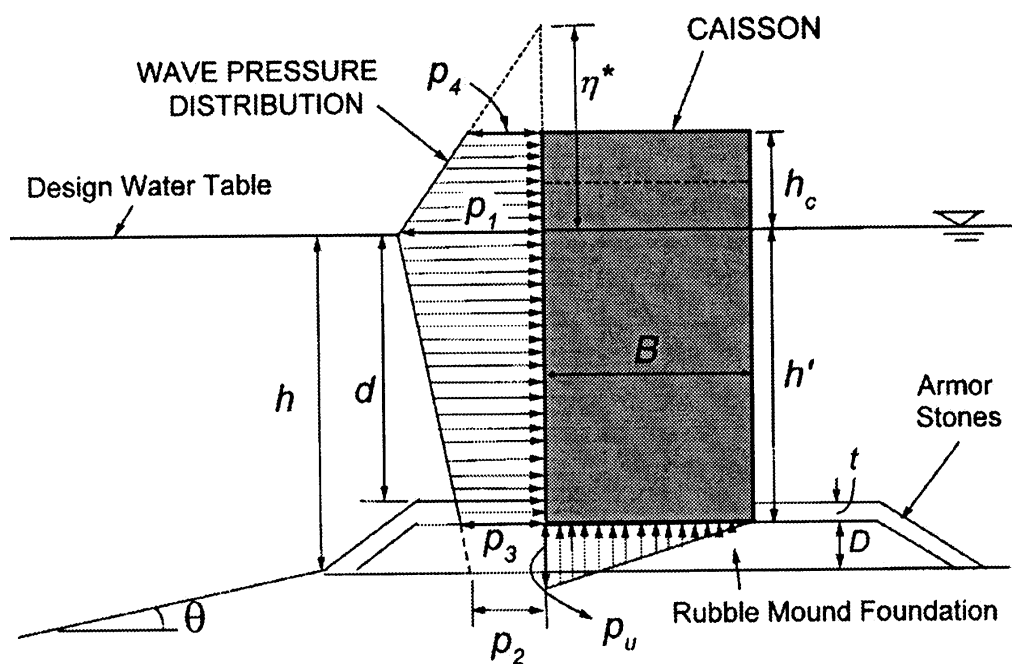
Fig 3.8 Wave pressure distributed by Goda's Formula (after Takahashi, 1996)
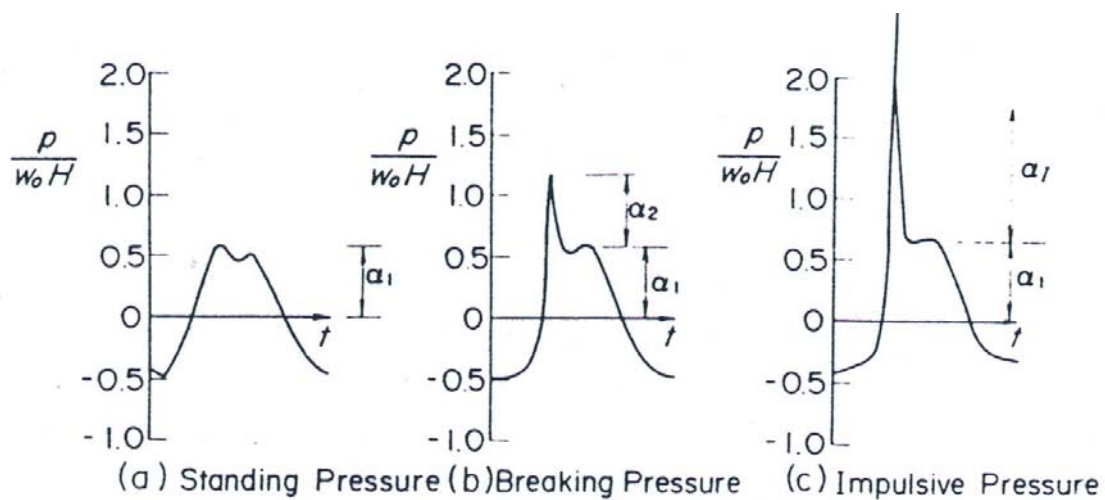
Fig. 3.9 Transition of wave pressure (after Takahashi et al., 1990)

(a) Entrapped air pocket
(double peak)

(b) No entrapped
(single peak)
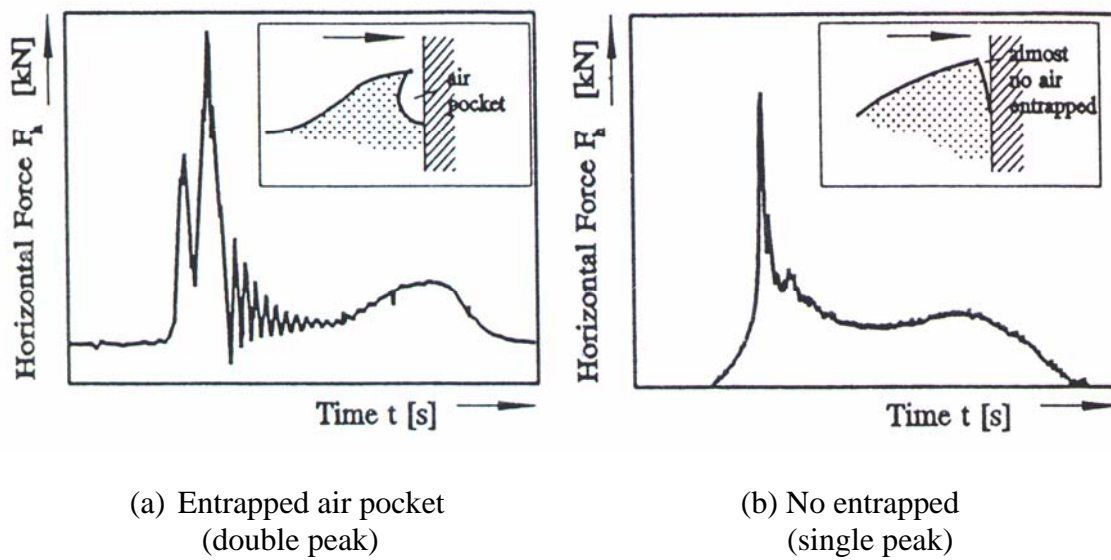
Fig. 3.10 Types of breaking wave forces (after Oumeraci, 1995)
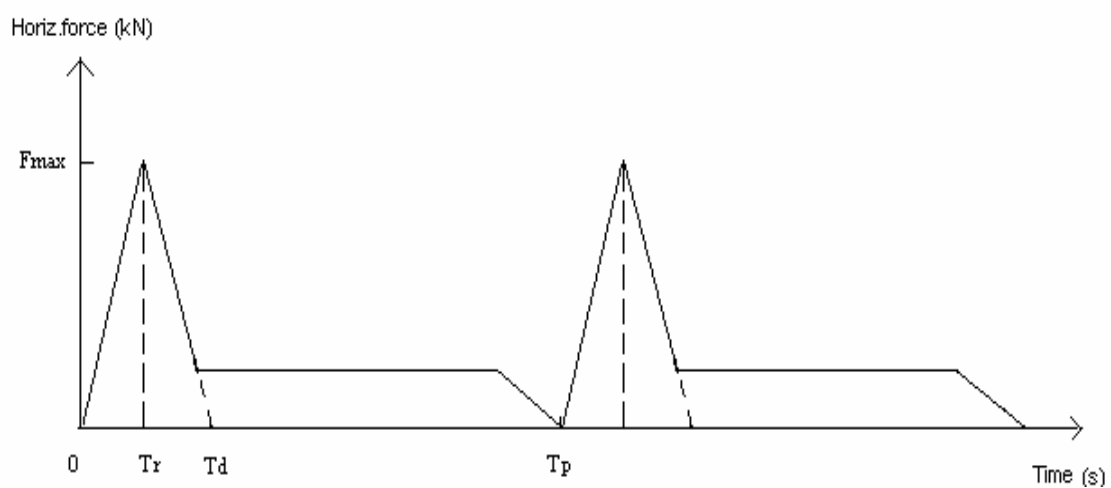
Fig 3.11 Wave impact force on caisson
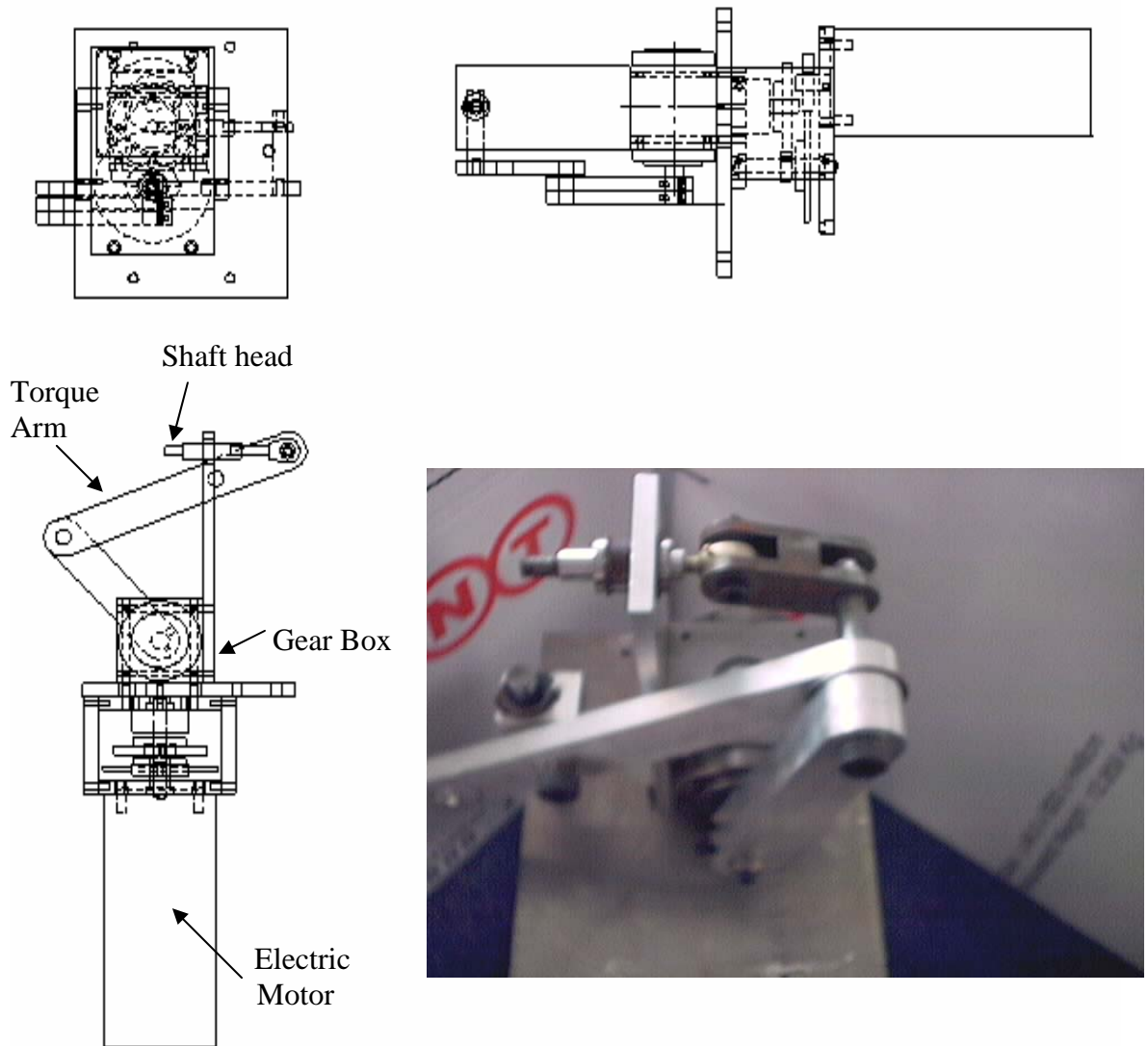
Fig. 3.12 Design of wave actuator apparatus
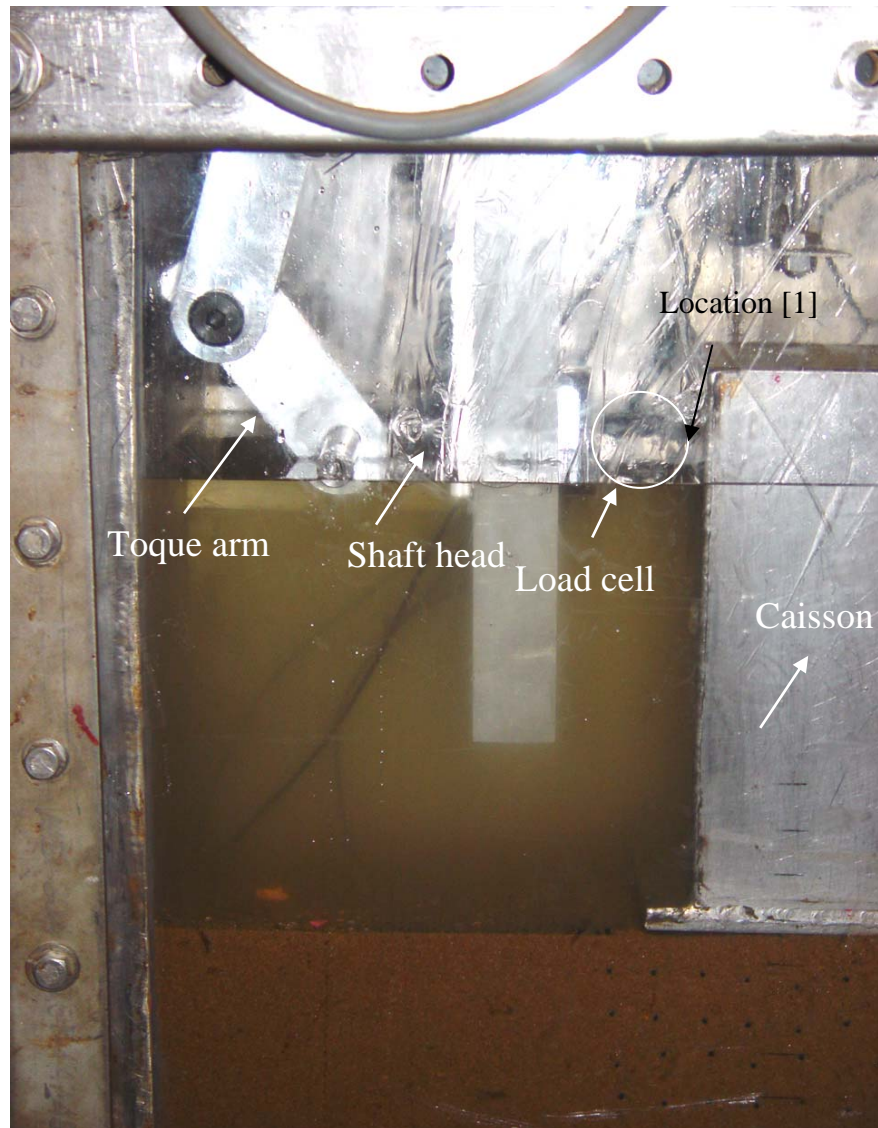
Fig. 3.13 Photograph of wave actuator apparatus
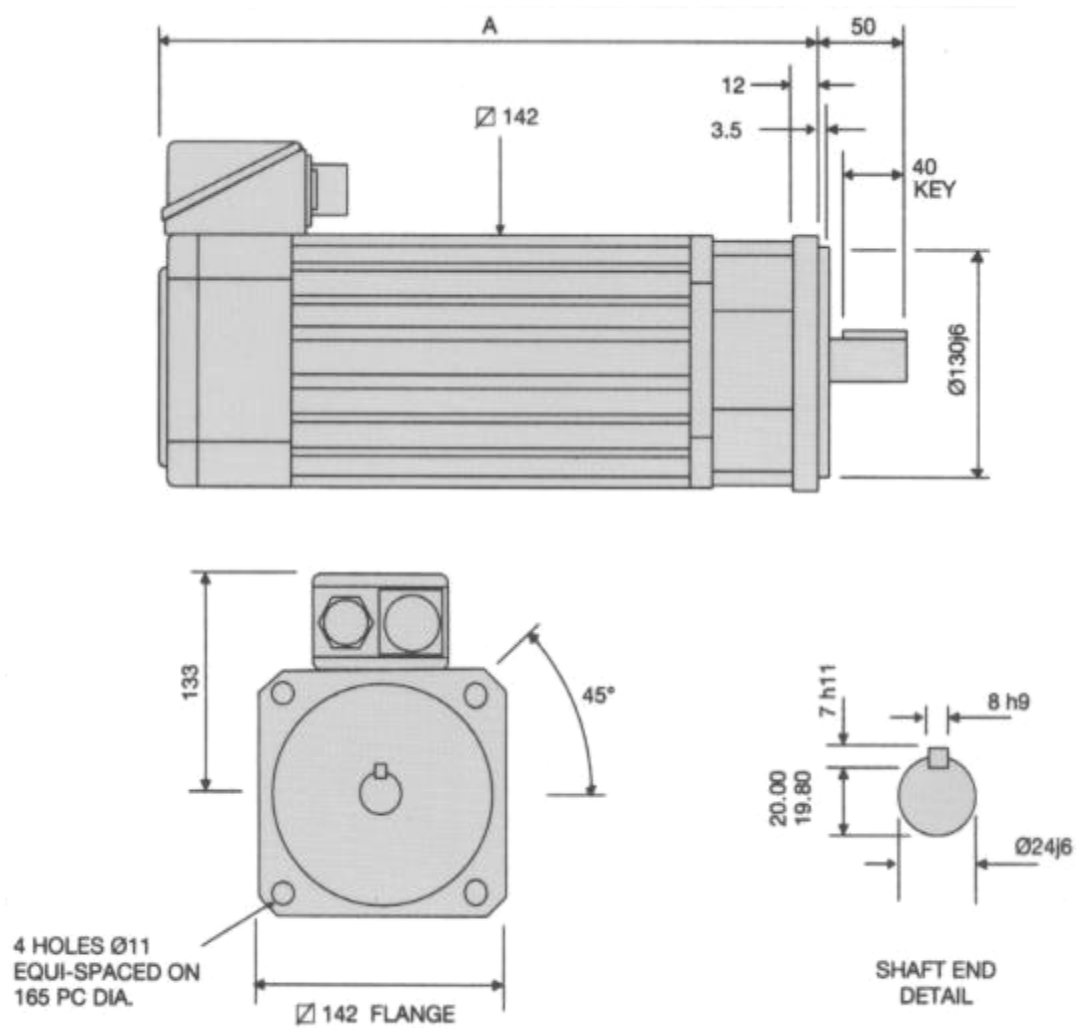
a) Sketch
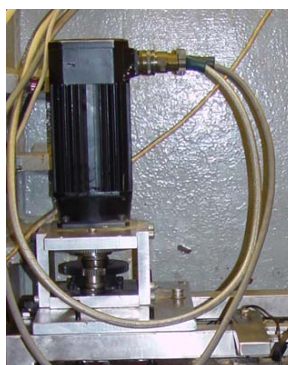
(b) Photograph

Fig. 3.14 Brushless DC/AC servomotor
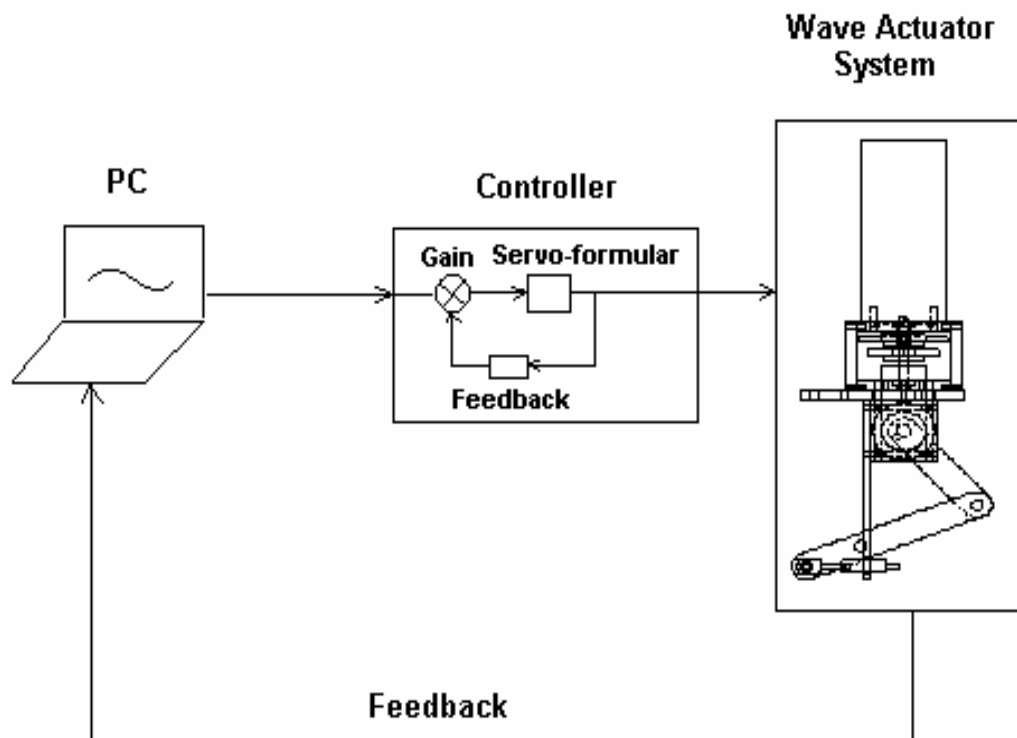
Fig. 3.15 Schematic of wave actuator system
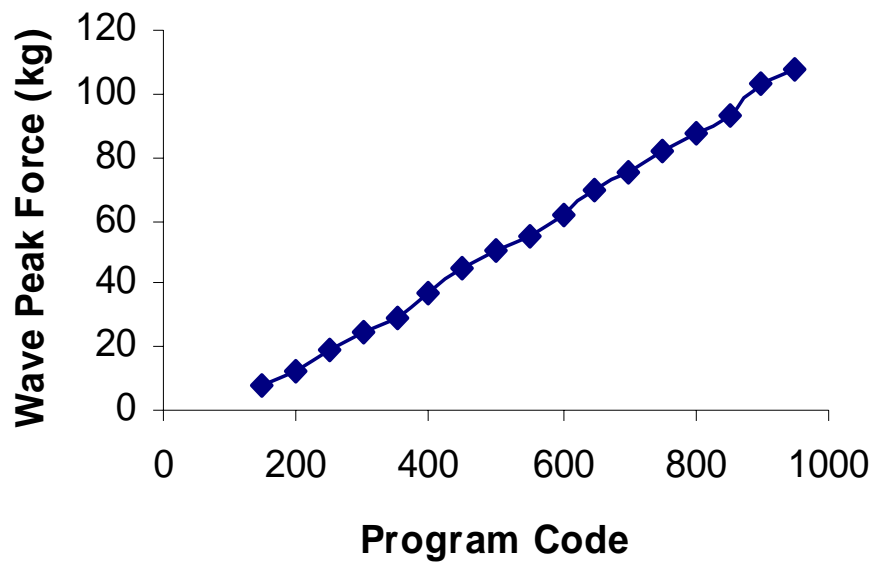
Fig. 3.16 Calibration of wave peak force
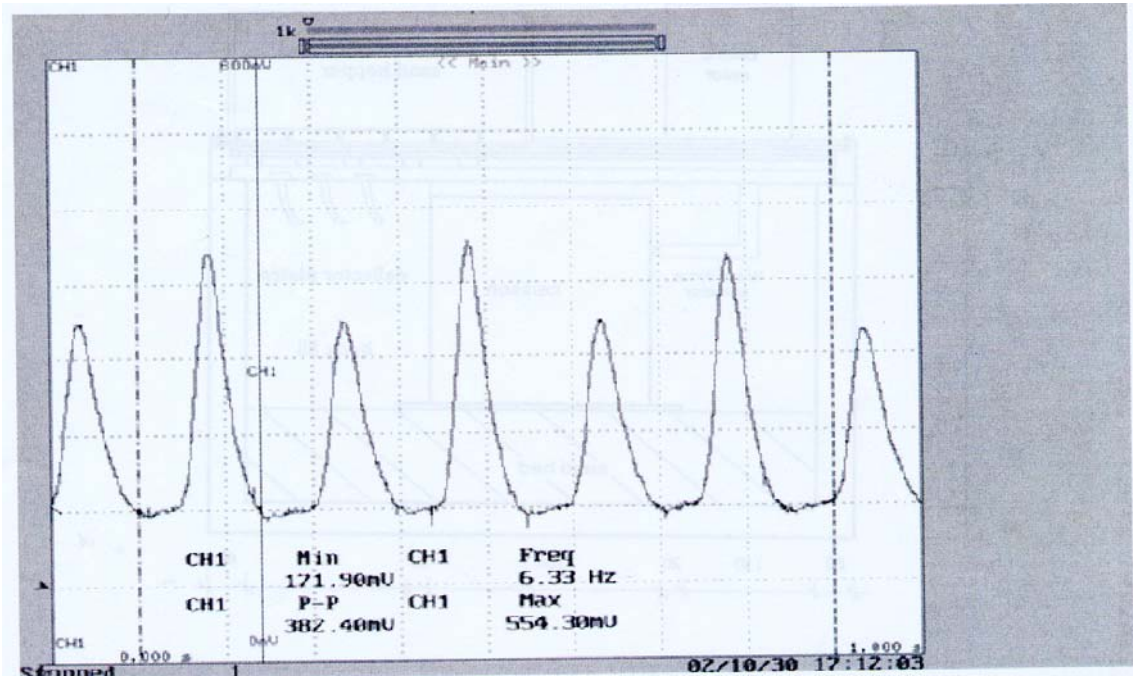
Fig. 3.17 Single-peak wave under 100g
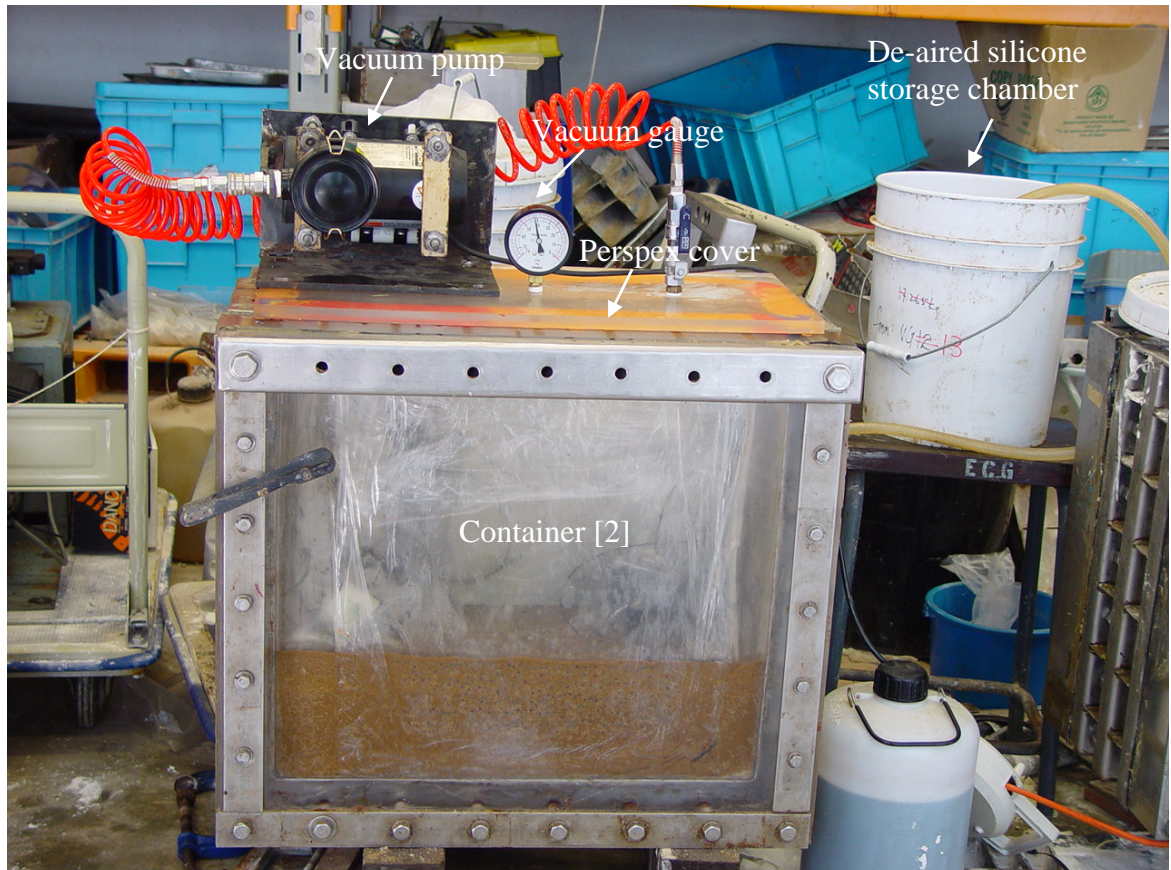
Fig. 3.18 Photograph of vacuum de-air apparatus
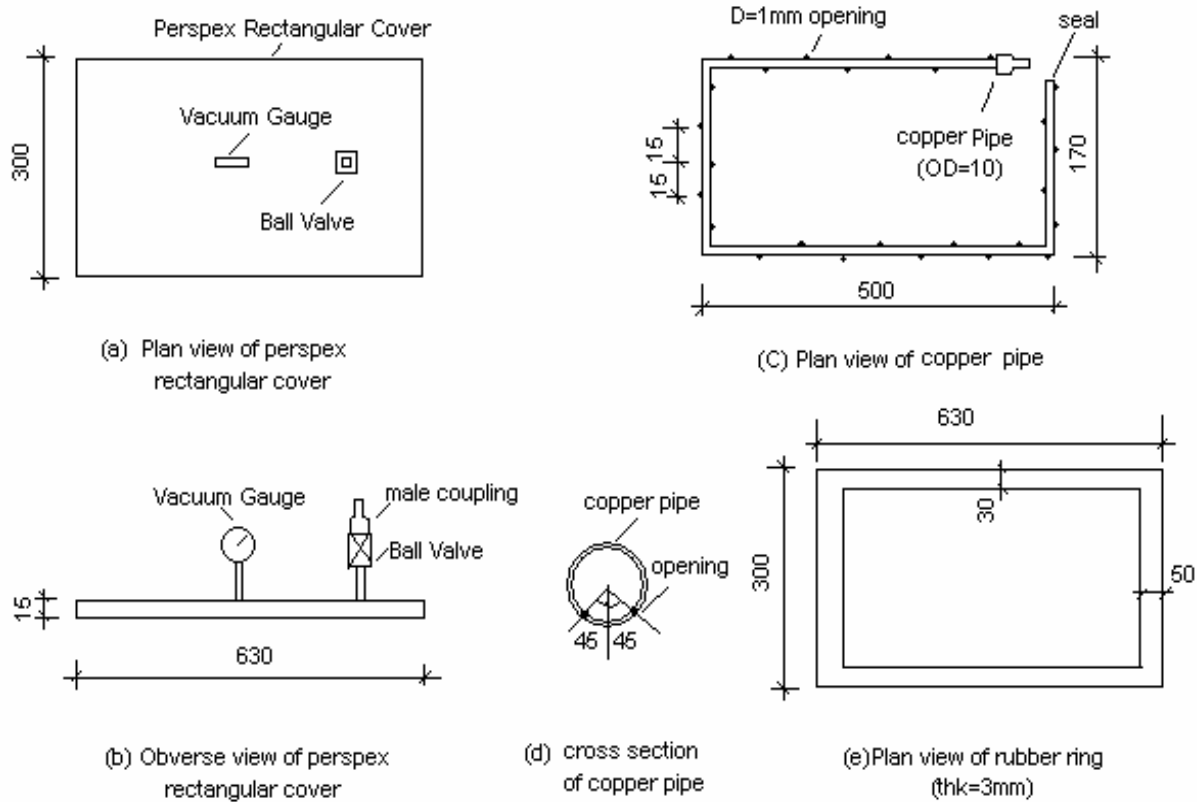
Fig. 3.19 Design of vacuum de-air apparatus
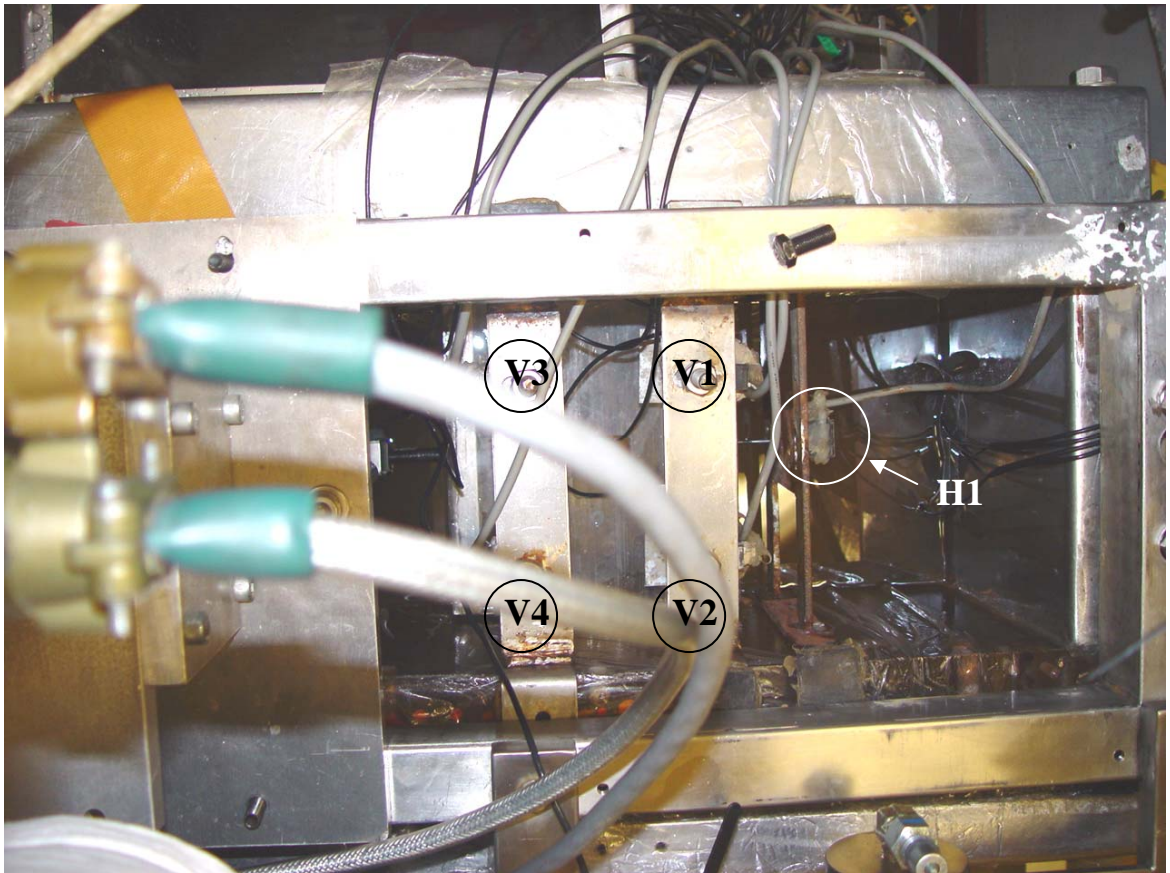
Fig. 3.20 Photograph of location of horizontal and vertical LVDTs
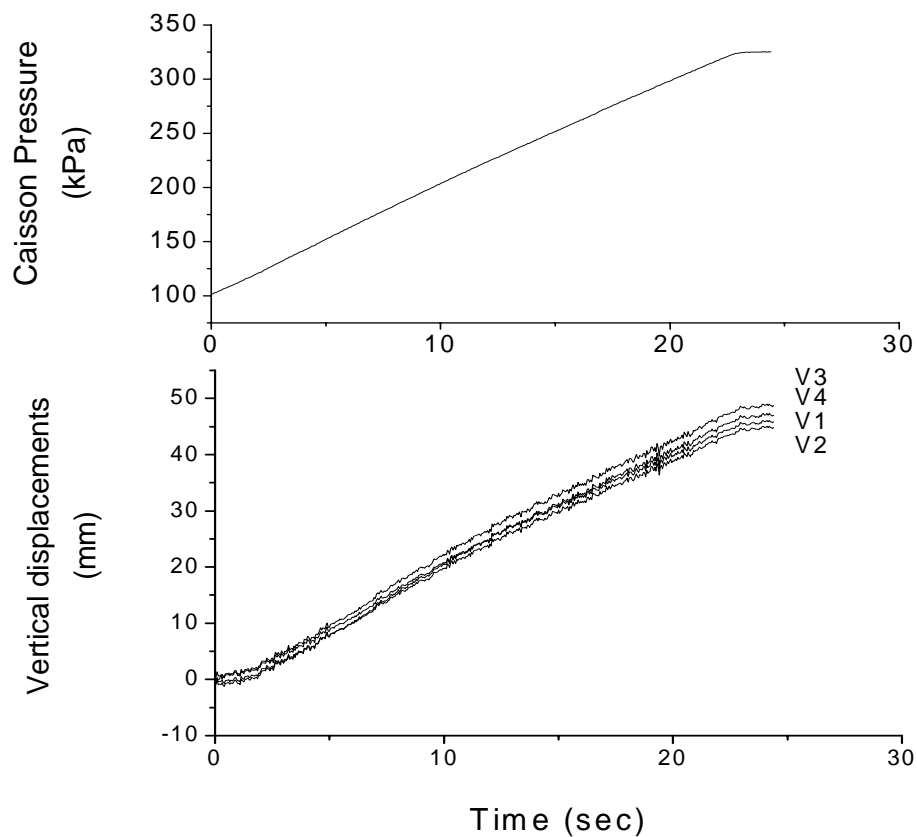
Fig. 3.21 Caisson movement response in infilling stage in test WL4 with RD=72%
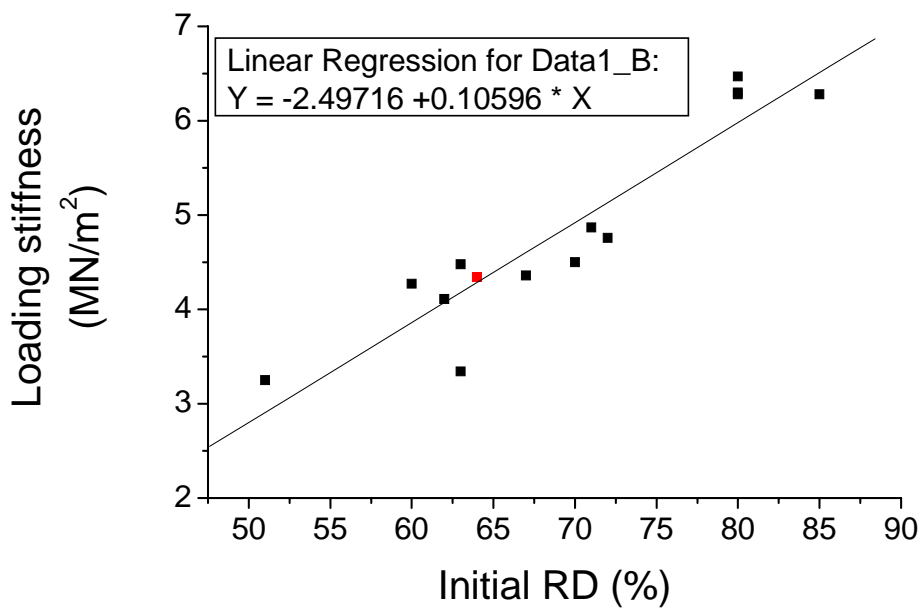
Fig. 3.22 Correlation between initial RD and loading stiffness after infilling

Chapter 4

Regular Non-Reversal Wave Loading Tests

4.1 Introduction

The experimental work consists essentially of two series of centrifuge model tests. In the first series, impulse actuator was configured with the objective of applying repeated impulse loading cycles on the caisson without any reversal of loading. As shown in Fig. 4.1, the target was to achieve a wave loading profile with the following two attributes:

(1) peak loads with equal magnitude, and

(2) troughs of loading cycles have zero magnitude.

This kind of target wave loading profile, Which is similar to the triangular load defined by Oumeraci (1995) shown in Fig. 4.2, will be termed hereafter as "regular, non-reversal" wave loading. For the case of non-resonant loading conditions in which the frequency of oscillation wave force does not coincide with caisson natural frequency, Oumeraci (1995) simplified the wave loading profile by ignoring the suction phase and approximating the single-peak "church roof" profile to a triangular profile. This is because the quasi-static load is relatively insignificant as compared with the peak load. In the present centrifuge tests, the wave loading frequency ranges at 18 to 22 H_z in model

type, which is equivalent to 0.18 to 0.22 H_z in prototype scale. From the mass-spring

model presented in Chapter 6, assuming there is no load on caisson breakwater, the

natural frequencies of caisson breakwater in the vertical, horizontal and rotational di-

rections can be obtained as 1.95 H_z, 1.34 H_z and 3 H_z. This means that phenomenon

of resonance does not possibly occur during the centrifuge tests.

The model tests discussed in this chapter were aimed at studying the response of

these models to such "regular non-reversal" wave loading. However, as will be seen

later, some occasional "irregularities" in the wave profile occurred within the 20,000 or

so wave cycles to which the models were subjected during each test. These so-called

irregularities are in fact the natural properties of the waves. However, for convenience

and simplicity, these are termed as "irregularities" in the present study. The rate of

occurrence of these irregularities averaged about 1 per 2,000 load cycles, which by itself

is a small proportion. However, they triggered large response in caisson movements

which far exceeded their relative proportion. This indicated a high degree of sensitivity

of the caisson models to the wave loading profiles.

Actual wave loading in the ocean is not strictly regular and non-reversal. For in-

stance, Fig. 4.3 shows that wave loading cycles from ocean waves on the Dieppe Cais-

son, fluctuations in the peak wave loading were noted. This is hardly surprising since

there is no particular reason why wind and wave loading should follow a strictly reg-

ular wave train profile. In fact, actual ocean wave loading profiles are not even "non-

reversal". Negative (i.e. reversal) phases are recorded in Fig. 4.3, arising from the

transient lowering in water level during the wave troughs. Moreover, the simplicity of

ignoring the negative phase by Oumeraci (1995) assumes that the negative phase does

not have a significant effect on the caisson performance. For these reasons, the effect of sign reversal in the wave loading on caisson response will be discussed in the next chapter. Finally, the effect of high wave peaks which formed a portion of the irregularities observed was investigated in Chapter 6 by comparing the results of a proposed analysis with the model test data.

4.2   Overall Caisson Response During Wave Loading

4.2.1   Data processing

Table 4.1 shows the test identification for caisson breakwater subject to regular, non-reversal wave loading. Fig. 4.4 shows the typical time history of a model "wave loading" episode of triangular profile of test WL4. Owing to the large number of wave cycles, only data for (i) first 12 wave cycles, (ii) 1000 to 1012th wave cycles and (iii) $10,000$ to $10,012^{th}$ wave cycles are presented. The wave load hereafter is expressed as a percentage of the effective caisson weight. In the non-reversal tests, the prescribed magnitude of the peak wave load is 0% to 10%. As can be seen, there is significant caisson response due to cyclic loading. The more gradual build-up of caisson movements and pore pressures may be masked by the cyclic component. Following the approach of Ng and Lee (2002), the time history plots were smoothed by averaging adjacent data points over a window of several wave cycles. This smoothing process has the property of a symmetric, low-pass, finite-impulse response filter, which suppresses the high-frequency cyclic component, thereby allowing the low-frequency trend to be visualized (Chen, 2001). As shown in Fig. 4.5(a) to (e), the displacement and excess pore pressure time histories show a significant decrease in the magnitude of cyclic components as the number of cycles over which averaging is performed is increased from 0 to 80 cycles.

This is to be expected, as Fig. 4.5 shows, the number of average cycles increases beyond 10, the relative improvement achieved by averaging over larger number of cycles diminishes to a sufficiently low level, which allows the displacement and pore pressure to be discerned. Comparison of Figs. 4.5(d) and (e) shows that, as the number of averaged cycles increases from 10 to 80, there is still a noticeable decrease in the cyclic pore pressure component but the decrease in the cyclic displacement component is much less noticeable. Thus, for the data in the present study, averaging over 10 cycles is sufficient to suppress the cyclic component to allow the trend to be clearly discerned. All subsequent data trends plotted are obtained by averaging the corresponding raw time history over 10 cycles.

4.2.2   Longitudinal and out-of-plane tilting

Fig. 4.6 shows the cycle-average settlements measured by the four potentiometers, V1 to V4 and the cycle-average horizontal movement measured by the potentiometer H1. As Fig. 3.1 shows, potentiometers V1 and V2 were located at the landward edge of the caisson while potentiometers V3 and V4 were located at the seaward edge of the caisson. Potentiometers V1 and V3 were located at the rear of the model container while potentiometers V2 and V4 were located at the window side of the model container. The vertical displacement trends of V1 to V4 show that, in addition to the tilt angle θ of the caisson in the longitudinal direction (i.e. seaward-landward), there is also a tilt angle θ_2 in the out-of-plane (i.e. cross-sectional) direction, that is, between the window side and the rear of the container. θ_2 can be determined as:

$$\theta_2 = \frac{1}{L}(\frac{V1 + V3}{2} - \frac{V2 + V4}{2}) \qquad (4.1)$$

in which L is the lateral offset between potentiometer pairs V1 & V2 and V3 & V4. The occurrence of tilt in the out-of-plane direction is not occasional. During high g level, the platform is lifted up and hence there is a 1-g gravity force downwards, which causes an inclination towards the rear of model caisson, as shown in Fig. 4.7. Hence, the window side was a little tilted up relative to the rear side of the caisson. Fig. 4.8 shows the build-up of tilt angle of the caisson in the longitudinal and out-of-plane direction. As can be seen, the longitudinal tilt is approximately 4 times as large as the out-of-plane tilt. This indicates that the out-of-plane tilting is relatively small compared to the longitudinal tilt.

4.2.3   Overall caisson movements and pore pressure response

As Fig. 4.9 shows, the tilt of the caisson does not increase in a smooth, continuous manner. Instead, it appears to be dominated by episodes of fairly sudden increase in tilt. Fig. 4.10(a) shows the build-up of tilt in four tests with different RD_i of sand bed. As can be seen, in all cases, the build-up of tilt is similarly dominated by instances of sudden increases, the latter varying significantly from test to test. In all of the tests involving non-reversal loading, the target value of the peak load is the same. As Fig. 4.4 shows, the actual peak loads are approximately equal. In spite of this, the cumulative tilt for a given number of wave cycles do not appear to exhibit a definite trend of behaviour in relation to the sand RD, see Fig. 4.10(a). Some of the tests, such as WL2, WL9 and WL7, show a consistent trend of settlement and tilt decreasing as sand RD increases. However, test WL4 clearly bucks the trend, with large tilt developing almost immediately at the start of loading and increasing apparently at discrete steps at five instances during the loading episode. In between steps, the increment in caisson tilt

is relatively small. At the same time, the settlement trend shows a reversal to a steady increase in heave shortly after the commencement of the loading episode. Stepwise increases in tilt are also present in tests WL2 and WL9, albeit in lesser numbers and smaller magnitudes. This is in stark contrast to the behaviour of the caisson during the infilling stage, wherein caisson settlement appeared to be reasonably well correlated to the RD. The reasons for this will be examined further below.

Fig. 4.10(b) shows the build-up of settlement at the caisson centerline for all tests involving non-reversal loading. This settlement value Set is computed by averaging all four potentiometers V1 to V4.

$$Set = (V1 + V2 + V3 + V4)/4 \qquad (4.2)$$

As in the case of caisson tilt, the caisson settlement also exhibits a similar "jerky" trend of increase and is also not well-correlated to the sand RD. Fig. 4.10(c) shows the build-up of horizontal movement in all tests. The "jerky" pattern and lack of correlation with RD are also reflected in the horizontal movement.

The lack of correlation of caisson movements with RD suggests that the RD is not the most important parameter influencing caisson movement in these series of tests, and that some other factors may be more dominant. One possible factor is the wave loading profile. This would be consistent with the episodes of sudden movement, if the latter is indeed related to irregularities in the wave train. At the material level, Festag (2001) also showed that plastic strain increment of triaxial sand samples suddenly occurred after some cyclic compression loading in which the vertical strain rate slowed significantly. However, Festag (2001) failed to give an explanation of this form of local

failure. Moreover, the significance of wave profile has already been alluded to by Poel and De Groot (1998) who showed that the plastic deformations of caisson were generated mainly by the highest peaks during irregular loading and the failure mechanism consisted of horizontal sliding in combination with a large rotation. This suggests that the soil can adapt and re-stabilize itself to a regular sequence of non-reversal load cycles, but this adaptation can be upset by the occurrence of irregularities in the loading pattern. Thus, Poel and De Groot's finding would suggest that, even at a caisson system level, it is not unreasonable to expect irregularities in the wave pattern to have a significant effect on caisson movements.

Fig. 4.11 to Fig. 4.13 show the trend of pore pressure accumulation during each of the tests except WL9 since PPTs were spoilt in that test. As can be seen, excess pore pressures are small, being no more than about 5 kPa in the maximum case. However, in test WL4, pore pressure "spikes" are clearly in evidence at the instances where there are sudden increases in caisson movements, as shown in Fig. 4.11.

The instantaneous pore pressures in the sand bed, that fluctuate during each wave cycle, are caused by the wave induced fluctuation of water pressure and by the rocking motions of the caisson breakwater. Because the breaking force is directly applied on the caisson breakwater by means of the wave actuator apparatus, the latter plays an important role in producing the instantaneous pore pressures. Fig. 4.4 shows the instantaneous pore pressure responses at different wave cycles in test WL4 with RD=72%. The pore pressure time history is highly unsymmetrical, with each cycle consisting of a long positive phase followed by a short negative phase. Moreover, the magnitude of the positive phase is also larger than that of the negative one. Higher excess pore pressures

always develop under the edges of the caisson base with quite small pore pressures at far away from the caisson base. It is noted a $180°$ phase difference between the seaward and landward pore pressure responses indicating the alternating loading and unloading of soils at the two edges. Under maximum forward load, the toe is unloaded, hence the sand below swells and the flow of silicone oil leads to the emergence of negative pore pressure. At the same time, the heel is loaded and the sand below the caisson heel continues to be under compression, causing the increase in positive pore pressures. When unloading to the minimum forward load, the caisson might settle back onto the softened sand and the pore pressures recover to its original situation. The pore pressures at the two sides of the shallow foundation when subjected to earthquakes were noted by Zeng (1998) to experience the same phenomena as the centrifuge tests.

It is also interesting to note that the peaks of the landward excess pore pressure occur at different times with those at shallow depths occur earlier than that at greater depths. In addition, large fluctuation of pore pressure at the edge of caisson breakwater also occurs at shallow depths, as indicated in Fig. 4.4. The impulsive wave loads are transferred to the sand bed through the rocking and swaying motion of the caisson breakwater and the only resistance opposed to these loads is provided by the shear strength of the foundation soil, inertia and damping forces (Oumeraci, 1994a). Hence, the cyclic wave loads are mostly felt by the surface soil just beneath the base of caisson and then transferred to a greater depth through rearranging the soil skeletons. On the other hand, the larger and earlier fluctuation of seaward pore pressure is found to occur in greater depths. When the breaking wave force loads on the caisson, the toe of caisson breakwater is unloaded and hence drainage could probably take place at the seaward

base of caisson.

4.2.4   Effects of irregularities in the wave profile

Figs. 4.14 and 4.15 show the wave loading, caisson tilt, settlement, horizontal move-
ment, seaward and landward pore pressure time histories at the episodes of sudden
increase in caisson movements in test WL4. All these plots were based on unaveraged
(i.e. raw) time history records. As can be seen, in all these episodes, irregularities were
indeed present. These irregularities can be categorized into two types. The first type
is wave spike, in which the peak impulsive load significantly exceeds the target value
by about four times. As shown in Fig. 4.9, these spikes occur on average about 1 in
5,000 wave cycles. They are attributed to the limited high frequency response of the
servo-motor, which resulted in the latter not being able to adjust the loading fast enough
when the caisson movement is too fast. However, this could be possible in the site as
the variation of foreshore geometries, wave height and wave period from time to time
also leads to the fluctuation in wave magnitude. In all cases, the wave spikes resulted
in a sudden increase in caisson movements and pore pressure response, which occurred
within the same cycle as the wave spike.

The second type of irregularity is a reversal phase within a wave cycle, as shown in
Fig. 4.15. The negative load on the actuator denotes a tensile force, which is indicative
of a "pull" by the actuator on the caisson. The magnitude of the peak reversal load is
much smaller than that of the peak impulsive load, being typically no more than about
2% of the caisson buoyant weight or 1235 kN. The cause of the reversal loading is less
obvious than that of the loading spike. This is because, in the non-reversal loading tests,
the actuator end is not attached to the caisson, it merely bears onto the latter. Thus, when

the actuator is retracted after every impulsive phase, it is free to detach from the caisson. The fact that there is a small tensile load in the actuator in a few cycles suggests that, in these cycles, the actuator tip is unable to detach (see location [1] in Fig. 3.13) cleanly from the caisson face. One possible cause of this reversal phase is the development of suction between the flatten end of the actuator and the face of the caisson. The level of the actuator coincides approximately with the surface of the silicone oil. Wetting of the actuator-caisson interface may therefore occur as a result of "splashing" of silicone oil by the actuator and caisson movement. Under such conditions, transient suction may develop between actuator and caisson owing to the high speed of the actuator and the high viscosity of the silicone oil (100 cst). By considering the contact area between actuator and caisson, it is shown that the suction needed to develop this tensile load at the actuator-caisson interface is of the order of 525 kPa. The large increase in caisson movement and pore pressure response typically occur during reloading of wave cycle after the reversal phase. The effect of wave spike and reversal-phase wave on caisson response will be examined in detail later.

Fig. 4.16(a) shows the build-up of caisson tilt at various stages of the loading episodes, after removal of the sudden increases caused by the irregularities. As can be seen, a much more consistent trend is now obtained between final tilt and RD_i. Thus, the occasional departure of the wave train from a perfectly regular and non-reversal profile, together with the sensitivity of the caisson foundation to such irregularities, has led to the influence of the RD being overwhelmed by influences from loading profile. There may well be an interaction between the effects of the irregularities and those of the regular segments of the wave train. Nonetheless, the fact that the effects of RD can

be reasonably well-presented by removing the sudden increases from the cumulative tilt suggests that these two effects (i.e. those of the regular and the irregular parts of the wave train) are largely superimposed. Similarly, as shown in Fig. 4.16(b) and (c), the correlation between the settlement, the horizontal movement and the RD_i are also much improved.

4.3 Caisson Response During Regular Wave, Wave spike and Reversal wave

4.3.1 Caisson response during the regular wave segments

Fig. 4.16(a) and (b) show, in test WL2 with RD=60%, caisson tilt during the "regular" wave segments stabilizes over the first 12,000 wave cycles, while in the other tests, caisson tilt and settlement rapidly stabilize within 2,000 wave cycles. Thereafter, increment in the tilt becomes quite minimal. This kind of "shakedown" type of response is similar in trend to those observed by Springman et al. (1996) on integral bridge abutments and Smith and Molenkamp (1980) on offshore structures. Fig. 4.16(c) shows that the same is true for the horizontal movement at the potentiometer H1.

It should however be noted that the horizontal caisson movement H1 is likely to consist of a significant component contributed by caisson tilt; the latter component being equal to the product of tilt angle and standoff from potentiometer H1 to the centre of rotation. Fig. 4.17 shows the horizontal movement H1 plotted against the angle of tilt θ for some number of wave cycles in test WL4. These figures show that the relationship between H1 and θ may be given by the linear relationship:

$$H_1 \ (in \ \ mm) = C + M * \theta \ (in \ \ radians) \tag{4.3}$$

In which C is the cumulative plastic horizontal movement due to sliding, and M reflects the vertical offset between the potentiometer H1 and the centre of tilt. It is considered that the sliding is absence in centrifuge tests; the peak horizontal impulsive load is only about 39% of the caisson's buoyant weight, which is equivalent to a mobilized angle of friction of about $21°$ at the caisson-sand interface. Such small value may not be able to induce significant caisson sliding. As Fig. 4.17 shows, in a given continuous sequence of regular wave cycles, C is almost unchanged from the 3rd wave cycle to the 27th wave cycle. Moreover, M is almost constant and has a value of about 8.5 m. This indicates that the caisson rocks about a centre of tilt which is practically stationary and is located at a depth of about 8.5 m (in prototype terms) below the potentiometer H1. Since potentiometer H1 is located $21\ m$ above the caisson base in prototype terms, this indicates that the centre of rotation is located very close to the caisson gravity centre. There was some initial suspicion that this might have been due to the added mass of silicone oil in front of and behind the caisson. However, as Fig. 4.18 shows, the centre of tilt remains around the mid-depth of the caisson even when the silicone oil level has been lowered down to the sand surface.

Fig. 4.19 shows the rotational stiffness during the regular wave segments, which is defined as the gradient of moment at caisson base over the angle of tilt. The rotational stiffness reduces slightly from the 2nd wave cycle to the 6th wave cycle, which is also consistent with the findings by Poel and De Groot (1998). After the first 200 cycles and before the occurrence of irregular waves, rotational stiffness during regular wave cycles remains almost constant, indicating that a stable (presumably elastic) state has been reached.

The excess pore pressure responses with the change of moment of caisson base under the regular waves are shown in Fig. 4.20(a) and (b). At the commencement of the loading cycle, positive pore pressure of soil under the caisson heel is generated as a result of increase in total stress and reduction in effective stress. In general, the effective stress appears to lead total stress. Thus, at the later stage of the loading phase, excess pore pressure decreases while the total stress continues to increase. Upon unloading, excess pore pressure decreases, probably driven largely by the decrease in total stress. Underneath the caisson toe, events are almost exactly out-of-phase compared to that underneath the heel. At the start of the wave loading episode, cyclic excess pore pressure fluctuations are not exactly in phase with the moment; this results in a loop in the excess pore pressure vs moment plot in Fig. 4.20(a) and (b). This can be attributed to shear-induced dilatancy of the sand bed. The larger loop developed on the landward side suggests more severe nonlinearity of the sand underneath the caisson heel. After 200 wave cycles, the area of the loop becomes smaller indicating that the excess pore pressure fluctuations are coming into phase with the moment, as the foundation stabilizes.

4.3.2   Caisson response during the wave spike

Fig. 4.21 shows the caisson response during wave spike at the 3720th wave cycle in test WL4. The caisson base was found to move in the direction of the load from the beginning, as shown in Fig. 4.21(a). As the wave loading increases past the level of the regular wave toward the peak of the wave spike, the horizontal movement increases faster than the tilt. This leads to a significant increase in vertical offset between point H1 and the centre of tilt. This implies that the centre of tilt is effectively migrating

downwards as the wave load increases. At the peak of the wave spike, M has a value of about 22.38 m. This indicates that the caisson rocks about a centre of tilt which is located at a depth of about 22.38 m (in prototype terms) below the potentiometer H1. Since potentiometer H1 is located 21 m above the caisson base in prototype terms, this indicates that the centre of tilt is located just beneath the caisson base. Similarly, in test WL11, the centre of tilt was found to be located at a depth of about 22.86 m as shown in Fig. 4.22.

The downward shift of the centre of tilt can be explained in terms of a simple elasto-plastic framework involving shear resistance along the caisson base and rotational failure mechanism. During low levels of wave loadings, such as those which occur during the regular wave cycles, the caisson foundation is largely elastic and tilt is relatively small. One may postulate that for a tall structure like a caisson, a significant portion of the balancing moment comes from the shear force at the caisson base. Under this condition, the centre of tilt of a tall structure like a caisson should lie above the caisson base. If the centre of tilt lies at the base of the caisson, then the shear force is required to develop under conditions of zero movement, which would need an infinitely stiff caisson foundation. Since this is clearly impossible, some waveward movement of the caisson base is inevitable and this brings the centre of tilt above the caisson base. As will be shown in the analysis in Chapter 6, the assumption of an elastic foundation does bring the centre of tilt to somewhere around the caisson mid-depth. As the wave load increases, significant rocking resistance develops underneath the caisson base due to the non-uniform distribution in bearing pressure. As the proportion of rocking moment resisted by this mechanism increases, so the proportion resisted by the shear force

along caisson base reduces, and the centre of tilt migrates downwards.

The soil rotational stiffness during the wave spike was found to be much smaller than that before and after the wave spike (i.e. regular wave), as shown in Fig. 4.21(b). However, the soil can adapt and re-stabilize itself to the regular sequence of non-reversal load cycles after the occurrence of irregularities in the loading pattern. This is indicated by the fact that the rotational stiffness before and after the wave spike was almost unchanged. Furthermore, bigger loops of excess pore pressures at both landward and seaward are also observed for the wave spike compared with those under regular wave, as shown in Fig. 4.21(c). This is reasonable since a larger wave load will probably elicit a more non-linear (probably plastic) response from the caisson foundation. As a result, excess pore pressure generation will become less in-phase with moment.

4.3.3   Caisson response during the reversal phase

Fig. 4.23 shows the caisson response during the reversal phase in test WL4 at the 1644th wave cycle. Due to the inertia effect, the horizontal movement and tilt angle increase only at the peak of wave reloading. Bigger loops of excess pore pressures at both edges of caisson base are again observed for the reversal wave compared with those under regular wave, but smaller than those under wave spike, as shown in Fig. 4.23(c). The effects of reversal wave loading with different strength on caisson response will be examined in greater detail in Chapter 5.

4.3.4   Soil movements underneath caisson base

Fig. 4.24 displays the two-grid vector maps of soil movements of sand bed after the infilling and wave loading stages of test WL4, respectively. These soil movement vectors

were obtained by attaching black line markers in the side view of sand bed surface and then analyzing the line marker movements using an image processing software OPTI-MAS. As soil movement decreases rapidly with depth, only soil movement down to 6 m depth was analyzed.

After the infilling stage, the soil movement decreases with increase in soil depth. Hence, most of the soil movements occur in the top layer. Close to the two edges of caisson base, the soil moves sideward. The symmetry of the soil movements along the mid-base of caisson indicates that the sand key prepared by using the vacuum de-air method is fairly uniform.

After the wave loading stage, the surface soil under the caisson base moves downwards as shown in Fig. 4.24(b), revealing residual settlement of the caisson base. In addition, there is a clockwise soil flow under the seaward caisson base. This explains why the caisson toe heaves after 1,000 wave cycles with the development of positive excess pore pressure. The larger downward movements occurring in the landward side means that the caisson heel settled more than the caisson toe. The soil outside the caisson toe heaved after wave loading. Because of lack of markers in the landward side, the movement of the soil outside the caisson heel cannot be ascertained. Nonetheless, the general picture that emerges from these markers is consistent with that discussed earlier. Firstly, tilt is a very important part of the caisson movement. Secondly, plastic soil flow seems to underscore the existence of a rotational failure mechanism underneath the caisson base, with the soil flowing from the heelside to the toeside, and this is supported by the permanent tilt of the caisson after the wave loading. This also explains the ground heave outside the caisson toe.

4.4   Parametric Studies

4.4.1   Caisson width

In the present study, the effective loading pressures underneath the caisson base for the three different caisson widths of 14 m, 16 m and 18 m are designed to be almost the same, 100 kPa. The effect of caisson width on its performance is investigated when the caisson is subjected to non-reversal wave loading.

The comparisons of average caisson movements with different caisson widths are shown in Fig. 4.25. Although irregular waves occasionally occurred in these three tests, its effect is overwhelmed by the caisson width effects, especially between the caissons with 14-m wide and 16-m wide. It is noted that during the wave loading stage, the magnitudes of tilt angle, settlement and horizontal movements are the most for the 14-m wide caisson as compared to the 16-m and 18-m wide caissons. This is reasonable as the factor of safety against sliding and overturning is significantly lower for the caisson with a smaller width because of the reduced total weight. The maximum tilt angle for the 14-m wide caisson is $0.25°$ as shown in Fig. 4.25(a), implying that this width may not be adequate to provide the necessary stability against overturning. At the same time, the horizontal movement of the 14-m wide caisson is up to 133 mm which also means it may not have enough stability against sliding (Zhang et al., 2005). Because the averaged tilt angles of 16-m and 18-m wide caissons are quite close, it is replotted after removal of the sudden movements due to the irregular wave as shown in Fig. 4.26. Still, there is a consistent trend between the caisson tilt angle and the caisson width.

Fig. 4.27 shows the residual pore pressure responses of the 16-m-wide caisson. The build-up of the residual pore pressure is fairly low although the instantaneous pore

pressure can be up to 15 kPa. Negative pore water pressures of the 14-m-wide caisson occurred from the beginning of wave loading, as shown in Fig. 4.28. This might be due to the occurrence of slip surface and hence lead to shear transfer localized underneath the caisson base. The decrease in total stress caused the occurrence of negative pore pressures under the two edges.

4.4.2   Caisson weight

During the construction of caisson breakwater, the caissons will be sunk by infilling with water and subsequently be placed to the prescribed level. Then the caisson cells are filled with sand and be placed in a continuous line, resulting in a plane strain loading condition. There may exist an interval to tow and align the row of caissons before infilling with sand and the caisson breakwater may be in a critical situation when subjected to breaking wave loads. Hence, test WL5 was conducted on the caisson breakwater exposed to non-reversal impulsive force without infilling $ZnCl_2$ solution. In this test, the bearing pressure under the caisson base is 100 kPa, while that of normal caisson is 325 kPa in test WL2.

Fig. 4.29 shows the comparisons of averaged movements of caisson with different weight. It is noted that the vertical displacement, horizontal movement and tilt angle greatly increase as the caisson weight becomes lighter. The caisson heel settles by 82 mm and the toe 28 mm with a tilt angle up to $0.26°$, which implies that the caisson may not have enough stability against overturning. Although wave spike occurred in both tests, the trend is pretty clear. It is in stark contrast to the RD effect, which is overwhelmed by the irregularities.

Relatively large residual pore pressures develop from the very beginning of wave

loading and then dissipate to the hydrostatic line, see Fig. 4.30. Therefore, the time interval between sinking the caisson breakwater to the prescribed water depth and then ballasting with sand should be as short as possible. Otherwise, extra maintenance work may need to be done to adjust the caisson movement.

4.4.3   Presence of rock berm

In the present study, only vertical breakwaters without rubble mound foundation are investigated. In practice, a trench is formed by dredging and removing the soft soil down to the desired level and replaced by sand. In addition, 150 mm to 325 mm diameter compacted cobbles are placed on the sand around the caisson area. The thickness of rock berm varies from about 2 m to 8 m depending on the loading and foundation conditions. The rock berm is intended to support the caisson weight against bearing capacity failure. Leung et al. (1997) found that placing a layer of rock berm between the caisson base and sand key will significantly reduce the horizontal displacement of the gravity caisson foundation. In view of this, further test was conducted on caisson breakwater to examine the effect of a 4-m thick rock berm underneath a caisson which is subjected to breaking wave loads.

The comparisons of averaged movements of caisson breakwater with and without presence of rock berm are summarized in Fig. 4.29. It seems that presence of rock berm can greatly suppress the caisson settlement and horizontal movement. The tilt angle is replotted after removal of sudden movements due to irregularities, as shown in Fig. 4.31. With the presence of rock berm, the tilt angle is reduced. The caisson heel settles a little in the first 100 wave cycles and then starts to heave. The caisson toe heaves all along during wave loading. This is because after infill stage, the void between the rock

skeletons completely closes. When subjected to wave loading, the rock sill may dilate due to its large angularity. This is confirmed by the residual pore pressure time history in Fig. 4.32 and the contour maps of excess pore pressure in Fig. 4.33. In the first several wave cycles, negative pore pressure emerges in the rock berm and localized in the top thin layer of seaward side, while bulbs of positive pore pressures develop in the landward side. Then the negative pore pressures propagate to the landward side and at about 5,000 wave cycles, the soil fully dilates. The pore pressure response of the soil bed is consistent with the caisson settlement response.

4.4.4 Slamming on top slab

The special service loads for vertical breakwater design include permanent loads (dead weight and reaction of foundation) and variable loads (pulsating and impact loads), see Fig. 4.34. The most likely mechanism for the generation of large dynamic loads from the harbor side is the plunge into the harbor of an overtopping wave. Hence, many breakwaters may experience significant static and dynamic loading on both seaward and rear face, and slamming on top slab as well. In test WL1, slamming on the top slab of caisson was simulated by infilling another appropriate quantity of $ZnCl_2$ of 60 kPa into the caisson while the caisson is subjected to non-reversal wave loading.

In test WL1, irregular waves were absent in the whole wave loading. Fig. 4.35 shows the averaged caisson movements and pore pressure response plotted against the number of wave cycles in a semi-log scale. The progressive seaward and landward settlements of the caisson breakwater increase exponentially from 200 to 800 or so wave cycles. After 800 wave cycles, there is a sudden increase in caisson settlement because slamming load is applied to the caisson, as indicated in the large increase in

caisson pressure in Fig. 4.35(a). Substantial increase in tilt angle due to wave loading and slamming is found in Fig. 4.36, compared to the tilt angle of caisson subjected only to wave loading.

Fig. 4.35(c) shows the average pore pressure-log time responses. It is found that the positive pore pressures reached the peak value in 150 or so wave cycles. After about 1000th wave cycles, the second peak excess pore pressures occurred due to further infilling of $ZnCl_2$ solution. After this, the positive pore pressures appear to dissipate gradually and fluctuate around the hydrostatic value. The increase in positive excess pore pressures reduces the effective stress in the oil-saturated sand bed and results in larger cyclic settlement of the caisson breakwater.

4.4.5 Cyclic preloading

After the wave loading stage in test WL2, the caisson breakwater achieves the new equilibrium for 10 minutes. Then another 16,000 non-reversal wave cycles with the same magnitude as in the earlier stage was reapplied onto the caisson breakwater to investigate the influence of cyclic preloading history on the behavior of caisson breakwater.

Fig. 4.37 shows the averaged caisson movements during wave loading and reloading stages. The effect of irregular wave was again masked by the effect of wave loading history. No apparent vertical or horizontal displacement occurred in this stage. Similar strengthening effect due to the small preshearing was also noted by Lee and Albaisa (1974) in their study of cyclic strength of dense sand through the use of cyclic triaxial test device. Another evidence of increased stiffness in the sand caused by the small preshearing was provided by Toki and Kitago (1974), who observed an increase in static modulus of loose dry sand that had undergone several hundred cycles of

small-amplitude vibratory stresses. Ng (1998) concluded that static displacement due to unloading-reloading below the preload level was observed to be largely elastic and recoverable, but this does not apply to cyclic settlement. Some rearrangement of sand particles appeared to have occurred during the reloading cycles in view of the cyclic settlement observed. However, whether the permanent settlement in this test is due to plasticity of cyclic loading effect or due to scouring is less certain. The residual pore pressure responses during wave reloading is shown in Fig. 4.38. Although the movement of caisson breakwater has been significantly suppressed due to cyclic preloading, there appears no clear decrease in the magnitude of residual pore pressures.

4.5   Summary

It has been established earlier that the effects of sand RD on the behavior of caisson breakwater subject to non-reversal breaking waves can be overwhelmed by the effects due to wave loading profile. In this section, a summary of findings on the responses of caisson breakwater subject to non-reversal breaking wave loads with different caisson configurations and boundary conditions is presented.

1) **RD of sand bed**

   Centrifuge model tests were conducted on caisson breakwater supported on sand bed with RD ranging from 60% to 80%. During the infilling stage, the caisson settlement can be reasonably well correlated to the foundation sand RD. However, during wave loading stage, the build-up of caisson tilt, horizontal and vertical displacements does not appear to exhibit a definite trend of behavior in relation to the sand RD. In all cases, the build-up of caisson tilt is observed to be dominated

by instances of sudden wave load intensity increases, the latter varying significantly from test to test. It is found that the occasional departure of the wave train from a perfectly regular and non-reversal profile, together with the sensitivity of the caisson foundation to such irregularities, has led to the effect of sand RD being overwhelmed by the effects due to wave loading profile. Once such sudden increases caused by wave irregularities are ignored, a more consistent trend is obtained between the final caisson movement and RD of the sand bed.

2) **Caisson width**

Centrifuge tests were conducted on 14-m, 16-m and 18-m wide caisson breakwaters on sand bed with RD of about 60%. It is noted that the maximum tilt angle for the 14-m wide caisson is $0.25°$ and the maximum horizontal caisson movement is 133 mm. The results imply that a 14-m wide caisson does not have sufficient safety factor against overturning and sliding failures. Hence, a minimum caisson width of 16 m is required to achieve the desired safety factor for stability when the caisson base is at -20 mCD.

3) **Caisson weight**

Tests were also conducted to evaluate the performance of caissons with different infill weights. The vertical displacement, horizontal movement and tilt angle of a caisson are found to greatly increase with decrease in caisson weight. The heel of an empty caisson settles by 82 mm and the toe by 28 mm with a tilt angle of $0.26°$, which implies that the caisson does not have enough stability against overturning. Although wave spikes occur in both tests, the trend of caisson movements is essentially unaffected. This is in stark contrast to the observations made in the

sand RD tests, which is overwhelmed by the wave irregularities.

4) **Presence of rock berm**

The presence of rock sill beneath a caisson breakwater is found to greatly suppress the caisson settlement and horizontal movement, despite that the rock sill has dilated due to its large angularity when subjected to wave loading. The dilation of rock sill is confirmed by the observed residual pore pressure time history and the contour maps of excess pore pressure.

5) **Slamming on top slab**

Slamming on top slab of a caisson structure due to overtopping wave may lead to substantial increase in caisson settlement and tilt angle when a caisson is subjected to breaking wave loads. Moreover, positive pore pressures are found to develop underneath the caisson base.

6) **Cyclic preloading**

The beneficial effect of cyclic preloading on a caisson may be taken into account in design as the caisson tilt angle, horizontal and vertical displacements are found to decrease greatly during wave reloading stage. This is probably due to the rearrangement of sand particles beneath the caisson during the reloading cycles.

Table 4.1 Test identification for caisson breakwater subject to regular, non-reversal wave loading with wave strength from 0% to 10% (all in prototype scale)

Test ID	Parametric study		Initial RDi (%)	Corrected RDc (%)	$ZnCl_2$ in infilling stage (kPa)	Tilt angle after infilling ($\times 10^{-4}$ rad)	Caisson settlement of centre after infilling (mm)	Horizontal displacement after infilling (mm)	Loading stiffness (MN/m^3)
WL2	(a) RD of sand bed	RDi=60%	60	63	218	0.125	51	-0.15	4.27
WL9		RDi=67%	67	65	218	0.12	50	-0.15	4.36
WL4		RDi=72%	72	68	224	-0.017	47	0.02	4.76
WL7		RDi=80%	80	83	230	-0.0008	36.5	0.001	6.30
WL2	(b) Caisson width	B=18 m	60	-	218	0.125	51	-0.15	4.27
WL8		B=16 m	62	-	216	-0.091	52	0.11	4.15
WL10		B=14 m	63	-	215	0.308	56	-0.37	3.84
WL2	(c) Caisson weight	Infilling till 218 kPa	60	63	218	0.125	51	-0.15	4.27
WL5		Without Infilling	60	-	-	-	-	-	-
WL2	(d) Presence of rock berm	Without rock berm	60	63	218	0.125	51	-0.15	4.27
WL6		With rock berm	63	66	223	0.725	49.8	-0.87	4.48
WL1	(e) Overtopping on caisson	Overtopping during wave loading	64	65	217	0.191	50	-0.23	4.34
WL2		Without overtopping	60	63	218	0.125	51	-0.15	4.27
WL2_2	(f) Cyclic preloading	Preloading before wave loading	60	-	218	0.125	51	-0.15	4.27
WL2		Without preloading	60	63	218	0.125	51	-0.15	4.27
WL11	Water level lowering to sand surface		62	-	-	-	-	-	-

Fig. 4.1 Target wave loading profile in centrifuge
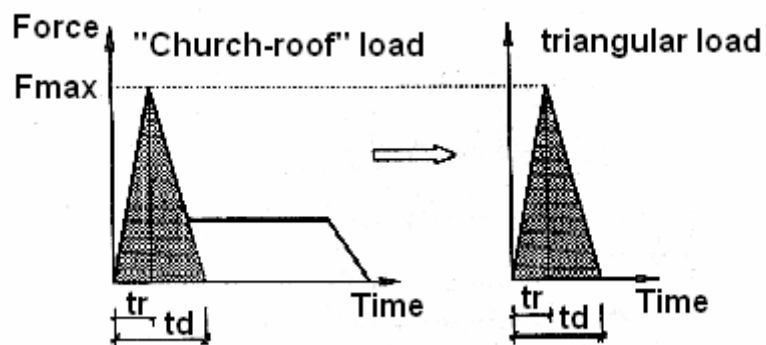
Fig. 4.2 Substitution of church-roof load by triangular load (after Oumeraci, 1995)
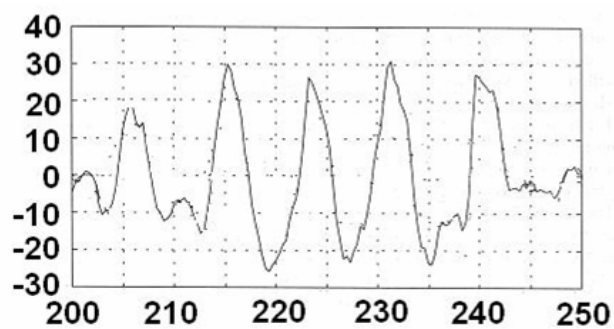
Fig. 4.3 Example of recorded time series of forces acting on Dieppe caisson
(after De Gerloni, 1997)
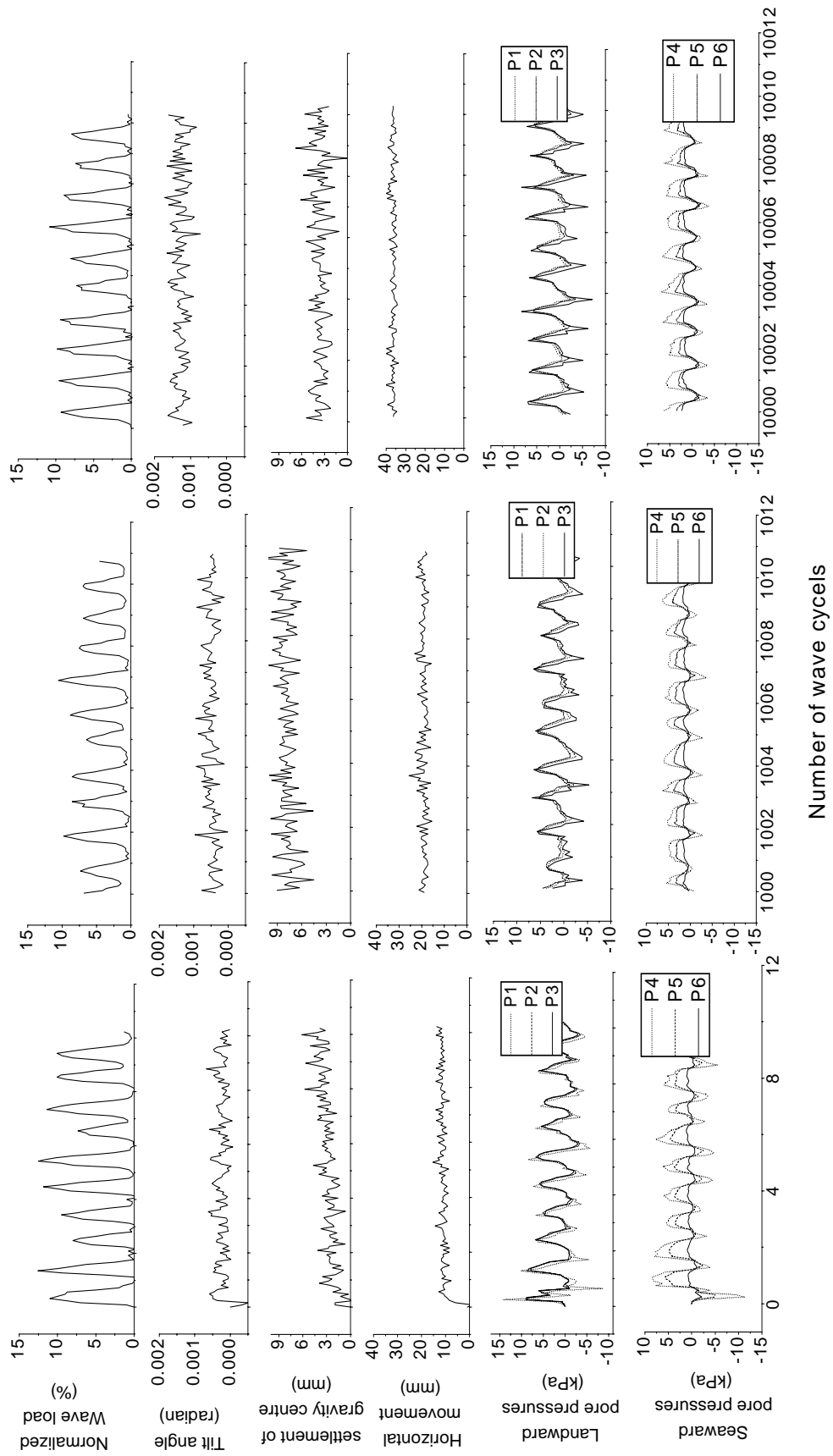
Fig. 4.4 Typical instantaneous movements and pore pressure responses under wave loading of test WL4 with RDi=72%
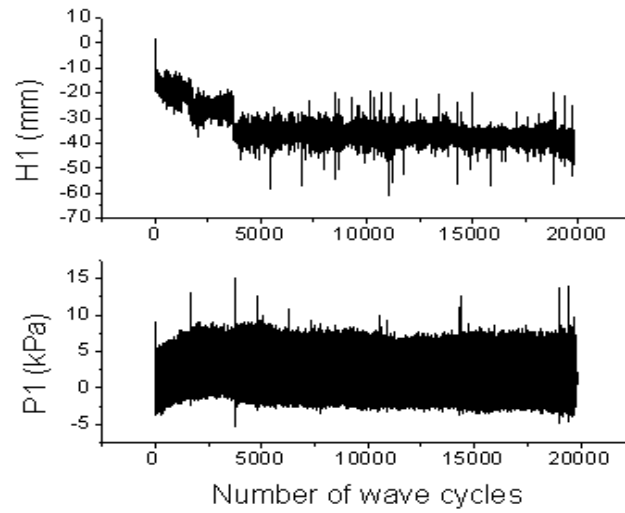
(a) Raw data
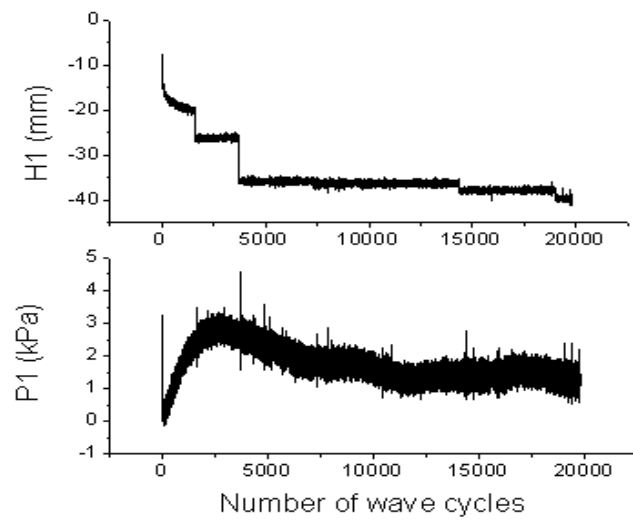
(b) Average cycles=2
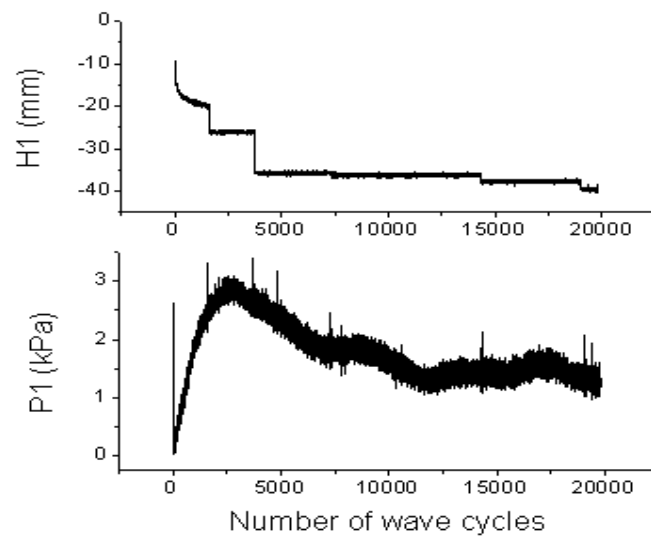
(c) Average cycles=5
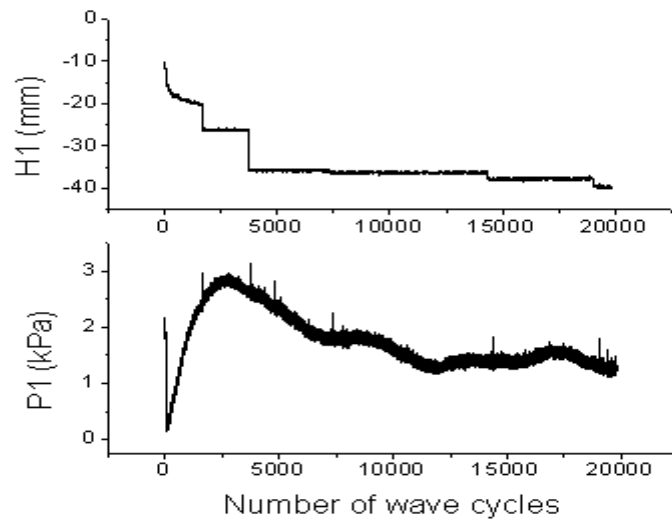
(d) Average cycles=10
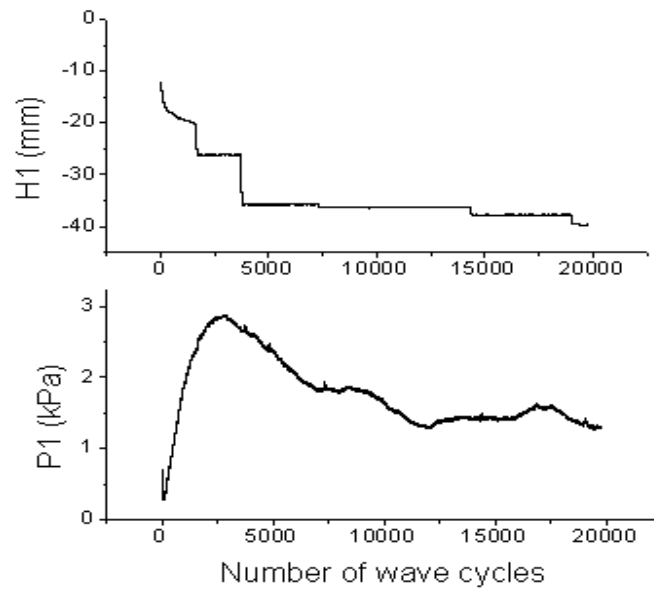
(e) Average cycles=80

Fig. 4.5 Averaged caisson movement and pore pressure response under different number of average cycles
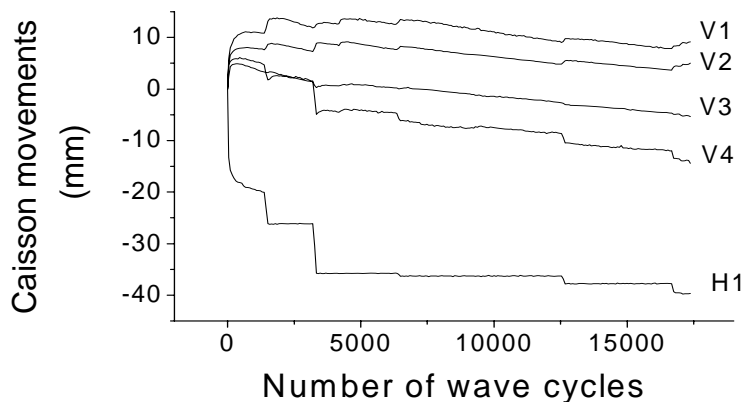
Fig. 4.6 Average caisson movements during wave loading stage in test WL4
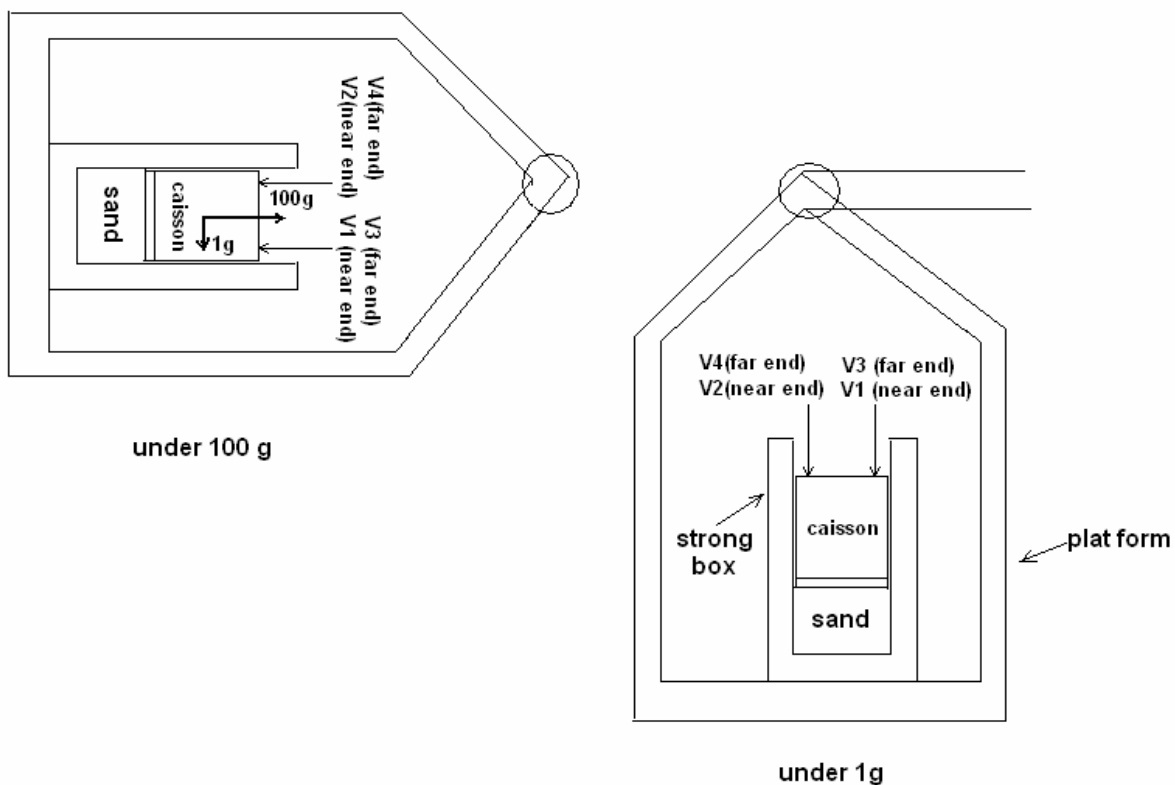
Fig. 4.7 Illustration of out-of-plane tilting of caisson under 100g
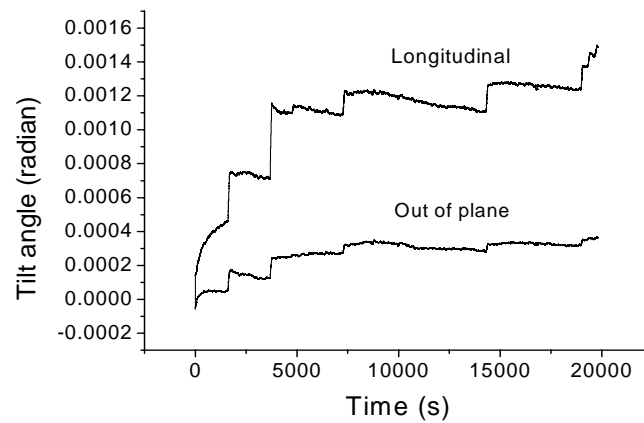
Fig. 4.8 Tilt angle in the longitudinal and out of plane directions during wave loading in test WL4
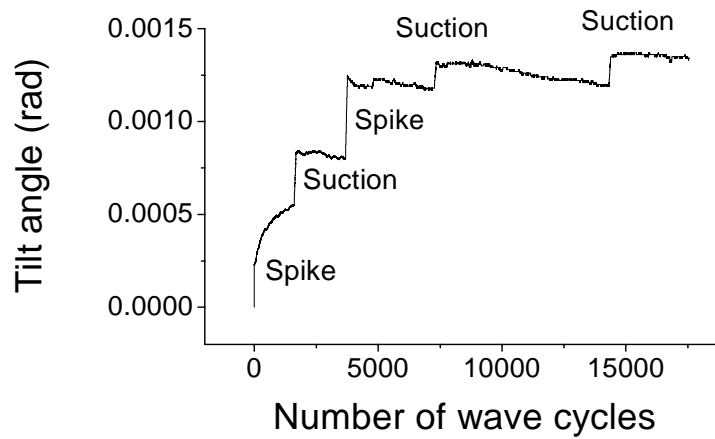
Fig. 4.9 Average caisson tilt angle with unsteady wave occurring in wave loading in test WL4
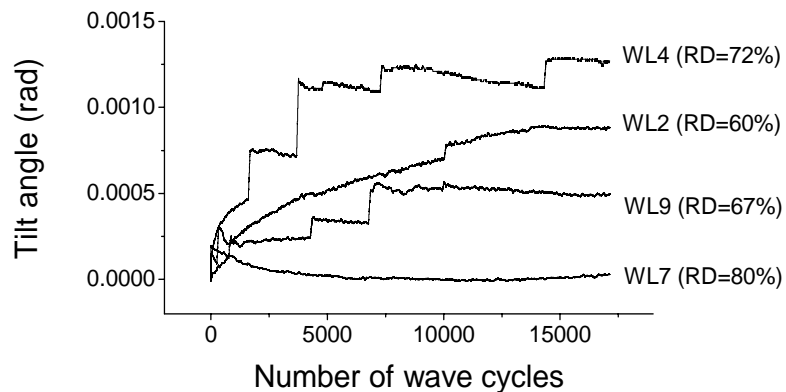
(a) Average tilt angle
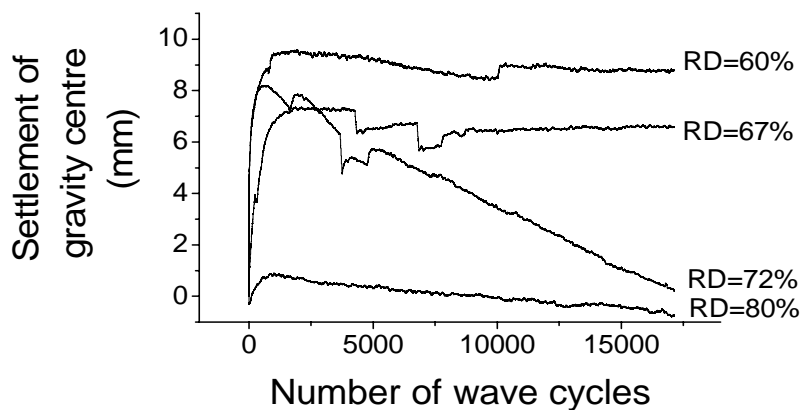
(b) Average centre settlement
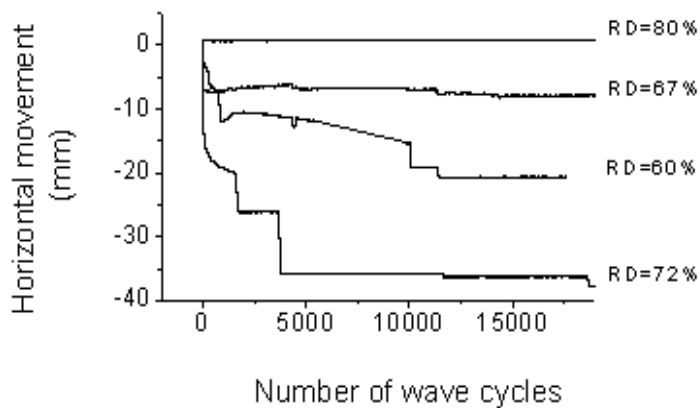
(c) Average horizontal movement

Fig. 4.10 Average movements of caisson breakwater on sand bed with different RDi
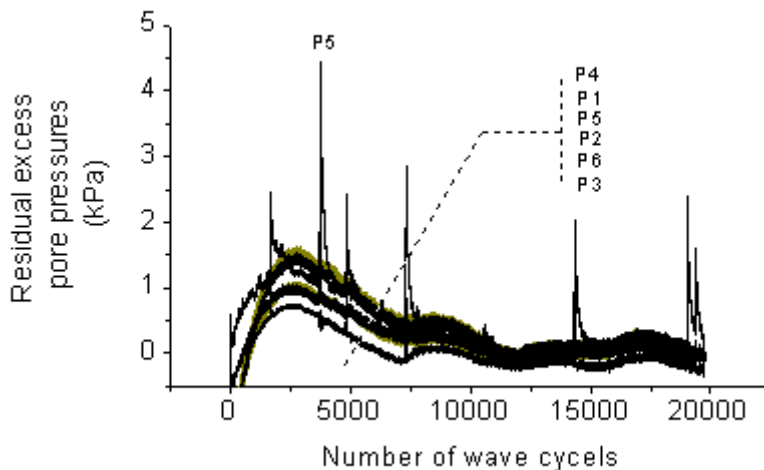
Fig. 4.11 Residual pore pressures during wave loading in test WL4 with RDi=72%
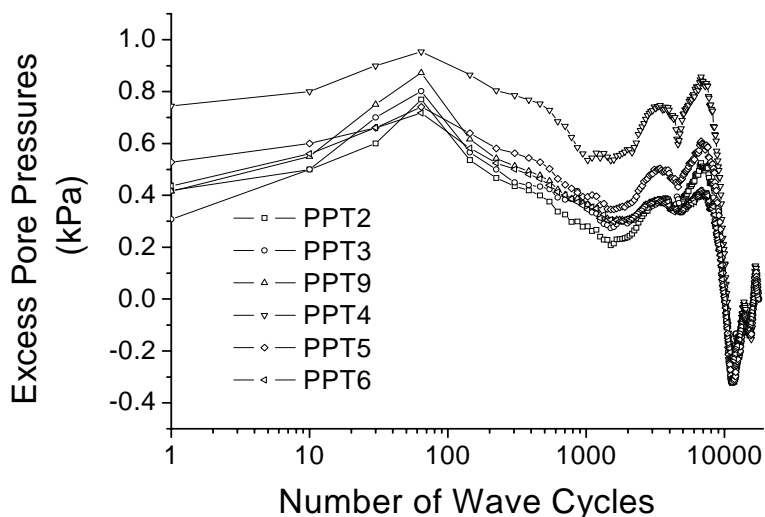
Fig. 4.12 Residual pore pressure response in centrifuge test WL2 with RDi=60%
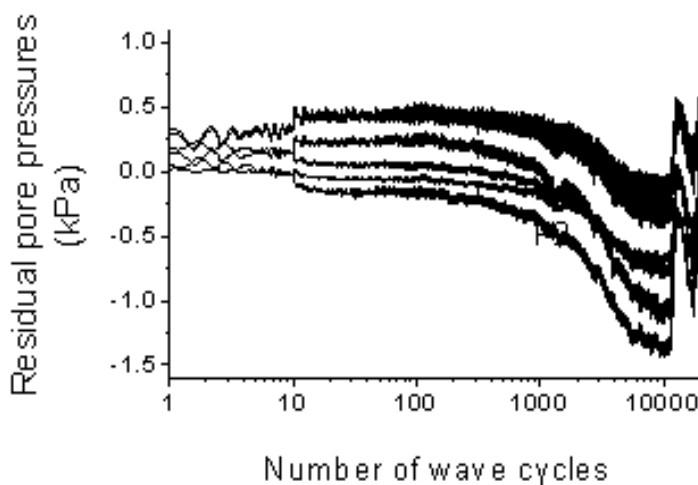
Fig. 4.13 Residual pore pressure during wave loading in test WL7 with RDi=80%
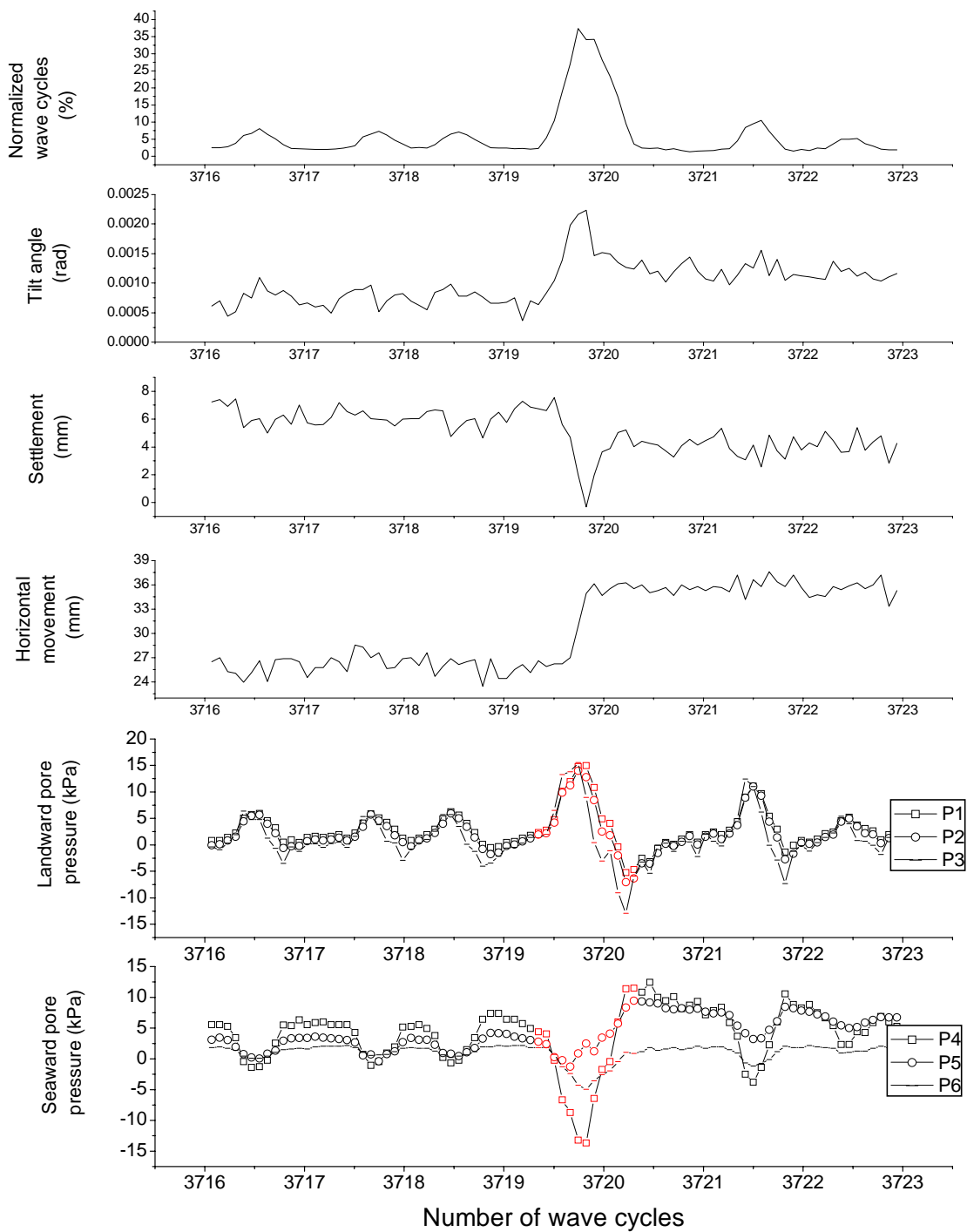
Fig. 4.14 Caisson movement and pore pressure responses in test WL4
with RDi=72% when subjected to wave spike
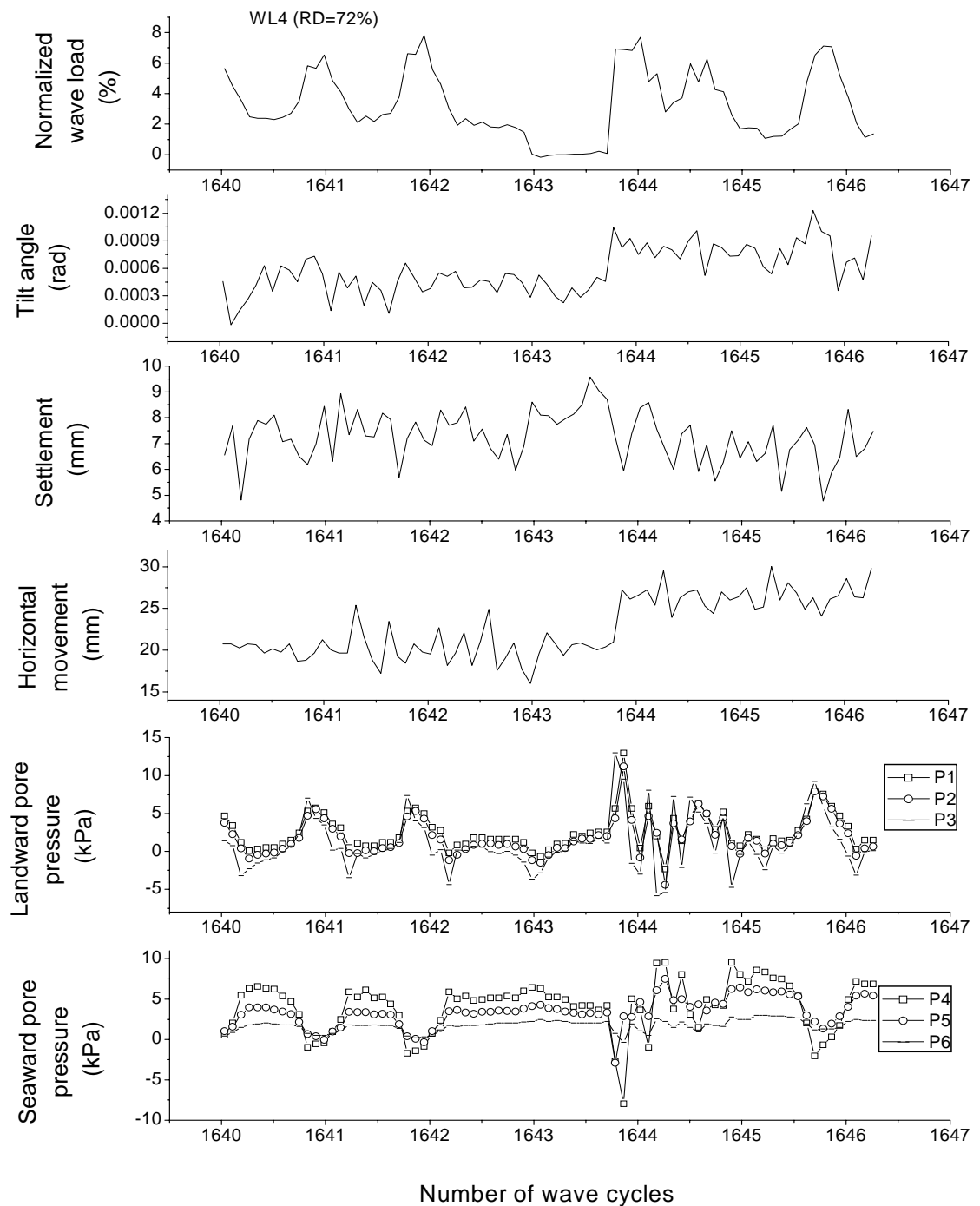
Fig. 4.15 Caisson movement and pore pressure responses in test WL4 with RDi=72% when subjected to reversal phase
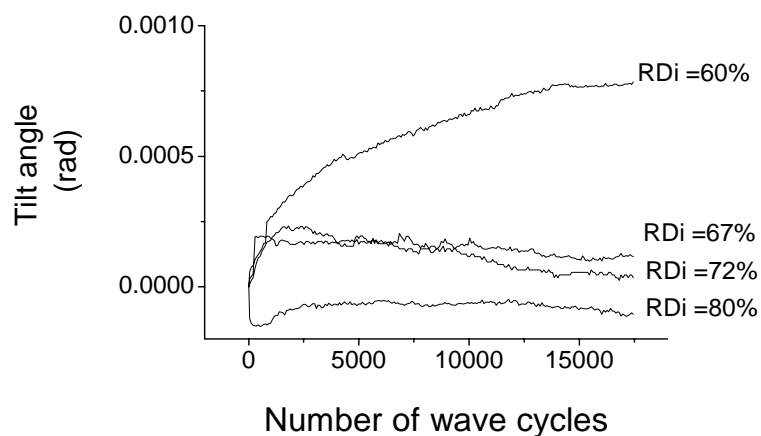
a) Average tilt angle
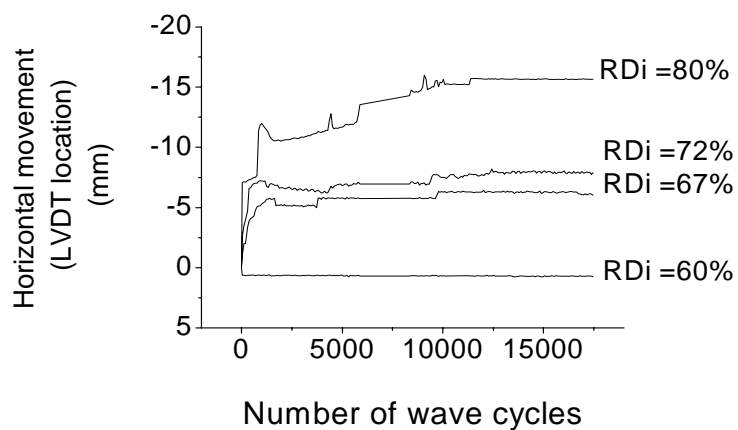
b) Average horizontal movement
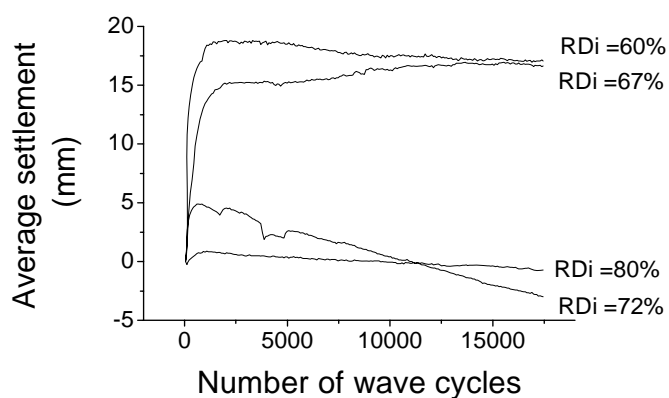
c) Average settlement of gravity centre

Fig. 4.16 Comparison of movement of caisson breakwater on sand bed with different RDi when neglecting the sudden movements under irregular wave
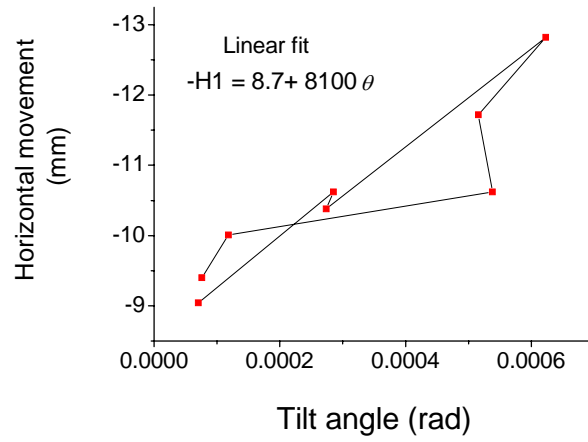
(a) 3rd wave cycle
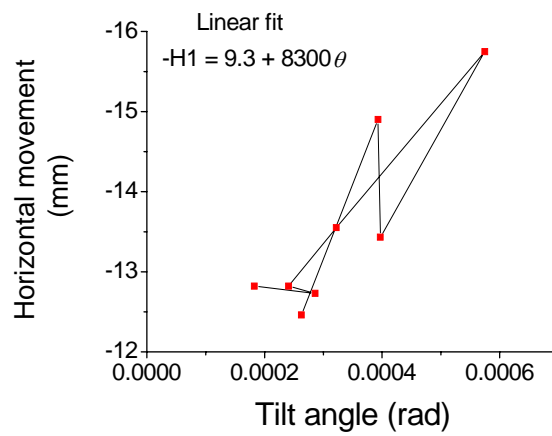
(b) 27th wave cycle

Fig. 4.17 Horizontal movement versus tilt angle during regular wave segments in test WL4
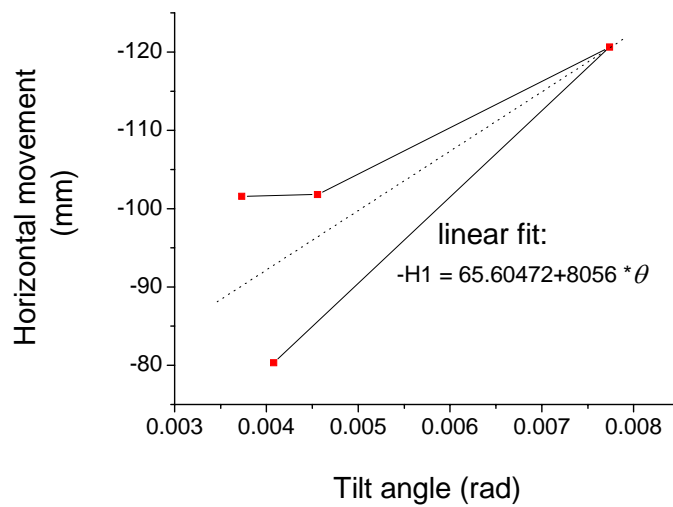
(a) 249th wave cycle
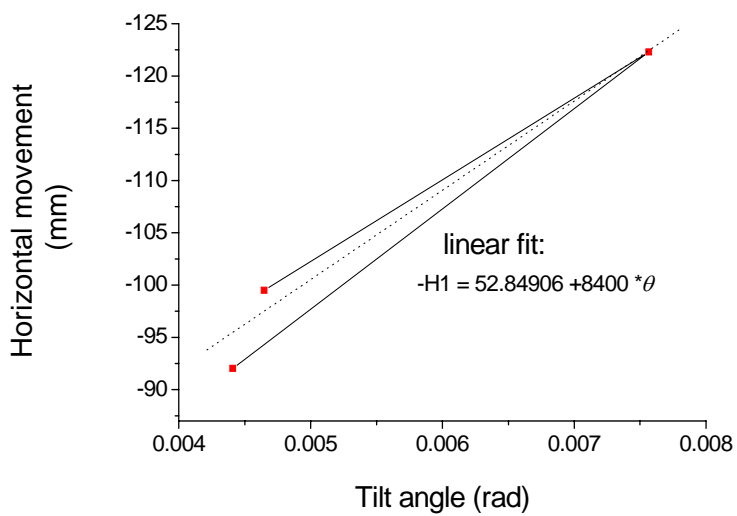
(a) 524th wave cycle

Fig. 4.18 Horizontal movement versus tilt angle during regular wave segments in test WL11
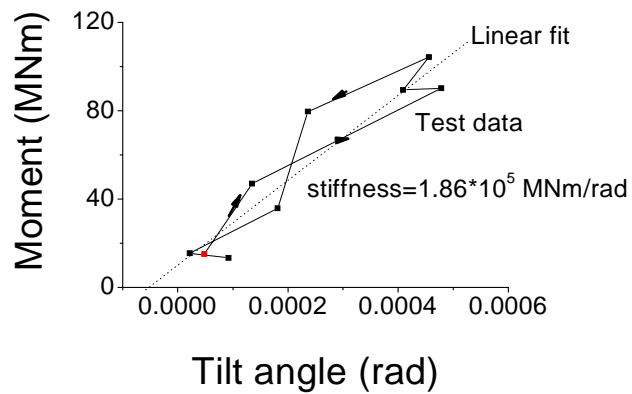
(a) 2nd wave cycle
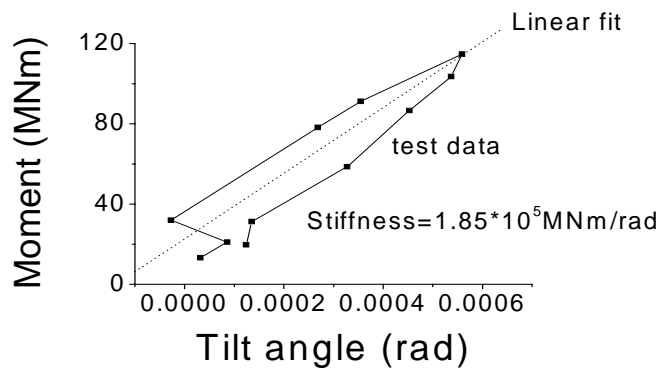
(b) 6th wave cycle

Fig. 4.19 Rotational stiffness during regular wave segments
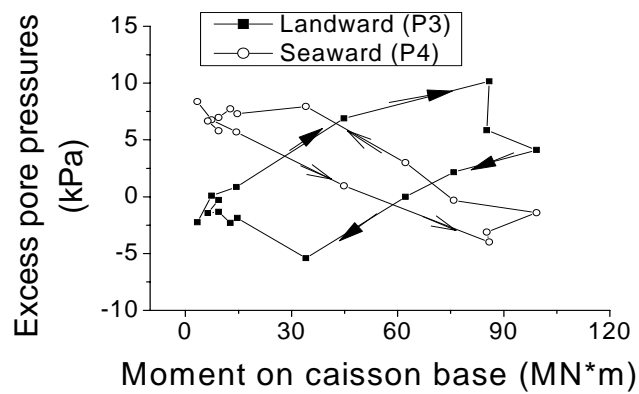
(a) 1st wave cycles
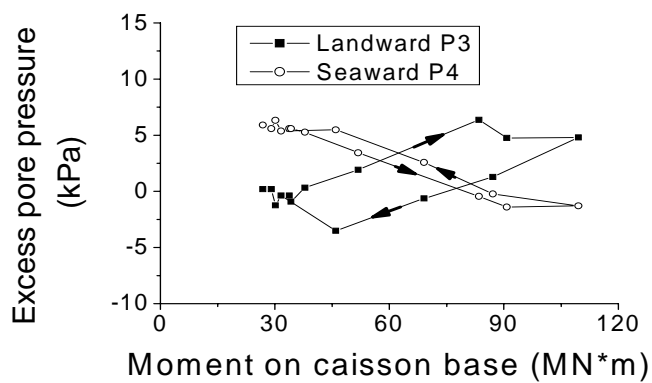
(b) 3716th wave cycles

Fig. 4.20 Excess pore pressure versus moment during regular wave segments
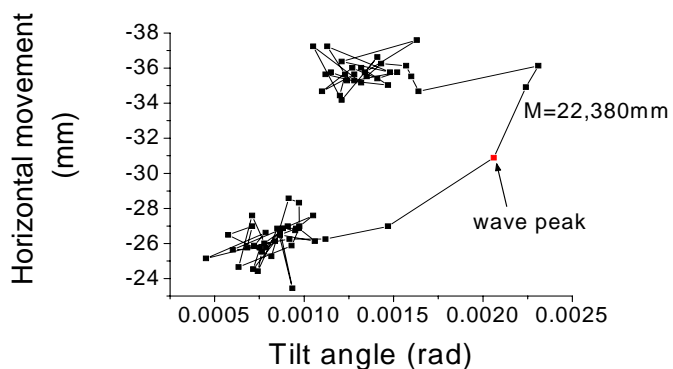
(a) Horizontal movement versus tilt angle
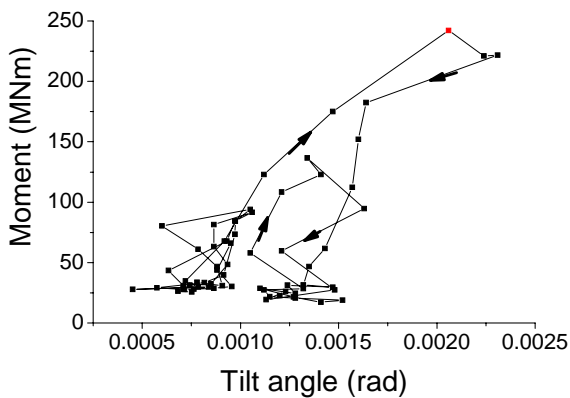
(b) Rotational stiffness
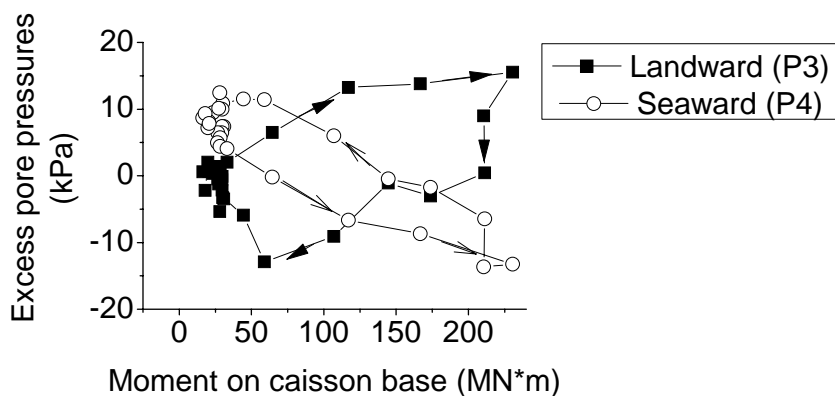
(c) Excess pore pressure versus moment

Fig. 4.21 Caisson responses during wave spike in test WL4 (3720th wave cycle)
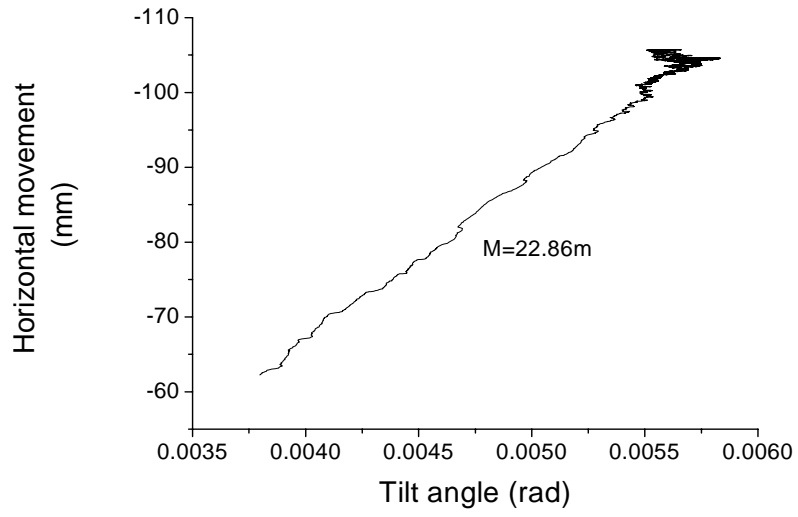
Fig. 4.22 Averaged horizontal movement versus averaged tilt angle in test WL11
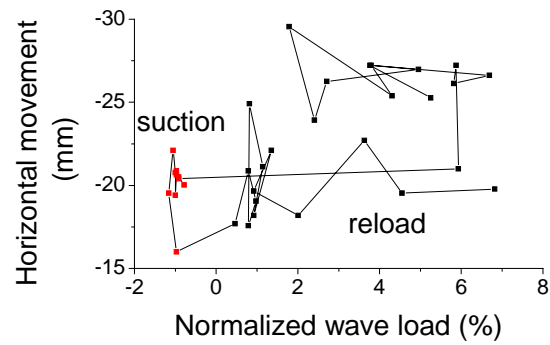
(a) Horizontal movement versus normalized wave load
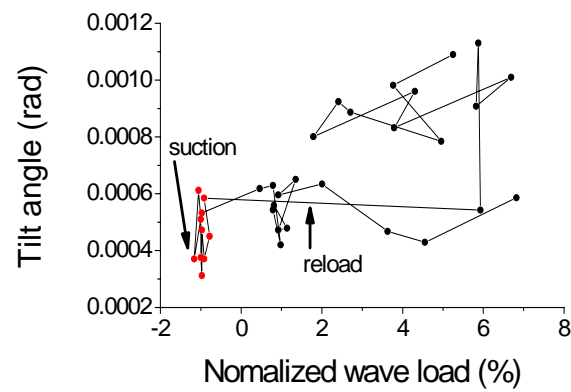
(b) Tilt angle versus normalized wave load
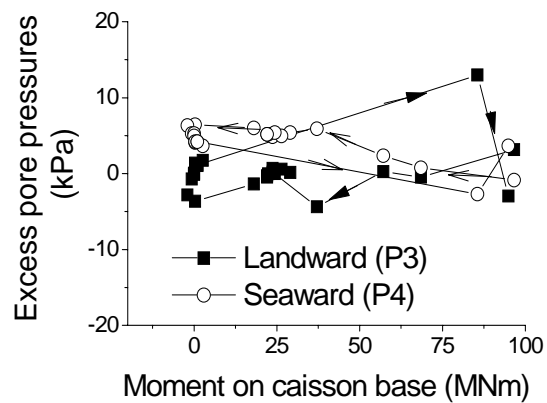
(c) Moment versus excess pore pressure

Fig. 4.23 Caisson responses during the reversal phase in test WL4 (1644th wave cycle)
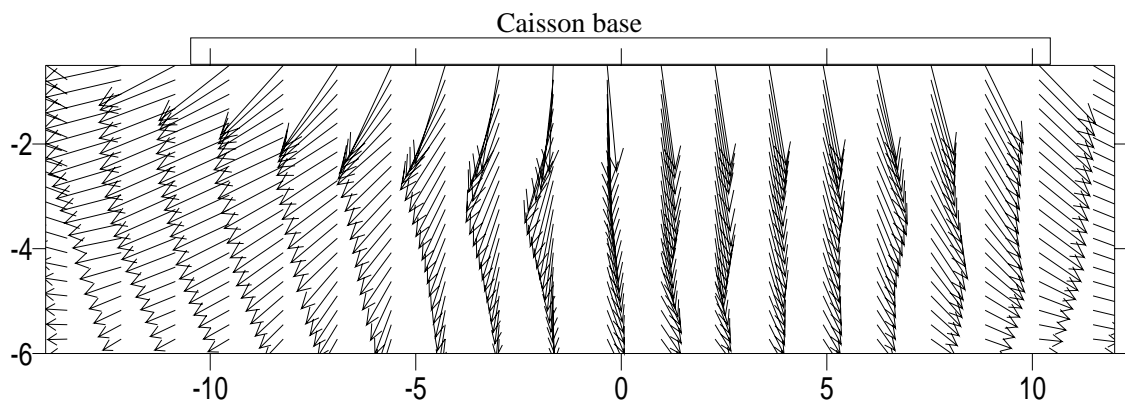
(a) Infilling stage
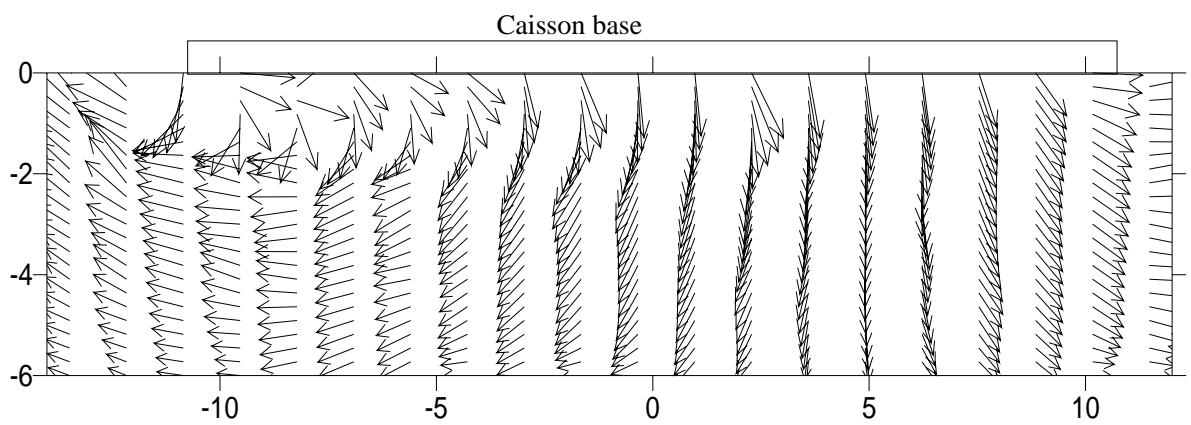
(b) Wave loading stage

Fig. 4.24 Vector map of incremental soil movement in test WL4
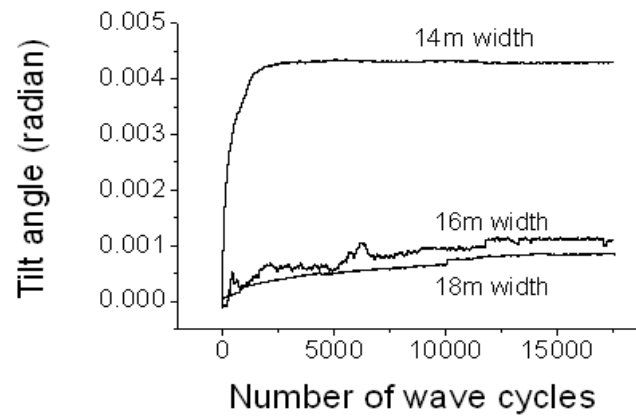
(a) Tilt angle
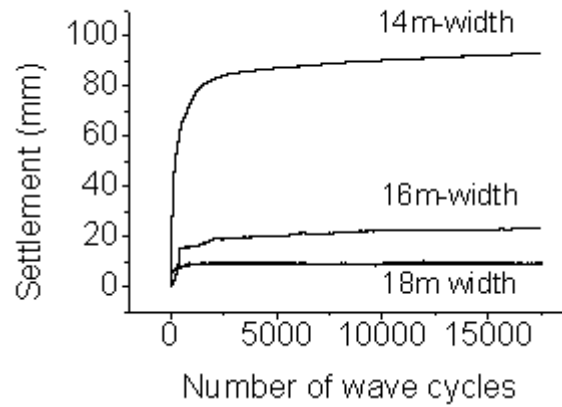
(b) Settlement of gravity centre
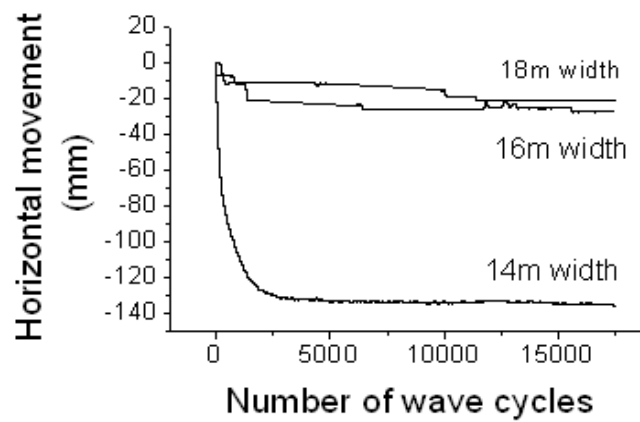
(c) Horizontal movement
Fig. 4.25 Comparisons of caisson movements with different widths
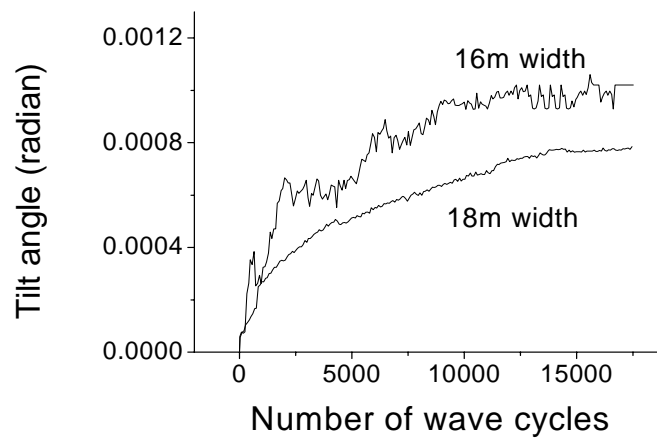
Fig. 4.26 Comparisons of tilt angle of caisson with different widths when neglecting sudden movement
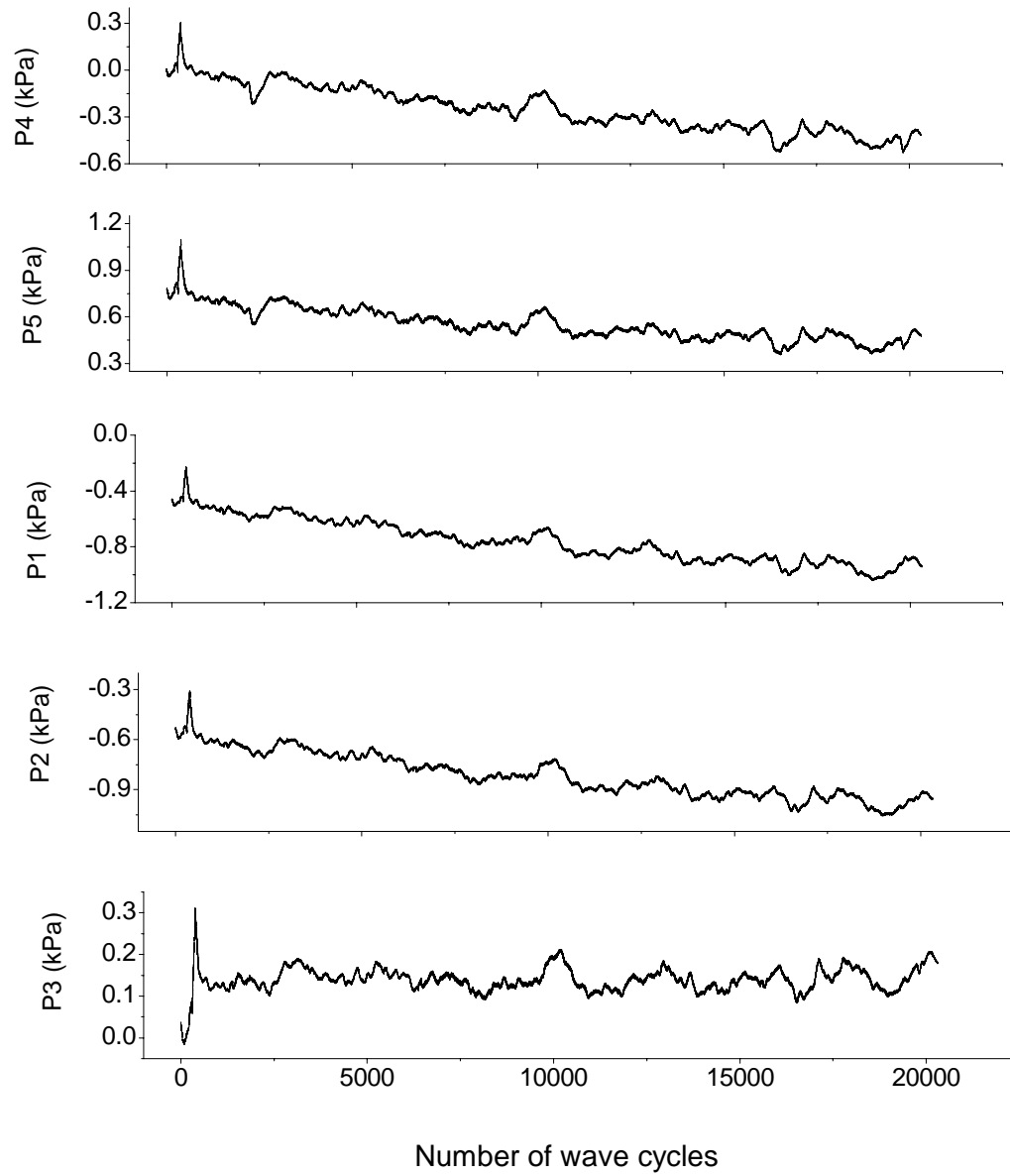
Fig. 4.27 Residual pore pressure response of caisson with 16 m width
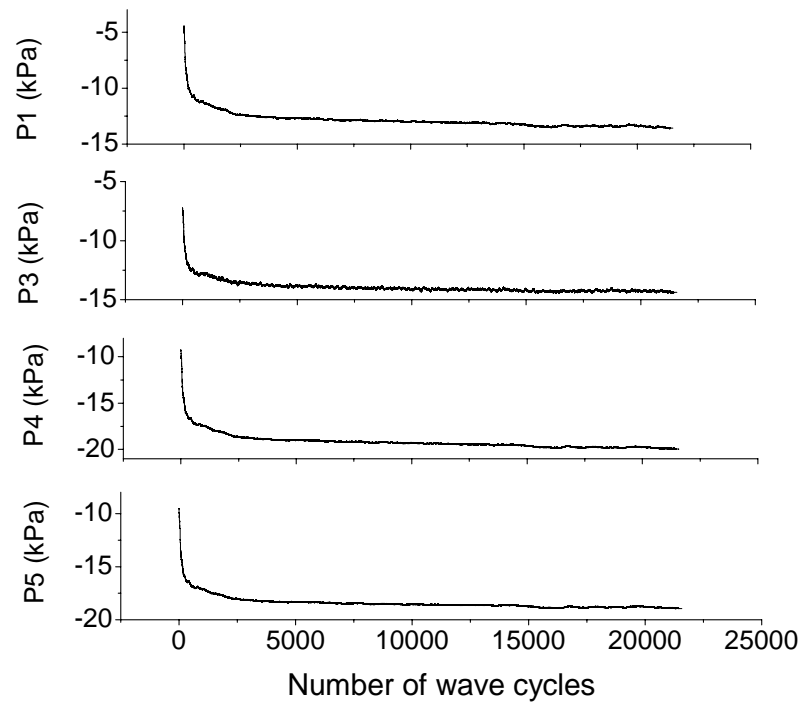
Fig. 4.28 Residual pore pressure response of caisson with 14 m width
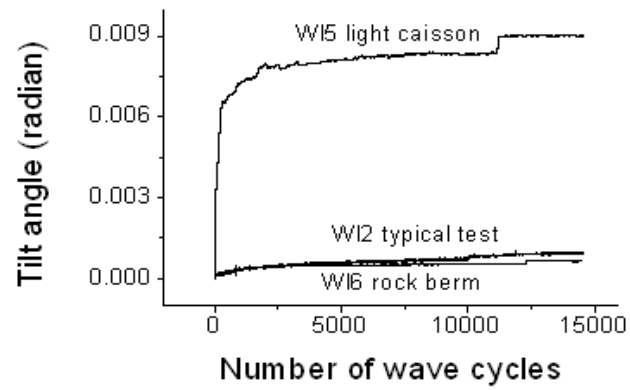
(a) Tilt angle
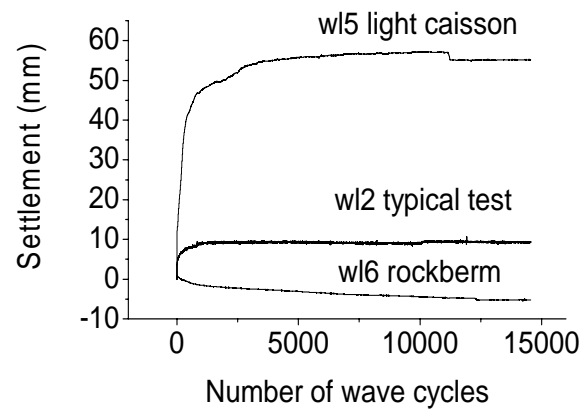
(b) Settlement of gravity centre
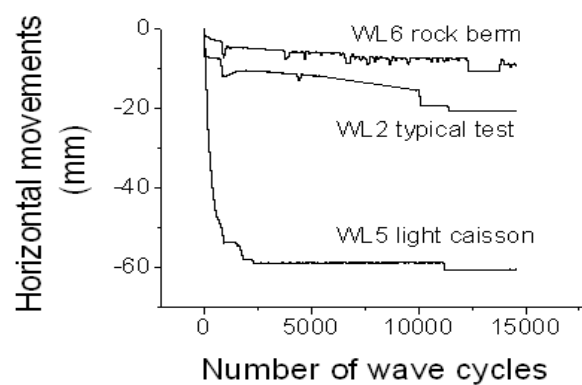
(c) Horizontal sliding
Fig.4.29 Comparison of caisson movements
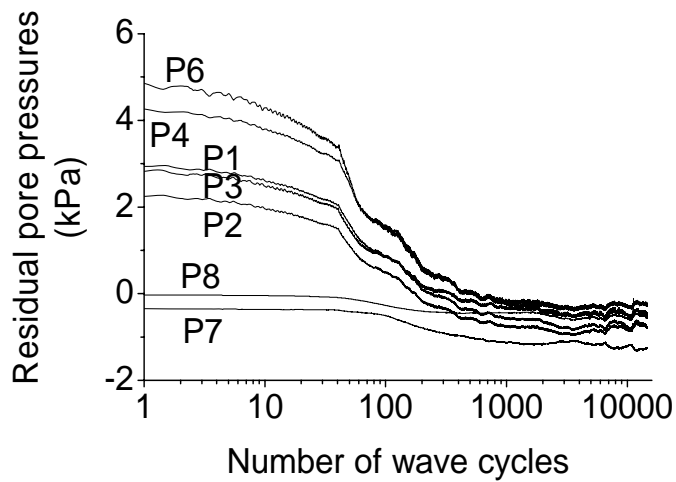
Fig. 4.30 Residual pre pressure of WL4 with light caisson
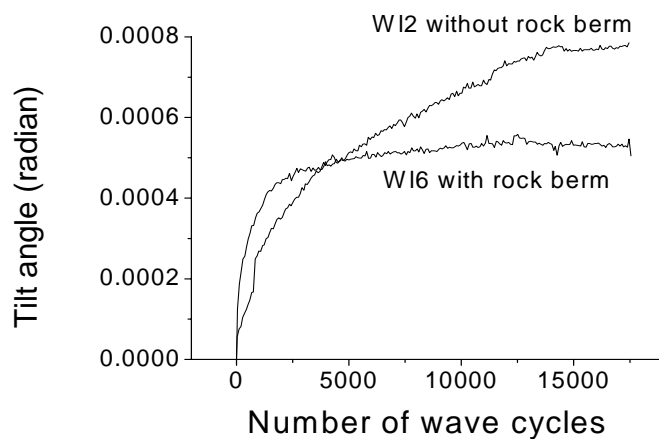
Fig. 4.31 Comparisons of tilt angle of caisson rest on sand bed with and without presence of rock berm when neglecting sudden movement
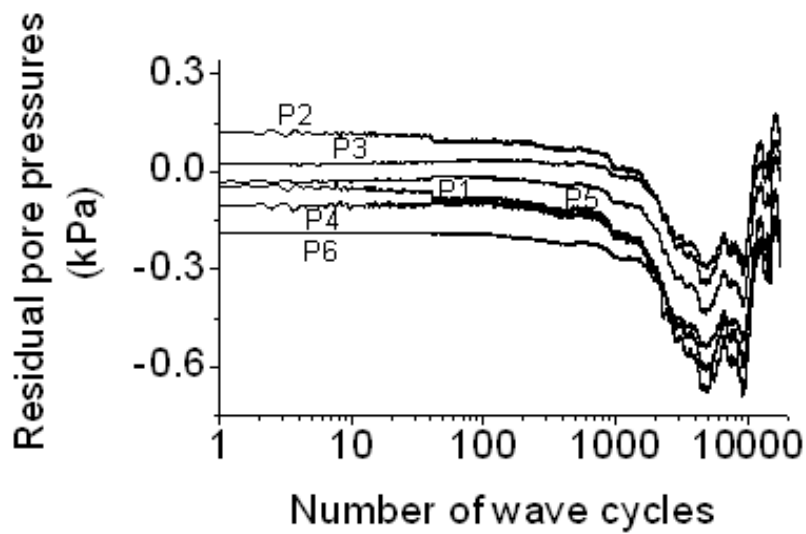
Fig. 4.32 Residual pore pressure of test WL6 with presence of rock berm

5th

1000th

5000th

17000th
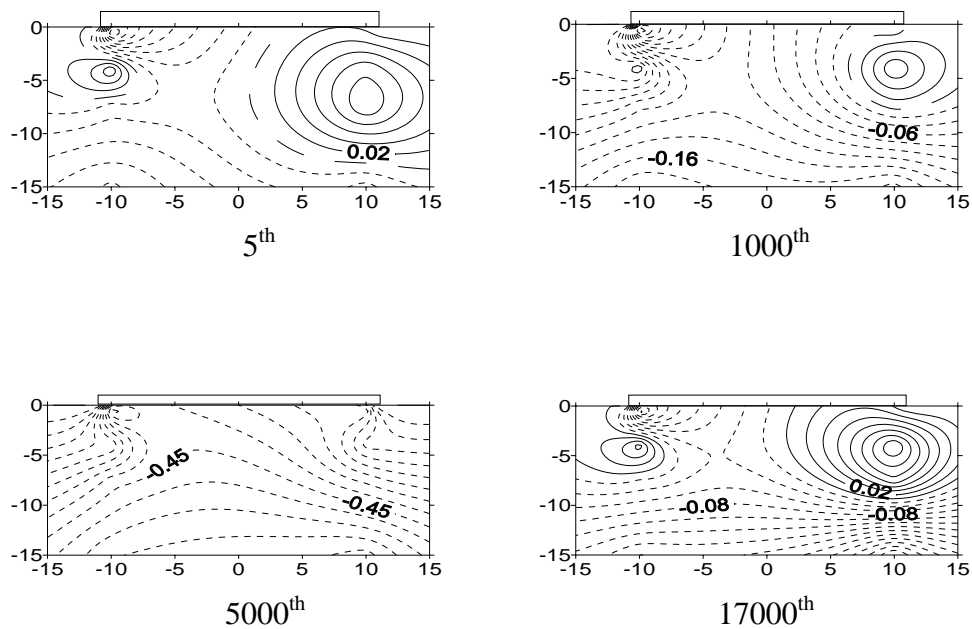
Fig. 4.33 Contour maps of excess pore pressure of test WL6 with presence of rock berm at different wave cycles (unit: kPa)
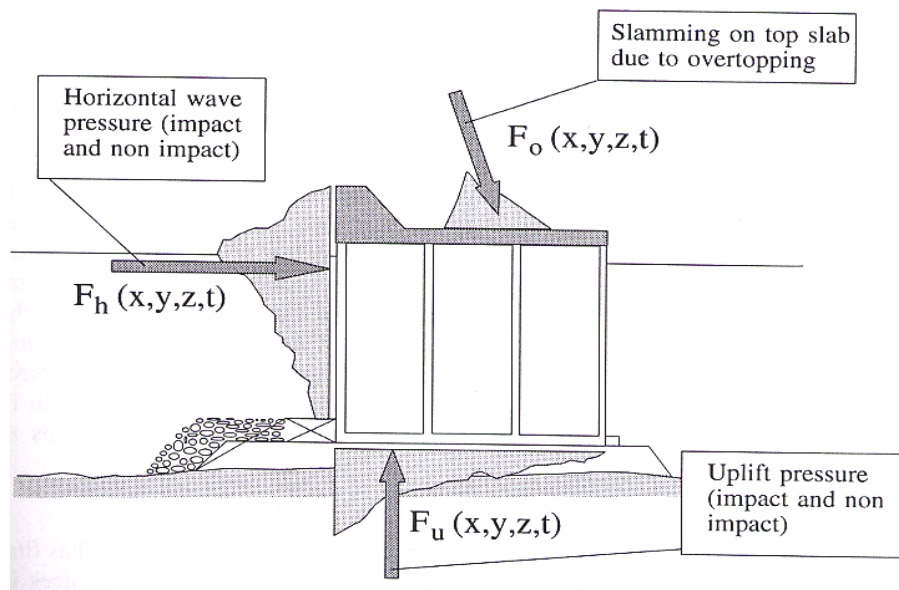
Fig.4.34 Spatial and temporal pressure distribution of pressure relevant for structural analysis of caisson breakwater during in-service conditions (after Oumeraci, 2001)
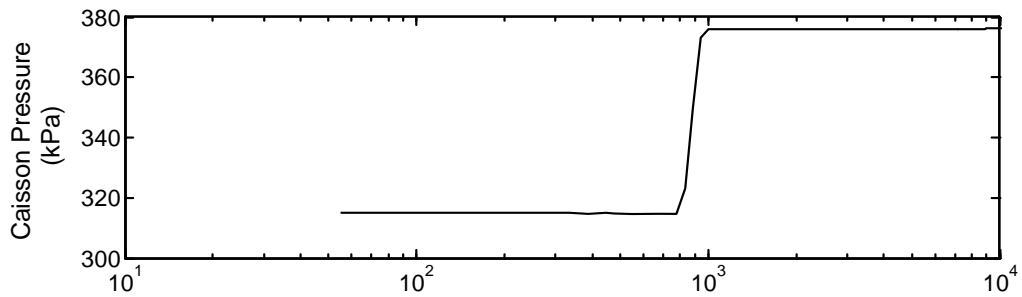
(a) Caisson bearing pressure
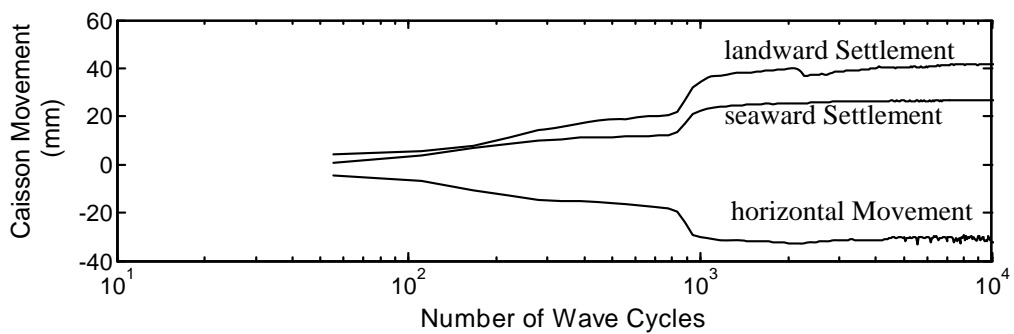
(b) Caisson movements
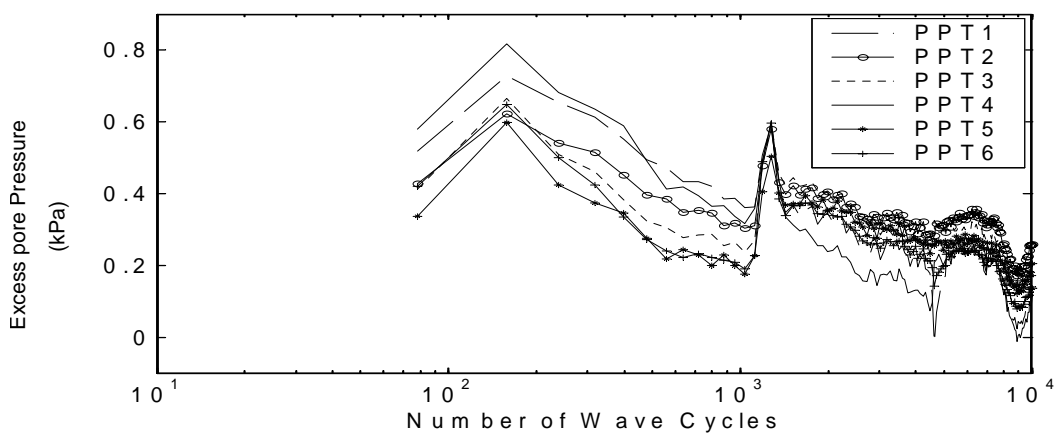
(c) Pore pressure response

Fig. 4.35 Overall caisson movements and pore pressure response of test WL1 during
wave loading and wave overtopping
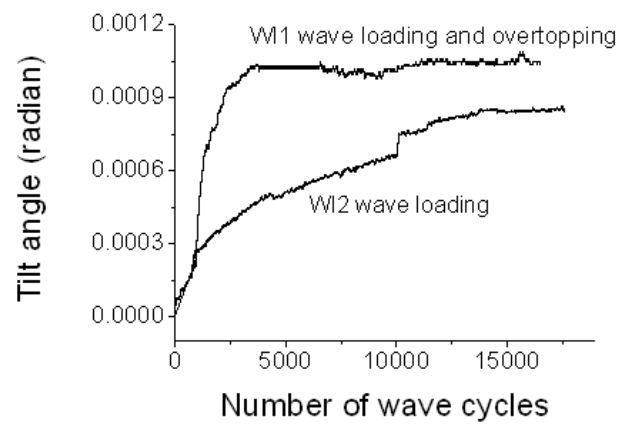
Fig.4.36 Comparison of caisson tilt angle with and without wave slamming
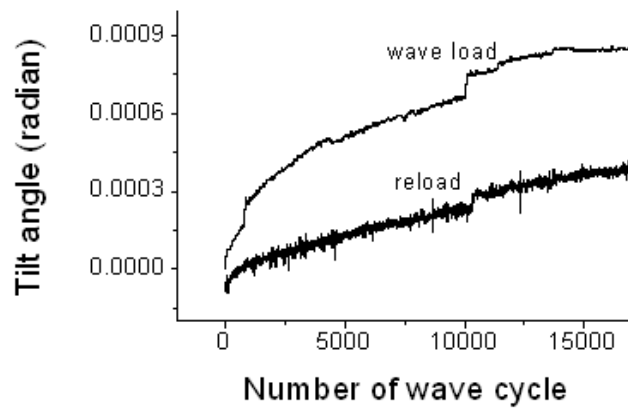
(a) Tilt angle
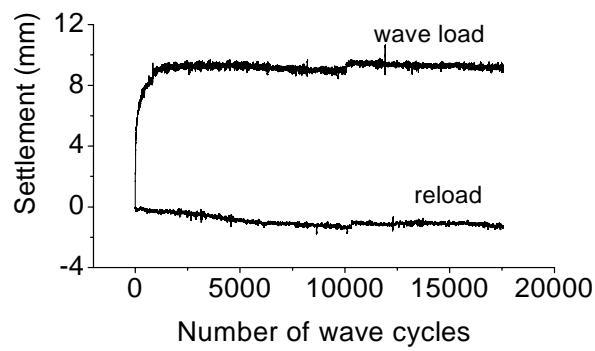
(b) Settlement of center
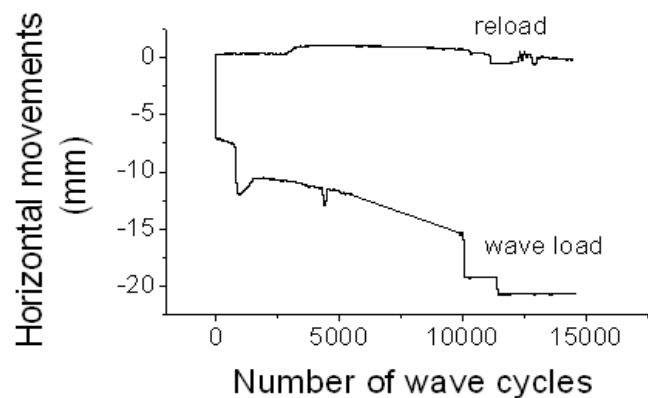
(c) Horizontal movement

Fig. 4.37 Comparisons of movements of caisson breakwater during wave loading and
reloading in test WL2 (cyclic preload ratio Rc=1)
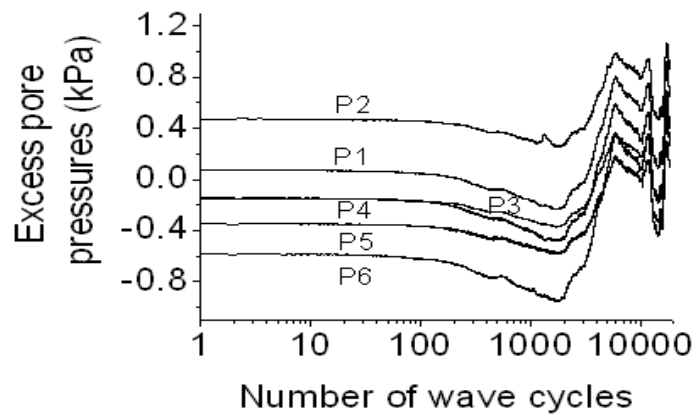
Fig. 4.38 Residual excess pore pressure history of test WL2 during wave reloading

Chapter 5

Reversal Wave Loading Tests

5.1 Introduction

Storm waves often produce a strong "push" on the caisson breakwater, followed by a weaker "drag" phase, as indicated in Fig. 4.3. The drag force is produced by the fact that as the wave retracts seawards, the sea water level behind the caisson is often higher than that in front of the caisson. The magnitude of the drag force is usually not more than half of that of the peak impulsive force. As discussed in the previous chapter, the occasional appearance of the reversal wave in an otherwise "non-reversal" wave train is one of the two reasons which accounted for most of the caisson tilt. Based on this, one may surmise that a "reversal" wave train, which has a "drag" phase in each cycle, is likely to have a much more serious effect on caisson movement than non-reversal wave train. This chapter discusses the results of reversal wave loading tests on caisson breakwater. In these tests, the load-controlled actuator was attached to the caisson face vide a hinge-and-slider system, see Fig. 5.1. Silicone grease is coated onto the hinge and slider so that the caisson may move freely in the horizontal, vertical and rotational directions. The test parameters for the reversal wave tests are summarized in Table 5.1, together with the tilting, vertical and horizontal movement responses after infilling

stage.

5.2 Reversal Wave Loading with Medium Strength from -2% to 4%

5.2.1 Behavior of caisson breakwater

The instantaneous caisson movement and pore pressure response of test WL16 with RDi=51% are indicated in Fig. 5.2 for (i) first 10 wave cycles, (ii) 1000th to 1010th wave cycles and (iii) $10,000^{th}$ to $10,010^{th}$ wave cycles. As can be seen, large settlement is induced from the start of the wave loading. The pore pressure responses beneath the landward and seaward toes of the caisson also show much larger increases than the "non-reversal" tests. Much of the increases occur between the second and the sixth cycles and coincides with the large increase in settlement. This suggests that the settlement is likely to be strongly linked to the excess pore pressure build-up; that would be consistent with Martin et al. 's (1975) observation that the tendency for volumetric densification in drained test is translated into excess pore pressure build-up in undrained test. The rate of increase in tilt angle also appears to be larger than that for "non-reversal" loading. However, this is difficult to confirm as there is a very strong cyclic component. Similarly, the trends for rotation and horizontal sliding are also masked by their respective cyclic components.

Fig. 5.3 shows the smoothed time history obtained by averaging the corresponding raw time history over 10 cycles. The results show that the movement of the caisson breakwater may be divided roughly into two stages, which are termed hereafter as settlement and stabilization as shown in Fig. 5.3. The settlement stage takes place within the first 5000 cycles. In this stage, the settlement increased significantly with the num-

ber of wave cycles and much of settlement occurred in this stage. Caisson tilt also increased significantly during this stage. This is consistent with the trend reported by Silver (1971).

As shown in Fig. 5.3(b), caisson settlement is strongly correlated to RD_i, with the loosest sand bed showing the largest settlement; this is to be expected and indicates that settlement is connected to densification of the sand bed. All four tests show the caissons listing seawards at the end of wave loading episode. The caisson tilt is also well-correlated to the sand RD_i. The horizontal caisson movement is also reasonably well-correlated to RD_i except for the model with RD_i=51%. This model shows a peak horizontal movement at the 570th wave cycle, followed by a progressive reduction. Examination of the data records shows that this is due to the relatively large seaward tilting offsetting the landward horizontal movement. After about 5000 cycles, there is little or no further increase in settlement. This is similar to Ng's (1998) observations on vertical cyclic loading on spudcans.

5.2.2   Positive pore pressure generation and progressive softening of soil bed

Fig. 5.4 shows the instantaneous pore pressure response of the four tests during the early part of the wave loading episode. As can be seen, the peak pore pressure is reached within the first five cycles of the loading episode. Thereafter, pore pressure dissipated relatively quickly. After about 20 cycles, little or no excess pore pressure is detected in the model. Furthermore, the denser the sand bed, the lower the instantaneous pore pressure is and the faster it dissipates.

Figs. 5.5 to 5.8 show the contours of excess pore pressure at various stages of the

test. In all but the densest model (i.e. test WL22), the pore pressure generation process can be divided into two episodes. An early episode produces the positive excess pore pressure, as noted in Fig. 5.4. A latter episode produces small negative excess pore pressure. In the case of the densest model i.e.WL22, the first episode is absent, this being attributable directly to the high sand RD_i as reflected in Fig. 5.4. This suggests that there may be two different processes. The first is directly related to the densification of the sand bed. The second process is less certain and will be examined further below.

In test WL16, which has the lowest RD_i, the initial bulb of positive excess pore pressure appears to be centred around the centreline and mid-depth of the caisson. This dissipated outwards rapidly until it is virtually completely dissipated after about 700 cycles. After about 1000 cycles, a bulb of negative pore pressure initiates around the bottom of soil bed. This bulb of negative pore pressure propagated much more slowly than the initial positive pore pressure bulb. After about 5000 cycles, the negative pore pressure zone appears to occupy the entire lower portion of the sand bed. It then propagated upwards until it almost reaches the caisson base after about 17000 cycles. Owing to the scarcity of the pore pressure transducers in the model, it is not entirely certain if negative pore pressures really cover the entire caisson width. What, however, seems clear is that the negative pore pressure initiates from the bottom of soil bed and appears to propagate upwards. This is similar to the phenomenon of soil column under triaxial shearing. The rocking of caisson may lead to shearing on the soil column under the caisson base. The loose soil column will be densified initially due to shearing and then dilated. That is why there is two episodes of pore pressure generation in the centrifuge test.

In tests WL18 and WL20, which have RD_i of 62% and 71%, respectively, the positive pore pressure were found to localize under the caisson base from the very beginning of wave loading. The initiation of negative pore pressure bulb beneath the landward caisson edge appears to take place at a shallower depth of the sand layer and at an earlier stage of the cyclic loading episode, compared to test WL16. For test WL18, it initiates after about 200 cycles. For test WL20, it initiates after about 100 cycles. Thus, the denser the model, the earlier appears to be the initiation of the negative pore pressure zone. On the other hand, for the densest sand, i.e. test WL22, which has an RD_i of 83%, the negative pore pressure zone initiates below the seaward edge of the caisson almost immediately upon commencement of the loading episode.

The negative pore pressure zone may be generated by three possible causes. The first is a reduction in total stress due to a drop in overburden pressure. This may occur, for instance, as a result of the caisson embedding itself into the sand bed and displacing some sand to the side. As this occurs, the total overburden due to the caisson and sand will reduce. Pore pressure changes due to this effect are transient and will dissipate once caisson settlement and tilt stabilize. Furthermore, if this is the cause, the maximum negative pore pressure should be located just below the caisson base. However, as shown in Figs. 5.5 to 5.8, the maximum negative pore pressure in all cases occurs at some distance below the base. The second is an upward movement of the pore pressure transducers. Under 100g model gravity, all it takes is about 1 mm of upward displacement of the pore pressure transducers to cause a drop in pore pressure of 1 kPa. It is, however, unclear, as to how the pore pressure transducer can possibly move upwards through the sand bed, when the latter is not near to a liquefied state. Any such pore pressure trans-

ducer movement in the absence of a liquefaction condition will require the entire sand bed beneath the caisson base to heave upward, which seems rather implausible in view of the fact that the caisson was settling. The third possibility is dilatancy of the sand bed. However, pore pressure changes due to dilatancy is transient and the persistence of negative pore pressure over the entire loading episode implies that there is likely to be on-going dilatancy which involves a significant region of the sand bed. This looks like the most plausible cause. If dilatancy is the real cause, then it would imply that, for all but the densest models (i.e. WL22), yielding of sand initiates from either the landward edge or bottom of the caisson and spreads over the entire caisson width. The initial yielding may not be too dissimilar from the local failure mechanism proposed by Oumeraci (1994a). The spreading of the plastic zone may be caused by cyclic mobility of the sand under reversal loading conditions, such as that observed by Lee and Schofield (1988) for sand embankments and islands.

Figs. 5.9(a) and (b) plot the pore pressure fluctuation with moment at the caisson base during the first wave cycle in tests WL16 and WL20. The pore pressure versus total stress response in these reversal tests is almost the same as that in non-reversal tests. In both cases, there is a distinct hysteresis loop in the excess pore pressure response to the caisson base moment. However, the loop is not closed in the reversal tests; this being due to the high residual pore pressure being induced from the first wave cycle. In both models, the pore pressure response underneath the seaward edge manifests a larger loop than that at the landward edge. This is consistent with the higher positive excess pore pressure beneath the seaward edge and simultaneously the seaward tilt of the caisson.

5.3 Reversal Wave Loading with Strong Strength from -7% to 10%

5.3.1 Onset of partial liquefaction of loose sand bed in strong wave load

Fig. 5.10 shows the response of the caisson and pore pressure in the loose sand bed under larger impulsive wave loading. In this test, i.e. test WL17, the maximum negative and positive wave peaks are -7% and 10% respectively. As can be seen, much of the vertical, horizontal and tilting movements occurred within the first 30 wave cycles. During this period, there is also substantial build-up of positive pore pressures. The contour maps of effective stress of soil bed after infilling stage is obtained by the numerical analysis using the geotechnical software Plaxis as shown in Fig. 5.11. The map shows that at the same sand depth, large effective stress is localized underneath the caisson base. Away from the base, the effective stress reduces substantially. Fig. 5.12 shows that the vertical effective stress increase with soil depth. There are spikes on the two edges of caisson base. The maximum landward and seaward excess pore pressure developed on the soil surface during wave loading are 80 and 60 kPa respectively at the 2nd wave cycle, while the vertical effective stresses at the two edges are about 84 and 62 kPa after infilling. Fig. 5.13 shows the variation of excess pore pressure ratio (defined as excess pore pressure divided by in-situ effective stress at that point) with depth. Owning to scarcity of PPT, only pore pressure generations at three different depths of surface, mid-depth and bottom were measured. As can be seen, excess pore pressure ratio reaches a value of about 1 on the soil surface, indicating that a state of zero vertical effective stress has been reached at the soil surface. After the centrifuge test, it is found that the caisson was deeply set into the soil bed, as shown in Fig. 5.14.

This reveals that the soil down to a depth of about 3m might have reached a state of very low effective stress level or even experience partial liquefaction in the first several wave cycles. However, as shown in Fig. 5.10, the excess pore pressure (in P1) started to drop almost immediately and hence recovered its shear strength by means of pore pressure dissipation. In other words, the upper portion of the sand bed had been momentarily liquefied. This is similar to the findings by Chen (2003) that the liquefaction of sea bed is limited to 7.5 m for a sand bed of 12.5 m thick when it is subjected to sinusoidal wave loading.

The dissipation of pore pressures that follows first began at the bottom and then gradually spread towards the soil surface. This is reasonable since the drainage may occur at the sand bed around the caisson base. The same phenomenon was observed in earthquakes (Tanaka, 1996) and in the flume test (Sumer et al., 1999). Fig. 5.14 is the photograph of caisson breakwater taken after test WL17, showing substantial tilting and settlement of the sand bed. Although tilting occurs in one direction only, observation of marker beads shows substantial outward movement of the soil beneath the caisson toe. This is consistent with the partial liquefaction of the upper layer of the sand bed, leading to settlement and tilt of the caisson.

Although the wave load with the same magnitude applied on the caisson again at about the 115th wave cycle, the pore pressure build-up is much lower than the previous maximum pressure, especially at the bottom as shown in Fig. 5.10. No caisson movement was recorded at this moment. This is because after the partial liquefaction, the ensuring densification of the soil bed actually increases the resistance of the sand bed to liquefaction. Hence, with less excess pore pressure build-up, liquefaction is unable

to occur again when the caisson is subjected to wave loadings of the same strength.

5.3.2   RD effect on caisson performance and pore pressure response

Tests WL25 and WL26 were conducted with the same wave loads but on sand bed with RD_i of 67% and 80%. Fig. 5.15 shows the comparisons of average caisson movements when the caisson rests on three different RD_i. As expected, the denser the sand bed, the less the caisson moves. Furthermore, as shown in Fig. 5.16, excess pore pressure build-up in these two tests is much lower than the in-situ effective stress, indicating that liquefaction has not occurred. In particular, there is little excess pore pressure build-up in test WL26.

Contours of excess pore pressures for tests WL25 and WL26 are indicated in Figs. 5.17 and 5.18, respectively. Again zones of positive excess pore pressure developed underneath the caisson base from the beginning of the wave loading episode in both tests. Zones of small negative pore pressure also developed in the latter stages of the test, after the first few hundred cycles of loading. For test WL25, the zone initiated from the landward side of the caisson at the lower part of the sand bed. For test WL26, the zone initiated from the seaward side of the caisson. This is similar to the observation in the "non-reversal" tests, where zones of dilation initiated from the landward edge of the caisson in most cases, but from the seaward edge of the caisson in the densest model, i.e. test WL7.

5.4 Reversal Wave Loading with Very Strong Strength from -10% to 10%

Fig. 5.19 shows the initial caisson and excess pore pressure responses for test WL23, which involves even large peak wave loading on the caisson breakwater resting on very dense sand with RD_i=82%. As can be seen, the response of caisson behavior to the stronger wave is fairly distinctive. Firstly, although very strong wave was applied on the caisson breakwater, liquefaction did not occur in the soil bed. Secondly, the caisson movement has not been suppressed because of very high sand RD_i of soil bed. Instead, densification of sand bed, seaward tilting and sliding occurred from the very beginning of wave loading. The average caisson movements indicated in Fig. 5.20 shows seaward horizontal movement at the point of measurement, the final movement being about 136 mm in prototype scale. Although the caisson breakwater rested on sand bed with almost the same density, the caisson response is very different in test WL7 with non-reversal wave loading of strength from 0% to 6%, or test WL22 with reversal wave loading of strength from -2% to 4%, or test WL26 with reversal wave loading of strength from -7% to 10%. The fact that the caisson tilted seaward indicates that a possible cause is the magnitude of the drag force.

Positive pore pressures were recorded by all PPTs from the first wave cycle. They reached a peak value at the 20th wave cycle, as indicated in Fig. 5.21. There appears to be two phases of negative pore pressure generation, one commenced at about the 150th cycle and the other at about the 5000th cycle. This appears to coincide with the rise in the rate of horizontal movement in Fig. 5.20 (a). Fig. 5.22 shows the contour of excess pore pressure in test WL23 with RD_i=82%. As discussed before, the horizontal,

vertical and tilt caisson movements will increase with number of wave cycles, but their increment will decrease with increasing number of wave cycles. However, although the horizontal increment decreases in the first 4,500 wave cycles, it unexpectedly increases from 4,500 to 5,000 wave cycles and then slows down again, as shown in Fig. 5.20(a). When the load episodes between this period is checked in Fig. 5.23(a), it is found that the deviation is caused by the inconsistency in wave strength which may arise from a fault in the servo-electric controller. Although it may affect the rate of build-up of horizontal movement, it should not affect the final movement as wave magnitude subsequently recovered, and the caisson movement has ceased for several thousands of load cycles towards the end of loading episodes.

5.5   Discussions

5.5.1   Effect of wave strength in reversal wave loading

The centrifuge model test data discussed sheds lights on the manner in which wave strength may affect the different aspects of behavior of caisson breakwater, pore pressure generation, progressive softening and partial liquefaction. Even for wave load with relatively low peak force, caisson breakwater resting on loose sand bed may experience significant pore pressure generation, with consequent accumulation of tilt and movement. For larger wave load, the effects are accentuated and excess pore pressure in the upper sand layers may reach levels approaching liquefaction. Caisson tilt may also increase considerably to values which may be sufficient to render the caisson unserviceable. The likelihood of large pore pressure build-up and liquefaction can be diminished by increasing the RD_i of sand bed. At RD_i of about 80% or higher, very little excess pore pressure is generated, and one may surmise that the likelihood of liquefaction-type

failure has been reduced to a sufficiently low level. If the drag phase is sufficiently high, seaward sliding failure may occur even in very dense sand.

In general, positive pore pressures usually develop in the initial stage of loading, often within the first 50 wave cycles. Then zones of negative pore pressure will initiate from either the bottom of soil bed, seaward or landward caisson edge. For sand with very low RD_i, these negative pore pressure zones tend to develop upwards. For sand with medium RD_i, negative pore pressure zones initiate from the landward edge. However, for very dense sand models, the negative pore pressure zones tend to initiate from the seaward edge.

5.5.2 Effect of non-reversal and reversal wave loading

The movement of caisson breakwater in reversal tests is significantly larger compared with that in non-reversal tests on sand beds with similar RD_i. The same can be said of the wave-induced excess pore pressures of the sand bed. Backward tilting towards the wave load direction occurred in all tests subjected to reversal wave loading. This is consistent with the findings by Rowe (1981) that the model caisson on undensified sand tilt back towards the applied loads when it is subjected to cyclic horizontal wave parcels. The RD_i of sand bed is the key factor in the reversal wave loading tests; it has a dominant influence on both the movement of caisson breakwater and the pore pressure build-up. Progressive softening becomes significant for reversal wave loading with positive pore pressure build-up in the first several wave cycles. In the actual prototype situations, the rock berm is always placed beneath the caisson base acting as the drainage path such that the pore pressure build-up is suppressed. On the other hand, in non-reversal tests, caisson movement is much more moderated and appears to depend

significantly on irregularities in the wave loading profile, such as spikes and accidental reversals.

The above findings indicate that experiments with non-reversal loadings may not adequately elucidate caisson response to real wave loading, which is likely to have a drag phase. Reversal wave loadings leads to much large pore pressure and caisson movement, which cannot be readily replicated in non-reversal tests.

Table 5.1 Test Identification for Caisson Breakwater subjected to reversal wave loads (All n prototype scale)

Test ID	Wave strength	Corrected		$ZnCl_2$ in infilling stage (kPa)	Tilt angle after infilling ($\times 10^{-4}$ rad)	Caisson settlement of center after infilling (mm)	Horizontal displacement after infilling (mm)	Loading stiffness (MN/m^3)
		Initial RDi (%)	RDc (%)					
WL16		51	54	218	-0.225	67	-0.27	3.25
WL18	-2%~4%	62	62	220	-0.344	53.5	-0.43	4.11
WL20		71	69	217	-0.075	44.5	-0.09	4.87
WL22		85	82	220	0.141666667	35	0.17	6.28
WL17		63	55	221	-0.13333333	66	-0.16	3.34
WL25	-7%~10%	70	66	236	0.083333333	52.5	0.1	4.5
WL26		80	82	220	-0.18461538	35	-0.24	6.28
WL23	-10%~10%	80	84	220	0.104	34	0.13	6.47
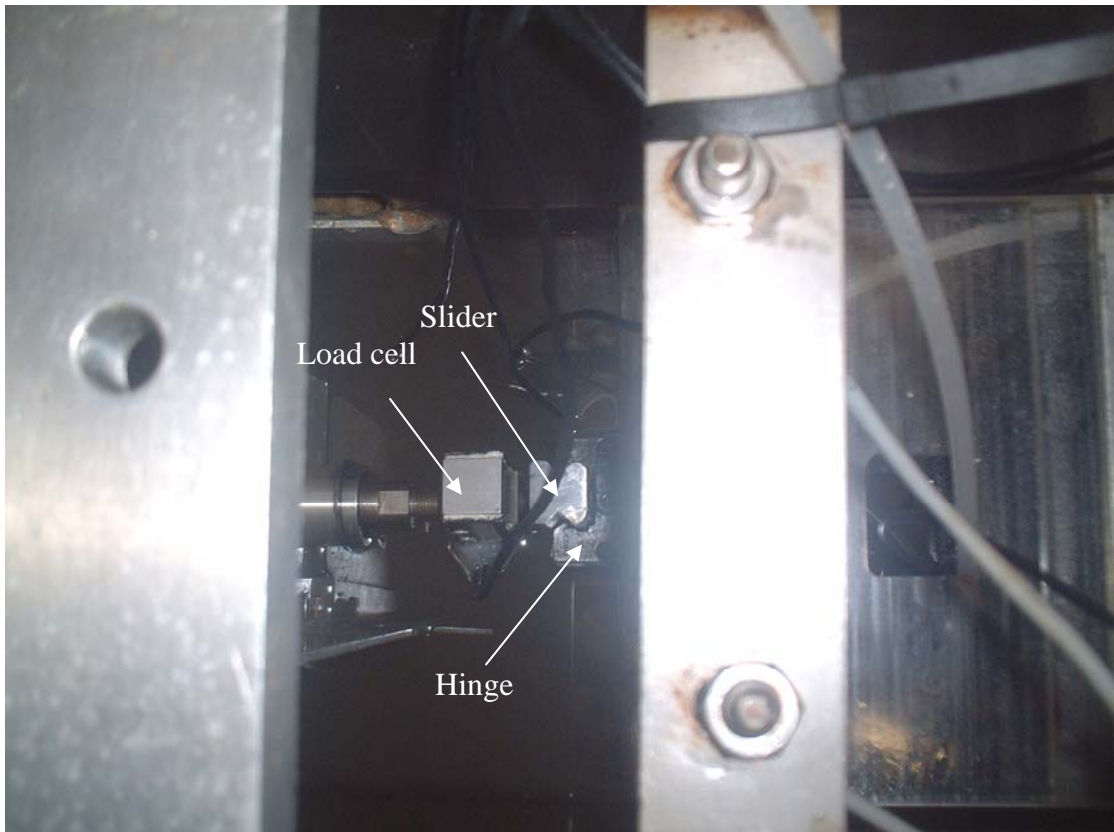
Fig. 5.1 Hinge-and-slider system to apply reversal wave loads
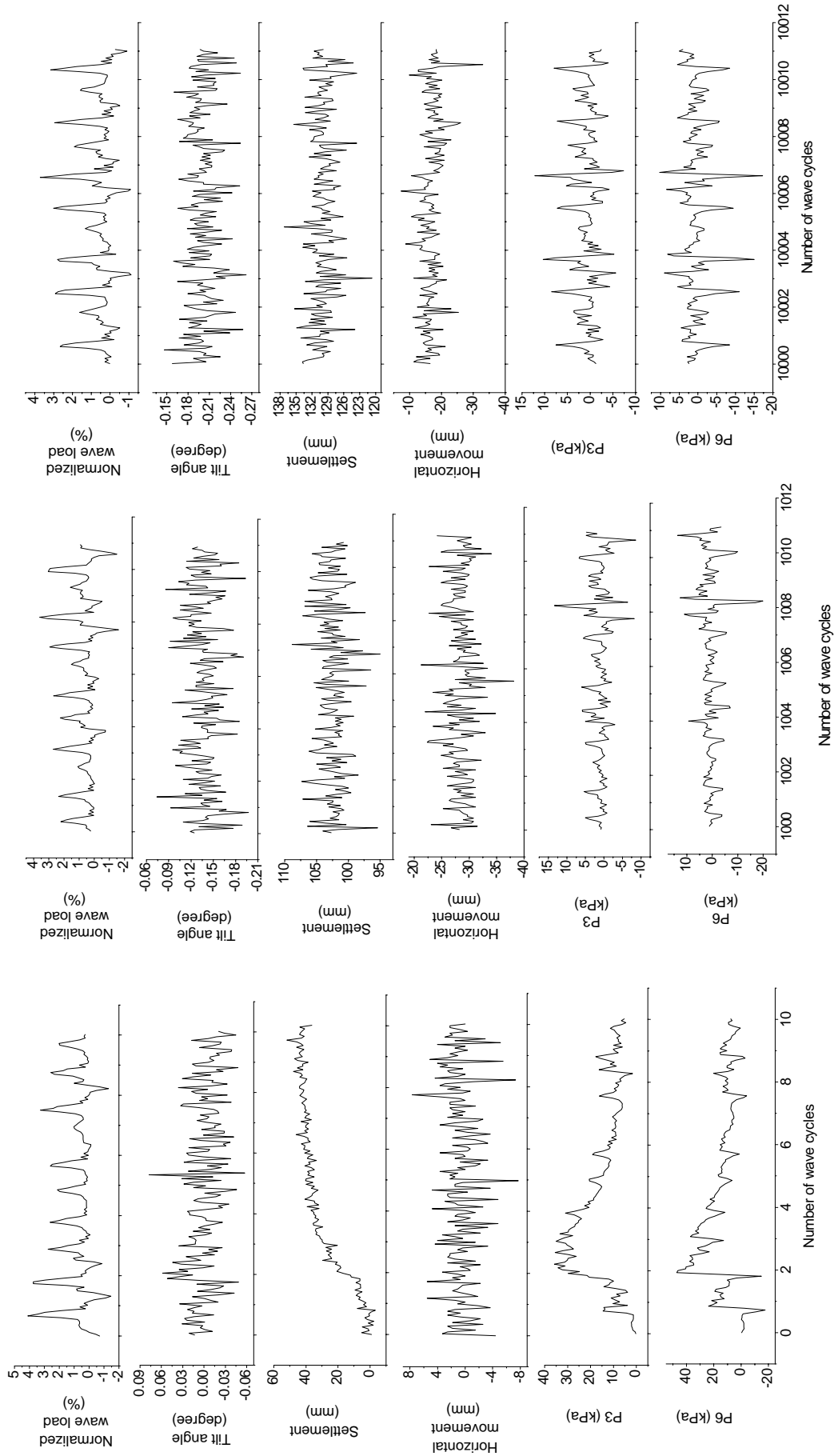
Fig.5.2 Typical instantaneous movement and pore pressure response under reversal wave loading of test WL16 with RDi=51%
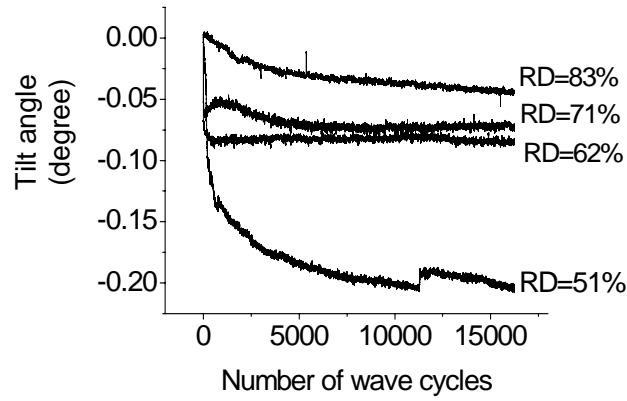
(a) Tilt angle
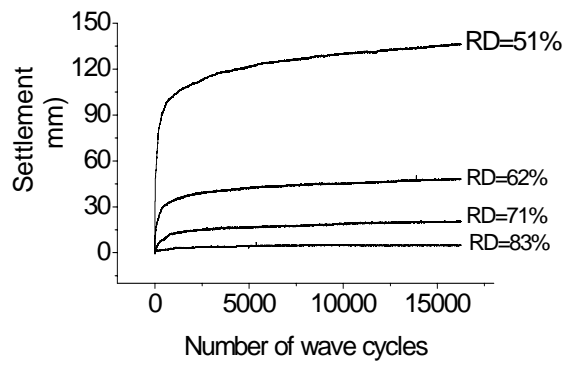
(b) Settlement of center
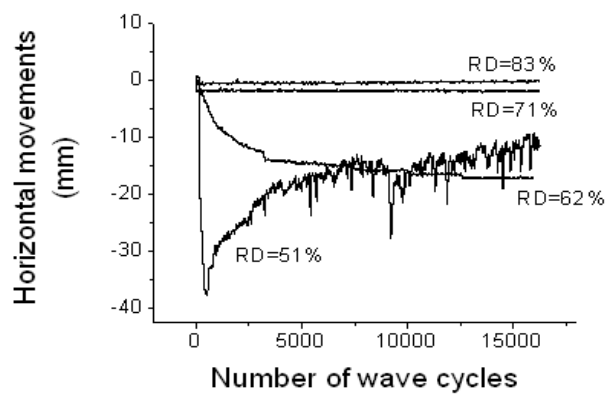
(c) Horizontal movement
Fig. 5.3 Averaged movements of caisson breakwater on different initial RD of sand
bed in reversal wave loading tests
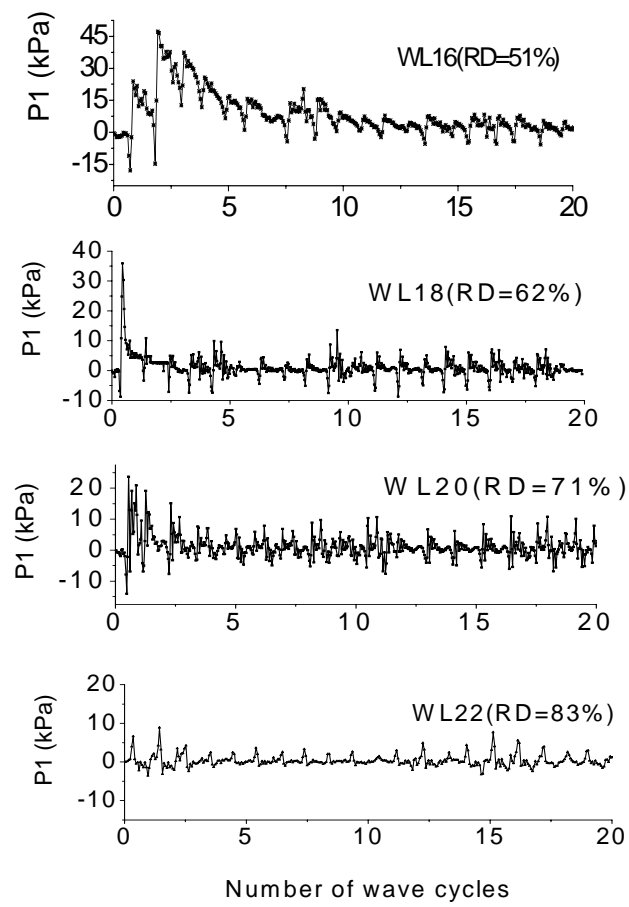
Fig. 5.4 Instantaneous pore pressures in sand bed of different initial RD in reversal tests
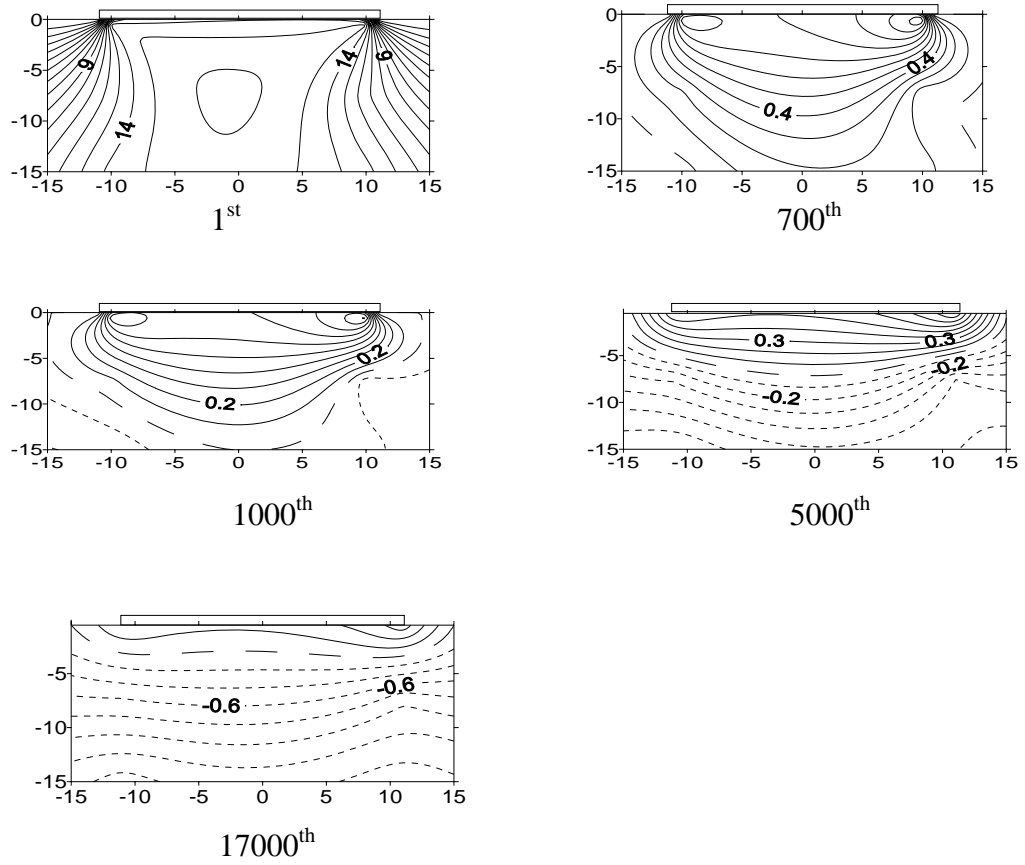
Fig. 5.5 Contour maps of excess pore pressure in test WL16 with RDi=51%
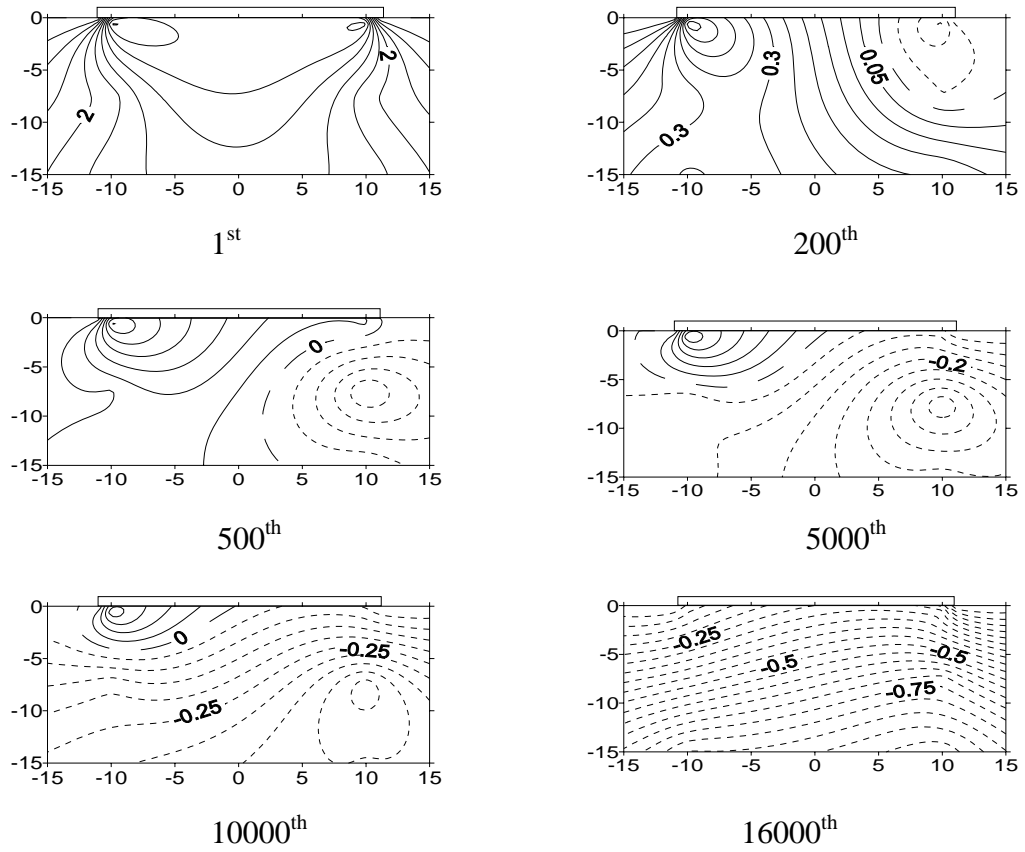
Fig. 5.6 Contour maps of excess pore pressure in test WL18 with RDi=62%

1st

100th

400th

500th

4000th

16000th
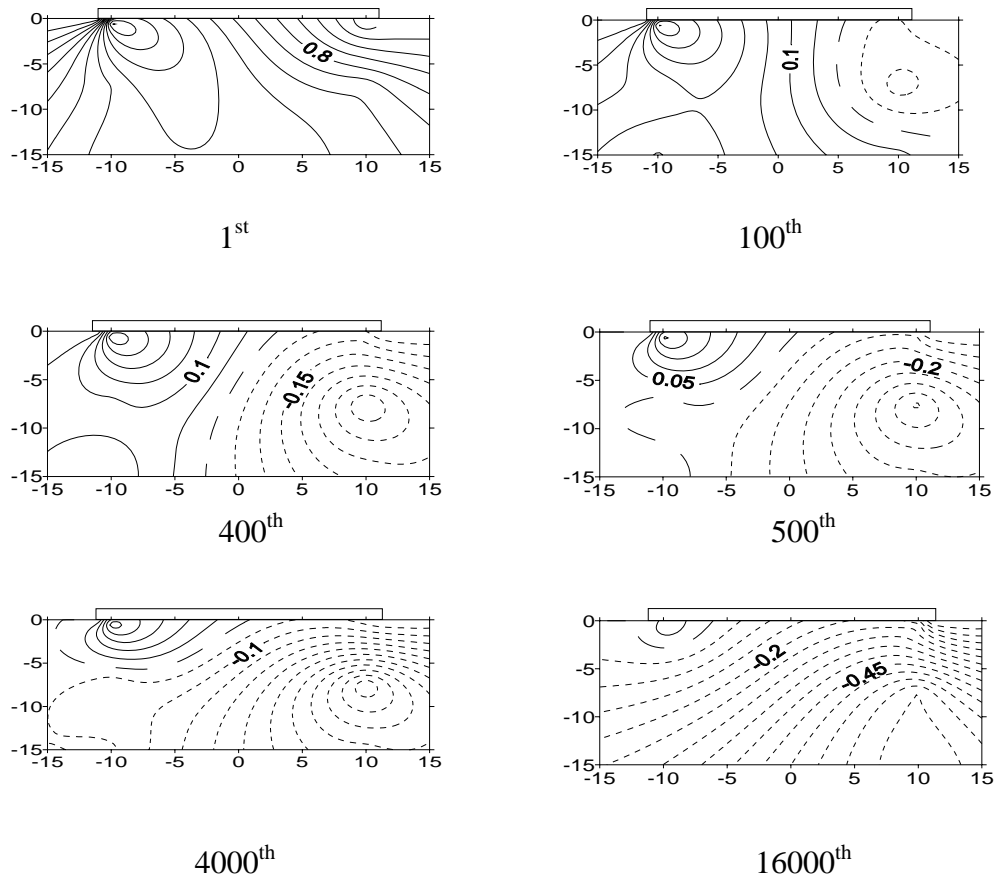
Fig. 5.7 Contour maps of excess pore pressure in test WL20 with RDi=71%

1st

10000th

17000th
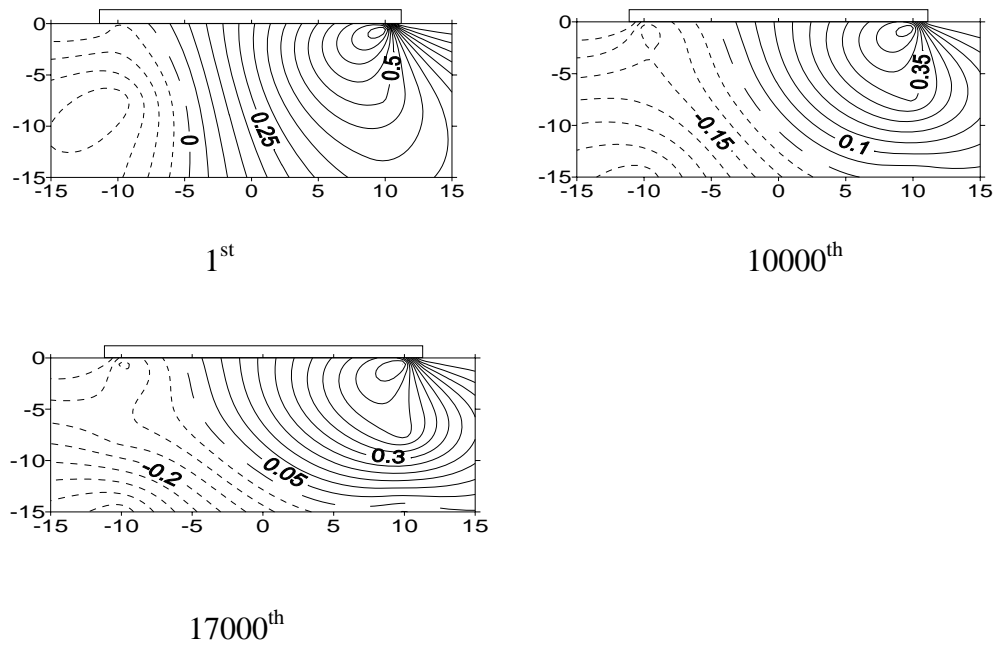
Fig. 5.8 Contour maps of excess pore pressure in test WL22 with RDi=83%
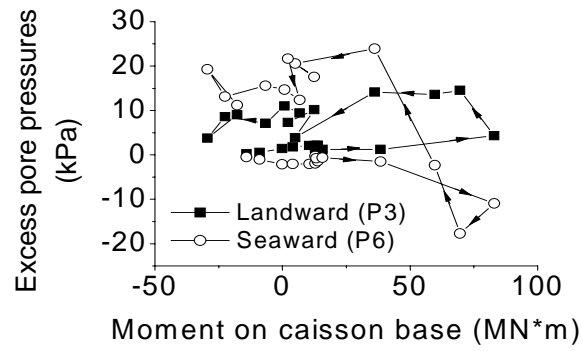
(a) WL16 (RDi=51%)
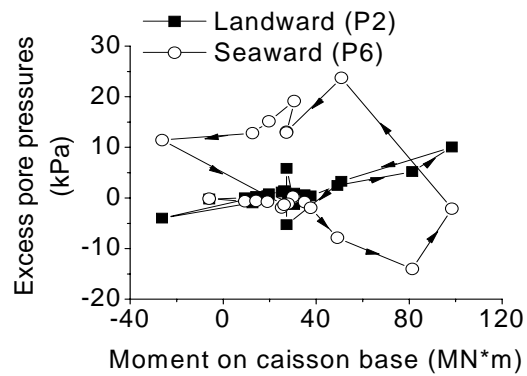
(b) WL20 (RDi=71%)

Fig. 5.9 Pore pressures response with moment of caisson base during the first wave cycle in reversal tests
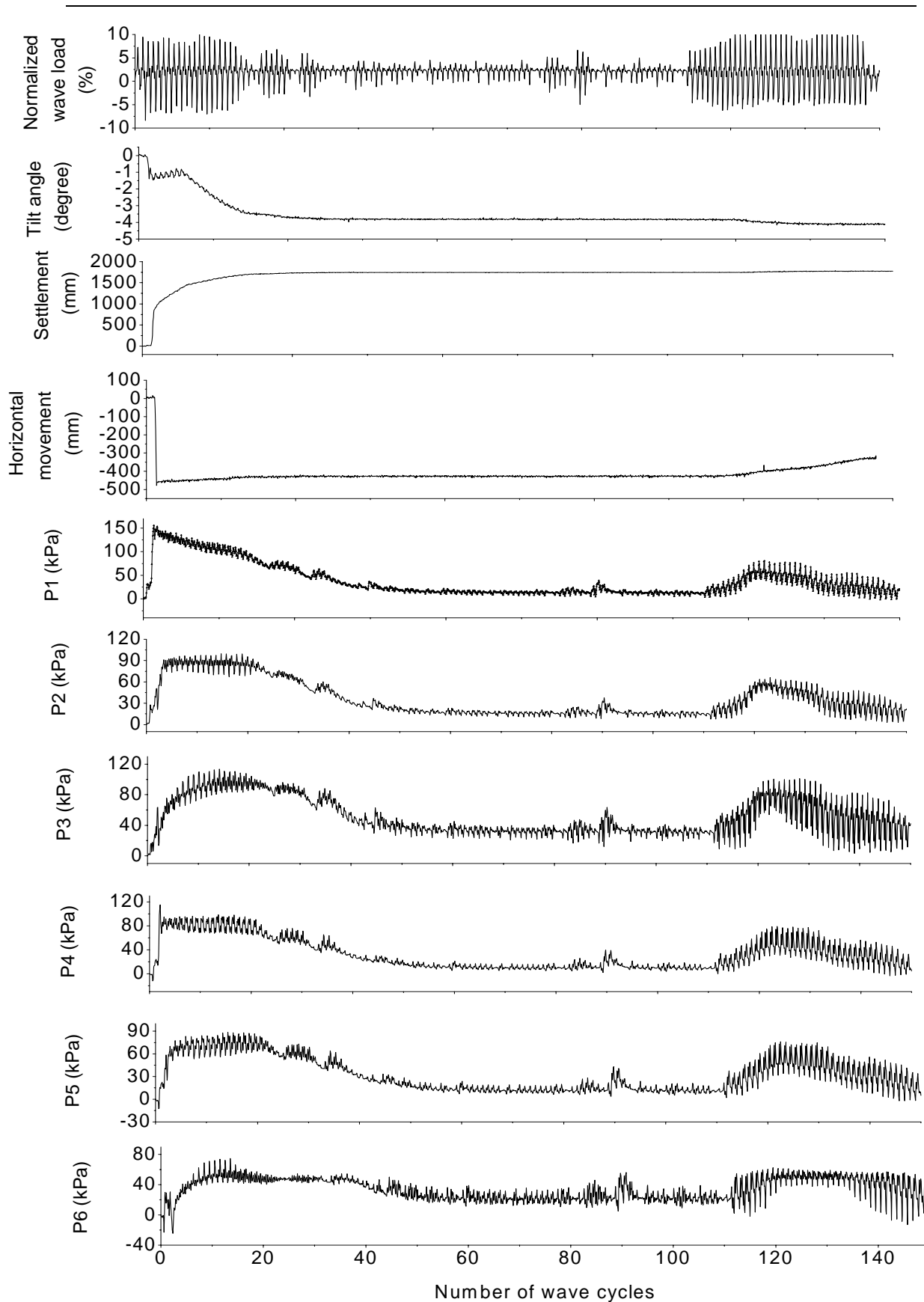
Fig. 5.10 Instantaneous caisson movements and pore pressure response in strong wave load in the test WL17 with RDi=55%
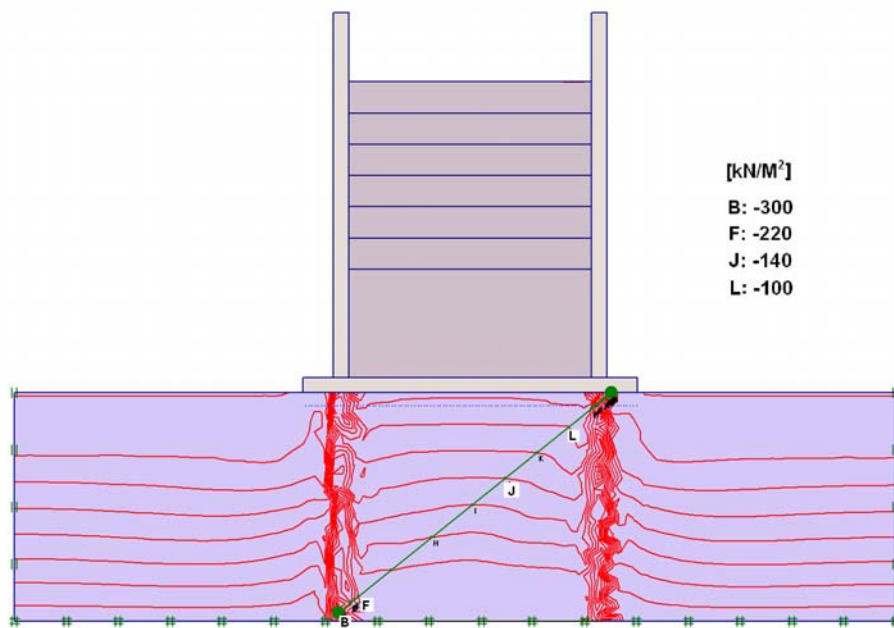
Fig. 5.11 Contour maps of vertical effective stress of sand bed after infilling stage
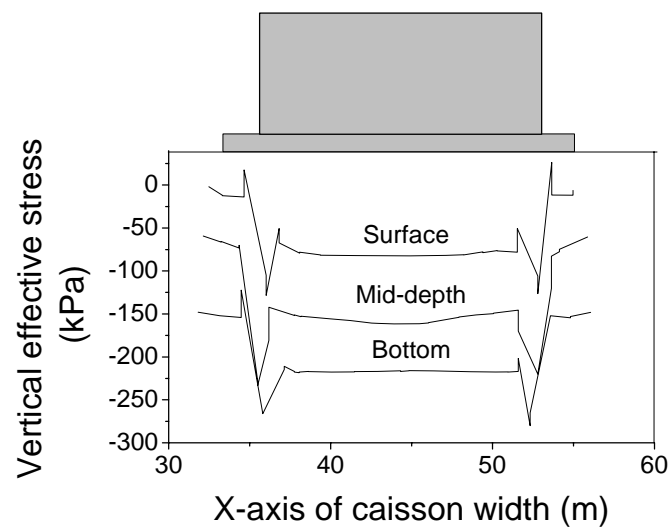
Fig. 5.12 Vertical effective stress of sand bed with depth after infilling stage
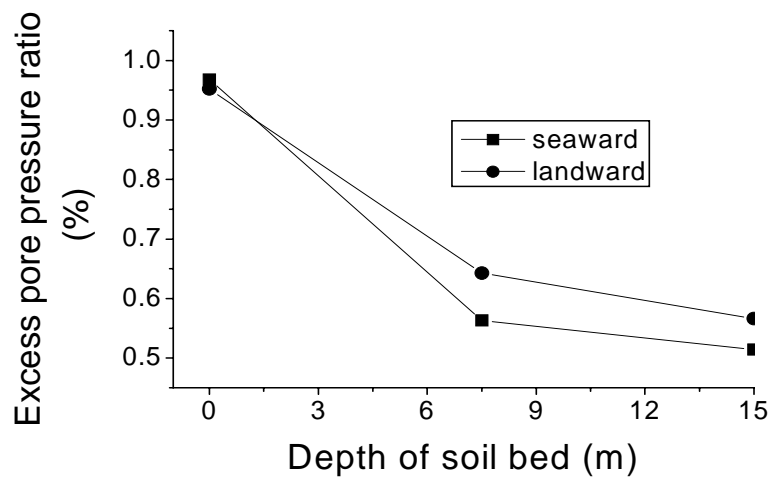
Fig. 5.13 Variation of excess pore pressure ratio with depth
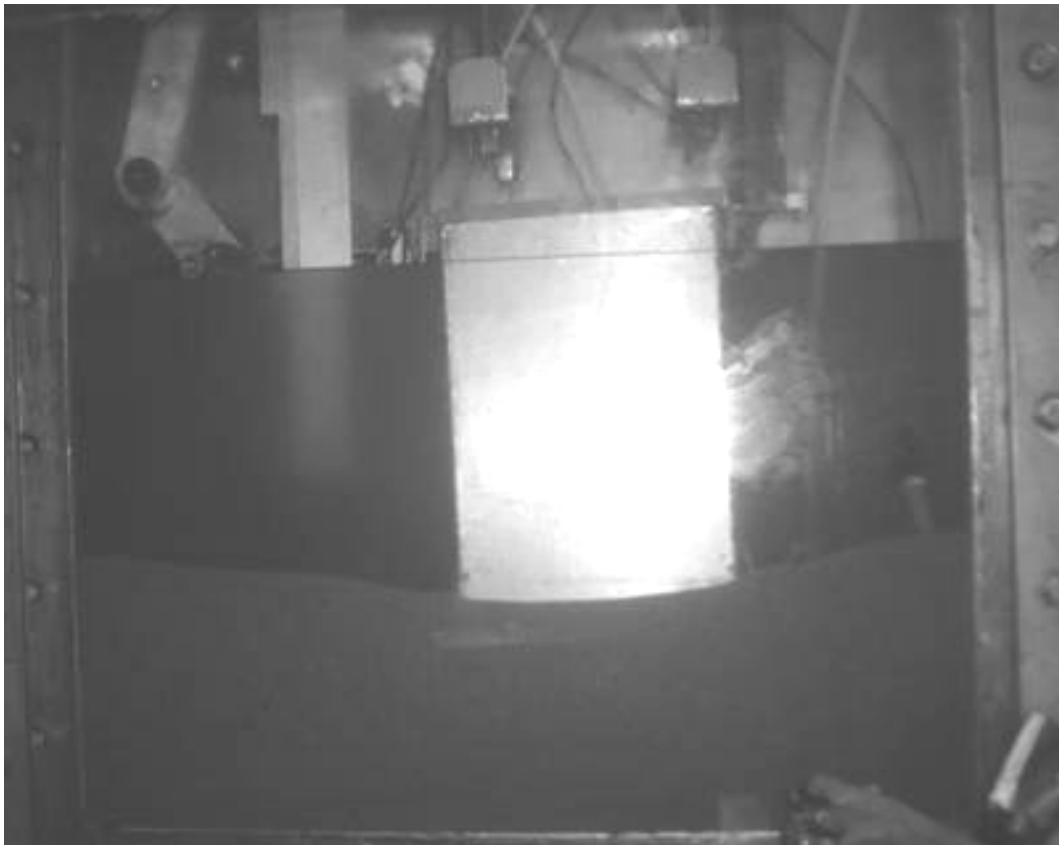
Fig. 5.14 Caisson breakwater after partial liquefaction
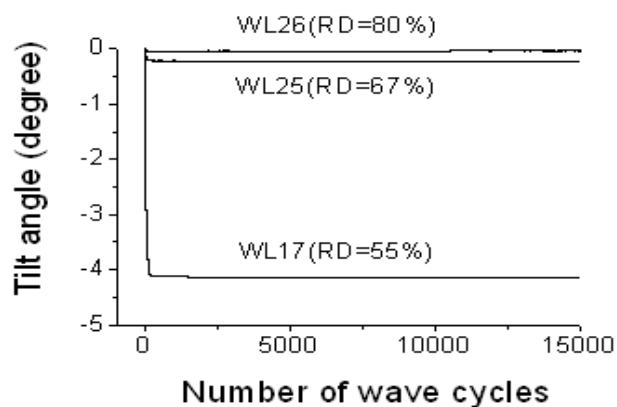
(a) Tilt angle
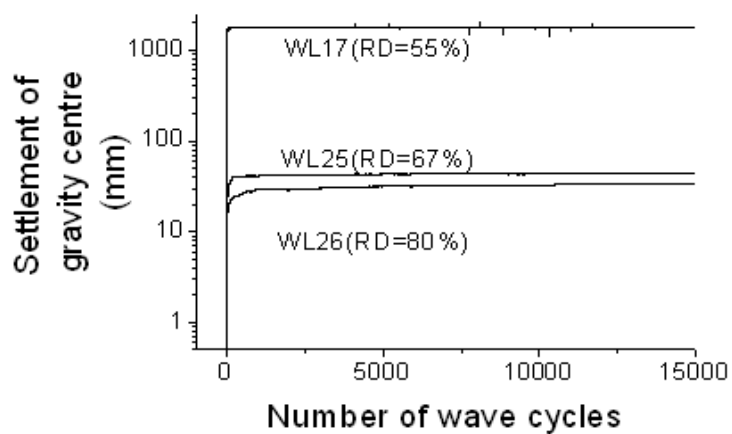
(c) Settlement of gravity centre
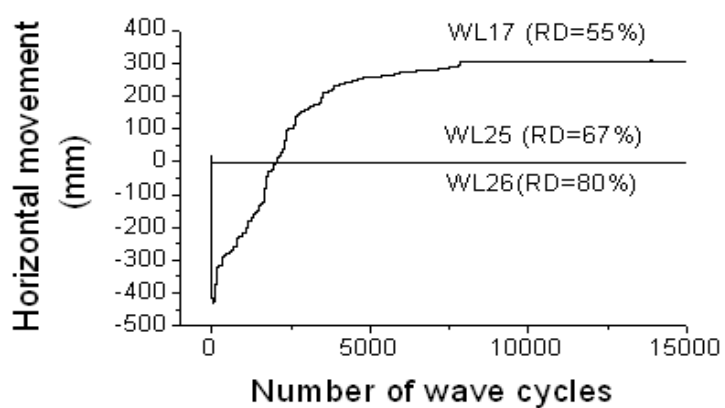
(c) Horizontal movement

Fig. 5.15 Averaged movements of caisson breakwater on different RDi of sand bed in reversal strong wave loading tests
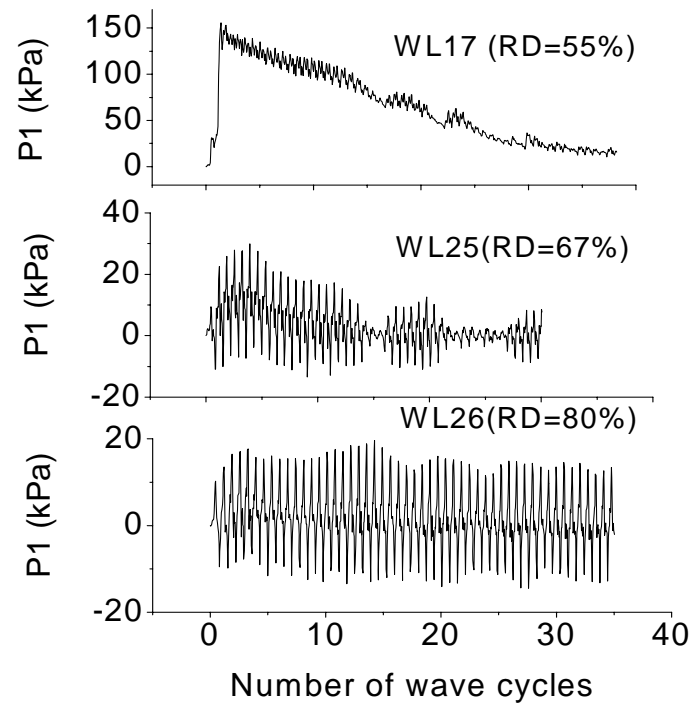
Fig. 5.16 Instantaneous pore pressures in sand bed of different RDi in reversal tests subjected to strong wave loads

1

50

100

500

10000

16000
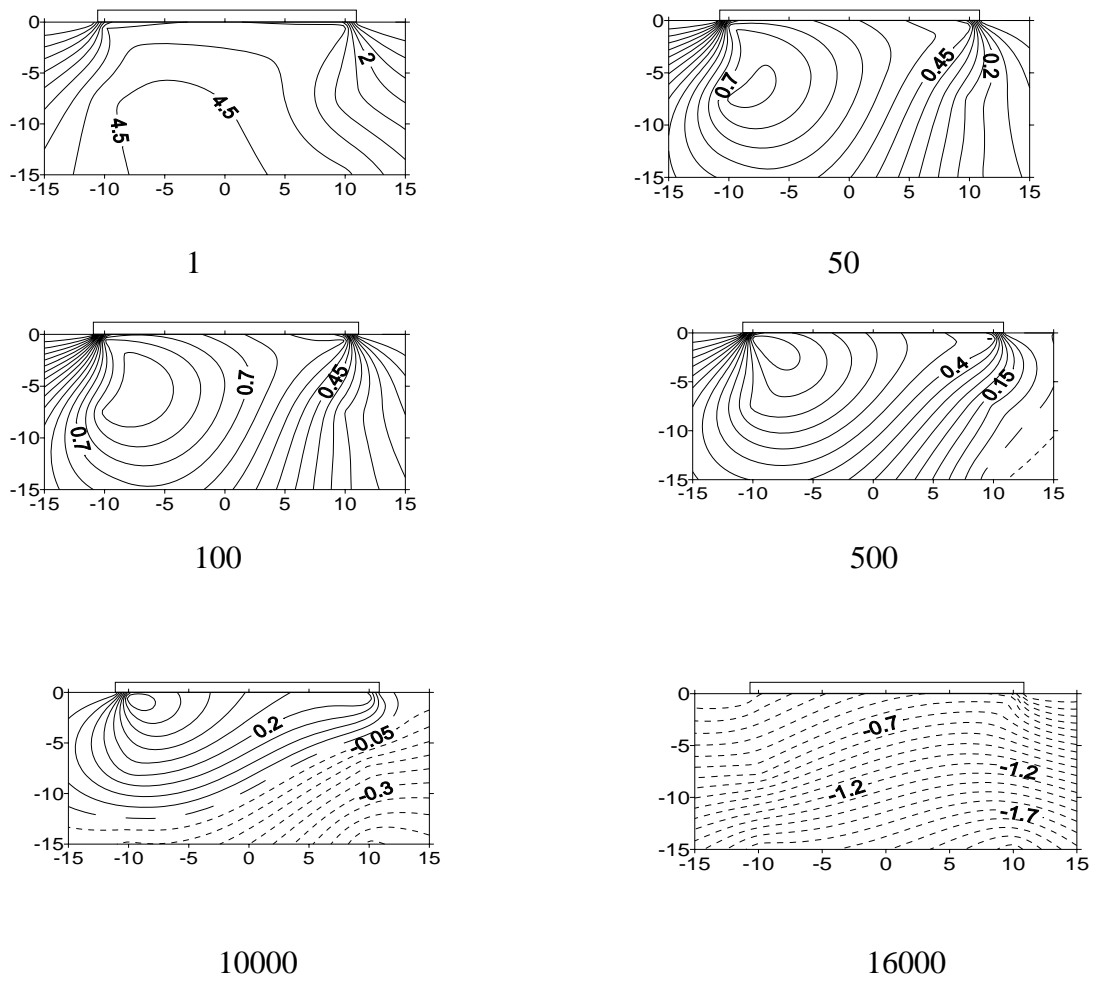
Fig. 5.17 Contour maps of excess pore pressure in test WL25 with RDi=67%

1

50

100

500

16000
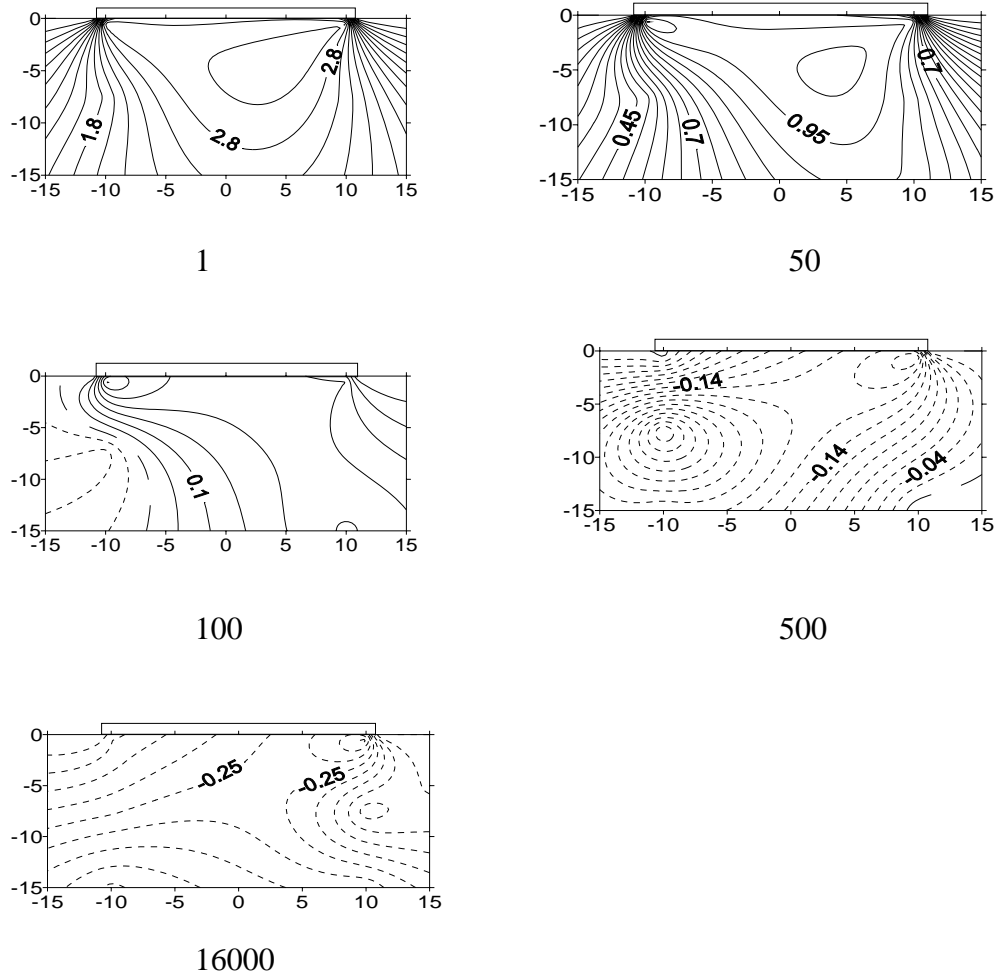
Fig. 5.18 Contour maps of excess pore pressure in test WL26 with RDi=80%
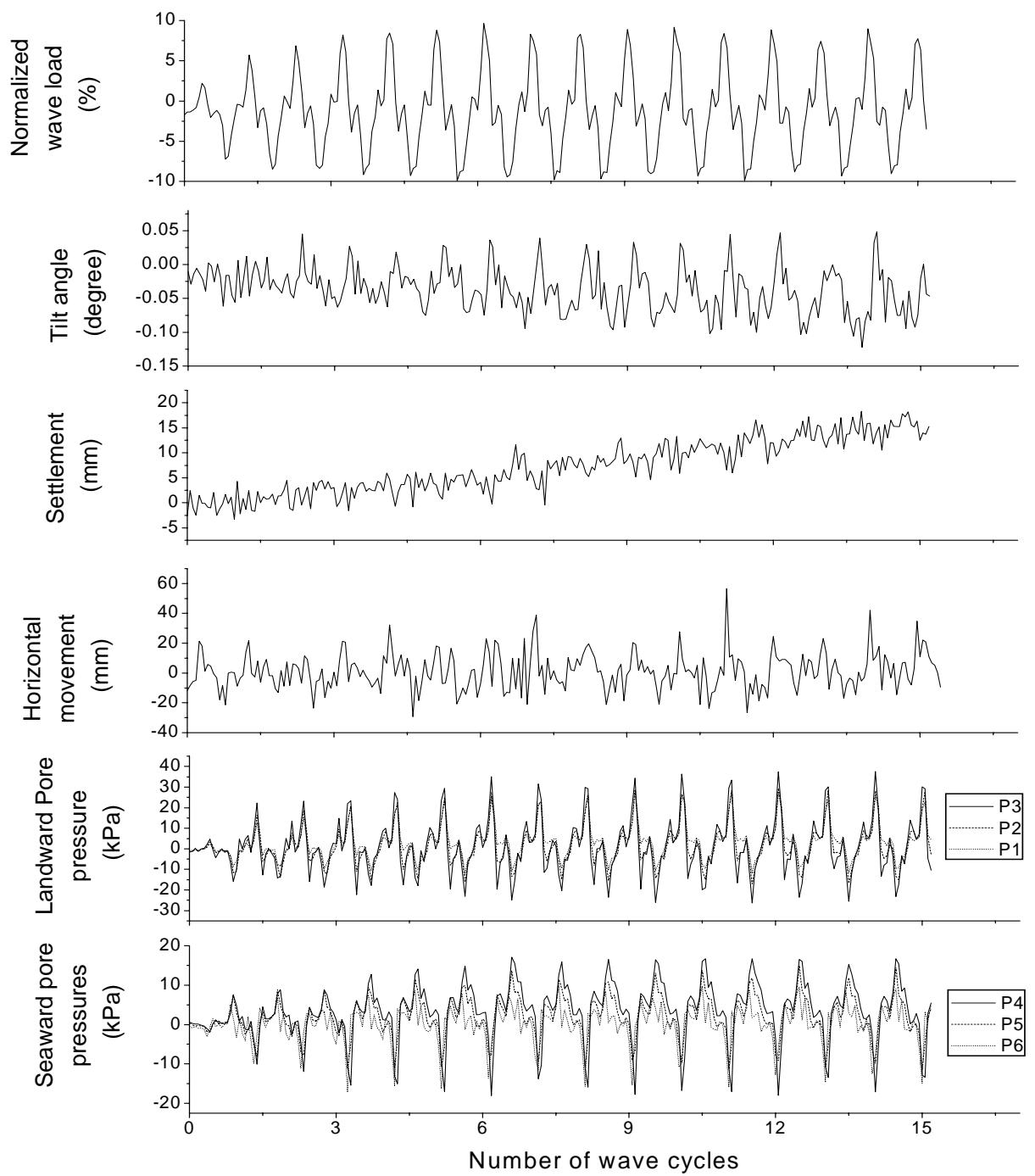
Fig. 5.19 Instantaneous caisson movements and pore pressure response in very strong
wave load in test WL23 with RDi=82%
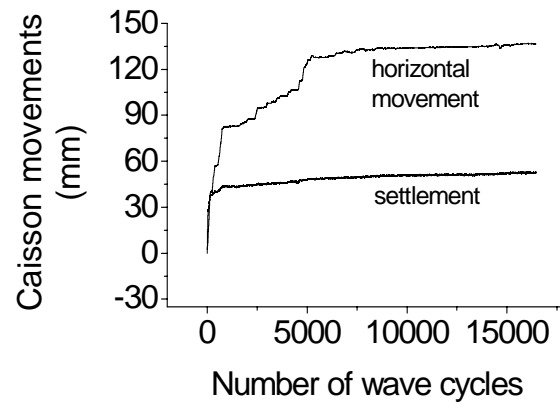
(a) Average caisson movements
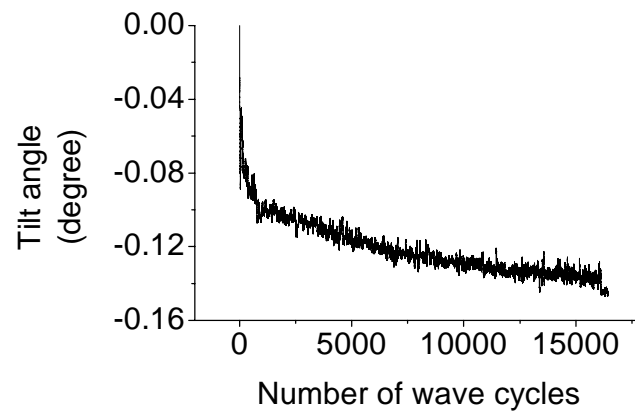
(b) Tilt angle

Fig. 5.20 Caisson movements in strong wave load in test WL23 with RDi=82%
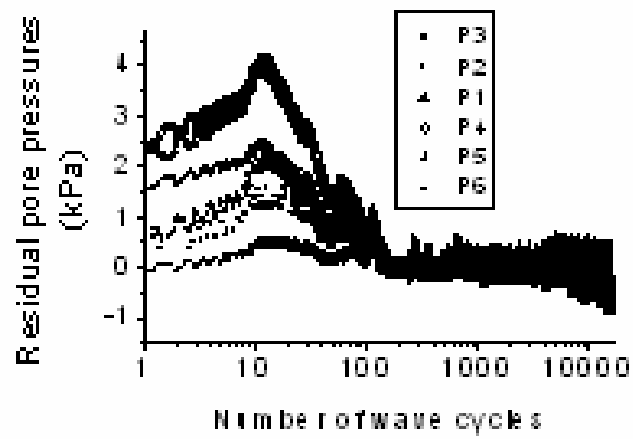
Fig. 5.21 Residual pore pressure response of test WL23 with RDi=82%
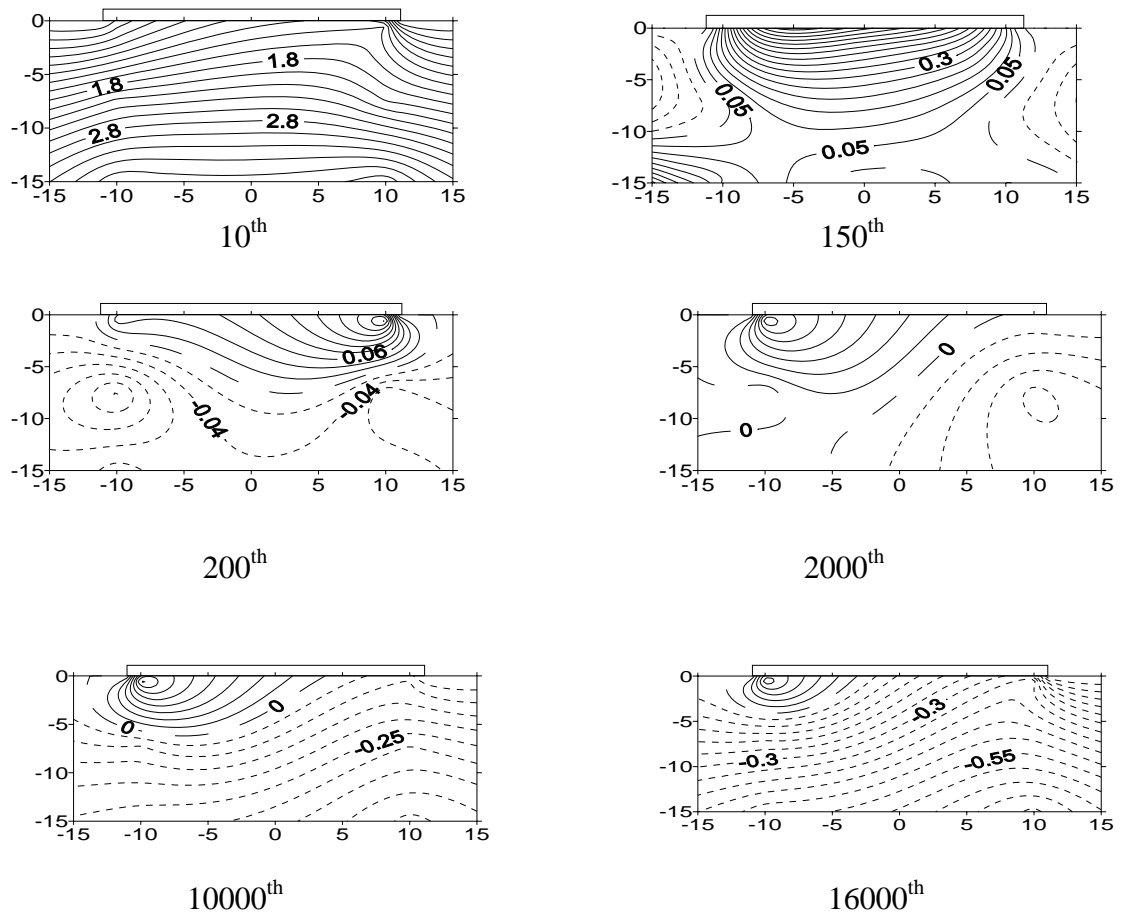
Fig. 5.22 Contour maps of excess pore pressure in test WL23 with RDi=82%
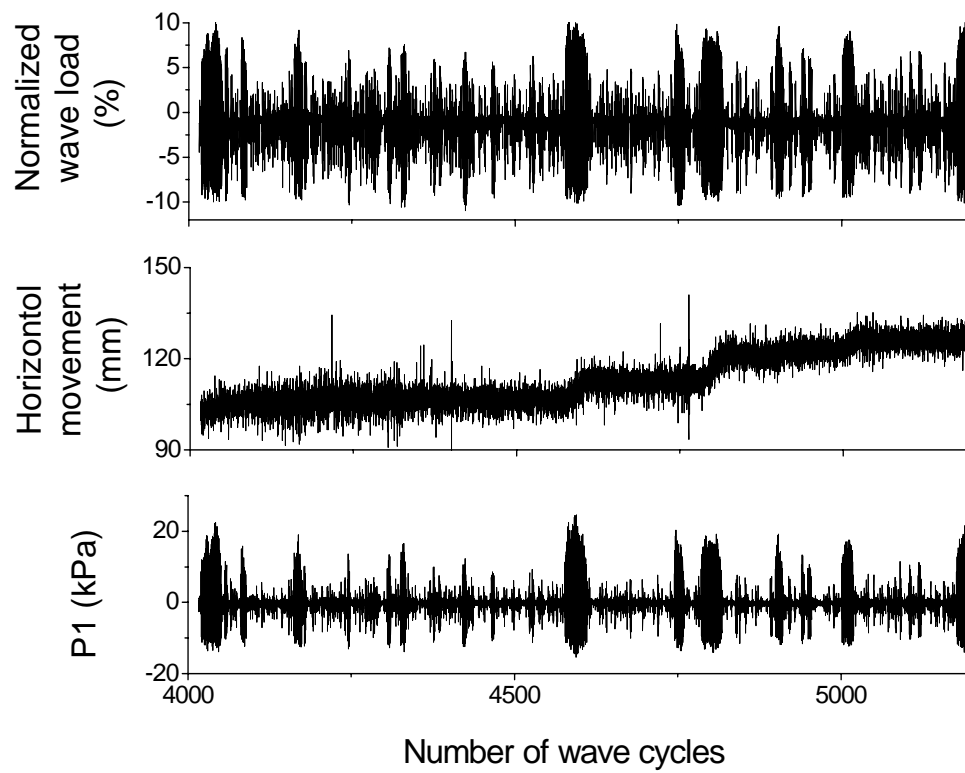
Fig. 5.23 Horizontal movement and pore pressure response from 4,500 to 5,000 wave cycles in test WL23 with RDi=82%

Chapter 6

Dynamic Analysis of Caisson Tilt during Wave Spikes

6.1 Introduction

The results from the non-reversal wave loading tests show that most of the caisson movements were induced by either wave spikes or suction waves. The wave spikes result in overloading of the bearing capacity of the caisson foundation, while generation of excess pore pressure is minimal. The results reveal that even the dense sand bed can be adversely affected by a wave spike of sufficient magnitude. The mechanism for suction waves could not be clearly discerned from non-reversal tests; however, it is clearly related to the reversal phase of the wave. Reversal loading tests indicate significant excess pore pressure build-up in the early stages of the loading episode, which suggests that a densification mechanism is involved. This is supported by the fact that very dense sand beds (i.e. test WL22 with RD = 85% and test WL26 with RD = 80%) do not seem to be seriously affected by reversal wave loadings.

The two different mechanisms associated with wave spikes and reversal wave loading have to be addressed separately in design. For the case of reversal wave loading, the results suggest that densification of sand bed is a possible solution. Since the num-

ber of cycles involved in wave loading is generally very large, any sand bed which has a potential to densify is likely to build up substantial pore pressure. This is very different from earthquake loading which consists of much fewer cycles. In view of this, a liquefaction analysis may be of dubious benefit. On the other hand, some form of dynamic analysis may well be viable for the wave spike. In this chapter, a simplified dynamic limit equilibrium analysis is proposed for analyzing the tilt mechanism associated with wave spikes. The tilt mechanism is chosen because tilting was observed to be a dominant failure mechanism in the centrifuge tests.

6.2 Previous Analytical Studies on Caisson Tilt under Wave Loading

Some of the previous analytical studies have been discussed in Chapter 2. These include studies of bearing capacity and overturning of caisson by Terashi and Kitazume (1987), Kobayashi et al. (1987a), Sekiguchi and Ohmaki (1992), and Sekiguchi and Kobayashi (1994), among others. Sekiguchi and Kobayashi (1994) proposed an overload factor beyond which a given caisson may be overturned, but the specific caisson movement was not obtained. Furthermore, the dynamic response of caisson breakwater has been idealized by a system of mass and spring for horizontal and rotational motions (Goda 1994; Oumeraci et al. 1994; Gao et al. 1988). Nonetheless, only elastic motions were calculated and the selection of spring constants was not apparent. A realistic analysis of caisson motion and seabed response may be modeled using Biot consolidation theory (Tsai et al. 1990; McDougal et al. 1986) where the soil stresses, the surface displacement and pore water pressures are modeled realistically. Such a procedure, because of its complex and arbitrary assumptions, is not considered a practical design method.

The analytical model discussed herein takes its direction from the findings of the centrifuge model studies. The results of the studies show that tilt may be induced by reversal loading as well as spikes. As Chapter 5 shows, the effects of reversal loading are probably best forestalled by densifying the sand bed to suppress the build-up of excess pore pressure and possible liquefaction. However, as Chapter 4 shows, the effects of wave spikes are largely unaffected by the densification of sand bed, so that even a caisson resting on a dense sand bed with RD=72% can be tilted by a wave spike (refer to results of test WL4). The discussion also indicates that the occurrence of tilt during wave spikes have features of a plastic mechanism.

Oscillatory motions of rocking and swaying as well as permanent tilt and sliding may be induced by impulsive wave loading, as shown in Fig. 6.1. In this Chapter, a simplified dynamic analysis for caisson breakwaters is proposed based on the concepts of elasto-plasticity. The elastic portion defines the transient but recoverable part of the tilt and is based on the solution of a simplified lumped-mass-spring foundation model. The plastic portion defines the irrecoverable part of the tile and is based on the partial optimization of a slip surface which is assumed to take the form of a circular arc. The general procedure for the plasticity calculations is firstly to assume a failure mechanism based on a circular arc slip plane and then to optimize the objective function with respect to a few parameters. In this way, a lower bound of the limit equilibrium load can be found. Based on Mohr-Coulomb model, the limiting shear force underneath the caisson base is defined assuming the slip soil model of circular arc by taking both sliding and rotating into account. The additional, i.e. out-of-balance, shear force is then fed into an equation of motion involving the rotational inertia of the caisson. The

magnitude of rotational displacement is obtained by double integrating this equation of motion. Then the proposed design approach is calibrated using centrifuge model test results. A preliminary assessment of the reliability of the method is conducted by comparing its predictions with the observations from a field case (Sekiguchi 1992). Finally parametric studies have been done to investigate the influence of various wave height, wave period, water depth, caisson effective weight, caisson width and angle of shear resistance of rubble mound. The elastic model will be dealt with first in the next section.

6.3   A Mass-Spring Model for Oscillatory Displacement

A simple mass-spring model of a vertical breakwater of height H, width B and length Lc will be considered to calculate the elastic behavior when it is exposed to breaking wave loads, as indicated in Fig. 6.2. The mass-spring model has two degrees of freedoms for wave loading stage and only the elastic displacements are accounted in this part. Richart et al. (1970) expressed the motion of rigid body in terms of the horizontal translation of the centre of gravity (CG) and the rotation of the body about the CG. This appears to correspond well with the centrifuge test observations that the caisson is found to rock about the point very close to the CG. The equations of vertical motion during infilling stage is sketched in Fig. 6.3(a) and given as:

$$m_{tot,ver}\ddot{x}_1 = -k_1 x_1 + F_1 \tag{6.1}$$

During wave loading stage, the equations of the horizontal and rotational motion of the system sketched in Fig. 6.3(b) are as follows:

$$m_{tot,hor}\ddot{x}_2 = -k_2 x_2 + \frac{H}{2}k_2 x_3 + F_2 \qquad (6.2)$$

$$\theta_{tot}\ddot{x}_3 = \frac{H}{2}k_2 x_2 - (\frac{H}{2})^2 k_2 x_3 - k_3 x_3 + F_2(A - \frac{H}{2}) \qquad (6.3)$$

The differential equations in matrix form for stage 2 wave loading is:

$$\begin{pmatrix} m_{tot,hor} & 0 \\ 0 & \theta_{tot} \end{pmatrix} \begin{bmatrix} \ddot{x}_2 \\ \ddot{x}_3 \end{bmatrix} + \begin{pmatrix} k_2 & -\frac{H}{2}k_2 \\ -\frac{H}{2}k_2 & (\frac{H}{2})^2 k_2 + k_3 \end{pmatrix} \begin{bmatrix} x_2 \\ x_3 \end{bmatrix} = \begin{bmatrix} F_2 \\ F_2(A - \frac{H}{2}) \end{bmatrix}$$

$$(6.4)$$

In which,

x_1 = Vertical translation,

x_2 = Horizontal translation,

x_3 = Rotational translation,

F_1 = Vertical load of infilling material,

F_2 = Horizontal wave loading,

k_1 , k_2 and k_3 = Stiffness of the foundation in vertical, horizontal and rotational direction, respectively,

$m_{tot,ver}$ = Total vetical caisson mass,

$m_{tot,hor}$ = Total horizontal caisson mass,

θ_{tot} = Total caisson mass moment of inertia,

H = Caisson height, and

A = Vertical distance from the elevation of wave load application to the caisson base.

6.4   Structure and Foundation Parameters of Caisson Breakwater

6.4.1   Mass

The total mass m_{tot} that should be taken into account is the mass of the caisson break-water itself m_{cai} , the added hydraulic mass m_{hyd} and the added mass of soil m_{geo} .

$$m_{tot} = m_{cai} + m_{hyd} + m_{geo} \tag{6.5}$$

When the caisson is subjected to wave impact loads, a certain mass of water is forced to move with the structure. This added mass of water is called hydro-dynamic mass. The hydro-dynamic mass can move in the horizontal or vertical direction. Pendulum tests on a caisson have been conducted for different water depths by Oumeraci et al. (1992) and the horizontal hydro-dynamic mass accounting for the water in front of and behind the caisson is given as:

$$m_{hyd,hor} = 1.4 L_c \rho_w d^2 \tag{6.6}$$

In which:

ρ_w = Density of sea water (=1025 kg/m^3),

d = Depth of water, and

L_c = Length of caisson.

The hydro-dynamic mass for vertical motion is:

$$m_{hyd,vert} = 0 \tag{6.7}$$

Similarly, a certain mass of soil beneath the structure is forced to move with the

latter, this added mass of soil is called geo-dynamic mass. Vink (1997) assumed the geo-dynamic mass to be the same for both horizontal and vertical oscillations. He considered that this assumption will not significantly influence the results of the calculations because wave impact usually results predominantly in horizontal and rotational oscillations with essentially no vertical oscillations. The geodynamic mass can be estimated using the relationship (MAST II 1995):

$$m_{geo} = m_{geo,hor} = m_{geo,vert} = \frac{0.76 \rho_s \left(\frac{BL}{\pi} \right)^{\frac{3}{2}}}{2 - \nu} \tag{6.8}$$

where ρ_s = Mass density of foundation soil,

ν = Poisson's ratio, and

B = Width of caisson.

The total mass for vertical oscillations $m_{tot,vert}$ is:

$$m_{tot,vert} = m_{cai} + m_{geo,vert} \tag{6.9}$$

The total mass for horizontal oscillations $m_{tot,hor}$ is:

$$m_{tot,hor} = m_{cai} + m_{hyd,hor} + m_{geo,hor} \tag{6.10}$$

6.4.2   Mass moment of inertia

To determine the mass moment of inertia θ_{tot}, the same procedure can be followed as for the determination of the mass of vertical breakwater (Vink, 1997).

$$\theta_{tot} = \theta_{cai} + \theta_{hyd} + \theta_{geo} \tag{6.11}$$

$$\theta_{cai} = \frac{1}{12} m_{cai}(B^2 + H^2) \tag{6.12}$$

It is assumed that the mass of caisson is equally distributed over its length, height and width. The center of gravity is assumed to be at the center of the cross section as shown in Fig. 6.2. Vink (1997) found that a good approximation of the magnitude of θ_{tot} can be found by neglecting θ_{hyd} and θ_{geo} and using $m_{tot,hor}$ instead of m_{cai} in equation (6.12).

6.4.3 Stiffness of spring

The shear and elastic moduli of the soil must be known to determine the stiffness of the springs k_1, k_2 and k_3. Richart et al. (1970) proposed that for angular-grained materials with void ratio e>0.6, the shear modulus G_s can be estimated by the relationship

$$\underset{(lb/in.^2)}{G_s} = \frac{1230(2.97 - e)^2}{1 + e} \sqrt{\underset{(lb/in.^2)}{\bar{\sigma}_0}} \tag{6.13}$$

where $\bar{\sigma}_0$ = average effective confining pressure. Both G_s and $\bar{\sigma}_0$ are expressed in lb/in^2.

Pedersen (1994) adopted Richart et al. (1970) but appeared to have set the representative effective confining pressure σ_0 as follows:

$$\bar{\sigma}_0 = 0.16 \frac{F_n}{B_{base} L_c} \tag{6.14}$$

It should be noted that the value of the representative pressure σ_0 is a complex one and it depends on the lateral earth coefficient k_0 and the representative point at which G_s is measured. However, there is no easy answer to such questions. It is beyond the scope of the study.

$$F_n = W - F_b - F_u \tag{6.15}$$

In which,

F_n = Normal force,

W = Caisson weight,

F_b = Caisson buoyancy,

F_u = Uplift force,

B_{base} = Caisson base width, and

L_c = Caisson length.

A common way to represent the horizontal stiffness of the ground k_2 and the rocking stiffness k_3 is to use Whitman and Richart's (1967) formulae, which were

$$k_2 = 2(1 + \nu)G_s\beta_x\sqrt{L_c B_{base}} \tag{6.16}$$

$$k_3 = \frac{G_s}{1 - \nu}\beta_\psi L_c^2 B_{base} \tag{6.17}$$

In which β_x and β_ψ are given values for various values of B_{base}/L_c . The Whitman and Richart's (1967) relation for horizontal stiffness was adapted and simplified from Barkan's (1962) relations, assuming that there is a linear relationship between the sliding of a foundation and the average shearing sliding stress developed along the foundation base contact area. The Barkan's relations (1962) for horizontal motion of a rectangular foundation are given by:

$$k_2 = \frac{E}{(1 - \nu)\sqrt{A}}k_\tau \tag{6.18}$$

In which A is the caisson base area and k_τ is a given value depending not only on the ratio of caisson base width to length, but also on the value of Possion's ratio. It should be noted that the stiffness values derived by Barkan (1962) refers to the quasi-static stiffness rather than dynamic or wave propagation. However, as Lysmer (1966) showed, by judicious selection of an appropriate mass and damping term to match the quasi-static stiffness, a reasonable solution to the motion of a foundation subjected to dynamic loading can be found. From the viewpoint of caisson analysis, this is unlikely to pose any problem since the frequency of wave loading on a caisson is often lower than its natural frequency.

On the other hand, Whitman and Richart's (1967) relation for rocking stiffness were simplified from Gorbunov-Passadov and Serebrajanyi 's (1961) relation which is given by:

$$\tan \varphi = \frac{1 - \upsilon^2}{E} K_1 \frac{8M}{L_c^3} \tag{6.19}$$

In which M is the external moment producing rotation of base of foundation, φ is the angle of rotation, K_1 is a factor changing with the ratio of length to width of rectangular footing. Hence, the rocking stiffness k_3 is:

$$k_3 = \frac{M}{\varphi} = \frac{G_s}{1 - \upsilon} B_{base} L_c^2 \frac{L_c}{4K_1 B_{base}} \tag{6.20}$$

Equation (6.20) is valid for small angle of rotation as $\tan \varphi$ is assumed to φ. As can be seen, Whitman and Richart (1967) and Richart (1970) simplified both relations by introducing the given values β_x and β_ψ. When calculating dynamic response of breakwaters, Vink (1997) and Goda (1994) acknowledged that their relations for spring stiffness were

also approximated from Richart et al. (1970). Barkan's (1962), Gorbunov-Passadov and Serebrajanyi 's (1961), and therefore Richart et al. 's (1970) relations apply only to rectangular foundation. However, caisson breakwaters are more commonly constructed in a row and therefore should be represented by a plane strain condition. In the centrifuge model, the caisson was also in a plane strain condition. Vink (1997) appeared to have obtained the approximation by assuming a caisson length-width ratio of $10 : 1$. However, closer examination of Barkan's (1962) formula shows that k_τ does not tend towards constant values as the length:width ratio tends to infinity, as shown in Table 6.1. Hence, to implicitly assume a length:width ratio of $10 : 1$ as approximately representative of plane strain condition is incorrect. Furthermore, Whitman and Richart's (1967) relation suggested that the stiffness increases with the square root of area. In a plane strain case, this is synonymous to implying that the stiffness increases with the square root of the caisson length, rather than the length itself, which is evidently counter-intuitive. The reason why this is so is because part of the effect arising from an increase length is captured by the β coefficients, which, as indicated above, do not tend to constant values as the length-width ratio tends to infinity.

It is proposed herein that a significantly better approach to the caisson problem is to use the solution of a rough strip footing on a finite layer. This approximates the scenario in the centrifuge model much better than a rectangular footing on an infinite half space. The problem of a rough strip, on a finite layer underlain by a rough rigid base, and subject to inclined eccentric loading, has been studied by Milovic et al. (1970) using a quasi-static finite element analysis, as seen in Fig. 6.4. Hence, the spring constant for horizontal motion k_2 was estimated using Milovic et al. (1970) relationship:

$$k_2 = \frac{P}{\rho_x} = \frac{EL_c}{\mu_0} \qquad (6.21)$$

In which P is the average shearing force in the soil at the place of contact with the foundation, ρ_x is the elastic part of the total horizontal sliding of the foundation base under the action of P. While that for rocking was estimated using Milovic et al. (1970):

$$k_3 = \frac{M}{\omega} = \frac{B_{base}^2 EL_c}{2\omega_{cm}} \qquad (6.22)$$

In Equations (6.21) and (6.22), ω_{cm} and μ_0 are the coefficients determined by Poisson's ratio and ratio of sand key thickness over caisson width. Equation (6.22) is valid for small angle of rotation.

6.5   Elastic Displacements of Caisson Breakwater

Equations (6.1) and (6.4) can be solved numerically by means of a direct time integration approach. In this study, the average acceleration method proposed by Newmark (1959) is used. Newmark's (1959) time integration method involves expressing the finite difference form as follow:

$$[M]\{\ddot{u}\} + [C]\{\dot{u}\} + [K]\{u\} = \{F^a\} \qquad (6.23)$$

where

$[M]$ = Structural mass matrix,

$[C]$ = Structural damping matrix,

$[K]$ = Structural stiffness matrix,

$\ddot{u}$ = Nodal acceleration vector,

$\dot{u}$ = Nodal velocity vector,

u = Nodal displacement vector, and

F^a = Applied load vector.

The Newmark method uses finite difference expansions in the time interval Δt, in which it is assumed that:

$$\{\dot{u}_{n+1}\} = \{\dot{u}_n\} + [(1 - \delta)\{\ddot{u}_n\} + \delta\{\ddot{u}_{n+1}\}]\Delta t \qquad (6.24)$$

$$\{u_{n+1}\} = \{u_n\} + \{\dot{u}_n\}\Delta t + \left[(\frac{1}{2} - \alpha)\{\ddot{u}_n\} + \alpha\{\ddot{u}_{n+1}\}\right]\Delta t^2 \qquad (6.25)$$

where

α, δ = Newmark integration parameters,

$\Delta t = t_{n+1} - t_n$,

u_n = Nodal displacement vector at time t_n,

$\dot{u}_n$ = Nodal velocity vector at time t_n,

$\ddot{u}_n$ = Nodal acceleration vector at time t_n,

u_{n+1} = Nodal displacement vector at time t_{n+1},

$\dot{u}_{n+1}$ = Nodal velocity vector at time t_{n+1}, and

$\ddot{u}_{n+1}$ = Nodal acceleration vector at time t_{n+1}.

The solution for the displacement at time t_{n+1} is obtained by first rearranging Equation (6.24) and (6.25), such that:

$$\{\ddot{u}_{n+1}\} = a_0\{\{u_{n+1}\} - \{u_n\}\} - a_2\{\dot{u}_n\} - a_3\{\ddot{u}_n\} \qquad (6.26)$$

$$\{\dot{u}_{n+1}\} = \{\dot{u}_n\} + a_6\{\ddot{u}_n\} + a_7\{\ddot{u}_{n+1}\} \qquad (6.27)$$

where

$a_0 = \frac{1}{\alpha \Delta t^2}$,

$a_1 = \frac{\delta}{\alpha \Delta t}$,

$a_2 = \frac{1}{\alpha \Delta t}$,

$a_3 = \frac{1}{2\alpha} - 1$,

$a_4 = \frac{\delta}{\alpha} - 1$,

$a_5 = \frac{\Delta t}{2} \left\{ \frac{\delta}{\alpha} - 2 \right\}$,

$a_6 = \Delta t (1 - \delta)$, and

$a_7 = \delta \Delta t$.

By substituting $\ddot{u}_{n+1}$ in Equation (6.26) into Equation (6.27), the equations for $\{\ddot{u}_{n+1}\}$ and $\{\dot{u}_{n+1}\}$ can be expressed in terms of the only unknown u_{n+1}. The equations are then combined with Equation (6.23) to form:

$$
\begin{aligned}
\left(a_0 \left[M \right] + a_1 \left[C \right] + \left[K \right] \right) \{ u_{n+1} \} \;=\; & \{ F^a \} + \left[M \right] \{ a_0 \{ u_n \} + a_2 \{ \dot{u}_n \} + a_3 \{ \ddot{u}_n \} \} \\
& + \left[C \right] \{ a_1 \{ u_n \} + a_4 \{ \dot{u}_n \} + a_5 \{ \ddot{u}_n \} \} \quad (6.28)
\end{aligned}
$$

Once a solution is obtained for u_{n+1}, velocity and accelerations are updated as described in Equations (6.26) and (6.27). The above equations are unconditionally stable when $\alpha = \frac{1}{4}$ and $\delta = \frac{1}{2}$, which is called the implicit average acceleration method. Fig. 6.5 shows a comparison between centrifuge and numerical results. The centrifuge test data are taken from a regular, non-reversal wave parcel from test WL4. The parameters used in the numerical model are shown in Table 6.2. As can be seen, during the wave loading stage, a reasonably good agreement was obtained between the magnitude of computed and measured caisson horizontal and tilt responses. However, the computed

response seems to be better correlated with the wave loading than the measured results. This is reasonable since the actual caisson response in the centrifuge tests may be influenced by other factors, such as cyclic degradation, wave actuator-caisson interaction or caisson-soil interaction, which are neglected in the analysis.

6.6   An Analytical Model with Coupled Rocking and Sliding for Permanent Displacement

According to Shimosako et al. (1994) and Ling et al. (1999), sliding of caisson breakwater will initiate when the defined yield wave coefficient for sliding is reached. In the present centrifuge tests, the peak wave coefficient, even for the wave spikes, is typically only about $C_{h,s} = 0.4$ which is much smaller than the yield wave coefficient $C_{hy,s}$ of 0.6. It means that pure sliding may not be initiated by the wave impact in the experiments. Notwithstanding this, however, the centrifuge test data show horizontal movement manifested almost immediately on the application of wave loads. This may be explained by the hypothesis that the horizontal movement is the result of caisson tilt rather than sliding. Furthermore, as mentioned in Chapter 4, Richart et al. (1970) considered that if the horizontal translation of the CG and the rotation of the body about the CG are in phase, superposition of both forces the centre of rotation to lie below the footing base. For these reasons, an analytical model with coupled rocking and horizontal displacement is developed to compute the permanent displacements.

6.6.1   Definition of soil limiting shear stress

The assumed failure mechanism consists of a circular slip plane beneath the caisson base, as shown in Fig. 6.6. In the quasi-static state, the elastic vertical, horizontal and

shear stresses of soil due to caisson weight, $\sigma'_{z,p}$, $\sigma'_{x,p}$ and $\tau'_{xz,p}$ can be obtained using

Poulos's (1974) formulae which give:

$$\sigma'_{z,p} = \frac{p'}{\pi}[\alpha + \sin\alpha\cos(\alpha + 2\delta)] \tag{6.29}$$

$$\sigma'_{x,p} = \frac{p'}{\pi}[\alpha - \sin\alpha\cos(\alpha + 2\delta)] \tag{6.30}$$

$$\tau'_{xz,p} = \frac{p'}{\pi}\sin\alpha\sin(\alpha + 2\delta) \tag{6.31}$$

In which p' is the effective overburden pressure and is obtained by dividing the caisson's

weight by the total caisson base area. This implicitly assumes that the caisson's weight

is uniformly distributed over the base, which is unlikely to be exactly correct. The

caisson is often much stiffer than the soil and there is likely to be concentration of

stress around the toe and heel of the caisson. If the soil is perfectly elastic, the stress

concentration will cause the stresses at the two locations to be infinite, which is clearly

unrealistic. In reality, some yielding will occur at these locations to mitigate the stress

concentration. For this reason, the actual stress distribution is likely to be quite complex

and may not be readily represented by closed-form relations. As such, it is felt that,

while the assumption of uniform distribution may not be entirely correct, it does have

the advantage of simplicity.

The effective vertical and horizontal stresses of soil due to soil self-weight, $\sigma_{z,w'}$

and $\sigma_{x,w'}$ are:

$$\sigma_{z,w'} = \gamma'(D + r\sin x) \tag{6.32}$$

$$\sigma_{x,w'} = K_0\gamma'(D + r\sin x) \tag{6.33}$$

Where γ' is the effective unit weight of submerged soil, p' is the effective pressure of caisson base, α is the angle from chord AB to chord AC, δ is the angle from vertical axis to chord AB and is positive anti-clockwise, r is the radius of the circular slip plane, D is the perpendicular distance from the center of the circular slip plane O to the caisson base, x is the angle from x axis to line OA, and point A is a general point on the circular slip plane. The lateral earth coefficient at rest K_0 is defined as:

$$K_0 = \frac{\nu'}{1 - \nu'} \tag{6.34}$$

In which ν' is the effective Poisson ratio of soil. Superposition of the stresses arising from the caisson's weight and the selfweight of the soil leads to the total vertical, horizontal and shear stresses of soil, σ_z', σ_x' and τ_{xz}' being given by

$$\sigma_z' = \sigma_{z,p}' + \sigma_{z,w'}' \tag{6.35}$$

$$\sigma_x' = \sigma_{x,p}' + \sigma_{x,w'}' \tag{6.36}$$

$$\tau_{xz}' = \tau_{xz,p}' \tag{6.37}$$

As indicated in Fig. 6.6, the slip zone is limited to the region within the circular slip plane underneath the caisson base. From the triangle ABC, it can be deduced that:

$$\frac{B_{base}}{\sin\alpha} = \frac{2r\cos(\beta + \delta)}{\sin(\frac{\pi}{2} - \delta - \alpha)} \tag{6.38}$$

$$\delta = \frac{\pi}{4} - \frac{\beta}{2} - \frac{x}{2} \tag{6.39}$$

$$\beta = \arctan(\frac{S}{D}) \tag{6.40}$$

$$r = \sqrt{S^2 + D^2} \tag{6.41}$$

in which β is the angle subtended by lines OB and OF, S is the length of line segment BF, $x \in (\beta - \frac{\pi}{2}, \frac{3\pi}{2} - \beta)$ and B_{base}=22 m.

The stress state at point A in Fig. 6.6 can be represented by Fig. 6.7. In Fig . 6.7, A represents the pole of Mohr Circle and A' represents the stress on the tangent to the slip plane at location A in Fig. 6.6. Thus in Fig. 6.7, τ_0 and σ_0' are the effective shear and normal stresses acting on the potential slip plane at location A, under the action of caisson's weight and the self-weight of soil.

In this study, the sand is assumed to be undrained for the duration of wave spike. During undrained loading, the effective stress σ_0' is constant while the shear stress τ increases from its original value until it reaches a value determined by the Mohr-Coulomb failure envelope. Thus, the maximum shear stress increment τ_{lim} which the wave loading can impose onto the potential slip surface is given by:

$$\tau_{lim} = \sigma_0' tan\phi' - \tau_0 \tag{6.42}$$

In which ϕ' is the angle of friction and c', the effective cohesion, is assumed to be zero. The convention for normal and shear stresses assumed herein is compression and counter-clockwise positive.

The other equations relating to the properties of a Mohr's Circle are as follows:

Radius R of the Mohr's circle is given by

$$R = \sqrt{(\frac{\sigma'_z - \sigma'_x}{2})^2 + \tau_{xz}^2} \tag{6.43}$$

The effective stress σ'_r at the centre of the Mohr's Circle is given by

$$\sigma'_r = \frac{\sigma'_x + \sigma'_z}{2} \tag{6.44}$$

The effective stress σ'_0 acting on the potential slip surface at location A is given by

$$\sigma'_0 = \sigma'_r + R\sin\theta \tag{6.45}$$

The shear stress τ_0 acting on the potential slip surface at location A is given by

$$\tau_0 = R\cos\theta \tag{6.46}$$

$$\theta = \frac{\pi}{2} + \kappa - 2\eta \tag{6.47}$$

$$\sin\kappa = \frac{\tau_{xz}}{R} \tag{6.48}$$

The angle of inclination η that the slip plane made to the horizon at location A is given by

$$\eta = \frac{\pi}{2} - x \tag{6.49}$$

The maximum shear stress T which the wave loading can impose onto the potential slip surface is given by

$$T = \int\limits_{\beta - \frac{\pi}{2}}^{\frac{3\pi}{2} - \beta} \tau_{\lim(x)} dx \tag{6.50}$$

Since τ_0 and σ_0 vary along the slip surface as well as $\tau_{\lim}$, Simpson's rule is used

to evaluate the integral (Penny and Lindfield, 2000). Fig. 6.8 shows the value of T at

different combinations of S and D. As expected, T increases with increase in S and D.

6.6.2 Selection of S and D for constrained optimization of the slip surface

The centrifuge test data show that the centre of rotation for the tilting mechanism appears to fall on the landward side of the centreline. After the non-reversal loading tests, the soil outside the loading area is found to be relatively uninvolved and there is practically no movement of the soil on the sides of the caisson. This would imply that the slip soil mass emerges at the ground surface beneath the caisson base. This means that the maximum S is given by

$$S_{\max} = \frac{B_{base}}{2} = 11m \tag{6.51}$$

The depth of the container in centrifuge tests is 15 m, and kinematic consideration

dictates that one end of the slip surface should pass through the landward edge of the

caisson. This means that

$$D + r = D + \sqrt{D^2 + S^2} \le 15m \tag{6.52}$$

Following Equation (6.52), the maximum value of D is reached with S = 0, i.e.

$$D_{\max} = 7.5m \tag{6.53}$$

Hence $0 \leq S \leq 11m$ and $0 \leq D \leq 7.5m$.

Equation (6.52) indicates that the maximum value of S is reached when $D = 0$ and

its value is $S_{max} = 15$ m, which is larger than that indicated by centrifuge test data. The

geometry and nomenclature of kinematical rotation and slide of soil mass are shown in

Fig. 6.9. At limit equilibrium, the moment equilibrium equation of the caisson is given

by,

$$F_{lim}(A + D) - W'(\frac{B_{base}}{2} - S) = \int_s \tau_{\lim} r ds = \int_\theta \tau_{\lim} r^2 L_c d\theta \qquad (6.54)$$

in which F_{lim} is the horizontal wave force which just overcomes the self-weight of

caisson and the shear resistance along the prescribed slip surface, and W' is the effective

caisson weight. The most critical situation is the combination of D and S, which results

in the lowest value of F_{lim}.

Thus,

$$F_{lim} = \frac{1}{A + D}[\int_\theta \tau_{lim} r^2 L_c d\theta + W'(\frac{B_{base}}{2} - S)] \qquad (6.55)$$

The value of F_{lim} corresponds to different combinations of S and D with an increasing

step of 0.1 respectively. Fig. 6.10 shows the variation of F_{lim} with S and D. It is evident

that when S and D are large, F_{lim} is also large owing to the large shear resistance along

the long slip surface. When S and D are small, F_{lim} is not at a minimum because

the submerged weight of the caisson is fully mobilized to resist the wave force. The

minimum value of F_{lim}, i.e. $F_{lim,min}$, is reached when $S = 4.7m$ and $D = 1.2m$. For

this set of S and D, the parameters for calculating the maximum shear stress T are

shown in Table 6.3.

6.6.3 Permanent tilt of caisson subjected to a single wave

When the wave force exceeds $F_{lim,min}$, the equation of motion of the caisson can be written as

$$\theta_{tot}\ddot{\psi} = F(A + D) - \int_{\beta - \frac{\pi}{2}}^{\frac{3\pi}{2} - \beta} \tau_{\lim} r^2 L_c d\theta - W' \frac{\frac{H}{2} + D}{\cos \zeta} \sin(\zeta - \psi) \tag{6.56}$$

in which θ_{tot} is the total caisson mass moment of inertia, and ψ is the tilt angle.

or

$$\ddot{\psi} = C_m - C_w \sin(\zeta - \psi) \tag{6.57}$$

in which

$$C_m = \frac{1}{\theta_{tot}} \left[F(A + D) - \int_{\beta - \frac{\pi}{2}}^{\frac{3\pi}{2} - \beta} \tau_{\lim} r^2 L_c d\theta \right] \tag{6.58}$$

$$C_w = \frac{W'}{\theta_{tot} \cos \zeta} \left(\frac{H}{2} + D \right) \tag{6.59}$$

and

$$\zeta = \arctan(\frac{\frac{B_{base}/2 - S}{1 + 2D/H}}{H/2}) \tag{6.60}$$

When a caisson tilts by an amount less than ζ, the caisson does not failure. However, if a caisson tilts by an amount equal to or larger than ζ, the center of gravity of caisson aligns outside the point of rotation, thereby rendering it unstable. Therefore, the second scenario is not necessary for the present study. In arriving at Equation (6.57), the caisson is considered as a rigid body with its damping and stiffness properties neglected.

Two methods were used to solve Equation (6.57). One is through an explicit approach while another is resorted to numerical method after doing an assumption.

Method 1

Equation (6.57) can be time-integrated using an explicit approach by writing

$$\ddot{\psi}_t = C_{m,t} - C_w \sin(\zeta - \psi_t) \tag{6.61}$$

in which the subscript t denotes values of variables at time t. The tilt $\psi_{t+\Delta t}$ can then be evaluated using the relationship:

$$\ddot{\psi}_t = \frac{\psi_{t+\Delta t} - 2\psi_t + \psi_{t-\Delta t}}{\Delta t^2} \tag{6.62}$$

Once combined with Equation (6.57), Equation 6.62) can be written as

$$\psi_{t+\Delta t} = 2\psi_t - \psi_{t-\Delta t} + \Delta t^2 [C_{m,t} - C_w \sin(\zeta - \psi_t)] \tag{6.63}$$

Which allows $\psi_{t+\Delta t}$ to be evaluated.

Method 2

Equation (6.57) can also be re-written for $t + \Delta t$ as

$$\ddot{\psi}_{t+\Delta t} = C_{m,t+\Delta t} - C_w \sin \zeta \cos \psi_{t+\Delta t} + C_w \cos \zeta \sin \psi_{t+\Delta t} \tag{6.64}$$

If $\psi_{t+\Delta t}$ is small, then Equation (6.64) can be approximated by

$$\ddot{\psi}_{t+\Delta t} = C_{m,t+\Delta t} - C_w \sin \zeta + C_w \cos \zeta \times \psi_{t+\Delta t} \tag{6.65}$$

Since $C_w sin\zeta$ is constant, Equation (6.65) now has the form of a standard equation of motion and can be integrated by a variety of time-integration methods. In this study, Equation (6.65) is integrated using the Runge-Kutta fourth-order method, as this has a high convergence rate. Even so, it is found that the centrifuge time step is too coarse for the numerical calculation, as the sample rate of measurement is 300 Hz per instrument. Hence, a polynomial fit of C_m is used to interpolate between successive time steps and provide sub-steps for the numerical calculation, as seen in Fig. 6.11.

Assume that f(t,y) is continuous and consider the initial value problem:

$$y' = f(t, y) \tag{6.66}$$

In which $y(a) = t_0 = \alpha$, over the interval $a \le t \le b$.

The Runge-Kutta method uses the formulas $t_{k+1} = t_k + h$, and

$$y_{j+1} = y_j + \frac{1}{6}(k_1 + 2k_2 + 2k_3 + k_4) \tag{6.67}$$

$$k_1 = hf(t_j, y_j) \tag{6.68}$$

$$k_2 = hf(t_j + \frac{h}{2}, y_j + \frac{k_1}{2}) \tag{6.69}$$

$$k_3 = hf(t_j + \frac{h}{2}, y_j + \frac{k_2}{2}) \tag{6.70}$$

$$k_4 = hf(t_j + h, y_j + k_3) \tag{6.71}$$

6.6.4   Validation of analytical solution with centrifuge tests

The normalized wave coefficient and the resultant plastic tilt angles using the above methods are shown in Fig. 6.12. It is found that the velocity and tilt angle calculated by the explicit approach are a little smaller than those calculated by the numerical method, which is due to the approximation made in the numerical method. Since the numerical method will always give a conservative tilt angle, this method is used in the following calculations. For this particular wave spike occurring in test WL4, the horizontal wave force increases to a peak value, leading to the positive yield coefficient. It has a short duration, for about $1s$ in prototype terms, during which the permanent tilt occurs. The velocity of the caisson also arrives at a peak value and then reduces to zero. The permanent tilt angle per wave cycle is calculated as 5.2×10^{-4} rad for this particular example.

Fig. 6.13 compares the measured tilt from the centrifuge test and the computed tilt. The computation superimposes both the elastic and plastic caisson responses. The horizontal movement in Fig. 6.13 refers to the displacement at the location of displacement transducer H1. As can be seen, the tilt and horizontal displacement are well predicted by the analytical model, especially the build-up of the permanent tilt. Both the centrifuge data and computed tilt shows that, after the caisson tilt reaches a peak value, it rebounds a little because of the elastic displacement. Oumeraci (1995) noted that under the impact and cyclic wave loads, the seabed soil may experience large unacceptable permanent displacements due to two possible reasons: one is the residual pore pressures developed in the subsoil and another is the exceedance of admissible strength. The analysis does not take into account pore pressure generation. The fact that its results agree

reasonably well with the measured data is further support of the earlier suggestion that, in wave spikes events, exceedence of shear resistance is the mechanism causing the observed permanent deformation.

Fig. 6.14 shows that tilting of the caisson will also lead to horizontal movement H1 at the horizontal LVDT location, which is given by

$$H1 = (A + D)\psi \tag{6.72}$$

or

$$D = H1/\psi - A \tag{6.73}$$

where ψ is the tilt angle. Equation (6.72) appears to ignore the possibility of a pure horizontal translational mode of displacement of the caisson. However, this is not entirely so because if the caisson merely displaces horizontally without tilting, then D = ∞. In a situation where there are both horizontal displacement and tilting, then it is more difficult to isolate the individual components. Notwithstanding this, the value of D calculated from Equation (6.73) represents an effective value of D encompassing both horizontal displacement and tilting. It should also be noted that horizontal displacement is used herein in preference to the term 'sliding', since the latter may be interpreted to imply a relative motion at the caisson-sandbed interface, which is difficult to verify.

From Equation (6.73), D can be readily obtained from centrifuge test as $H1$, ψ and A are already known. Fig. 6.15 shows the plot of horizontal movement versus tilt angle during the same time series of 15350-15380 s in centrifuge. The plot shows that the gradient of horizontal movement and tilt angle, which is equal to $A + D$, increases as the tilt angle increases, thereby indicating a lowering of the equivalent centre of rotation

as the wave load increases to the peak and thereafter. It is about 22.38 m just after the peak of the wave spike. The vertical offset A from the LVDT H1 to the caisson base is 21 m. Thus, D is 1.38 m in centrifuge test. In other words, just after the wave peak has passed, the equivalent centre of rotation is located about 1.4 m beneath the caisson base. Fig. 6.15 also reveals that in the early stages of wave loading, the equivalent centre of rotation is located above the caisson base. This has been discussed in Chapter 4 and is attributable to the added inertial from water on both sides of the caisson. From the analytical model, the minimum wave force needed to initiate soil slippage is reached when S = 4.7 m and D = 1.2 m. Thus, the value of D computed by the analytical model with coupled rocking and sliding is in agreement with that from the centrifuge data after the wave peak has passed, but not before. This is probably because the analytical model does not account for the added inertial in a sufficiently accurate manner.

Fig. 6.16 compares the horizontal caisson displacement and tilt movements in the same centrifuge test between 80870-80900s after commencement of wave loading. As can be seen, reasonably good agreement was obtained between computed and measured tilt angle. However, the computed results appear to show a larger elastic recovery of horizontal displacement than the centrifuge data would suggest. The reason for this is not clear but this may be due to changes in elastic properties in the sand bed during the course of the wave spike.

Fig. 6.17 compares the computed results with those from test WL7 with RD = 80%. In this test, wave spike occurred between 51465-51510s after commencement of wave loading, but its peak load is not large enough to produce the plastic displacements. This implies that the induced displacements are purely elastic. As can be seen, better

agreement was found in the magnitude of the measured and calculated displacements.

6.6.5 Permanent displacement of caisson breakwater subjected to continuous wave loading

Figs. 6.18 and 6.19 show the elastic and plastic displacements when the caisson is subjected to a wave train comprising eight wave cycles. As Fig. 6.19 shows, plastic displacements accumulate in a stepwise fashion with the passing of each large wave peak. This is consistent with the observation in the storm waves of Shin-Nagasaki (Sekiguchi et al., 1992) wherein caissons were tilted at various angles after the storm. Current practice in caisson design often entails only a limit equilibrium check on the possibility of overturning of the caisson (e.g. PHRI, 1991). The results above indicate that the real picture is often not a clear case of overturning or no overturning, but rather the cumulative tilt which the caisson will incur in an extreme storm condition. Thus, in the design of caisson foundations, the cumulative tilt angle may need to be considered through a proper dynamic analysis. It is found in Fig. 6.20 that the magnitude of elastic displacements is negligible when compared with that of plastic ones. Usually there are some hundreds of impacts during the whole storm. Hence, a single increment plastic horizontal displacement, say of the order of centimetres, in a single wave cycles, may accumulate to give a total displacement of several meters over a large number of cycle.

6.7   Case Study

In this section, the proposed analytical method is assessed by comparing its computed results with the observations from a field case (Sekiguchi, 1992). On August 1987, a large typhoon hit the Southern part of Japan, causing almost complete failure of a 1090-

m long caisson breakwater. Yamaguchi et al. (1989) estimated the wave conditions by using two kinds of shallow water wave prediction models based on the radiative transfer equation. The significant wave height $H_{1/3}$ is found to be 8.9 m and the wave period $T_{1/3}$ is 13.2 s. The cross-section of caisson breakwater through Stretch C is shown in Fig. 2.8 (b). The caisson breakwater is seated on a rubble mound and the soft silty sediments underneath the seabed were treated with the sand compaction method. Since the caisson foundation is made up of composite ground, the accurate estimation of the angle of friction is more difficult than the conditions in the centrifuge tests. Moreover, very little information was available on the material making up the original silty sediments and the sand compaction ground. The estimated critical state angle of shearing resistance φ', is given by BS8002:1994 as

$$\varphi' = 30 + A + B \tag{6.74}$$

A = angularity of the particles,

B = grading of the sand/gravel.

For the base friction angle δ, BS8002:1994 suggests

a) $\delta = \varphi'$, for a rough base having a texture coarser than that of the median particle size of the soil;

b) $\delta = 20°$, for a smooth base with a texture finer than that of the median particle size of the soil.

In view of this, a range of "equivalent" friction angles ranging from $30°$ to $36°$ has been attempted. This range has been established to be a reasonable range for the angle of friction of the composite ground. The corresponding range for the angle of friction

at the caisson-soil interface δ is taken to be from $22°$ to $28°$. The horizontal wave force and uplift force acting on the caisson are determined from the Goda formulae and the extended Goda formulae developed by Takahashi et al. (1994b). In this case, the horizontal movement of caisson is not only caused by tilting, but also sliding which is determined using Ling's analytical model (Ling et al, 1999).

The tilt angles of a total of 14 caissons at the Shin-Nagasaki Fishing Port are plotted against the lateral displacements at the base in Fig. 6.21. There is a positive correlation between the tilt and the lateral displacement, Sekiguchi (1992) considered it to be a manifestation of cyclic plasticity of the rubble mound. According to Yamaguchi et al. (1989), the storm lasted for about 1 hour, which means at most 300 wave cycles were applied on the caisson, if the wave period is 13.2 s. However, the actual number of wave cycles that have sufficient wave force to induce plastic displacement of caisson breakwater is more difficult to ascertain. For this reason, the relationship between tilt angle and lateral displacement may be a better way to compare the field data with the analytical result. Several combinations of δ and φ' were used to predict the caisson displacement per cycle. Making use of the final tilt and lateral displacements measured in the field, the rough number of wave cycles may be estimated. It is found in Fig. 6.21 that the combination of $\delta = 28°$ and $\varphi' = 35°$ may lead to 95 wave cycles, while $\delta = 26°$ and $\varphi' = 30°$ lead to 30 wave cycles. Both combinations give a better prediction of the gradient of tilt angle and lateral displacement. Since the critical state angle of shearing resistance of rubble mound φ' is normally larger than $30°$, the first combination is believed to reflect the field situation more accurately.

6.8 Parametric Studies

Fig. 6.22 illustrates the parameters involved in assessing the cumulative tilt of cais-
son breakwater using the above method. The relevant input parameters for the design
approach are annotated in Fig. 6.23. The height of the rubble mound H_r is set as 8
m for all cases. For different caisson widths with the same water depth, the effective
pressure underneath the caisson base was assumed to be the same. The individual runs
are shown in Appendix B. There are nine independent factors which determine the tilt
angle for one wave cycle ψ:

$$\psi = f(T, H_w, d, B, H, L_c, W', \gamma'_w, \varphi') \tag{6.75}$$

In which T and H_w are the wave period and wave height, respectively; d is the water
depth; B, H, L_c and W' are the caisson width, height, length and effective weight,
respectively; and γ'_w and φ' are effective unit weight of submerged soil and angle of
shearing resistance of rubble mound, respectively.

Based on dimensionless analysis, four sets of non-dimensional π groups are ob-
tained and written as:

$$\pi_1 = \left(\frac{d + H_w}{H}\right)^{0.16} \tag{6.76}$$

$$\pi_2 = \frac{H_w \gamma_w (d + H_w)}{W'/L} \tag{6.77}$$

$$\pi_3 = (\frac{L_0}{B})^{0.4} \tag{6.78}$$

$$\pi_4 = (\varphi')^{-0.1} \tag{6.79}$$

Where the wave length in deep water L_0 is:

$$L_0 = \frac{gT^2}{2\pi} \tag{6.80}$$

In which g is the gravity acceleration. If the original choice of variables contained all the relevant physical quantities, the solution for the tilt angle has the following form:

$$\psi = f\left(\left(\frac{d+H_w}{H}\right)^{0.16}, \frac{H_w \gamma_w (d+H_w)}{W'/L}, \left(\frac{L_0}{B}\right)^{0.4}, (\varphi')^{-0.1}\right) \tag{6.81}$$

6.8.1   Influence of wave height and water depth in front of caisson

The range of parameters studied for the influence of wave height H_w and water depth d is summarized in Table 6.4 based on a fixed value of wave period of $15s$. Fig. 6.24 shows the effects of wave height, caisson width, angle of shearing resistance of rubble mound and water depth (to rubble mound level) on the tilt angle increment per wave cycle. The X axis has been normalized as $X = \left(\frac{d+H_w}{H}\right)^{0.16} \frac{H_w \gamma_w (d+H_w)}{W'/L} \left(\frac{L_0}{B}\right)^{0.4} (\varphi')^{-0.1}$. It is evident from Fig. 6.24 that the tilt angle increment per wave cycle increases with wave height as well as the water depth in front of caisson. This is not surprising since increases in both the wave height and water depths have destabilizing effects on the caisson. Moreover, there is a limiting wave height below which no permanent tilt is incurred. Not surprisingly, this limiting wave height increases as the water depth decreases. Above the limit wave height, permanent tilt angle increases rapidly with wave height. It should be noted that this relationship depends strongly on the weight of cais-

son. The influence of water depth d may be explained in terms of the increasing ratio of effective caisson weight over inertia moment of mass with decreasing water depth. The parametric study shows that over a range of angle of shear resistance of rubble mound φ' between $30°$ to $38°$, variations of φ' was found to have relatively insignificant influence on the permanent tilt angle increment compared to wave height H_w.

6.8.2   Influence of wave period and water depth in front of caisson

Table 6.5 shows the range of parameters studied for the influence of wave period T and water depth d with a fixed wave height of 10 m. Fig. 6.25 illustrates the interaction among caisson width, angle of shearing resistance of rubble mound, water depth (to rubble mound level) and the permanent tilt angle for one wave cycle. The X axis is again normalized as $X = \left(\frac{d+H_w}{H}\right)^{0.16}\frac{H_w\gamma_w(d+H_w)}{W'/L}\left(\frac{L_0}{B}\right)^{0.4}(\varphi')^{-0.1}$. As Fig. 6.25 shows, the permanent tilt angle per wave cycle increases exponentially with X axis magnitude. This is because the higher wave period with a fixed wave height will lead to a longer wave length and hence larger impulsive wave force and longer duration of loading. There is a limiting wave period below which no permanent tilt is incurred. The change of critical state angle of shearing resistance of rubble mound φ' is again found to have relatively insignificant influence on the tilt angle.

6.8.3   Summary for parametric studies

Combining Figs.6.24 and 6.25, the chart of tilt angle ψ for one wave shows a clear exponential increase, as indicated in Fig. 6.26, in which a_0 and a_1 are constants. The relationship can hence be expressed as follow:

$$\psi = a_0 + a_1 f\left(\left(\frac{d + H_w}{H}\right)^{0.16} \frac{H_w \gamma_w (d + H_w)}{W'/L} \left(\frac{L_0}{B}\right)^{0.4} (\varphi')^{-0.1}\right) \qquad (6.82)$$

Moreover, there exists a lower bound ψ_1 and a upper bound line ψ_2 of the tilt angle as follows:

$$\psi_1 = 2.02801 \times 10^{-9} e^{\frac{x}{0.13917}} \qquad (6.83)$$

$$\psi_2 = -0.00252 + 5.58446 \times 10^{-5} e^{\frac{x}{0.39811}} \qquad (6.84)$$

$$x = \left(\frac{d + H_w}{H}\right)^{0.16} \frac{H_w \gamma_w (d + H_w)}{W'/L} \left(\frac{L_0}{B}\right)^{0.4} (\varphi')^{-0.1} \qquad (6.85)$$

If the calculated ψ_1 or ψ_2 are less than zero, then the tilt angle is zero which means the caisson is stable enough to be against overturning. If the calculated ψ_1 or ψ_2 are larger than 1.57 which is equivalent to the tilt angle of $90°$, it means that the caisson has been already overturned. Thus Equations (6.83) and (6.84) can be used to estimate the range of caisson tilt angle for given wave parameters.

Table 6.1 Values of the coefficient k_τ [Equation 6.18] for varying values of the Poisson ratio υ and of the ratio α of the length to the width of a foundation

υ	α				
	1	2	10	100	1000
0.3	0.870143	0.870364	1.07368	1.998176	4.456933
0.4	0.792452	0.783463	0.948638	1.744316	3.869817
0.5	0.704402	0.687379	0.81565	1.480915	3.267257

Table 6.2 Structure and foundation parameters when calculating caisson elastic movements

	$m_{tot,ver}$ (kg)	$m_{tot,hor}$ (kg)	θ_{tot} (kgm^2)	k_1 (N/m)	k_2 (N/m)	k_3 (Nm/rad)
1. Infilling stage	1.15×10^7	-	-	1.71×10^9	-	-
2. Wave loading stage	-	2.808×10^7	6.6×10^9	-	3.78×10^9	5.86×10^{11}

Table 6.3 Calculated shear stress when S=4.7m and D=1.2m with $\phi' = 34°$

	S=4.7m, D=1.2m, $\phi' = 34°$								
x (rad)	-0.2500	0.2052	0.6604	1.1156	1.5708	2.0260	2.4812	2.9364	3.3916
η (rad)	1.8208	1.3656	0.9104	0.4552	0	-0.4552	-0.9104	-1.3656	-1.8208
δ (rad)	0.2500	0.0224	-0.2052	-0.4328	-0.6604	-0.8880	-1.1156	-1.3432	-1.5708
α (rad)	1.3200	1.4487	1.5801	1.7243	1.8938	2.1066	2.3846	2.7400	3.1402
θ (rad)	-0.7491	0.2110	0.7239	1.3229	1.9952	2.7241	3.5059	4.3427	5.2110
σ_x' (kPa)	69.6196	69.9548	69.6964	70.2081	72.9980	79.8031	92.7500	113.6171	140.1758
σ_z' (kPa)	48.2818	87.8181	125.5830	155.8554	174.6181	180.4110	174.3833	159.4931	140.3000
τ_{xz} (kPa)	41.9258	44.1939	41.1125	33.4072	22.9606	12.4648	4.6858	0.9354	-0.0001
$\tau_{lim}(x)$ (kPa)	-11.7892	15.4921	50.8196	98.4293	140.7420	149.3063	118.6075	85.9635	94.5252
Output	T=$\int \tau_{lim}(x)d\theta$ =318.611184318 (kPa)								

Table 6.4 Range of parameters for the influence of wave height and water depth

no.	wave height (m)	wave period (s)	Caisson width (m)	water depth in front of caisson (m)	critical state angle of friction of rubble mound ϕ'
1	10	15	14	14	30°
2	12	15	18	18	34°
3	14	15	22	22	38°

Table 6.5 Range of parameters for the influence of wave period and water depth

no.	wave height (m)	wave period (s)	caisson width (m)	water depth in front of caisson (m)	critical state angle of friction of rubble mound ϕ'
1	10	13	14	14	30°
2	10	15	18	18	34°
3	10	17	22	22	38°
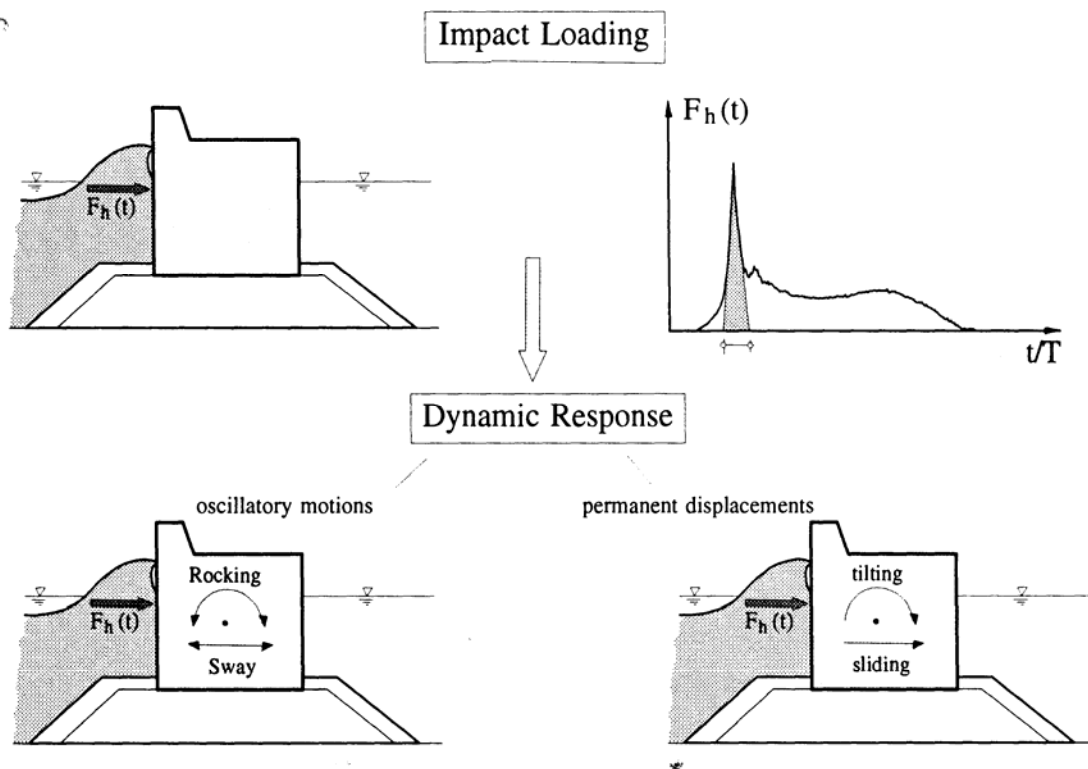
Fig. 6.1 Effect of breaking wave impact on structure response
(after Oumeraci et. al. 2001)
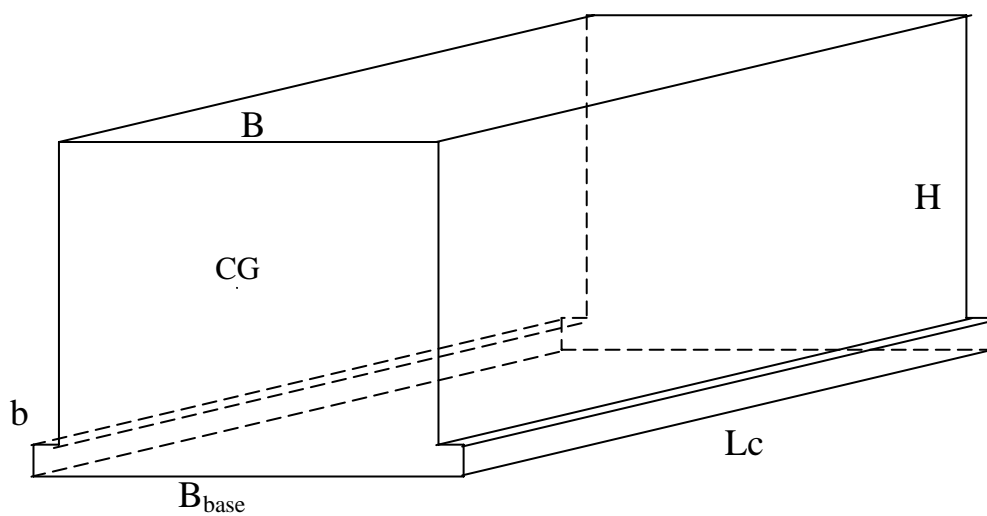
Fig. 6.2 Three-dimensional view of caisson breakwater
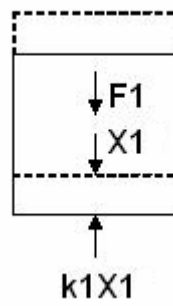
(a) Infilling stage
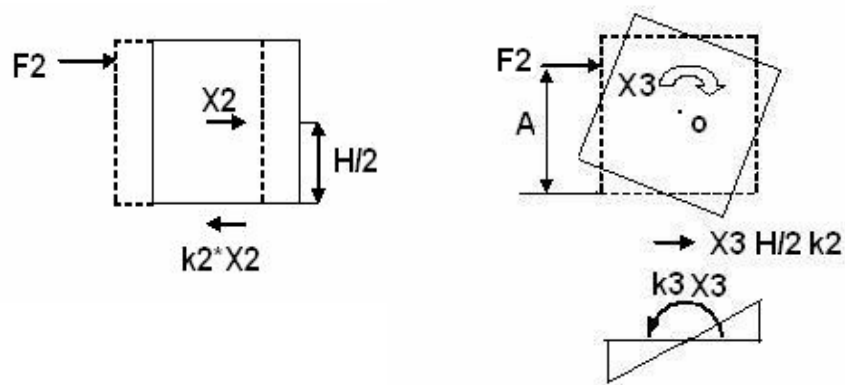
(b) Wave loading stage
Fig. 6.3 Unit displacement and forces for derivation of mass-spring model
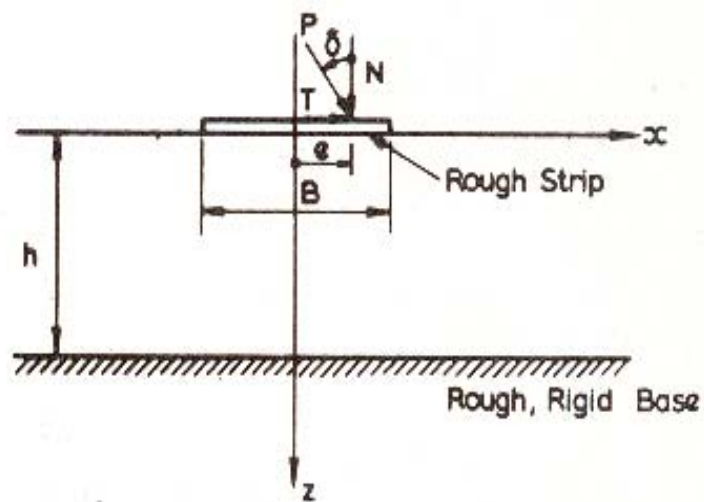
Fig. 6.4 Infinite strip on finite layer (after Poulos and Davis, 1974)
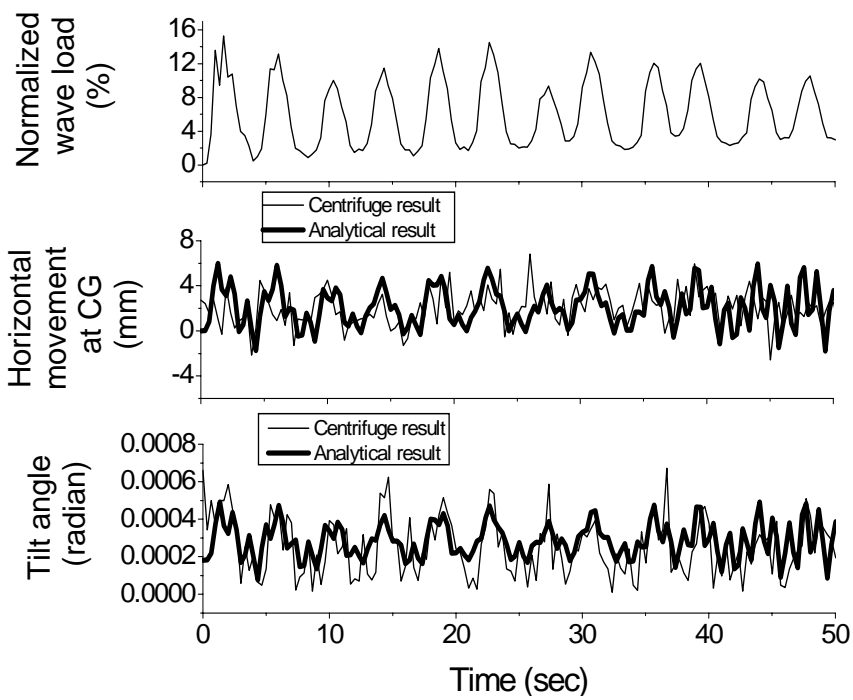
Fig. 6.5 Simulation of elastic behavior of caisson breakwater using mass-spring model
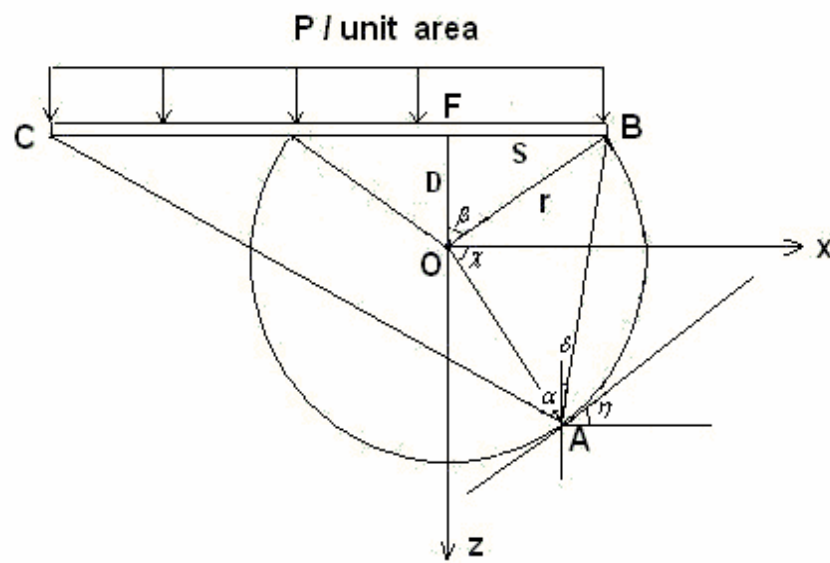
Fig. 6.6 Uniform vertical loading on the soil mass
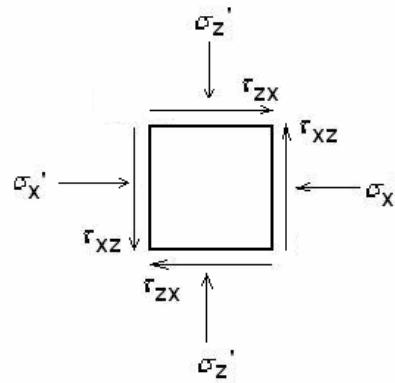
(a) Soil element
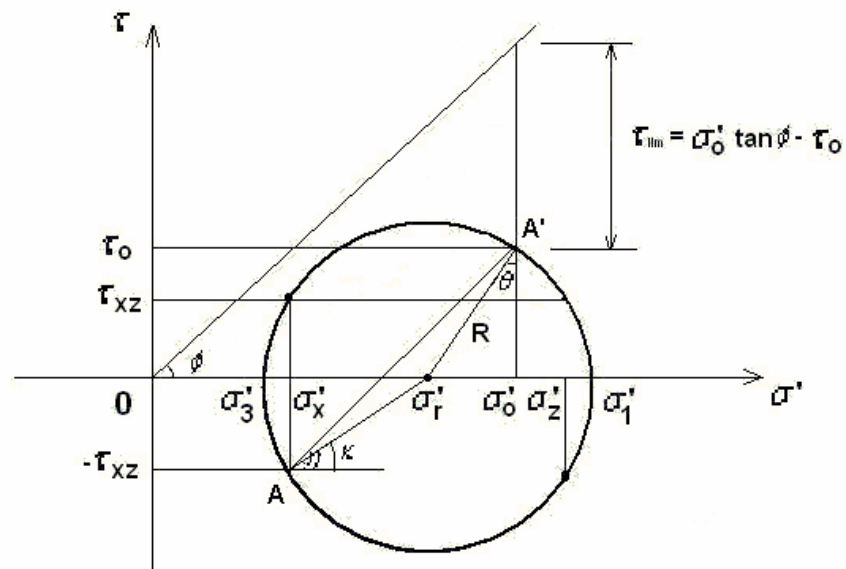
(b) Limiting shear stress τ_{lim}

Fig. 6.7 Definition of limiting shear stress τ_{lim} in Mohr-Coulomb model for plane

strain condition
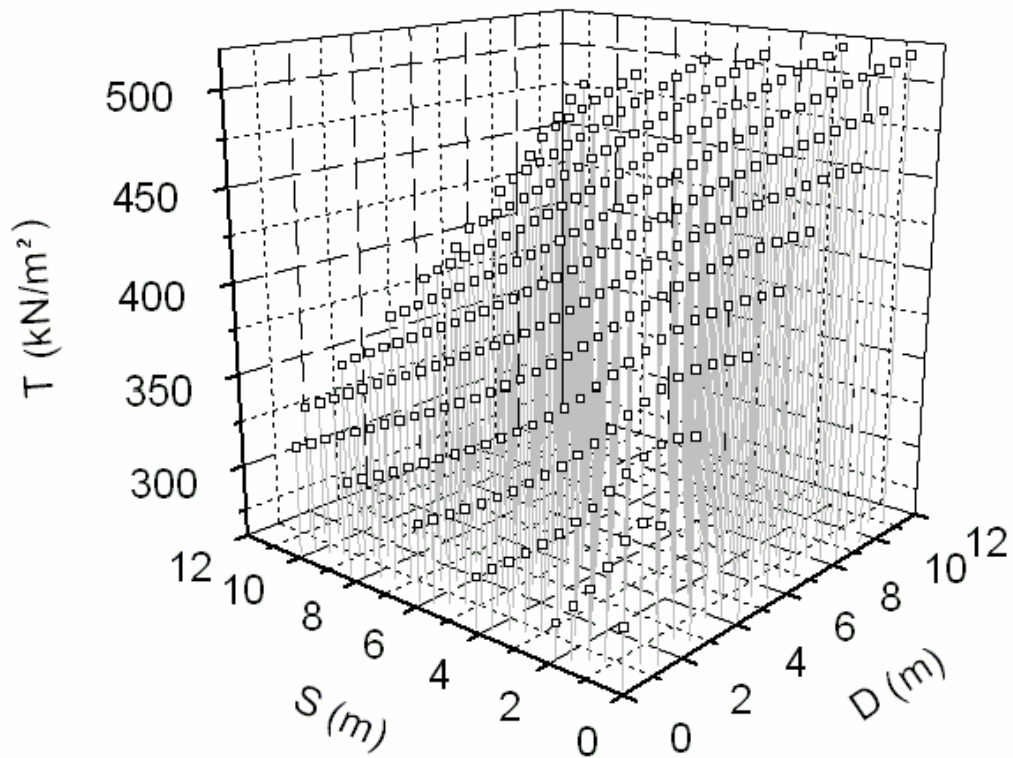
Fig. 6.8 Shear force using soil model of circular arc
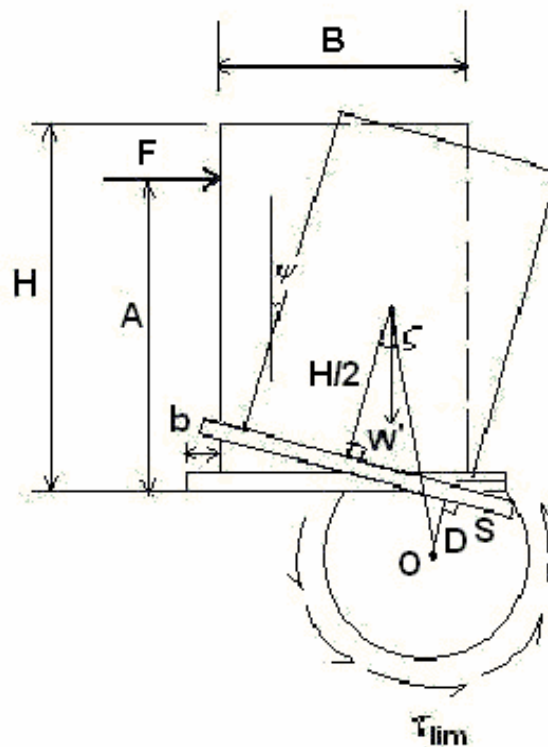
Fig. 6.9 Kinematical rotation and slide of soil mass
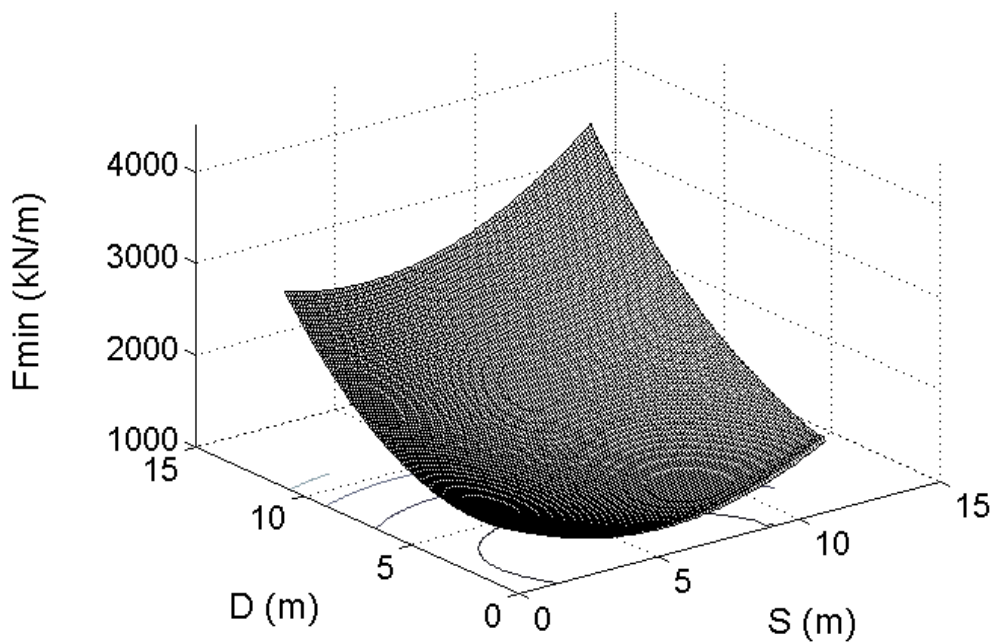
Fig. 6.10 Minimum wave force to initiate soil slippage (S=4.7m, D=1.2m)
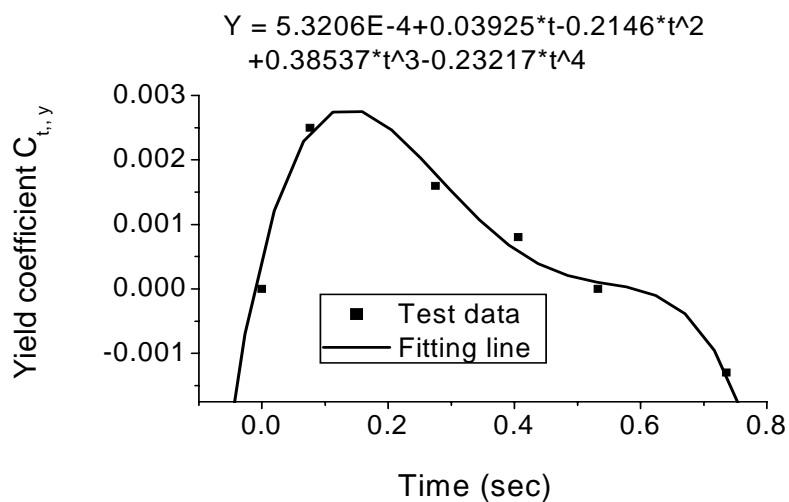
Fig. 6.11 Polynomial fit of yield coefficient
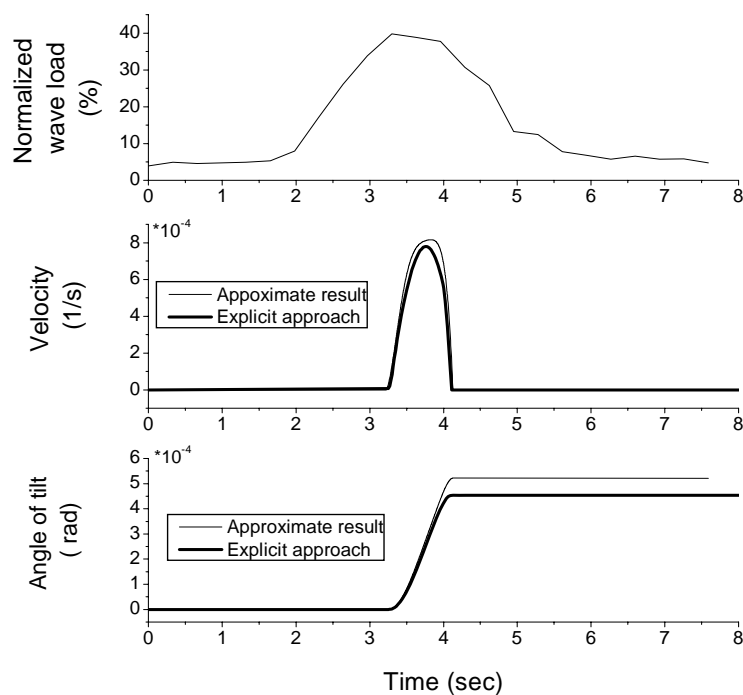
Fig. 6.12 Calculated permanent tilt angle
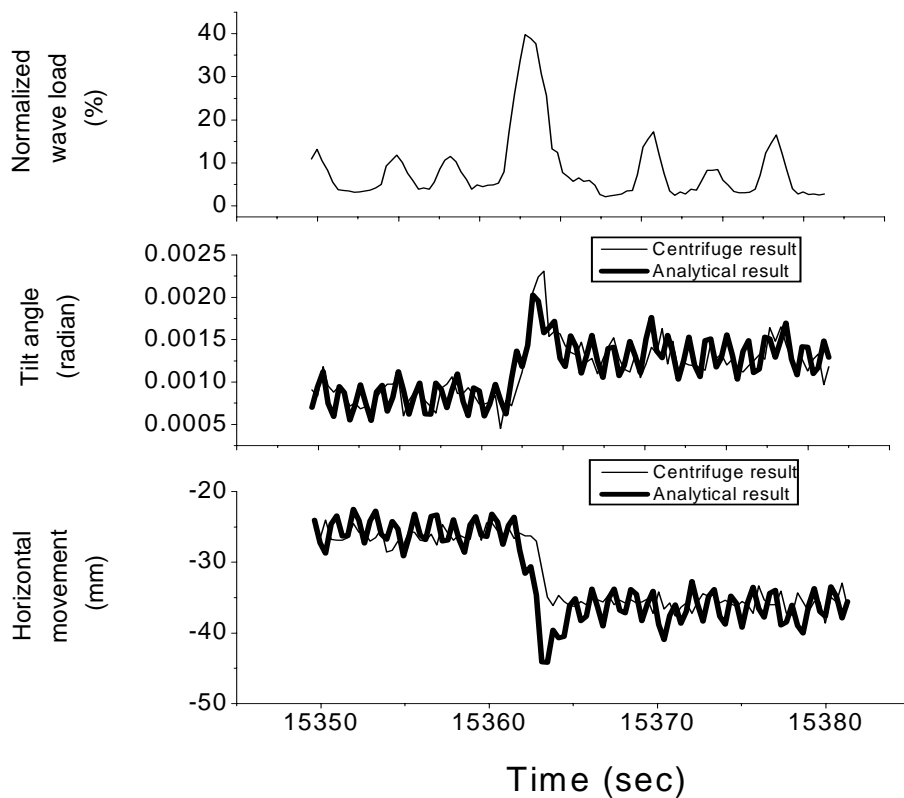
Fig. 6.13 Comparisons of total movements of caisson breakwater subject to wave loading in centrifuge and analytical model
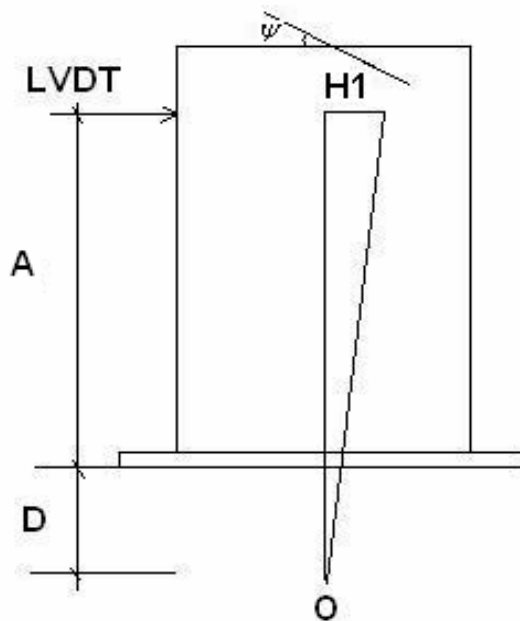
Fig. 6.14 Tilt mechanism of caisson breakwater
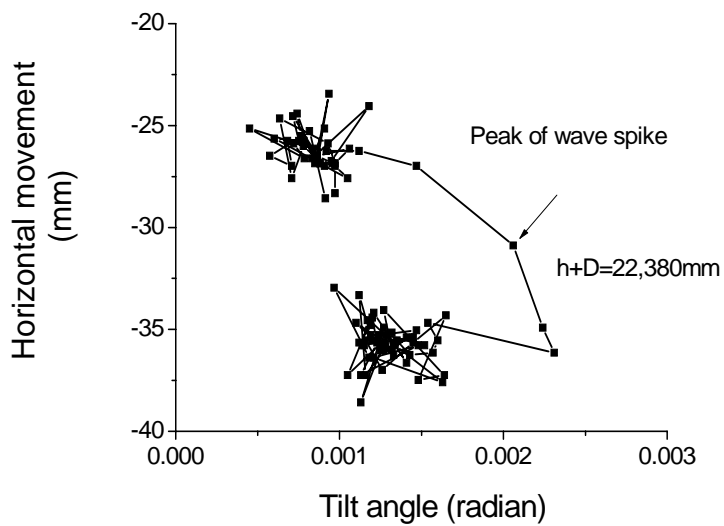
Fig. 6.15 Horizontal movement versus tilt angle during time series of 15350-15380
second in centrifuge test WL4
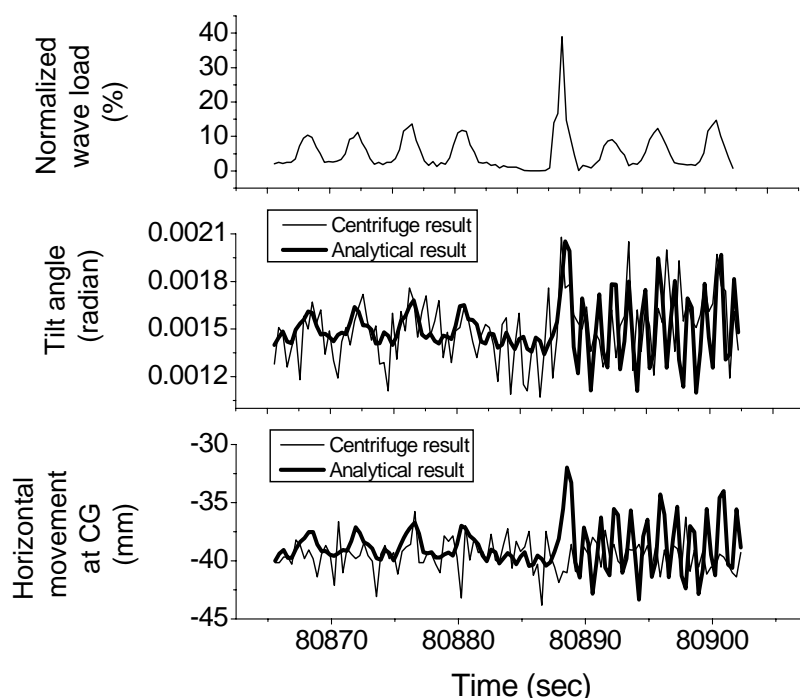
Fig. 6.16 Comparisons of measured and analytical total movements of caisson breakwater subject to wave loading during 80870-80900 s in WL4 (RD=72%)
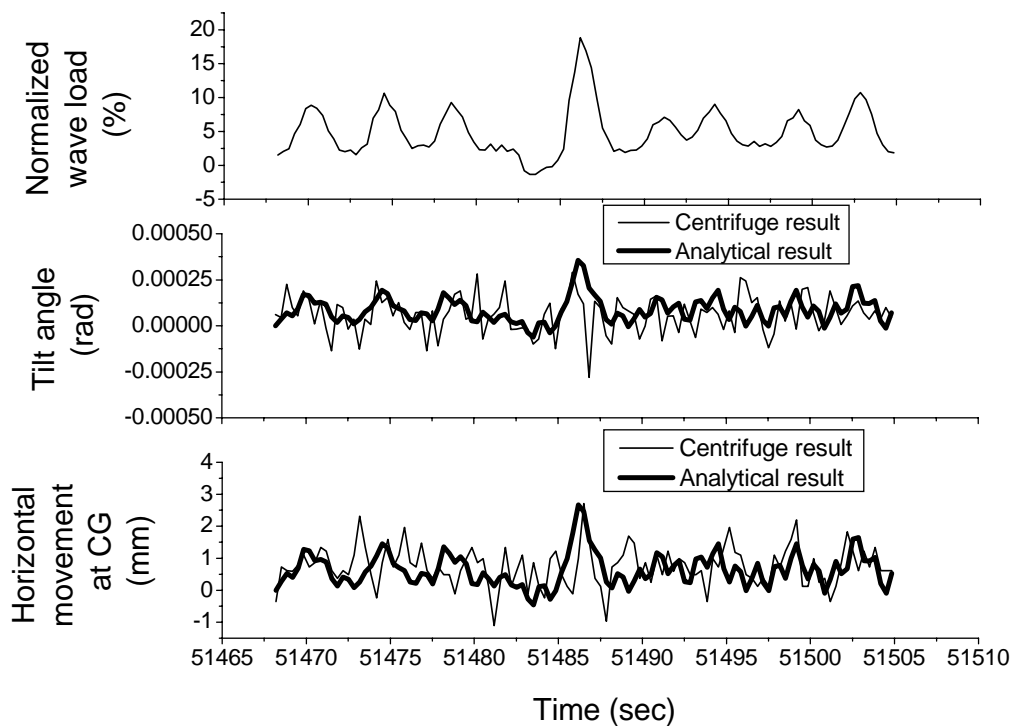
Fig. 6.17 Comparisons of measured and analytical total movements of caisson breakwater subject to wave loading during 51465-51510 s in WL7 (RD=80%)
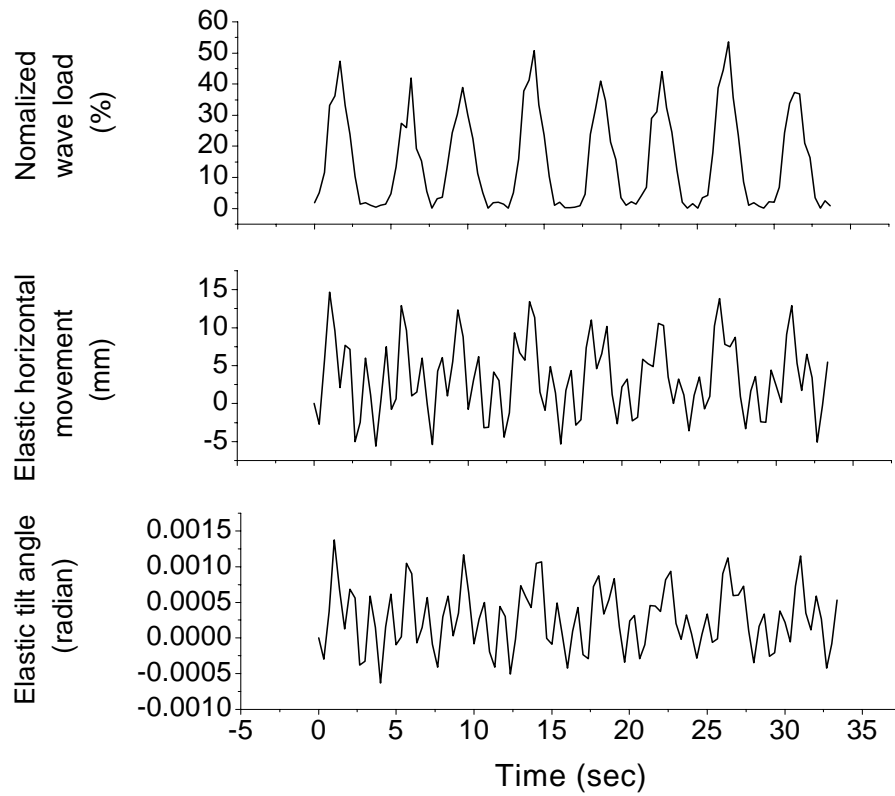
Fig. 6.18 Elastic movements of caisson subjected to strong waves
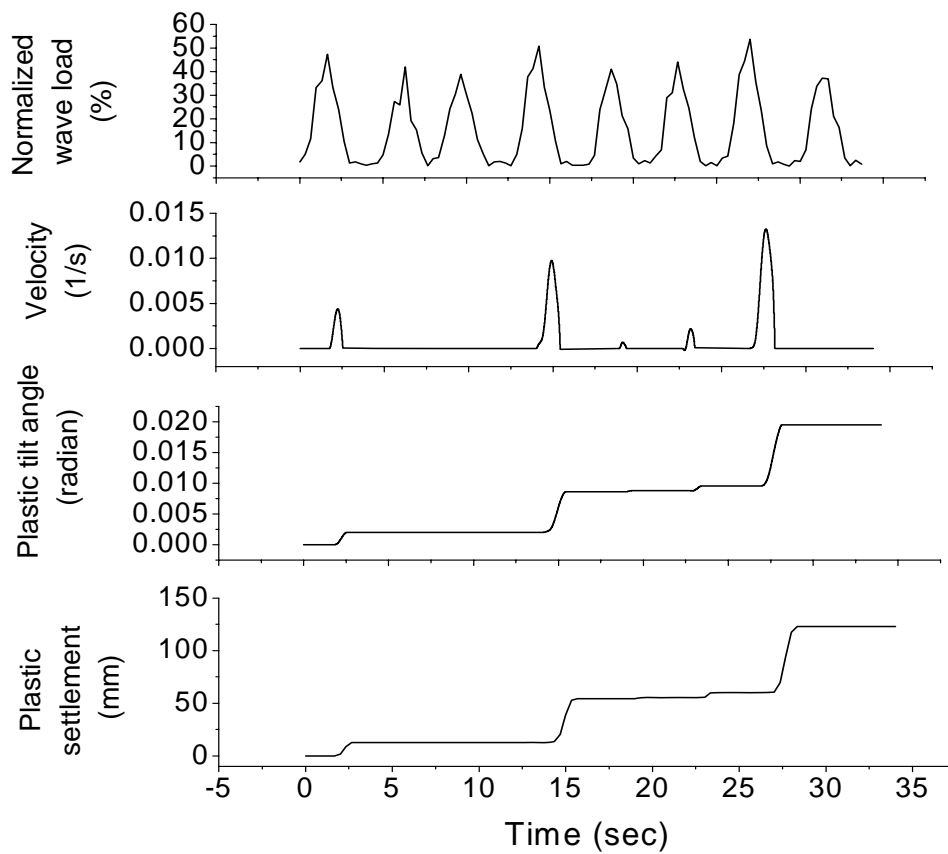
Fig. 6.19 Plastic movements of caisson subjected to strong waves
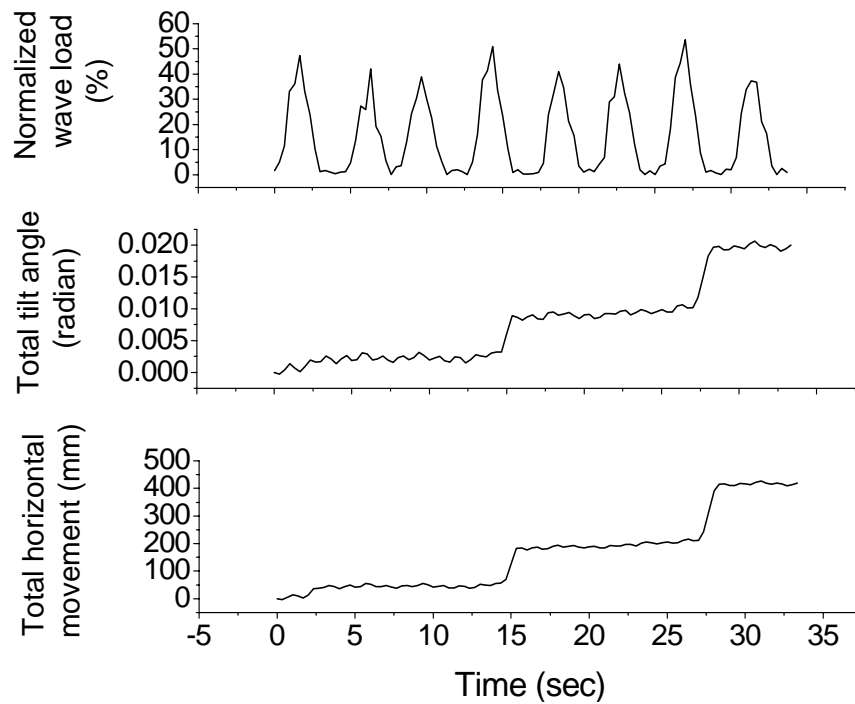
Fig. 6.20 Total movements of caisson subjected to strong waves
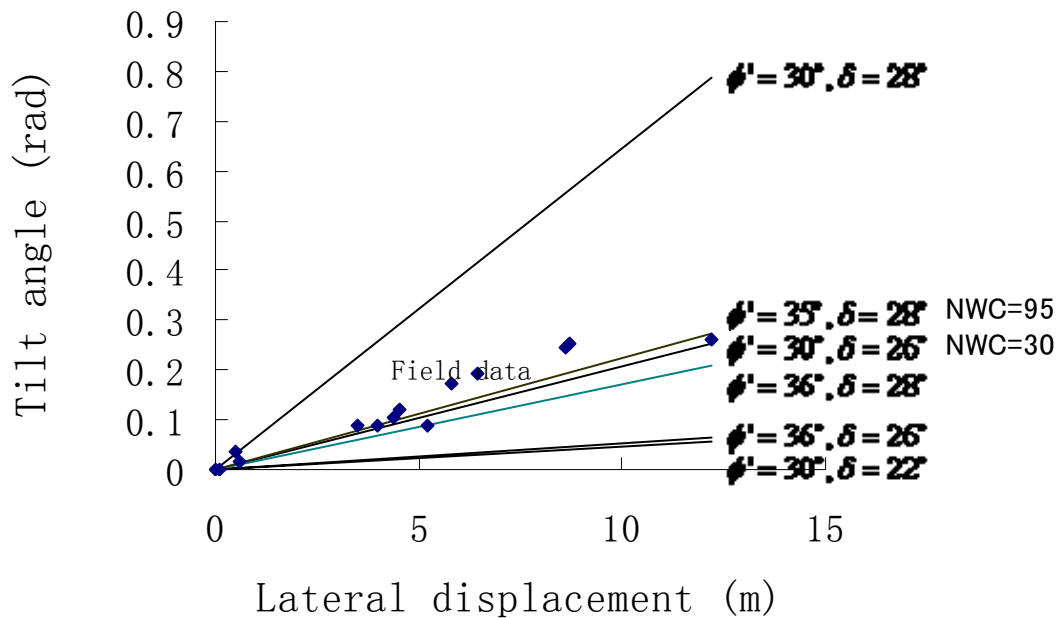
Fig. 6.21 Comparisons of analytical data with the field data of Typhoon case 8712 at
Shin-Nagasaki Fishing Port (NWC=number of wave cycles)
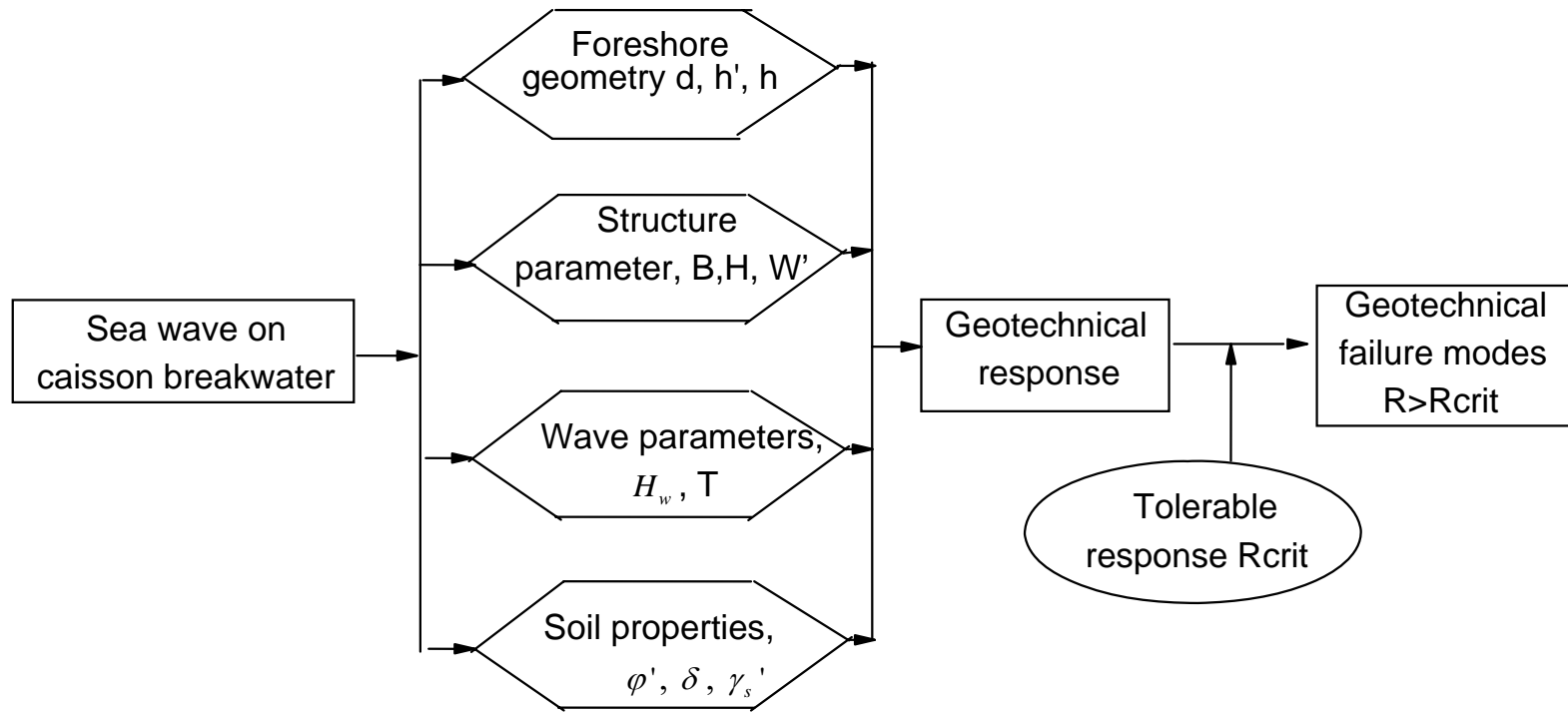
Fig. 6.22 Problem definition in the rotational failure of caisson breakwater
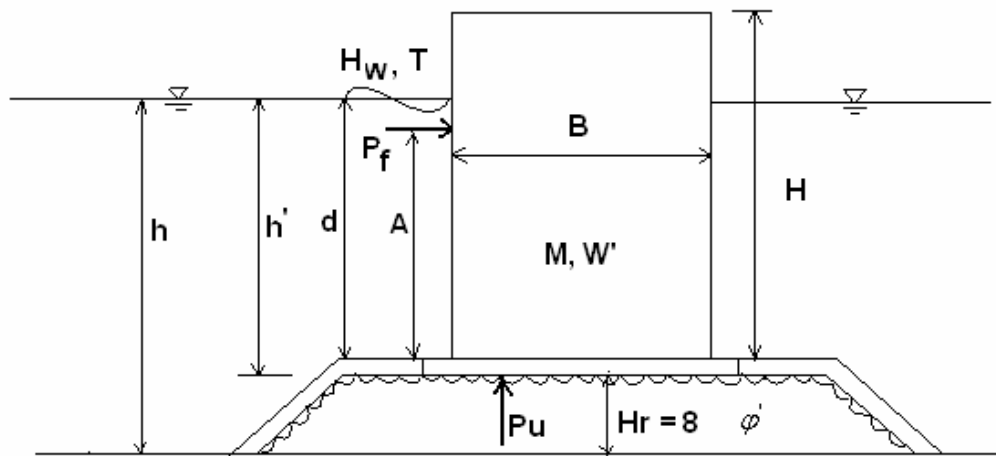
Fig. 6.23 Cross-section of designed caisson breakwater

$$X= \left(\frac{d+H_w}{H}\right)^{0.16} \frac{H_w \gamma_w (d+H_w)}{W'/L} (\frac{L_0}{B})^{0.4} (\varphi')^{-0.1}$$
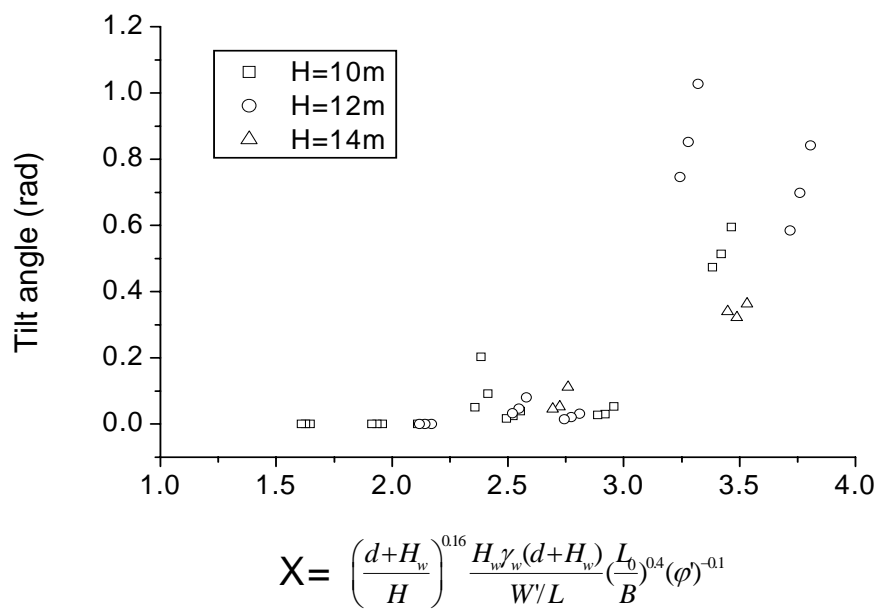
Fig. 6.24 Tilt angle for one wave under different wave height with a fixed wave period

$$X= \left(\frac{d+H_w}{H}\right)^{0.16} \frac{H_w \gamma_w (d+H_w)}{W'/L} (\frac{L_0}{B})^{0.4} (\varphi')^{-0.1}$$
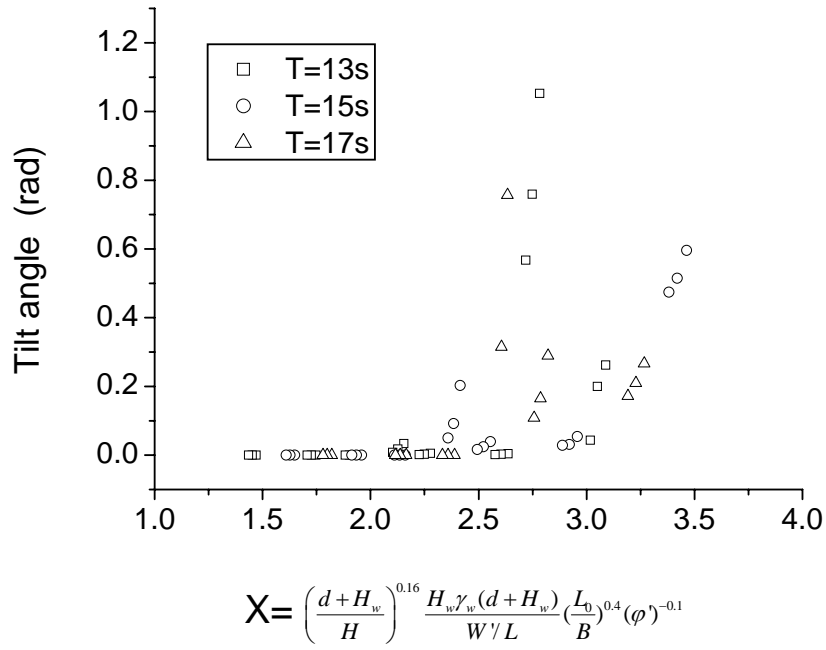
Fig. 6.25 Tilt angle for one wave under different wave period with a fixed wave height

$$X= \left(\frac{d+H_w}{H}\right)^{0.16} \frac{H_w \gamma_w (d+H_w)}{W'/L} (\frac{L_0}{B})^{0.4} (\varphi')^{-0.1}$$
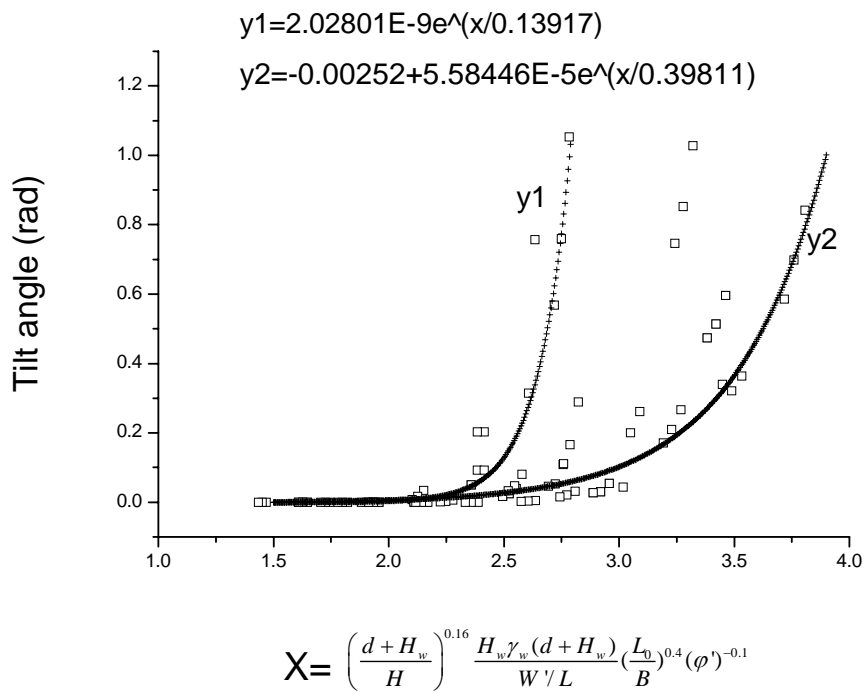
Fig. 6.26 Tilt angle for one wave bounded in two lines y1 and y2

Chapter 7

Conclusions

7.1 Summary of Findings

In the present study, the behaviour of caisson breakwater on sand has been studied by both physical and analytical modeling approaches. Centrifuge model tests on caisson breakwater subjected to regular, reversal or non-reversal wave loadings were conducted to simulate caisson infilling and wave loading stages. Centrifuge test results on reversal wave loading indicate significant excess pore pressure build-up in the early stages of the loading episode, which suggests that densification of sand bed may be a practical way to reduce the caisson displacements. On the other hand, wave spikes may cause an increase in stress on the caisson foundation, while generation of excess pore pressure is minimal. The results reveal that even a dense sand bed can be adversely affected by wave spikes of sufficiently high magnitude. To back analyze the test data, analytical models were developed to simulate the oscillatory and permanent caisson displacements during wave spikes. The findings arising from the present study are summarized below.

7.1.1 Tests on reversal and non-reversal wave loading

(1) Caisson responses due to non-reversal wave loading fall into two major categories. Regular non-reversal waves lead to a rapid stabilization of caisson move-

ments: including settlement, rotation and horizontal displacement. Observed excess pore pressures in the sand bed are generally small and appear insignificant. However, caisson responses are found to be sensitive to irregularities in wave loading. In the present study, two types of irregularities which have a significant influence on caisson movement were observed. The first is a wave spike, which has a peak load that is much higher than the rest of the wave cycles. The second is a wave cycle which has a small amount of reversal loading in it. The effects of these irregularities can be much more significant than the effects of sand bed relative density. As such, the influence of sand bed relative density could not be discerned without discounting the effects of these irregularities. Once the effects of the wave irregularities are discounted, the effects of sand bed relative density become much more apparent as the caisson movements clearly reduce with increasing sand RD. Thus it can be concluded that, under non-reversal wave loading, the effects of wave profile are more significant than those due to sand relative density.

(2) Caisson responses due to reversal wave loading are very different from those due to non-reversal loading. Very significant excess pore pressures and caisson movement were generated within the first 100 or so wave cycles. The caisson movements were much larger than those under non-reversal loading. Backward tilting towards the wave load direction occurred in all the tests. The caisson settlement induced by reversal loading could be attributed to the sand densification mechanism. For loose sand beds, liquefaction was observed. This is not surprising if one considers reversal wave loading as an extreme case of a suction wave

train being applied to the caisson. Since the recession of a wave from a caisson may actually lead to reversal wave loading, this possibility cannot be discounted. The findings above indicate that, if excess pore pressure and liquefaction is a concern, caisson tests should be conducted using reversal wave loading instead of non-reversal loading.

(3) The sand RD is found to be the key factor that dominates the caisson movement and pore pressure build-up during the reversal wave loading. The possibility of liquefaction can be minimized by appropriately densifying the sand bed. However, the centrifuge test data show that even the dense sand bed is not immune to large caisson tilt movements under large wave spikes. For this reason, the accumulation of caisson tilt under successive wave spikes should be considered in design.

The overall scheme of progressive behaviour of caisson breakwater subjected to reversal and non-reversal wave loading is summarized in Table 7.1.

7.1.2   Parametric studies on non-reversal wave loading

Further centrifuge model tests were conducted to investigate the performance of caisson breakwater subject to non-reversal wave loading with different caisson configuration and boundary conditions. The findings arising from the parametric studies are summarized as follows:

(1) **RD of sand bed**

The caisson settlement was found to decrease with increase in sand RD during infilling stage. However, during wave loading stage, the build-up of tilting, hori-

zontal and vertical displacements of caisson breakwater do not appear to exhibit a definite trend of behaviour in relation to sand RD. The inconsistent trend of caisson movements induced by the irregular waves suggests that the wave loading history has played a more dominant role in deciding the behavior of caisson breakwater than the initial sand RD. Once the sudden increases caused by the wave irregularities are ignored, a much more consistent trend is obtained as the final caisson movements decrease with increasing RD of sand bed.

(2) **Caisson width**

The results of tests on caisson width varying from 18m to 14m show that a minimum caisson width of 16m is required to achieve a stable caisson which is subjected to non-reversal breaking wave loads.

(3) **Caisson weight**

The caisson with lighter infill weight is prone to rotation failure with a maximum tilt angle of $0.26°$. Relatively large residual pore pressures are found to develop from the very beginning of wave loading and then dissipate to the hydrostatic line.

(4) **Presence of rock berm**

The presence of rock sill underneath a caisson is found to greatly reduce the caisson tilt, horizontal and vertical displacements, despite the occurrence of dilation of rock sill at the caisson base.

(5) **Slamming on top slab**

Slamming on top slab of a caisson structure due to overtopping wave aggravates the caisson tilt and vertical displacements. The increase in positive excess pore pressures reduces the effective stress in the oil-saturated sand bed and this results in a larger cyclic settlement of the caisson breakwater.

(6) **Cyclic preloading**

The beneficial effect of cyclic preloading on a caisson can be taken into account in design as the caisson displacements are greatly reduced during wave reloading.

7.1.3   Analytical study

A simplified dynamic analysis for caisson responses under wave spikes was proposed based on the constraint optimization of assumed circular slip surfaces beneath the caisson base. The conclusions are drawn as follows.

(1) The oscillatory vertical displacement of caisson breakwater during infilling stage increases linearly with time, which can be predicted well by the analytical model. During wave loading stage, a reasonably good agreement was obtained between the magnitude of computed and measured oscillatory caisson horizontal and tilt displacements, although the phase angle may not be matched well.

(2) The plastic caisson displacements always initiate around the wave peak and last for a very short duration. The magnitude of elastic displacements is negligible when compared with that of plastic ones. It is found that in wave spike events, exceedence of shear resistance is the mechanism causing the observed permanent deformation. Cumulative effect of the small plastic displacements is considered

as a stepwise failure, which may lead to the collapse of caisson breakwater after a certain number of high impulsive loadings.

(3) There is some threshold values of H_w or T for which a rotational permanent displacement is initiated. A clear tendency of the permanent tilt angle is found to increase exponentially with the dimensionless parameter X (refer to Chapter 6 for full definition of X). A design chart is developed to determine the caisson tilt angle according to the in-situ wave conditions, caisson geometries and foreshore properties.

7.2 Design Implications

The findings of the present research have improved the understanding of stability and failure mechanism of caisson breakwaters. The procedure is realistic and practical in the sense that it takes into account the soil degradation due to repetitive loading, instantaneous and residual excess pore pressure effects.

Water pressures along the seaward slope of the rubble mound fluctuate during each wave cycle, whereas the water pressures at the harbor side remain nearly constant. The corresponding fluctuating pressure gradients cause a fluctuation in the pore flow though the rubble mound. However, the wave induced pore pressure is not simulated in the centrifuge tests because the impulsive load is directly applied on the caisson due to the space constraint in the experimental setup. The use of Goda formula has clarified the concept of uplift pressure on the caisson bottom, since the buoyancy of the upright section in still water and its uplift pressure due to wave action are defined separately. The distribution of the uplift pressure is assumed to be triangular shape based on earlier

theoretical and laboratory studies, as indicated in Fig. 3.8. De Groot (1999) considered that the non-stationary effects of the direct component may enlarge the uplift force with up to 30% compared to the value found with stationary flow. In most cases, however, the non-stationary effects yield a reduction of the uplift force.

During the non-reversal wave loading tests, an impulsive wave force of 10% of caisson weight may produce an uplift force of 2.25% of caisson effective weight according to the Goda formula when the designed wave height is 3 m and wave period is 6 s. When taking the non-stationary effect into account, the uplift force can be as high as 2.92%. On the other hand, the non-stationary effect may reduce the uplift force in most cases, which means that uplift force varies from 0 to 2.92% of caisson weight when considering the non-stationary effect. This may to some extent influence the behavior of caisson breakwater. Nevertheless, the mechanism and trend described here are still applicable.

As presented in the previous chapters, the failure of caisson subjected to reversal wave loading may be induced by the progressive softening of soil bed. In natural storms, there are no fundamental wave height and wave period, only the maximum ones can be recorded after the storm. A similar effect may still be induced if the peak wave causing the largest caisson movements can be captured. Simplistic equivalent linear elastic models which do not incorporate any pore-pressure-induced softening are unlikely to reproduce the caisson movements. Therefore, to fully exploit the performance of caisson breakwater in analysis and design, more sophisticated models which take into account progressive softening of soil bed induced by pore pressure build-up must be incorporated into the foundation model, as presented by MacDougal et al. (1986) and Tsai

et al. (1990). The focus of the present study is the improvement of the understanding of the physical process and failure mechanisms involved in the wave-structure-foundation interaction. Further work is needed to develop suitable models for practical purposes.

7.3   Recommendations for Future Works

The main function of any breakwater is to prevent excessive wave attack in a certain area. Assuming the structure itself survives, it is still possible that it fails to fulfill its function due to wave energy passing over the breakwater. Hence,improvements to the present wave apparatus are recommended to produce real breaking wave loads by a wave stroke. Hence, the wave induced uplift force, wave transmission over caisson, wave overtopping discharge and wave reflection can be incorporated into the physical modeling. Moreover, the phenomenon of seaward scouring which is one of the most important factors that leads to caisson failure can be reproduced and investigated in centrifuge tests.

The largest impulsive wave loadings applied in the present study are merely 10% of the caisson effective weight, which is significantly lower than that experienced during the storm. Moreover, in some circumstances, the wave period is very short and the dynamic effect of the structure-foundation interaction can be substantial. Therefore, the existing wave actuator system needs to be improved to provide better closed-loop control. This can be achieved by using on-board hydraulic servo-control system. With high flow rate supplied by the accumulators, the frequency response of servo-actuators and amplitude of wave loadings can be greatly increased.

Under certain conditions, such as offshore platforms, it is useful to consider a caisson foundation directly on the sand bed, which constitutes the main design objective

of the present study. However, composite breakwaters with rubble mound foundation are often used for reflecting and breaking the waves offshore. In the present centrifuge tests, only one test with 4 m thick rubble mound is designed to investigate its effect on caisson behavior, which may not be far enough. Although the high-mound composite type is unstable, it may help to understand the wave-generated impulsive pressure and scouring caused by breaking waves. In addition, the mechanism of stability of composite breakwaters with low-mound is more practical and useful for port engineers.

More centrifuge tests may be undertaken to investigate three-dimensional failure mechanisms of caisson breakwaters. Three or more caissons may be parallel along the width of container to simulate the plane strain condition and the middle ones can reflect the 3-D effect well, as presented by Poel and De Groot (1998).

Centrifuge tests may also be conducted to study the effects of static preloading on caisson performance with different static preloading ratios. This can be realized by infilling different amount of $ZnCl_2$ solution into the caisson and then released to the designed level. According to Ng (1998), the pore pressure generation characteristic is found to be heavily dependant on the stress state of the soil just prior to loading.

The simple analytical analysis presented in Chapter 6 highlights its application in simulating the oscillatory and permanent tilting displacement of caisson breakwater with negligible residual pore pressure build-up in the subsoil. The model may be improved to incorporate the progressive softening of soil bed with change of soil stiffness.

Table 7.1 Overall scheme of progressive behavior of caisson breakwater subjected to different pattern of wave loading

Wave load patterns	Caisson movements	Pore pressure response	Failure mechanisms
Non-reversal wave loading tests Wave strength from 0% to 10%	• Caisson tilts landward. • Majority of caisson movements occur under unsteady wave. • Clockwise soil flow circulation was found underneath the caisson base during the wave loading stage. • Magnitude of caisson movements is negligible.	• Positive residual pore pressures develop underneath the caisson base from the very beginning, even in the very dense sand. • The magnitude is negligible.	• Rotation failure occurred in the dense sand with RD=72%. • Wave loading history is the key factor that influences caisson movements.
Reversal wave loading tests a) Wave strength from -2% to 4% b) Wave strength from -7% to 10% c) Wave strength from -10% to 10%	• Caisson tilts seawards. • Two stages of caisson movements: settlement stage and stabilization stage. • Majority of caisson movements are caused by densification of sand bed. • Magnitude of caisson movements is relatively large.	• Progressive softening becomes significant with positive pore pressure build-up in the first several wave cycles and then dissipated towards the hydrostatic line • The denser the sand bed, the faster the instantaneous pore pressure dissipates	• Partial liquefaction occurs in the loose sand with RD=55% (wave strength from -7% to 10%). • Sliding and rotation failures occur in sand bed with RD=51% (wave strength from -2% to 4%). • Backward sliding failure occurs in the very dense sand with RD=82% (wave strength from -10% to 10%). • RD of sand bed is the key factor that dominates the movement of caisson breakwater and pore pressure build-up. • The likelihood of failure is greatly diminished with increase in RD of sand bed.

References

Barkan, D.D. Dynamics of Bases and Foundations. McGraw-Hill Book Co., New York. 1962.

Bielby, F. Triaxial Tests on Oil Saturated Sand. Project Repot, Department of Engineering, Cambridge University. 1989.

British Standarts Institution. Code of Practice for Earth Retaining Structures. BS 8002. British Standarts Institution, London, UK. 1994.

Chen, C.T. Digital signal processing: spectral computation and filter design. New York: Oxford University Press. 2001.

Chen, C. Sand Bed Response under Wave Loadings Using a Centrifuge. Master Thesis. Nation University of Singapore. 2003.

De Groot, M.B. Holscher, P. Meijers, P. and Kortenhaus, A. Stability of Caisson Breakwater under Wave Impact Loading. Geotechnical Engineering for Transportation Infrastructure, Rotterdam, Vol(2),pp.747-754. 1999.

De Gerloni, M., Colombo,D., Pastori, S. and Boldrini, F. Wave Force on Caisson Breakwaters: Optimization of Hydraulic Model Test Procedures. Proceedings 1st Overall Project Workshop, MAST III, PROVERBS-Project: Probabilistic Design Tools for Vertical Breakwaters, Las Palmas, Gran Canaria, Annex 1F, pp.17. 1997.

Dean, R.G. and Dalrymple, R.A. Water Wave Mechanics for Engineers and Scientists, World Scientific, River Edge, N.J.,1991.

Eyton, D.G.P. Triaxial Tests on Sands with Viscous Pore Fluid. Project Repot, Engineering Department, Cambridge University. 1982.

Festag, G. Experimental Investigation on Sand under Cyclic Loading. Constitutive and Centrifuge Modelling: Two Extremes, Springman (ed.), pp.269-275, 2001.

Gao, M., Dai, G. and Yang, J. Dynamic Studies on Caisson-Type Breakwaters. Coastal Enginnering, pp.2469-2478, 1988.

Goda, Y. Laboratory Investigation of Wave Pressure Exerted upon Vertical and Composite Walls. Rept. Port and Harbour Res. Inst., Vol.11(2),pp.3-45, 1972.

Goda, Y. Random Seas and Design of Maritime Forces, University of Tokyo Press, Tokyo, Japan, 1985.

Goda, Y. Dynamic Response of Upright Breakwaters to Impulsive Breaking Wave Forces. Coastal Engineering, 22, pp.135-158, 1994.

Gorbunov-Passadov, M.I. and Serebrajanyi, R.V. Design of Structures upon Elastic Foundations. In Proc. 5th ICSMFE, 1961, Vol. I, pp.643-648, 1961.

Hansen, B and Christensen, N. H. Discussion on Theoretical Bearing Capacity of very Shallow Footings, Journal of Soil Mech. and Found. ASCE, 95(6):1568-1572, 1969.

Hitachi, S. Case Study of Breakwater Damages, Mutsu-Ogawara Port. In Proc. Intern. Workshop on Wave Barriers in Deepwaters, Port and Harbor Research Institute, Yokosuka, Japan, pp.308-329, 1994.

Kimura, Y., Kondo, H., Kuwabara, S. and Kawamori, A. Improvement of Composite Breakwater on Solid Bottom against Severe Tsunamis. Coastal Engineering 1996: Proceedings of the Twenty-fifth International Conference. Sep. 2-6, pp.1707-1719. 1996.

Klammer, P., Oumeraci, H. and Partenscky, H.-W. Oscillatory Motions and Permanent Displacements of Caisson Breakwaters Subject to Impulsive Breaking Wave Loads. In Proc. 24th Int. Conf. Coastal Eng., pp.1255-1268. 1994.

Ko, H-Y. Modeling Seismic Problems in Centrifuge. Centrifuge 94, Balkema, Rotterdam, pp.3-12. 1994.

Kobayashi, M., Tersashi, M. and Takahashi, K. Bearing Capacity of Rubble Mound Supporting a Gravity Structure. Report of Pore and Harbour Research Institute 26(5), pp.234-241. 1987a.

Kobayashi, M., Terashi, M. and Takahashi, K. Oscillatory Motions and Permanent Displacements of Caisson Breakwaters Subjected to Impulsive Breaking Wave Loads. Proc. 24th Int. Conf. on Coast. Engrg., ASCE, Reston, pp.1255-1268. 1987b.

Khoo, E., Okumura, T. and Lee F. H. Side Friction Effects in Plain Strain Models. Centrifuge 94, Singapore, pp.115-120, 1994.

Lambe, T. W. and Whitman, R.V. Soil Mechanics. SI Version. Singapore. 1969.

Lee, F. H. Centrifuge Modeling of Earthquake Effects on Sand Embankments and Islands. Ph. D Thesis, Cambridge University. 1985.

Lee, F. H. and Schofield, A.N. Centrifuge Modelling of Sand Embankments and Islands in Earthquake. Geotechnique, Vol.80, No.1, pp.45-58. 1988.

Lee, F. H., Tan, T. S., Leung, C. F., Yong, K. Y., Karunaratue, G. P. and Lee, S. L. Development of Geotechnical Centrifuge Facility at National University of Sinagpore. Centrifuge 91, 1991, Balkema, Rotterdam. 1991.

Lee, F. H. The National University of Singapore Geotechnical Centrifuge-Users Manual. Research Report No. CE001, National University of Singapore, July, 1992.

Lee, K.L. and Albaisa, A. Earthquake Induced Settlement in Satuarate Sands. Journal of the Geotechnical Engineering Division, ASCE, Vol. 100(4), pp.387-406. 1974.

Leung, C. F., Lee, F. H., and Tan, T. S. Principles and Appicaiton of Geotechnical Model Testing. Journal of Institute of Engineers Singapore, vol.31, No.4, pp.39-45. 1991.

Leung, C. F., Lee, F. H., and Khoo, E. Behaviour of Gravity Caisson on Sand. Journal of Geotechnical and Geoenvironmental Engineering, Vol.123, No.3, pp.187-196. 1997.

Ling, H. I., Cheng H. D., Mohri, Y. and Kawabata, T. Permanent Displacement of Composite Breakwaters Subjected to Wave Impact. Journal of Waterway, Port, Coastal, and Ocean Engineering, Jan. pp.1-8. 1999.

Ling, H. I. Recent Application of Sliding Block Theory to Geotechnical Design. Soil Dynamics and Earthquake Engineering 21, pp.189-197. 2001.

Lysmer, J. and Richart F.E. Dynamic Response of Footings to Vertical Loadings. Berkeley, University of California, Institute of Transportation and Traffic Engineering, Soil Mechanics and Bituminous Materials Research Laboratory, 1966.

Loginov, V.N. Nonlinear Oscillations of Vertical Breakwaters Subject to Wave Impact Loads. Trudy Soiuzmorniiproekta, Vyp.2, pp.47-59 (in Russia). 1969.

Madabhushi, S.P.G. Effect of Pore Fluid in Dynamic Centrifuge Modeling. Centrifuge 94. Leung, Lee and Tan edit. pp.127-133. 1994.

MacDougal, W.G., Tsai, Y.T., and Sollit, C.K. Verification of the Analytical Model for Ocean Wave-Soil-Caisson Interaction. Proc. 20th Int. Conf. on Coastal Engrg., pp.2089-2103. 1986.

Martin, G. R., Finn, W. D. L. and Seed, H. B. Fundamentals of Liquefaction under Cyclic Loading. J. of Geotechnical Engineering Div., Vol. 101, GT5, pp.423-438. 1975.

MAST II MSC. Monolithical Vertical Structures. Annex I General Document Foundation of Design of Caisson Breakwaters, 1995.

Marinski, J.G. and Oumeraci, H. Dynamic Response of Vertical Structures to Breaking Wave Forces- Review of the CIS Design Experience. In Proc. of 10th Coastal Eng. Conf., ASCE, pp.1357-1370. 1992.

Milovic, D.M., Touzot, G. and Tournier, J.P. Stresses and Displacements in An Elastic Layer Due to Inclined and Eccentric Load Over a Rigid Strip. Geotechnique, Vol.20, No.3, pp.231-252. 1970.

Newmark, N. M. A Method of Computation for Structural Dynamics. American Society of Civil Engineers, 1959.

Ng, T. G. Cyclic Behavior of Spudcan Footing on Sand. Ph. D thesis, National University of Singapore, Singapore. 1998.

Ng, T.G and Lee, F. H. Cyclic Settlement Behavior of Spudcan Foundations. Geotechnique 52, No.7, pp.469-480. 2002.

Oumeraci, H. Wave Impact Loading on Vertical Structures. Proc. of the First Workshop of Project 2/MSTG6-S: Research on Coastal Structures, Hanover. 1991.

Oumeraci, H., Partenscky, H.W. and Tautenhain, E. Breaking Wave Loads on Vertical Gravity Structures. In Proc. Of 2nd International Offshore and Polar Engineering Conference, USA, pp.532-539. 1992.

Oumeraci, H. Review and analysis of vertical breakwater failures-lessons learned, Coastal Engineering, Vol.22, pp.3-39. 1994a.

Oumeraci, H.,Klammer, P.and Kortenhaus, A. Impact Loading and Dynamic Response of Vertical Breakwaters-Review of Experimental Results. Proc. Int. Workshop on Wave Barriers in Deep waters, Jan 10-14, pp.374-359. 1994b.

Oumeraci, H. and Kortenhaus, A. Analysis of the Dynamic Response of Caisson Breakwaters, Coastal Engineering, Vol.22, pp.159-183. 1994c.

Oumeraci, H. Vertical Breakwaters-A Plea for An Integrated Design Approach. In Wave Forces on Inclined and Vertical Wall Structures / Task Committee on Forces on Inclined and Vertical Wall Structures of the Committee on Waves and Wave Forces of the Waterway, Port, Coastal and Ocean Division of ASCE, pp.205-231. New York. 1995.

Oumeraci, H., Kortenhaus, A., Allsop, W., De Groot, M., Crouch, R. Vrijling, H. and Voortman, H. Probabilistic Design Tools for Vertical Breakwaters. The Netherlands: A.A.Balkema Publishers. 2001.

Ovesen, N. K. Centrifugal Testing Applied to Bearing Capacity Problems of Footing on Sand. Geotechnique, Vol.25, No.2, pp.394-401. 1975.

Pedersen, J. Dynamic Response of Rubble Mound Breakwater Crown Walls. In Proc. of the Second Projetc Workshop, Milan, Italy. April 14-15, 1994.

Penny, J. and Lindfield, G. Numerical Methods Using Matlab. Prentice Hall, Upper Saddle River, NJ. 2000.

PHRI, Technical Standard for Port and Harbour Facilities in Japan. The overseas Coastal Area Development Insititute of Japan. 1991.

Poel, J.T.van der. and De Groot, M.B. Cyclic Load Tests on a Caisson Breakwater Placed on Sand. In Proc. Int. Conf. Centrifuge 98, Tokyo, Balkema, Rotterdam, Vol 1, pp.403-408. 1998.

Poulos, H.G. and Davis, E.H. Elastic Solution for Soil and Rock Mechanics. John Wiley & Sons, Inc. 1974.

Richart, F. E., Woods, R.D. and Hall, J.R. Vibrations of Soils and Foundations. PRENTICE-HALL, INC., Englewood Cliffs, N.J. 1970.

Rowe, P.W. and Craig, W.H. Studies of Offshore Caissons Founded on Oosterschelde Sand. Design and Construction of Offshore Structure, Institution of Civil Engineers, London, pp.49-60, 1976.

Rowe, P.W. Use of Large Centrifuge Models for Offshore and Nearshore Works. Symposium on Geotechnical Aspects of Coastal and Offshore Structures, Bangkok, pp.21-33. 1981.

Sassa, S. and Sekiguchi, H. Wave-Induced Liquefaction of Beds of Sands in a Centrifuge. Geotechnique, Vol 49, No 5, pp.621-638. 1999.

Schmidt, R., Oumeraci, H. and Partenscky, H.-W. Impact Loading Induced by Plunging Breakers on Vertical Structures. ASCE Proc. 23rd Interational Conference Coastal Engineering, Vol.2, Venice, Italy, pp.1545-1558, 1992.

Schofield, A.N. An Introduction Centrifuge Modelling. Centrifuges in Soil Mechanics. Craig, James & Schofield (eds). Balkema, Rotterdam, pp.3-11. 1988.

Sekiguchi, H. and Ohmaki, S. Overturning of Caisson by Storm Waves. Soild and Found., Tokyo,32(3), pp.144-155. 1992.

Sekiguchi, H. and Kobayashi, S. Sliding of Caisson on Rubble Mound by Wave Force. Proc. 13rd Int. Conf. on Soil Mech. and found. Engrg., Balkema, Rotterdam, The Neitherlands, pp.1137-1140. 1994.

Shimosako, K., Takahashi, S. and Tanimoto, K. Estimating the Sliding Distance of Composite Breakwaters due to Wave Forces Inclusive of Impulsive Forces. ASCE. In Proc. 24th .International Conference Coastal Engineering, pp.1581-1594. 1994.

Silver, M. L. and Seed, H. B. Volume Changes in Sands during Cyclic Loading. In Journ. of Soil Mechanics and Foundations Div., ASCE, Vol. 97, No SM9, pp.1171-1182. 1971.

Smith, I.M. and Molenkamp, F. Dynamic Displacements of Offshore Structures due to Low Frequency Sinusoidal Loading. Geotechnique, 30(2), pp.179-205. 1980.

Springman, S.M, A.R.M.Norrish, and C.W.W. Ng. Cyclic loading of sand behind integral bridge abutment. TRL Report TRL 146, Crownthorne, TRL limited, 1996.

Sumer, B. M., Fredsoe, J., Christensen, S. and Lind, M. T. Sinking/floating of Pipelines and Other Objects in Liquefied Soil under Waves. Coastal Engineering. Vol.38: pp.53-90. 1999.

Takahashi, S., Kimura, K., and Tanimoto, K. Stability of Armor Units of Composite Breakwater Mound against Oblique Waves. Report of Port and Harbour Research Institute, Vol. 29, No. 2, (in Japan). 1990.

Takahashi, S. Tanimoto, K. and Shimosako, K. Dynamic Response and Sliding of Breakwater Caissons against Impulsive Breaking Wave Forces. Proc Int. Workshop on Wave Barriers in Deep waters, Port and Harbor Research Institute, Yokosuka, Japan, pp.362-399. 1994a.

Takahashi, S., Tanimoto, K. and Shimosaka, K. A Proposal of Impulsive Pressure Coefficient for Design of Composite Breakwaters, Proc. Int. Conference on Hydrotechnical Eng. For Port and Harbor Construction, Port and Harbor Res. Inst. Japan, pp.489-504. Oct. 19-21, 1994b.

Takahashi, S. Design of Vertical Breakwaters. Reprinting of Coastal Structures (ICCE 96 Short Course), Port and Harbour Research Institute, Ministry of Transport, Japan. 1996.

Tan, T.S. and Scott, R. F. Centrifuge Scaling Considerations for Fluid-Particle Systems, Geotechnique, 35(4), pp.461-470. 1985.

Tan, S.L., Radhakrishnan, R., Lim, B.N., and Pang, P.Y. Design and construction of causeway from Keppel to Pulau Brani using caisson method. Proc., Semenar on Engrg. for Coast. Devel., Kozai Club, Singapore, pp.199-210. 1991.

Tanaka, Y. Liquefaction of Reclaimed Lands along Osaka Bay by Great Hanshin Earthquake. In Proc. of the 6th International Offshore and Polar Engineering Conference, Los Angeles, USA, Vol. 1, May 26-31, pp.20-28. 1996.

Taniguchi, E., Koga, Y., I. and Yasuda, Y. Centrifuge Model Tests on Reinforced Embankments by Non-woven Fabric. In Proc. of International Conference on Geotechnical Centrifuge Modeling, Paris, pp.253-258. April,1988.

Tanimoto, K., Moto, K., Ishizuka, S., and Goda, Y. An Investigation on Design Wave Force Formula of Composite-type Breakwaters. In Proc. 23rd Japanese Conf. Coastal Eng., pp.11-16. 1976.

Terashi, M. and Kitazume, M. Bearing Capacity of a Foundation on Top of High Mound Subjected to Eccentric and Inclined Load. Rep. of Port and Harbor Res. Inst.,26(2), pp.3-24, 1987.

Toki, S. and Kitago, S. Effects of Repeated Loading on Deformation Behavior of Dry Sand. Journal of the Japanese Society of Soil Mechanics and Foundation Engineering, Vol.14, No.1, pp.95-103. 1974. (in Japanese)

Tsai, Y.T., McDougal, W.G. and Sollitt, C.K. Response of Finite Depth Seabed to Waves and Caisson Motion. Journal of Waterway, Port, Coastal and Ocean Engineering. Vol. 116, no. 1, pp.1-20. Jan. 1990.

Yamaguchi, M., Hatada, Y., Ikeda, A. and Hayakawa, J. Hindcasting of High Wave Conditions During Typhoon 8712. In Proc. Japan Soc. Civil Eng., No. 411, II-12, pp.237-246. 1989. (in Japanese).

Yamamoto, M., Endo, T., Hasegawa, A. and Tsunakawa, K. Random Wave Tests on a Damaged Breakwater in Himekawa Harbor, Japan. Coastal engineering, 5, pp.275-294. 1981.

Vink, H.A.Th. Wave Impacts on Vertical Breakwaters. Master Degree Thesis, Delft University of Technology, Netherlands.1997.

Whitman, R.V. and Richart, F.E., Jr. Design Procedures for Dynamically Loaded Foundations. J. of Soil Mech. and Found. Div., Proc. ASCE, Vol.93, No.SM 6, Nov., pp.169-193. 1967.

Zeng, X. and Steedman, R.S. Bearing Capacity Failure of Shallow Foundations in Earthquakes. Geotechnique 48, No. 2, 235-256. 1998.

Zhang X. Y., Leung C.F. and Lee F.H. Breaking Wave Loads on Caisson Breakwater. 17th KKCNN Symposium on Civil Engineering, Ayuthaya, Thailand, pp.469-474. Dec, 2004.

Zhang X. Y., Leung C.F. and Lee F.H. Performance of Caisson Breakwater subjected to Breaking Wave Loads. In International Symposium on Frontiers in Offshore Geotechnics, Perth, Western Australia, Australia. September 2005.

APPENDIX A

The following equation is derived to calculate the amount of the sand bed of different relative density. Since every test the sand is prepared and pounded to the same prescribed thickness, when the relative density of the sand is known, so as the amount.

$$\rho_d = \frac{G_s * \rho_w}{1+e} \tag{A2.1}$$

$$\gamma = \rho_d * g = \frac{G_s * \rho_w * g}{1+e} \tag{A2.2}$$

$$e = \frac{G_s * \rho_w * g}{\gamma} - 1 \tag{A2.3}$$

$$R = \frac{e_{max} - e}{e_{max} - e_{min}} \tag{A2.4}$$

$$e = e_{max} - R * (e_{max} - e_{min)} \tag{A2.5}$$

ρ_d is dry density of sand, ρ_w is density of water, G_s is specific gravity of sand, e is sand void ratio, e_{max} is the maximum void ratio of sand, e_{min} is the minimum void ratio of sand, g is the gravity acceleration, γ is the unit weight of sand. The value of G_s, e_{max} and e_{min} are summarized in Table 3.1. The amount of sand used for sand bed according to different RD is given in Table A.1.

Table A.1 Amount of Sand According to Different RD

Minimum Void Ratio, e_{min}	0.836		
Maximum Void Ratio, e_{max}	1.07		
Sand Volume, V (m^3)	$1.71*10^{-2}$		
Relative Density, RD (%)	50	60	70
Void ratio, e	0.896	0.861	0.825
Dry Density, ρ_d (Kg/m^3)	$1.398*10^3$	$1.424*10^3$	$1.451*10^3$
Sand Amount, m (Kg)	23.8	24.2	24.7

APPENDIX B

Table B.1 Calculated tilt angle per wave cycle for different wave height with a fixed wave period

no.	wave height (m)	wave period (s)	Caisson width (m)	water depth (m)	ϕ'	remark	Caisson mass (kg)	d (m)	W' (kN) *10^3	P' (kPa)	Pf (kN/m)	Pu (kPa)	S (m)	D (m)	Tau (kPa)	Tilt angle (rad)
1	10	15	18	26	34	ϕ'=34 B=18,d=18	13821183.7	18	70356	159.9	2123.2281	72.882844	3.7	1.5	366.46	0.0249
2	12	15	18	26	34		13821183.7	18	70356	159.9	2672.3335	87.45941	3.5	1.4	363.47	0.8523
3	14	15	18	26	34		13821183.7	18	70356	159.9	3258.861	102.036	3.3	1.3	360.41	3.14
4	10	15	18	26	30		13821183.7	18	70356	159.9	2123.2281	72.882844	4.2	1.6	318.97	0.0396
5	12	15	18	26	30	ϕ'=30	13821183.7	18	70356	159.9	2672.3335	87.45941	4	1.5	316.33	1.0272
6	14	15	18	26	30		13821183.7	18	70356	159.9	3258.861	102.036	3.8	1.3	311.15	3.14
7	10	15	18	26	38		13821183.7	18	70356	159.9	2123.2281	72.882844	3.2	1.5	421.17	0.0168
8	12	15	18	26	38	ϕ'=38	13821183.7	18	70356	159.9	2672.3335	87.45941	3.1	1.3	414.72	0.7465
9	14	15	18	26	38		13821183.7	18	70356	159.9	3258.861	102.036	2.9	1.2	411.29	3.14
10	10	15	14	26	34	ϕ'=34 B=14,d=18	11039877.6	18	57564	159.9	2123.2281	72.882844	3.2	1.1	350.21	1.3354
11	12	15	14	26	34		11039877.6	18	57564	159.9	2672.3335	87.45941	3	1	347.28	3.14
12	14	15	14	26	34		11039877.6	18	57564	159.9	3258.861	102.036	2.8	0.9	344.2	3.14
13	10	15	14	26	30		11039877.6	18	57564	159.9	2123.2281	72.882844	3.7	1.1	301.87	1.6503
14	12	15	14	26	30	ϕ'=30	11039877.6	18	57564	159.9	2672.3335	87.45941	3.5	1	299.23	3.14
15	14	15	14	26	30		11039877.6	18	57564	159.9	3258.861	102.036	3.3	0.9	296.47	3.14
16	10	15	14	26	38		11039877.6	18	57564	159.9	2123.2281	72.882844	2.8	1	400.2	1.2366
17	12	15	14	26	38	ϕ'=38	11039877.6	18	57564	159.9	2672.3335	87.45941	2.6	0.9	396.84	3.14
18	14	15	14	26	38		11039877.6	18	57564	159.9	3258.861	102.036	2.5	0.8	393.27	3.14
19	10	15	22	26	34	ϕ'=34 B=22,d=18	16602489.8	18	83148	159.9	2123.2281	72.882844	4.1	2.1	387.4	0
20	12	15	22	26	34		16602489.8	18	83148	159.9	2672.3335	87.45941	3.9	1.9	381.71	0.0214
21	14	15	22	26	34		16602489.8	18	83148	159.9	3258.861	102.036	3.7	1.7	375.83	0.3214
22	10	15	22	26	30		16602489.8	18	83148	159.9	2123.2281	72.882844	4.7	2.2	337.82	0

23	12	15	22	26	30	$\phi'=30$	16602489.8	18	83148	159.9	2672.3335	87.45941	4.5	2	332.81	0.031664
24	14	15	22	26	30		16602489.8	18	83148	159.9	3258.861	102.036	4.3	1.8	327.66	0.363298
25	10	15	22	26	38		16602489.8	18	83148	159.9	2123.2281	72.882844	3.6	2	441.28	0
26	12	15	22	26	38	$\phi'=38$	16602489.8	18	83148	159.9	2672.3335	87.45941	3.5	1.8	434.94	0.015395
27	14	15	22	26	38		16602489.8	18	83148	159.9	3258.861	102.036	3.3	1.6	428.34	0.339483
28	10	15	18	22	34	$\phi'=34$	13821183.7	14	84821	192.8	2059.446	78.48372	3.8	1.9	450.25	0
29	12	15	18	22	34	B=18,d=14	13821183.7	14	84821	192.8	2723.6487	94.180469	3.6	1.7	445.1	0.04714
30	14	15	18	22	34		13821183.7	14	84821	192.8	3465.413	109.8772	3.5	1.5	439.5	2.600829
31	10	15	18	22	30		13821183.7	14	84821	192.8	2059.446	78.48372	4.5	2	380.3	0
32	12	15	18	22	30	$\phi'=30$	13821183.7	14	84821	192.8	2723.6487	94.180469	4.3	1.8	375.79	0.08
33	14	15	18	22	30		13821183.7	14	84821	192.8	3465.413	109.8772	4.1	1.6	371.07	3.14
34	10	15	18	22	38		13821183.7	14	84821	192.8	2059.446	78.48372	3.4	1.8	502.34	0
35	12	15	18	22	38	$\phi'=38$	13821183.7	14	84821	192.8	2723.6487	94.180469	3.3	1.6	496.28	0.033011
36	14	15	18	22	38		13821183.7	14	84821	192.8	3465.413	109.8772	3.1	1.5	493.47	2.103455
37	10	15	18	30	34	$\phi'=34$	13821183.7	22	55891	127	2130.483	67.72848	3.3	1.2	305.12	0.51431
38	12	15	18	30	34		13821183.7	22	55891	127	2614.1946	81.27417	3.1	1.1	301.47	2.269414
39	14	15	18	30	34	B=18, d=22	13821183.7	22	55891	127	3118.6	94.81987	2.9	1	297.74	3.14
40	10	15	18	30	30		13821183.7	22	55891	127	2130.483	67.72848	3.8	1.3	260.67	0.59576
41	12	15	18	30	30	$\phi'=30$	13821183.7	22	55891	127	2614.195	81.27417	3.6	1.2	257.66	2.444678
42	14	15	18	30	30		13821183.7	22	55891	127	3118.6	94.81987	3.4	1	252.07	3.14
43	10	15	18	30	38		13821183.7	22	55891	127	2130.483	67.72848	3	1.2	341.85	0.473809
44	12	15	18	30	38		13821183.7	22	55891	127	2614.195	81.27417	2.8	1.1	338.1	2.058218
45	14	15	18	30	38	$\phi'=38$	13821183.7	22	55891	127	3118.6	94.81987	2.6	0.9	330.8	3.14
46	10	15	14	22	34	B=14, d=14	11039877.6	14	68814	191.2	2059.446	78.48372	3.3	1.3	411.86	0.202527
47	12	15	14	22	34	$\phi'=34$	11039877.6	14	68814	191.2	2723.6487	94.180469	3.2	1.2	409.24	1.242234
48	14	15	14	22	34		11039877.6	14	68814	191.2	3465.413	109.8772	3	1.1	406.69	3.14
49	10	15	14	22	30		11039877.6	14	68814	191.2	2059.446	78.48372	4.5	2	380.3	0.092326
50	12	15	14	22	30	$\phi'=30$	11039877.6	14	68814	191.2	2723.6487	94.180469	4.3	1.8	375.79	3.14
51	14	15	14	22	30		11039877.6	14	68814	191.2	3465.413	109.8772	4.1	1.6	371.07	3.14
52	10	15	14	22	38		11039877.6	14	68814	191.2	2059.446	78.48372	3.4	1.8	502.34	0.050281

53	12	15	14	22	38	ϕ'=38	11039877.6	14	68814	191.2	2723.6487	94.180469	3.3	1.6	496.28	3.14
54	14	15	14	22	38		11039877.6	14	68814	191.2	3465.413	109.8772	3.1	1.5	493.47	3.14
55	10	15	14	30	34	ϕ'=34	11039877.6	22	46314	128.6	2130.483	67.72848	3	0.8	282.62	3.14
56	12	15	14	30	34	B=14, d=22	11039877.6	22	46314	128.6	2614.1946	81.27417	2.8	0.8	282.06	3.14
57	14	15	14	30	34		11039877.6	22	46314	128.6	3118.6	94.81987	2.6	0.7	278.49	3.14
58	10	15	14	30	30	ϕ'=30	11039877.6	22	46314	128.6	2130.483	67.72848	3.4	0.9	246.82	3.14
59	12	15	14	30	30		11039877.6	22	46314	128.6	2614.1946	81.27417	3.2	0.8	243.79	3.14
60	14	15	14	30	30		11039877.6	22	46314	128.6	3118.6	94.81987	3	0.7	240.62	3.14
61	10	15	14	30	38	ϕ'=38	11039877.6	22	46314	128.6	2130.483	67.72848	2.6	0.8	324.54	3.14
62	12	15	14	30	38		11039877.6	22	46314	128.6	2614.1946	81.27417	2.4	0.7	320.6	3.14
63	14	15	14	30	38		11039877.6	22	46314	128.6	3118.6	94.81987	2.3	0.6	316.67	3.14
64	10	15	22	22	34	ϕ'=34	16602489.8	14	100827	193.9	2059.446	78.48372	4.4	2.5	460.24	0
65	12	15	22	22	34	B=22, d=14	16602489.8	14	100827	193.9	2723.6487	94.180469	4.2	2.3	455.05	0
66	14	15	22	22	34		16602489.8	14	100827	193.9	3465.413	109.8772	4	2.1	449.68	0.052573
67	10	15	22	22	30		16602489.8	14	100827	193.9	2059.446	78.48372	5	2.7	402.16	0
68	12	15	22	22	30	ϕ'=30	16602489.8	14	100827	193.9	2723.6487	94.180469	4.8	2.4	395.22	0
69	14	15	22	22	30		16602489.8	14	100827	193.9	3465.413	109.8772	4.6	2.2	390.47	0.111444
70	10	15	22	22	38		16602489.8	14	100827	193.9	2059.446	78.48372	3.9	2.4	525.89	0
71	12	15	22	22	38	ϕ'=38	16602489.8	14	100827	193.9	2723.6487	94.180469	3.7	2.1	516.96	0
72	14	15	22	22	38		16602489.8	14	100827	193.9	3465.413	109.8772	3.6	1.9	510.72	0.045448
73	10	15	22	30	34	ϕ'=34	16602489.8	22	65469	125.9	2130.483	67.72848	3.7	1.7	313.2	0.0306
74	12	15	22	30	34	B=22, d=22	16602489.8	22	65469	125.9	2614.1946	81.27417	3.5	1.5	307.06	0.697857
75	14	15	22	30	34		16602489.8	22	65469	125.9	3118.6	94.81987	3.3	1.3	300.74	2.779939
76	10	15	22	30	30	ϕ'=30	16602489.8	22	65469	125.9	2130.483	67.72848	4.2	1.8	276.38	0.053575
77	12	15	22	30	30		16602489.8	22	65469	125.9	2614.1946	81.27417	4	1.6	271	0.84145
78	14	15	22	30	30		16602489.8	22	65469	125.9	3118.6	94.81987	3.7	1.4	265.16	3.14
79	10	15	22	30	38	ϕ'=38	16602489.8	22	65469	125.9	2130.483	67.72848	3.3	1.6	358.14	0.028089
80	12	15	22	30	38		16602489.8	22	65469	125.9	2614.1946	81.27417	3.1	1.4	351.22	0.585175
81	14	15	22	30	38		16602489.8	22	65469	125.9	3118.6	94.81987	2.9	1.3	347.41	2.449798

Table B.2 Calculated tilt angle per wave cycle for different wave period with a fixed wave height

no.	wave height (m)	wave period (s)	caisson width (m)	water depth (m)	ϕ'	remark	M	d (m)	P' (kPa)	W'*10^3 (kN)	Pf (kN/m)	Pu (kPa)	arm (m)	S (m)	D (m)	Tau (kPa)	Tilt angle (rad)
1	10	13	18	26	34		13821183.7	18	159.9	70356	1952.453	64.187778	13.07864	3.8	1.6	369.26	0.0023
2	10	15	18	26	34	ϕ'=34	13821183.7	18	159.9	70356	2123.2281	72.88284	12.94875	3.7	1.5	366.46	0.0249
3	10	17	18	26	34	B=18,d=18	13821183.7	18	159.9	70356	2257.519	79.72719	12.86101	3.6	1.5	366.36	0.1650
4	10	13	18	26	30		13821183.7	18	159.9	70356	1952.453	64.187778	13.07864	4.3	1.7	321.42	0.0057
5	10	15	18	26	30	ϕ'=30	13821183.7	18	159.9	70356	2123.2281	72.88284	12.94875	4.2	1.6	318.97	0.0396
6	10	17	18	26	30		13821183.7	18	159.9	70356	2257.519	79.72719	12.86101	4.1	1.6	318.84	0.2890
7	10	13	18	26	38		13821183.7	18	159.9	70356	1952.453	64.187778	13.07864	3.3	1.5	421.19	0.0009
8	10	15	18	26	38	ϕ'=38	13821183.7	18	159.9	70356	2123.2281	72.88284	12.94875	3.2	1.5	421.17	0.0168
9	10	17	18	26	38		13821183.7	18	159.9	70356	2257.519	79.72719	12.86101	3.2	1.4	417.99	0.1087
10	10	13	14	26	34	ϕ'=34	11039877.6	18	159.9	57564	1952.4528	64.187778	13.07864	3.3	1.1	350.26	0.7595
11	10	15	14	26	34	B=14,d=18	11039877.6	18	159.9	57564	2123.2281	72.882844	12.948749	3.2	1.1	350.21	1.3354
12	10	17	14	26	34		11039877.6	18	159.9	57564	2257.519	79.72719	12.86101	3.1	1	347.32	3.14
13	10	13	14	26	30		11039877.6	18	159.9	57564	1952.4528	64.187778	13.07864	3.8	1.1	301.98	1.0523
14	10	15	14	26	30	ϕ'=30	11039877.6	18	159.9	57564	2123.2281	72.882844	12.948749	3.7	1.1	301.87	1.6503
15	10	17	14	26	30		11039877.6	18	159.9	57564	2257.519	79.72719	12.86101	3.6	1.1	301.77	3.14
16	10	13	14	26	38		11039877.6	18	159.9	57564	1952.4528	64.187778	13.07864	2.9	1	400.2	0.5675
17	10	15	14	26	38	ϕ'=38	11039877.6	18	159.9	57564	2123.2281	72.882844	12.948749	2.8	1	400.2	1.2366
18	10	17	14	26	38		11039877.6	18	159.9	57564	2257.519	79.72719	12.86101	2.7	1	400.24	3.14
19	10	13	22	26	34	ϕ'=34	16602489.8	18	159.9	83148	1952.4528	64.187778	13.07864	4.3	2.1	387.62	0
20	10	15	22	26	34	B=22,d=18	16602489.8	18	159.9	83148	2123.2281	72.882844	12.948749	4.1	2.1	387.4	0
21	10	17	22	26	34		16602489.8	18	159.9	83148	2257.519	79.72719	12.86101	4	2	384.57	0
22	10	13	22	26	30		16602489.8	18	159.9	83148	1952.4528	64.187778	13.07864	4.8	2.2	337.97	0
23	10	15	22	26	30	ϕ'=30	16602489.8	18	159.9	83148	2123.2281	72.882844	12.948749	4.7	2.2	337.82	0
24	10	17	22	26	30		16602489.8	18	159.9	83148	2257.519	79.72719	12.86101	4.6	2.1	335.33	0
25	10	13	22	26	38		16602489.8	18	159.9	83148	1952.4528	64.187778	13.07864	3.8	2	441.38	0

26	10	15	22	26	38	$\phi'=38$	16602489.8	18	159.9	83148	2123.2281	72.882844	12.948749	3.6	2	441.28	0
27	10	17	22	26	38		16602489.8	18	159.9	83148	2257.519	79.72719	12.86101	3.6	1.9	438.15	0
28	10	13	18	22	34	$\phi'=34$	13821183.7	14	192.8	84820.8	1940.653	70.52432	11.51304	3.9	1.9	450.05	0
29	10	15	18	22	34	B=18,d=14	13821183.7	14	192.8	84820.8	2059.446	78.48372	11.42487	3.8	1.9	450.25	0
30	10	17	18	22	34		13821183.7	14	192.8	84820.8	2163.309	84.53352	11.36575	3.7	1.9	450.49	0
31	10	13	18	22	30		13821183.7	14	192.8	84820.8	1940.653	70.52432	11.51304	4.6	2.1	382.49	0
32	10	15	18	22	30	$\phi'=30$	13821183.7	14	192.8	84820.8	2059.446	78.48372	11.42487	4.5	2	380.3	0
33	10	17	18	22	30		13821183.7	14	192.8	84820.8	2163.309	84.53352	11.36575	4.4	2	380.39	0
34	10	13	18	22	38		13821183.7	14	192.8	84820.8	1940.653	70.52432	11.51304	3.5	1.8	502.1	0
35	10	15	18	22	38	$\phi'=38$	13821183.7	14	192.8	84820.8	2059.446	78.48372	11.42487	3.4	1.8	502.34	0
36	10	17	18	22	38		13821183.7	14	192.8	84820.8	2163.309	84.53352	11.36575	3.3	1.8	502.63	0
37	10	13	14	22	34	B=14, d=14	11039877.6	14	191.2	68814.4	1940.653	70.52432	11.51304	3.4	1.4	414.37	0.017254
38	10	15	14	22	34	$\phi'=34$	11039877.6	14	191.2	68814.4	2059.446	78.48372	11.42487	3.4	1.3	411.66	0.092326
39	10	17	14	22	34		11039877.6	14	191.2	68814.4	2163.309	84.53352	11.36575	3.3	1.3	411.86	0.757342
40	10	13	14	22	30		11039877.6	14	191.2	68814.4	1940.653	70.52432	11.51304	3.9	1.4	360.23	0.033597
41	10	15	14	22	30	$\phi'=30$	11039877.6	14	191.2	68814.4	2059.446	78.48372	11.42487	3.8	1.4	360.37	0.202527
42	10	17	14	22	30		11039877.6	14	191.2	68814.4	2163.309	84.53352	11.36575	3.8	1.4	360.37	1.93923
43	10	13	14	22	38		11039877.6	14	191.2	68814.4	1940.653	70.52432	11.51304	3	1.3	480.82	0.007901
44	10	15	14	22	38	$\phi'=38$	11039877.6	14	191.2	68814.4	2059.446	78.48372	11.42487	2.9	1.3	481.18	0.050281
45	10	17	14	22	38		11039877.6	14	191.2	68814.4	2163.309	84.53352	11.36575	2.8	1.2	478.28	0.314502
46	10	13	22	22	34	$\phi'=34$	16602489.8	14	193.9	100827	1940.6533	70.52432	11.51304	4.5	2.6	462.78	0
47	10	15	22	22	34	B=22, d=14	16602489.8	14	193.9	100827	2059.446	78.48372	11.42487	4.4	2.5	460.24	0
48	10	17	22	22	34		16602489.8	14	193.9	100827	2163.309	84.53352	11.36575	4.3	2.5	460.38	0
49	10	13	22	22	30		16602489.8	14	193.9	100827	1940.653	70.52432	11.51304	5.2	2.7	402.03	0
50	10	15	22	22	30	$\phi'=30$	16602489.8	14	193.9	100827	2059.446	78.48372	11.42487	5	2.7	402.16	0
51	10	17	22	22	30		16602489.8	14	193.9	100827	2163.309	84.53352	11.36575	5	2.6	399.83	0
52	10	13	22	22	38		16602489.8	14	193.9	100827	1940.653	70.52432	11.51304	4	2.4	525.69	0
53	10	15	22	22	38	$\phi'=38$	16602489.8	14	193.9	100827	2059.446	78.48372	11.42487	3.9	2.4	525.89	0
54	10	17	22	22	38		16602489.8	14	193.9	100827	2163.309	84.53352	11.36575	3.8	2.3	523.02	0
55	10	13	18	30	34	$\phi'=34$	13821183.7	22	127	55891.2	1933.0861	58.50766	14.14302	3.4	1.3	308.34	0.199699

56	10	15	18	30	34		13821183.7	22	127	55891.2	2130.483	67.72848	13.97188	3.3	1.2	305.12	0.51431
57	10	17	18	30	34	B=18, d=22	13821183.7	22	127	55891.2	2294.849	75.38909	13.85358	3.2	1.2	304.77	3.14
58	10	13	18	30	30		13821183.7	22	127	55891.2	1933.0861	58.50766	14.14302	4	1.4	263.61	0.261843
59	10	15	18	30	30	$\phi'=30$	13821183.7	22	127	55891.2	2130.483	67.72848	13.97188	3.8	1.3	260.67	0.59576
60	10	17	18	30	30		13821183.7	22	127	55891.2	2294.849	75.38909	13.85358	3.7	1.2	257.97	3.14
61	10	13	18	30	38		13821183.7	22	127	55891.2	1933.0861	58.50766	14.14302	3.1	1.2	342.13	0.043025
62	10	15	18	30	38		13821183.7	22	127	55891.2	2130.483	67.72848	13.97188	3	1.2	341.85	0.473809
63	10	17	18	30	38	$\phi'=38$	13821183.7	22	127	55891.2	2294.849	75.38909	13.85358	2.9	1.1	338.36	2.958016
64	10	13	14	30	34	$\phi'=34$	11039877.6	22	128.6	46313.6	1933.0861	58.50766	14.14302	3.1	0.9	285.74	3.14
65	10	15	14	30	34	B=14, d=22	11039877.6	22	128.6	46313.6	2130.483	67.72848	13.97188	3	0.8	282.62	3.14
66	10	17	14	30	34		11039877.6	22	128.6	46313.6	2294.849	75.38909	13.85358	2.9	0.8	282.33	3.14
67	10	13	14	30	30	$\phi'=30$	11039877.6	22	128.6	46313.6	1933.0861	58.50766	14.14302	3.5	0.9	247.12	3.14
68	10	15	14	30	30		11039877.6	22	128.6	46313.6	2130.483	67.72848	13.97188	3.4	0.9	246.82	3.14
69	10	17	14	30	30		11039877.6	22	128.6	46313.6	2294.849	75.38909	13.85358	3.3	0.8	244.09	3.14
70	10	13	14	30	38	$\phi'=38$	11039877.6	22	128.6	46313.6	1933.0861	58.50766	14.14302	2.7	0.9	328.09	2.811867
71	10	15	14	30	38		11039877.6	22	128.6	46313.6	2130.483	67.72848	13.97188	2.6	0.8	324.54	3.14
72	10	17	14	30	38		11039877.6	22	128.6	46313.6	2294.849	75.38909	13.85358	2.5	0.8	324.32	3.14
73	10	13	22	30	34	$\phi'=34$	16602489.8	22	125.9	65468.8	1933.0861	58.50766	14.14302	3.9	1.7	313.8	0.003085
74	10	15	22	30	34	B=22, d=22	16602489.8	22	125.9	65468.8	2130.483	67.72848	13.97188	3.7	1.7	313.2	0.0306
75	10	17	22	30	34		16602489.8	22	125.9	65468.8	2294.849	75.38909	13.85358	3.6	1.6	310.15	0.209185
76	10	13	22	30	30	$\phi'=30$	16602489.8	22	125.9	65468.8	1933.0861	58.50766	14.14302	4.4	1.8	276.98	0.004586
77	10	15	22	30	30		16602489.8	22	125.9	65468.8	2130.483	67.72848	13.97188	4.2	1.8	276.38	0.053575
78	10	17	22	30	30		16602489.8	22	125.9	65468.8	2294.849	75.38909	13.85358	4.1	1.7	273.7	0.266322
79	10	13	22	30	38	$\phi'=38$	16602489.8	22	125.9	65468.8	1933.0861	58.50766	14.14302	3.4	1.7	361.52	0.001788
80	10	15	22	30	38		16602489.8	22	125.9	65468.8	2130.483	67.72848	13.97188	3.3	1.6	358.14	0.028089
81	10	17	22	30	38		16602489.8	22	125.9	65468.8	2294.849	75.38909	13.85358	3.2	1.5	354.71	0.171215